Aerosol Characteristics and Radiative Effects over Asia

A thesis submitted in partial fulfilment of

the requirements for the degree of

Doctor of Philosophy

by

Kamran Ansari

Roll No.: 20330010

Under the supervision of

Prof. S. Ramachandran

Space and Atmospheric Sciences Division

Physical Research Laboratory, Ahmedabad, 380009, India

Department of Physics

Indian Institute of Technology Gandhinagar

August 2025

DECLARATION

I, **Kamran Ansari (Roll No.: 20330010)**, hereby declare that this thesis titled **Aerosol Characteristics and Radiative Effects over Asia** submitted to Indian Institute of Technology Gandhinagar towards the partial requirement of **Doctor of Philosophy** in **Physics** is an original work carried out by me under the supervision of **Prof. S. Ramachandran**. All information and facts provided in this thesis are correct to the best of my knowledge. I also declare that wherever I have borrowed any ideas or results from someone else, I have properly cited the sources. No part of this thesis has formed the basis for the award of any other degree in any university or institution.

Date: 6th November 2025

Place: Ahmedabad, India

Kamran Ansari
Space and Atmospheric Sciences Division
Physical Research Laboratory
Ahmedabad, Gujarat, 380009, India

CERTIFICATE

It is to certify that the work contained in the thesis titled **Aerosol Characteristics and Radiative Effects over Asia** submitted by **Kamran Ansari (Roll No.: 20330010)** to Indian Institute of Technology Gandhinagar has been carried out under my supervision at Space and Atmospheric Sciences Division, Physical Research Laboratory, Ahmedabad and it has not been submitted elsewhere for the award of any degree.

Date: 6th November 2025

Place: Ahmedabad, India

Prof. S. Ramachandran
(Ph.D. Supervisor)
Senior Professor
Space and Atmospheric Sciences Division
Physical Research Laboratory
Ahmedabad, Gujarat, 380009, India

THESIS APPROVAL

Certified that the thesis titled

Aerosol Characteristics and Radiative Effects over Asia

submitted by **Mr. Kamran Ansari** (IITGN Roll No. **20330010**) to the **Indian Institute of Technology (IIT) Gandhinagar,** is approved for the degree of ***Doctor of Philosophy*.**

Date: 6th November 2025 Place: Ahmedabad, India

Prof. Dilip Ganguly
External Examiner,
IIT Delhi

Prof. Sameer Patel
FDC Member,
IIT Gandhinagar

Prof. Harish Gadhavi
DSC and FDC Member,
PRL Ahmedabad

Prof. Neeraj Rastogi
DSC and FDC Member,
PRL Ahmedabad

Dr. Amzad Hussain Laskar
DSC and FDC Member,
PRL Ahmedabad

Prof. S. Ramachandran
PhD Supervisor and FDC Member,
PRL Ahmedabad

Dedicated to my family and to all those who work tirelessly to make our Earth cleaner, healthier, and more livable for future generations

Acknowledgements

Over the past five years, I have devoted myself to pursue a Ph.D., a journey enriched with learning, joy, excitement, challenges, and moments of both triumph and setback, all of which have contributed to my growth in both professional and personal life. This experience has taught me to learn, unlearn, and relearn; to think critically and multi-directionally; to ask questions, foster curiosity, and work with diligence, efficiency, and integrity. I firmly believe that this journey and work presented in the thesis did justice to earn the honor of a Ph.D. Nevertheless, this accomplishment would not have been possible without the generous support and steadfast contributions of many remarkable individuals, to whom I extend my deepest gratitude.

First and foremost, I feel both grateful and privileged to express my profound and heartfelt gratitude to my Ph.D. supervisor, Prof. S. Ramachandran, for his unwavering support, insightful guidance, constructive discussions, care, and constant motivation throughout my doctoral journey. His deep knowledge, enthusiasm for research, and relentless drive have continually inspired me to pursue my work with dedication. I am especially thankful for his patience, encouragement, and steadfast belief in me, even during times when my performance fell short of expectations. I remain deeply indebted to his sincerity, patience, genuine concern, and wholehearted support, all of which were instrumental in the successful completion of this thesis.

I extend my sincere gratitude to my DSC members, Prof. Harish Gadhavi, Prof. Neeraj Rastogi, and Dr. Amzad Hussain Laskar for their insightful suggestions, discussions, and feedback during the DSC seminars. Their comments have enabled me to approach my work from a broader and more comprehensive perspective. I am also grateful for their kind cooperation throughout the DSC, annual, and synopsis review processes.

I am profoundly thankful to Dr. T. A. Rajesh for fruitful discussions, suggestions, constructive support, genuine concern, and care. My heartfelt thanks to my fellow lab members, Vishnu, Nitin, and Bhavesh, for their invaluable support, encouragement, discussions, and for providing a conducive and healthy working environment.

I extend my heartfelt thanks to Prof. Anil Bhardwaj (Director), Prof. D. Pal-

lamraju (Dean), Prof. Dibyendu Chakrabarty (Head), Prof. L. K. Sahu (Deputy Head-1), and Prof. Som Kumar Sharma (Deputy Head-2) for their kind support and approval for my national and international trips, and for all important academic matters. I am thankful to various other divisions at PRL, including Computer Networking and Information Technology (CNIT) (especially Mr. Girish Padia, Mr. Atul Manke, Mr. Hitendra Mishra, Mr. Vaibhav, and Mr. Lakum), Library (especially Dr. Pragya Pandey), Accounts (especially Amee Ma'am, Mr. Suresh Patel), purchase (especially Sneha Ma'am), administration (especially Richa Ma'am), dispensary, CMG, transport, all canteen staff, and housekeeping staff for their kind cooperation at various stages. I also acknowledge the support from the Academic and Administrative personnel at IIT Gandhinagar for providing the necessary resources and smooth processing of official formalities.

I sincerely acknowledge all the principal investigators (PIs) of each AERONET site for maintaining and establishing the AERONET sites. I am thankful to all the scientists and associated personnel at NASA, ECMWF, and PCMDI for providing the open-access datasets from satellite retrievals and model simulations. I am very thankful to Dr. Ribu Cherian for his valuable comments, suggestions, and for providing the required datasets. I also want to acknowledge Dr. Xiaoli Wei (Shanghai Meteorological Service, China), Dr. Feng Zhang (Fudan University, China), Mr. Gaurav (University of Valencia, Spain), and Dr. Shikuan Jin (China University of Geosciences, China) for their help and discussions. I am deeply grateful to the Department of Space (DOS), Department of Science & Technology (DST)-Science and Engineering Research Board (SERB), Surface Ocean – Lower Atmosphere Study (SOLAS), and German Ministry for Education and Research (BMBF) for providing the funding to attend the international conference and school.

This Ph.D. journey would never have been with so much joy and happiness without the immense and unconditional love and care from my dearest friends. I had the privilege of residing in "Lobby – B" of PRL Navrangpura hostel and spent most of my unforgettable and lifelong memories during the last five years with my amazing and lovely lobbymates/batchmates – Debashis, Dharmendra, and Gurubhai. These guys are truly amazing and good human beings, and they have provided the unconditional help and support in every situation and made the most friendly environment. I am very grateful to all my batchmates – Arup Bhai, Wafikul (W bhai), Mansi, Akanksha, Chandrima, Trinesh, Sanjay, Aditya bhau, Sandeep, Arup M, Malika, and Ananya. My

heartfelt thanks and respect to my seniors – Gourav, Meghna, Monika, Yogesh, Sunil, Bijoy, Ankit, Sovan, Supriya, Sougata, Chandrima, Sourabh, Bharti, Atif, Siddhartha, Abdur, Kshitiz, and others. I have cherished the interaction and joyful time with juniors – Ms. Komal, Sandip, Shivam, Samarpan, Namit, Abhishek, Aakash, Bandhu, Harithasree, Shuvendu, Rahul, Fahad, Jana, Shreya, Dibyani, Achintyaa, Ankita, and others. I also appreciate the joyful experiences and connections with Dr. Harshbardhan (National Atmospheric Research Laboratory (NARL), Gadanki, India) and Ms. Garima (National Institute of Oceanography (NIO), Goa, India).

I truly enjoyed all the sports activities (e.g., cricket, volleyball, badminton, table tennis, and frisbee) and the festival celebrations in the hostel. They provided me a break and refreshing escape from my professional work. I am deeply thankful to all the enthusiastic and passionate players whose energy made the sports moment both enjoyable and competitive, perfectly blending intensity with fun. I always appreciate Ganesh bhai for his excitement and energetic nature towards sports, even in his old age. It was an honor and a privilege to play as a smasher for my division's Volleyball team, and we won three consecutive championships, which reflected our unity, dedication, and unmatched determination on the court.

Most importantly, I extend my deepest gratitude to my family—Mummy, Papa, Bhaiyas, and Bhabhis. During my doctoral studies, I spent several months away from home, and they always endured my absence, especially during many family events and festivals. Yet, they continually encouraged, supported, and stood with me, offering love and care without placing any pressure on me, making this journey smoother and more fulfilling. Finally, I wish to express my sincere appreciation to every individual, as well as to those who are unintentionally missed, whose invaluable support, assistance, and encouragement contributed to the successful completion of my Ph.D. thesis and who have been part of this important chapter in my academic life.

Kamran Ansari

Abstract

The uncertainty in assessing direct aerosol radiative forcing is notably higher over Asia. The accurate simulation and future projection of aerosol-climate interactions over Asia remain challenging due to evolving aerosol emissions with large heterogeneity, the limited ability of climate models to simulate recent aerosol trends, and the limited accurate observational constraints on columnar aerosol optical and radiative properties on the seasonal scale with their large inherent uncertainties over Asia. Thus, an accurate examination of aerosols using high-quality observations is essential over Asia. This thesis presents a comprehensive investigation of the spatial and regional distribution of aerosol columnar optical and radiative properties over Asia and other regions of the globe, utilizing high-quality AErosol RObotic NETwork (AERONET) datasets during the study period of 2015–2019 on annual and seasonal scales. Further, spatiotemporal collocated validations/evaluations of columnar aerosol optical and radiative properties, simulated by models (Modern-Era Retrospective Analysis for Research and Applications-2 (MERRA-2) and Copernicus Atmosphere Monitoring Service (CAMS)), and retrieved by satellite (Clouds and the Earth's Radiant Energy System (CERES)), are performed with results obtained from AERONET analysis.

Regionally, South Asia – I (Indo-Gangetic Plain) exhibits the highest regional and annual mean aerosol optical depth ($AOD_{0.50}$: 0.63 $\pm$ 0.15), followed by South Asia – II (0.37 $\pm$ 0.14), East (0.36 $\pm$ 0.13), Southeast (0.33 $\pm$ 0.10), and Central Asia (0.16 $\pm$ 0.07), due to the abundance of both fine- (e.g., anthropogenic) and coarse-mode (e.g., natural) aerosols. High AOD with lower single scattering albedo (SSA) results in high absorption AOD ($AAOD_{0.50}$: $\sim$0.06) and aerosol direct radiative effect (DRE) at each level (surface (DRE_{SFC}: $\sim$–70 Wm^{-2}) and top of atmosphere (DRE_{TOA}: $\sim$–30 Wm^{-2}) cooling, and atmospheric heating (DRE_{ATM}: $\sim$40 Wm^{-2})) over South Asia – I with statistically significant spatial and seasonal variations. In comparison, annual mean AOD, AAOD, and DRE are $\sim$40% lower in East and Southeast Asia. AOD, total volume concentration, DRE, and aerosol-induced atmospheric heating rate over North America, Europe, and Australia are $\sim$2–4 times lower than in Asia, with less spatiotemporal variations on an annual scale. These relative differences are even higher during winter, exhibiting lower ratios ($\sim$4–6 times) compared to Asia.

Global distribution of aerosol types reveals that South Asia – I is predominantly influenced by Mixed-fine (fine-dominated aerosols in Mixed type) aerosol type ($\sim$41%). A novel classification scheme is developed to accurately identify different absorbing aerosol types by leveraging the spectral characteristics of AOD and SSA of different absorbing aerosols, which remarkably reduces the contribution of unidentified type to almost nil ($\sim$2%) globally, demonstrating the robustness and enhanced accuracy of this new method. This scheme reveals the dominance of Mixed absorbing aerosol type over South Asia – I. Whereas, East North America and Europe are mostly influenced by Urban-industrial aerosol type and black carbon (BC) absorbing aerosol type (>50%) primarily due to fossil fuel combustion. Biomass burning emissions amplify the contribution of absorbing aerosol types of BC and carbonaceous aerosols (CA), and significantly enhance the AOD and AAOD over Africa, Southeast Asia, and South America during their respective dry seasons.

The performance of CAMS is found to be more effective than MERRA-2 in simulating AOD over Asia. MERRA-2 highly underestimates AERONET AOD over South Asia – I during winter and autumn, and over Southeast Asia during biomass burning seasons. However, the performance of both models is poor in simulating Ångström exponent, revealing the challenges in simulating the spectral distribution of fine- and coarse-mode aerosols. Despite the significant differences in aerosol content and composition regionally, MERRA-2 simulated SSA mostly lies in the moderately absorbing aerosols range ($0.90 \leq$ SSA < 0.95). Biases in AODs are low under low AOD conditions, whereas these biases (i.e., underestimations) increase in high AOD conditions globally in both models. In comparison to Asia, the performances of MERRA-2 and CAMS AODs are better (lower bias and higher Global Climate Observing System (GCOS) fraction) over Australia, North America, Europe, South America, and South Africa. Large underestimation of MERRA-2 simulated AOD in high AOD conditions leads to high underestimations in MERRA-2 simulated DREs. Underestimations in MERRA-2 DREs are higher over Asia, especially South Asia, due to frequent high AOD conditions, while MERRA-2 DREs align better with AERONET over North America, South America, Europe, and Australia, where AODs are lower. MERRA-2 performs better than CERES in reproducing the AERONET DREs, however, both exhibit significant biases over Asia, emphasizing the need to improve model simulations and satellite retrievals in high AOD regions.

This global study provides accurate observational constraints of aerosol colum-

nar optical and radiative properties on a seasonal scale, with a robust evaluation of model simulations and satellite retrievals by identifying their potential causes of biases, hitherto unavailable. The findings of this study are crucial to fine-tune and improve the aerosol optical properties and processes in both regional and global climate models, thereby enhancing the accuracy of present-day simulations and future projections of radiative and climate impact of aerosols.

Keywords: *Aerosol Optical Depth, Single Scattering Albedo, Aerosol Types, Absorbing Aerosol Types, Aerosol Direct Radiative Effect, Collocated Validation*

List of Abbreviations

AAE	Absorption Ångström Exponent
AAOD	Absorption Aerosol Optical Depth
AERONET	AErosol RObotic NETwork
AE	Ångström Exponent
AOD	Aerosol Optical Depth
ARF	Aerosol Radiative Forcing
ATM	Atmosphere
BB	Biomass Burning
BC	Black Carbon
BrC	Brown Carbon
CA	Carbonaceous Aerosols
CAMS	Copernicus Atmosphere Monitoring Service
CERES	Clouds and the Earth's Radiant Energy System
CMIP6	Coupled Model Intercomparison Project Phase 6
CVF	Coarse Volume Fraction
DRE	Direct Radiative Effect
DREE	Direct Radiative Effect Efficiency
DISORT	DIScrete Ordinate Radiative Transfer
ECMWF	European Centre for Medium-Range Weather Forecasts
EE	Expected Error
FMF	Fine Mode Fraction
FVF	Fine Volume Fraction
g	Asymmetry parameter
GAME	Global Atmospheric ModEl
GCOS	Global Climate Observing System
GF	GCOS Fraction
GOCART	Goddard Chemistry, Aerosol, Radiation, and Transport
HR	Heating rate
IGP	Indo-Gangetic Plain

IPCC	Intergovernmental Panel on Climate Change
MBE	Mean Bias Error
MATCH	Model for Atmospheric Transport and Chemistry
MERRA-2	Modern-Era Retrospective Analysis for Research and Applications-2
MODIS	MODerate resolution Imaging Spectroradiometer
NASA	National Aeronautics and Space Administration
OA	Organic Aerosols
OC	Organic Carbon
OPAC	Optical Properties of Aerosols and Clouds
RMSE	Root Mean Square Error
SA	Surface Albedo
SDA	Spectral Deconvolution Algorithm
SBDART	Santa Barbara DISORT Atmospheric Radiative Transfer
SFC	Surface
SSA	Single Scattering Albedo
TOA	Top Of the Atmosphere
TVC	Total Volume Concentration
UI	Urban-Industrial
VOC	Volatile Organic Carbon

Contents

List of Figures

List of Tables

1

Introduction

Earth's atmosphere is predominantly composed of nitrogen (∼78%) and oxygen (∼21%). The remaining volume (∼1%) is occupied by several minor trace gases and suspended particles (i.e., aerosols). Despite their small amount, aerosols are one of the most spatially and temporally inhomogeneous constituents that significantly affect the radiative balance of the Earth-atmosphere system. A brief introduction to atmospheric aerosols, their size distribution, sources, formation and removal mechanisms, residence time, optical properties, radiative effects, and climatic impacts, is provided in this chapter. The recent changes in aerosol characteristics over Asia, based on ground-based, satellite, and model simulations, are discussed. Furthermore, a critical review of recent studies on columnar aerosol properties and radiative effects over Asia is provided, highlighting existing major research gaps in these studies. These discussions provide the scientific rationale and motivation for defining the major objectives and the analyses required to fulfill the objectives of the thesis.

1.1 Atmospheric aerosols

Atmospheric aerosols are a mixture of solid and/or liquid particles suspended in air, with the exception of all hydrometeors (e.g., cloud droplets, ice crystals, raindrops, and snowflakes). Aerosols are one of the most spatially and temporally inhomogeneous components of the Earth's atmosphere due to the large heterogeneity in their sources and relatively shorter residence time in the lower atmosphere. The size of aerosols is an essential parameter for characterizing their behavior, impact, and residence time in the atmosphere. The residence time of aerosols varies as a function of their size from a few hours to a week in the troposphere. Depending on their size, they are divided into *nucleation* (0.001< radius <0.1 μm), *accumulation* (0.1< radius <1 μm), and

coarse (radius >1 μm) mode aerosols (Whitby, 1978) (Figure 1.1). Nucleation mode aerosols are mostly formed from the condensation of vapors and gas-to-particle conversion, and they have a shorter residence time of a few hours to a day, as they have high physical mobility and chemical activity. Nucleation mode eventually gets transformed into accumulation mode aerosols through coagulation and coalescence growth, and by the condensational growth of vapor by chemical reaction, resulting in gas-to-particle conversion onto the existing particles. Accumulation mode aerosols have the longest residence time of about a week. Both nucleation and accumulation mode aerosols are referred to as *fine* mode aerosols (0.001< radius <1 μm). Coagulation among accumulation mode aerosols is a slow process and does not effectively transfer into the coarse mode as the nucleation mode gets transformed into the accumulation mode (Seinfeld & Pandis, 2016). Coarse mode aerosols, such as wind-driven dust particles and sea salt aerosols, are mainly generated by mechanical processes. These particles are directly emitted into the atmosphere and they reside in the atmosphere for a few days.

According to the sources, aerosols are classified as *natural* and *anthropogenic* (Figure 1.1). The natural sources of aerosols are oceans, deserts, volcanoes, and vegetation. The anthropogenic sources of aerosols are emissions from traffic, industrial activities, construction, biomass burning, and domestic activities. However, forest fires can be caused by both natural and anthropogenic activities. Anthropogenic aerosols are predominantly found in the fine mode, whereas natural aerosols are mostly present in the coarse mode.

Depending on the formation processes, aerosols are classified into *primary* and *secondary* (Figure 1.1). Aerosols that are directly emitted in particulate form into the atmosphere are called primary aerosols. Primary aerosols are produced by the incomplete combustion of fossil fuels and biomass burning (such as black carbon (BC)), fly ash from industrial activities, biological materials, sea salt, and mineral dust particles. Secondary aerosols are not emitted directly in particulate form but are formed by chemical reactions through gas-to-particle conversion of gas-phase species such as SO_2, NO_x (=NO+NO_2), and volatile organic carbon (VOC), producing sulfate, nitrate, and secondary organic aerosols (OA).

The residence time of aerosols in the atmosphere is relatively shorter compared to greenhouse gases, due to the efficient removal processes. Aerosols are removed from the atmosphere by *dry deposition* and *wet deposition* (Figure 1.1). Dry deposition is

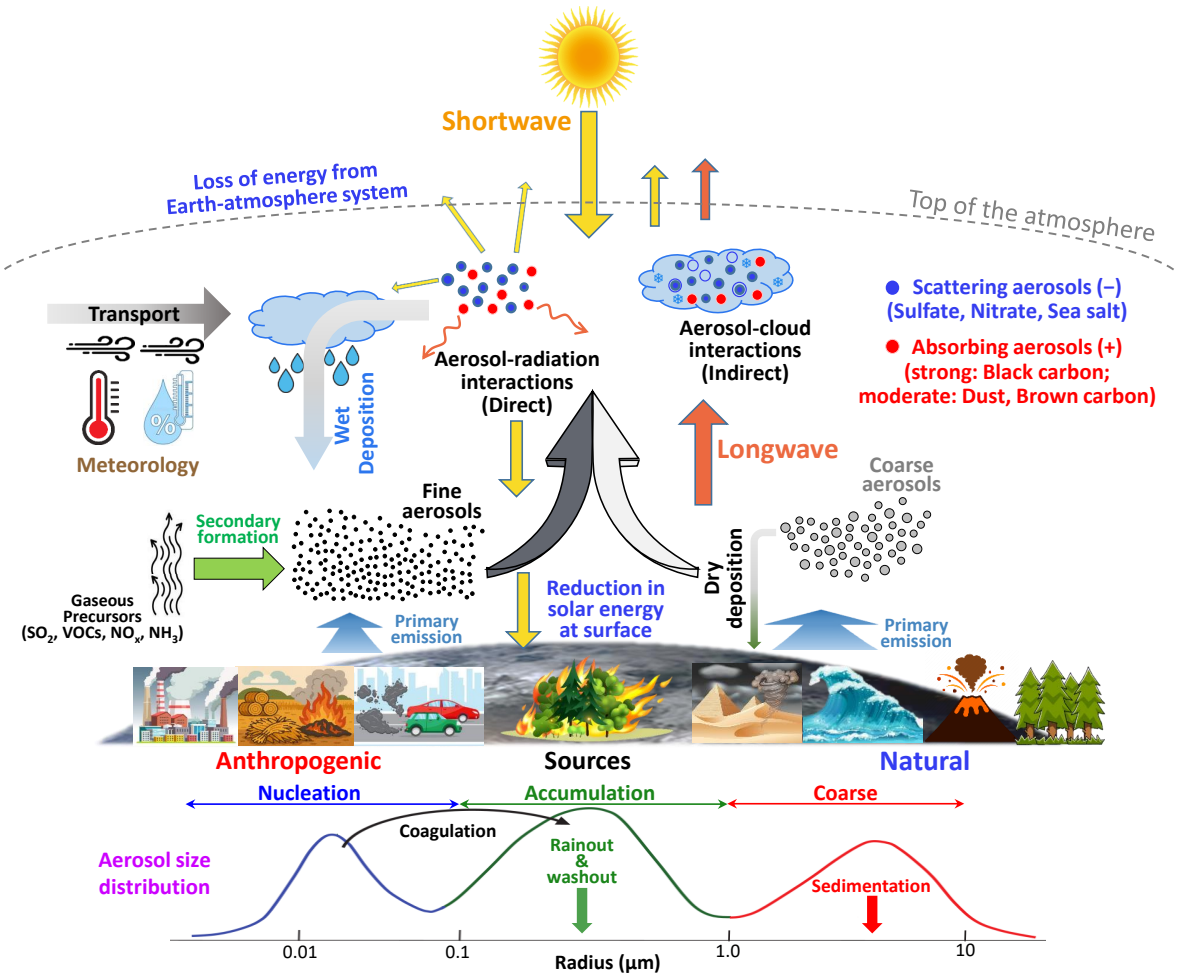

Figure 1.1: *Schematic of size distribution, sources, formation and removal processes, and radiative effects of atmospheric aerosols. Scattering aerosols are indicated by blue dots and induce a cooling effect (negative (–) radiative forcing), whereas absorbing aerosols are shown by red dots and induce a warming effect (positive (+) radiative forcing). Yellow and orange arrows represent shortwave (solar) and longwave (thermal) radiation, respectively. The thin yellow arrows show the scattered radiation by scattering aerosols, and curved red lines indicate the re-emitted radiation by absorbing aerosols. Water droplets and ice crystals inside a cloud are shown by unfilled blue circles and stellar dendrites, respectively. The thickness of all arrows qualitatively represents the strength and magnitude of radiation, formation, and removal processes.*

the settling of aerosols to the Earth's surface by gravitation, diffusion, and impaction. Aerosols larger than 10 μm are effectively removed by dry deposition (e.g., gravitational settling due to higher settling velocity for larger particles) (Jaenicke, 1993; Seinfeld & Pandis, 2016). Wet deposition includes all removal processes of aerosols from

the atmosphere in aqueous form, e.g., rain, fog, and snow. Wet deposition is the main removal mechanism for aerosols in the size range between 0.1 and 10 μm (Ramachandran, 2018). Due to the relatively fast removal mechanisms and the heterogeneous spatial distribution of emission sources, tropospheric aerosols exhibit significant spatial and temporal variations. Considering a mean residence time of aerosols to be around 5 days, they can be transported to thousands of kilometers (Bellouin et al., 2020).

1.2 Radiative and climate effects of aerosols

Radiative forcing (quantified in the unit of Wm^{-2}) is the change in the net radiative flux in the solar (shortwave) and terrestrial (longwave) spectra of the Earth-atmosphere system caused by changes in forcing agents (e.g., aerosols, greenhouse gases, solar flux, etc.) over a defined period. A positive radiative forcing refers to warming, while a negative forcing indicates cooling. Depending on the optical properties of aerosols (governed by their size distribution, refractive index, and chemical composition), they scatter and absorb shortwave and longwave radiation (Fig. 1.1). Scattering aerosols (e.g., sulfates, nitrates, sea salt, ammonium) increases the part of solar radiation reflected towards space, which results in a reduction of incoming solar radiation at the Earth's surface, and cooling of the climate system. Absorbing aerosols (e.g., BC, brown carbon (BrC), and dust) absorb the solar radiation, which increases the energy of the Earth-atmosphere system and results in warming the atmosphere. However, they still reduce the radiation reaching the surface and thus, cool the surface. BC, the strongest absorber per unit mass, has higher absorption in the near-IR range, and it has the largest contribution to total aerosol absorption (Bond & Bergstrom, 2006; Samset et al., 2018). BrC has highly wavelength-dependent absorption and has strong absorption in the near-UV range, which significantly decreases in the visible range ($>$0.4 μm) (Kirchstetter et al., 2004; Jethva & Torres, 2011; Kirillova et al., 2016; Samset et al., 2018). Similarly, dust absorption increases in shorter wavelengths (UV and short visible) and decreases in longer wavelengths (Bergstrom et al., 2007; Samset et al., 2018; Ansari & Ramachandran, 2025a).

The scattering and absorption of the shortwave and longwave radiation by aerosols is known as the *aerosol-radiation interactions* or *aerosol direct effect*, and it significantly influences the radiative balance of the Earth-atmosphere system (Myhre et al., 2013a; Bellouin et al., 2020). However, the effect of aerosol cooling and warming also

depends on the surface albedo (i.e., aerosols present over a brighter surface can enhance the absorption and reduce the surface cooling) and the presence of clouds (Keil & Haywood, 2003; Feng & Christopher, 2015; Zhang et al., 2016; Thorsen et al., 2020). Aerosols also alter the cloud microphysical properties by acting as cloud condensation nuclei (CCN). An increase in aerosols leads to an increase in CCN, and it generally increases the cloud droplet number concentration with more droplets in the smaller size for constant liquid water content, which eventually increases the cloud reflectivity and cloud lifetime. This effect is known as the *aerosol-cloud interaction* or *aerosol indirect effect*. The atmospheric warming by absorbing aerosols also alters the vertical temperature profile, which impacts atmospheric stability, relative humidity, and thus affects the cloud amount (i.e., cloud evaporation or cloud burn-off) (Allen & Sherwood, 2010; Wilcox, 2010, 2012). This effect is known as the aerosol *semi-direct effect*.

Aerosols exert both warming and cooling effects on Earth's climate, depending on their physical, optical, and chemical properties, and underlying surface albedo. The net radiative effect of aerosols is cooling globally, and this is higher over Asia (Li et al., 2022). Globally, anthropogenic aerosols are estimated to produce a net cooling of $\sim$–1.3 $\pm$ 0.7 Wm^{-2} at the top of the atmosphere (TOA), and this net aerosol cooling offsets a substantial part (up to one-third) of greenhouse gas-induced warming (Forster et al., 2021). An accurate characterization of aerosols is difficult due to their diverse sources, spatial distributions, complex chemical composition, and relatively shorter residence times. As a result, it is challenging to accurately constrain the aerosol optical and microphysical properties, represent them in climate models, and simulate their climate effects (Ramaswamy et al., 2019; Gliß et al., 2021; Li et al., 2022). Thus, despite their significant importance, aerosols remain the most uncertain forcing agent in quantifying present-day radiative effect, including the anthropogenic contribution (i.e., radiative forcing), and future climate projections (Forster et al., 2021).

1.3 Motivation of the thesis and research gaps

Anthropogenic aerosol emissions across Asia are exhibiting rapid change, both in content and composition, and in their spatial distribution (Li et al., 2017; Myhre et al., 2017; Ramachandran et al., 2025). In contrast to the decrease in anthropogenic aerosol emissions over Europe and North America as a result of effective mitigation policies, Asia has emerged as the largest emitter of anthropogenic aerosols and their precursors

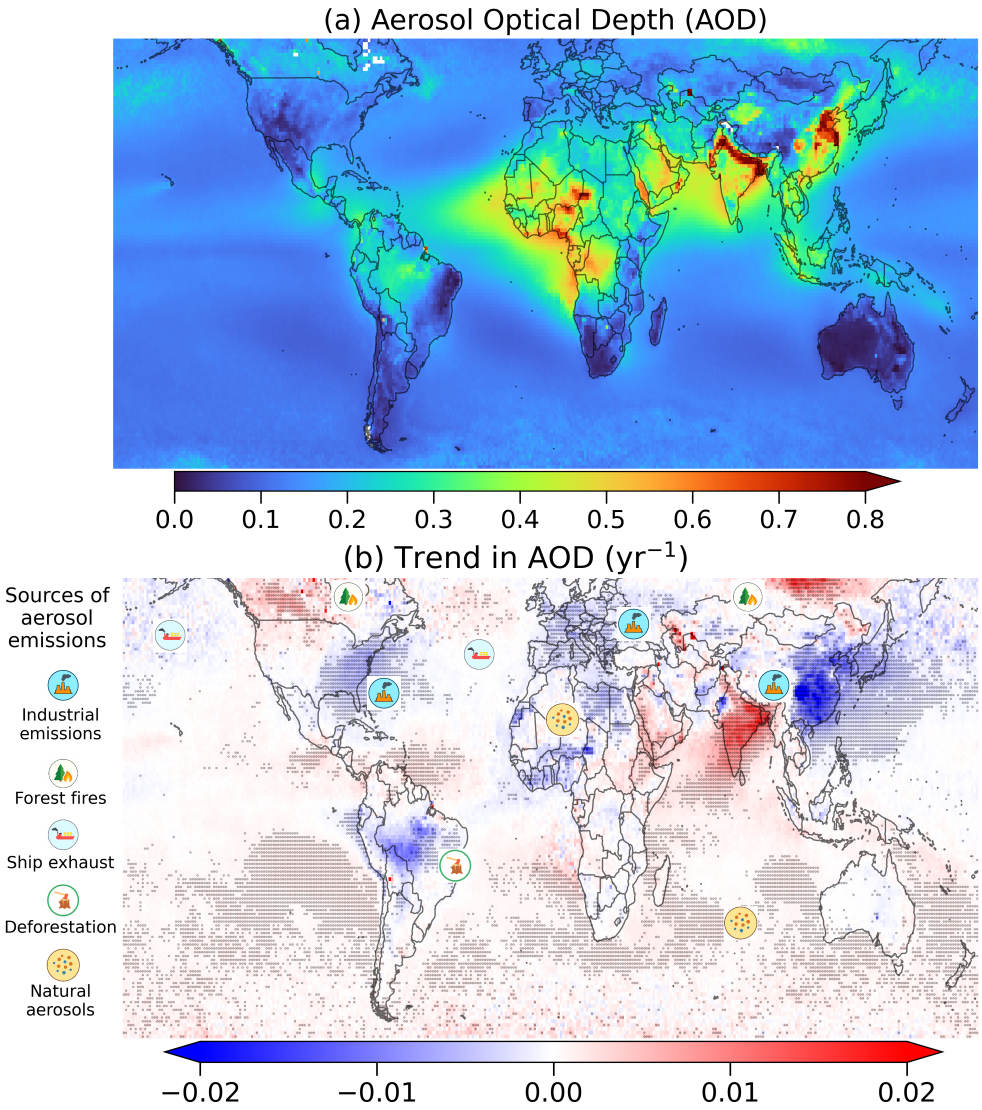

Figure 1.2: *(a) Global distribution of MODerate resolution Imaging Spectroradiometer (MODIS) (Terra + Aqua) retrieved annual mean (2015–2019) aerosol optical depth (AOD). (b) Trend in AOD (yr^{-1}) from 2003 to 2019 calculated by Theil–Sen's slope and statistically significant AOD trends (p-value <0.05; calculated by Mann-Kendall test) are shown by black dots. Major sources of aerosol emissions, responsible for the observed AOD changes, are shown by icons on the map in (b) (modified from Persad et al. (2023)).*

over the last few decades (Fig. 1.2b) (Li et al., 2016; Quaas et al., 2022). Further, since the pre-industrial period, the global dust mass loading has increased by ∼55 ± 30%, primarily due to increased dust emissions from Asia and North Africa, which has contributed to a change in the Earth's energy budget (Kok et al., 2023). Based on Coupled Model Intercomparison Project Phase 6 (CMIP6) model simulations (utilized in the recent Intergovernmental Panel on Climate Change (IPCC) assessments), the direct aerosol radiative forcing (ARF) at TOA is found to be highly negative over Asia (Li et al.,

2022; Zhang et al., 2022; Elsey et al., 2024). Large and dense populations, rapid urban growth, and strong seasonal variation in precipitation make Asia (particularly South and East Asia) one of the most vulnerable regions to climate change risks (Hoegh-Guldberg et al., 2018; Samset et al., 2019). Anthropogenic aerosol emissions have significantly decreased over East Asia (particularly China) since 2010 due to the implementation of stringent air pollution control measures over China, which led to a rapid reduction in SO_2 (Li et al., 2017) and other pollutants (i.e., BC, NO_x, organic carbon (OC)) (Zheng et al., 2018). Whereas a persistent increase in aerosol emissions has been observed over South Asia due to increased industrialization and urbanization (Samset et al., 2019; Ramachandran et al., 2020a; Ramachandran & Rupakheti, 2022a). Additionally, the significant increase in seasonal-scale intense agricultural crop residue burning, emitting massive amounts of carbonaceous aerosols, increases the aerosol loading over South Asia (Jethva et al., 2018, 2019). This significant reduction in aerosol optical depth (AOD) over East Asia and a persistent increase in AOD over South Asia in the last two decades have created an Asian aerosol dipole between South and East Asia (Fig. 1.2) (Samset et al., 2019; Ramachandran et al., 2020a). The aerosol-radiation-cloud interactions arising from these significant changes in aerosol emissions over Asia can have large-scale atmospheric responses, which can have a wide range of climate and societal impacts over the source region of Asia and beyond (Zhao et al., 2019; Samset et al., 2019). For example, recent reductions in aerosol emissions over East Asia likely had a strong influence on the accelerated surface warming observed since 2010, both globally and in the North Pacific (Samset et al., 2025). Accurately capturing the recent evolving aerosol trends over Asia by the state-of-the-art climate models in CMIP6 remains challenging, which is primarily due to limitations in the utilized emission inventories and the representation of aerosol properties, transport, and removal processes (Wang et al., 2021; Ramachandran et al., 2022; Ren et al., 2025).

The uncertainty related to direct ARF is slightly reduced in the IPCC assessment report 6 (AR6) compared to IPCC AR5 (Myhre et al., 2013b; Forster et al., 2021), however, this uncertainty in IPCC AR6 is still found to be large, on the order of 100% (global direct ARF is -0.3 ± 0.3 Wm^{-2}) (Forster et al., 2021; Elsey et al., 2024). One of the major contributors to the high uncertainty in direct ARF is associated with aerosol absorption which is largely attributed to their insufficient global measurements and characterization, unconstrained by observations (Samset et al., 2018), and uncertainty

in residence time, morphology, and composition of absorbing aerosols (i.e., BC, mineral dust) utilized in the model (Di Biagio et al., 2019; IPCC, 2021; Li et al., 2022; Kelesidis et al., 2022). The aerosol absorption is highly underestimated by current climate models across different regions, especially over Asia (Shindell et al., 2013; Myhre et al., 2017; Ramachandran et al., 2022). The spread in CMIP6 inter-model simulated direct ARF is found to be higher over Asia (where direct ARF is more negative), which is linked to high uncertainty in direct ARF over Asia (Li et al., 2022; Zhang et al., 2022). The simulation and future projection of aerosol impacts on climate over Asia remain challenging due to dynamic changes in aerosol emissions with large heterogeneity, limited ability to capture recent aerosol trends, and the lack of seasonal-scale regional characterization of columnar aerosol optical and radiative properties utilizing high-quality observational datasets (IPCC, 2021; Li et al., 2022; Kok et al., 2023). Therefore, an assessment of columnar aerosol properties and radiative effects based on high-quality ground-based observations is essential over Asia, where both the magnitude and variability of aerosol amount and radiative effect are especially pronounced, for providing accurate observational constraints and for reducing the associated uncertainties in the assessment of radiative and climate impact of aerosols over Asia and beyond (IPCC, 2021; Li et al., 2022; Zhang et al., 2022).

Ground-based (e.g., AErosol RObotic NETwork (AERONET)) measurements are more accurate and are used to investigate aerosol properties and radiative effects, and calibrate and validate other observational datasets and model simulations (Andrews et al., 2017; Giles et al., 2019; Schutgens et al., 2021). In view of the significant local, regional, and global impacts of Asian aerosols, several studies have been carried out to examine the spatiotemporal distributions of optical, physical, and radiative properties of aerosols over different parts of Asia using ground-based observations (Gautam et al., 2013; Kedia et al., 2014; Che et al., 2018, 2019a,b; Ramachandran et al., 2020a,b; Ramachandran & Rupakheti, 2022a; Rupakheti et al., 2020, 2023). Most of the studies over Asia using ground-based observations, including the above, were conducted over a few locations and further, were restricted to a limited time period. On the other hand, studies conducted over Asia using satellite observations and model simulations (Kumar et al., 2018; Rupakheti et al., 2019; Banerjee et al., 2021; Jin et al., 2023) were restricted to AOD and Ångström exponent (AE), and have higher uncertainties compared to ground-based observations.

In addition to observational datasets, outputs from NASA's Modern-Era Retrospective Analysis for Research and Applications-2 (MERRA-2) and ECMWF's Copernicus Atmosphere Monitoring Service (CAMS) reanalysis are widely utilized, especially over those regions that have sparse observations, as they provide a variety of aerosol products with higher spatial resolution on a global scale constrained by observational datasets (Randles et al., 2017; Inness et al., 2019; Yang et al., 2021; Wei et al., 2022; Zhao et al., 2024; Ansari & Ramachandran, 2024a). Long-term validation of these models with high-quality ground-based datasets is required to substantially improve their parameterization, inputs, and physical processes at regional and seasonal scales, especially over Asia, where the aerosol loading is relatively higher with mixed aerosol types that arise from both anthropogenic and natural sources. Past studies have compared the MERRA-2 and CAMS simulated AODs with ground-based AOD observations on an annual scale globally, including Asia (Inness et al., 2019; Gueymard & Yang, 2020; Salamalikis et al., 2021; Ou et al., 2022; Su et al., 2023). A few studies validated MERRA-2 simulated aerosol absorption parameters (single scattering albedo (SSA) and absorption AOD (AAOD)) globally on an annual scale (Bakatsoula et al., 2023; Su et al., 2023). However, seasonal scale validations of MERRA-2 and CAMS simulated AOD and AE, and MERRA-2 simulated aerosol absorption parameters and aerosol radiative effects over the large domain of Asia in the recent period (last decade), when both MERRA-2 and CAMS simulations are independent of assimilated AERONET observations, and their comparison with other regions of the globe are still lacking. In this context, a comprehensive analysis of columnar aerosol optical, physical, and radiative properties using high-quality ground-based AERONET datasets over Asia, along with spatiotemporal collocated validations of MERRA-2 and CAMS simulations, on seasonal and annual scales, is essential for more accurate evaluation of aerosol radiative impacts and for providing accurate observational constraints for model simulations over Asia.

1.4 Objectives and scope of the thesis

This thesis work is focused on investigating the regional and spatial distributions of aerosol columnar optical properties and radiative effects over Asia on annual and seasonal scales, along with the spatiotemporal collocated validation of model simulations. The results obtained on aerosols over Asia are compared and contrasted with other regions of the globe. This work is performed by utilizing multi-source (ground-based

(AERONET), satellite (MODerate resolution Imaging Spectroradiometer (MODIS), and Clouds and the Earth's Radiant Energy System (CERES)), model (MERRA-2, CAMS, and CMIP6)) aerosol datasets. The major objectives of the thesis are as follows:

1. **Aerosol columnar optical characteristics and radiative effects over Asia using AERONET observations**: Perform a comprehensive analysis to examine the spatial variations of variety of columnar optical, physical, and radiative properties of aerosols using the high-quality AERONET datasets on annual and seasonal scales during the recent 5-year (2015–2019) period over Asia, covering Central, South, Southeast, and East Asia.

2. **Validations of model simulations and satellite retrievals with AERONET measurements over Asia**: Assess the regional and seasonal scale spatiotemporal collocated validations of MERRA-2 and CAMS simulated aerosol columnar optical parameters (e.g., AOD, AE, SSA, AAOD), and MERRA-2 simulated and CERES retrieved aerosol radiative properties with AERONET datasets over Asia.

3. **Comparison of aerosol properties and radiative effects over Asia with other regions of the globe**: Compare and contrast the columnar aerosol properties and radiative effects, and model and satellite performances over Asia with other regions of the globe, such as North America, South America, Europe, North Africa, South Africa, Middle East, and Australia, where aerosol concentrations, types, and emissions differ significantly from those in Asia.

A detailed description of the datasets, methodology, and analysis procedure utilized is provided in *Chapter 2*. *Chapter 3* presents the important findings from the spatial and regional distribution of columnar optical and physical properties of aerosols on annual and seasonal scales from AERONET datasets over Asia and other regions of the globe. This chapter also includes the collocated validations of MERRA-2, CAMS, and CMIP6 models simulated aerosol columnar optical properties with AERONET observations. A new classification scheme to quantify more accurately the absorbing aerosol types is developed as a part of this thesis and described in *Chapter 4*. The regional and seasonal variations of the different aerosol types, and absorbing aerosol types based on the new classification scheme are discussed in this chapter, in addition to identifying the potential sources of aerosol emissions. In *Chapter 5*, the regional and spatial variations in aerosol radiative parameters utilizing AERONET observations, CERES retrievals, and MERRA-2

and CMIP6 simulations over Asia and other regions of the globe on seasonal and annual scales are examined. The summary of the results obtained from this thesis work and the scope for future research are presented in *Chapter 6*.

2

Data, Methodology, and Analysis

A detailed description of the observational, model, and satellite datasets utilized in this thesis is provided in this chapter. Various aerosol optical, microphysical, and radiative parameters derived from AERONET direct measurements and inversion products, along with their associated uncertainties, are discussed. Details of the methodology and statistical analysis performed for spatiotemporal collocated validations of model and satellite datasets against AERONET observations are provided in this chapter.

2.1 AErosol RObotic NETwork (AERONET) measurements

AERONET is a global network of autonomously operated ground-based CIMEL Sun-sky multispectral radiometers that measure the direct solar irradiance and directional diffuse sky radiances to provide high-quality columnar aerosol optical, microphysical, and radiative properties (Holben et al., 1998; Giles et al., 2019; Sinyuk et al., 2020). Direct Sun measurements in the radiometer are performed at 9 wavelengths nominally centered at 0.34, 0.38, 0.44, 0.50, 0.675, 0.87, 0.935, 1.02, and 1.64 μm. These direct solar measurements are used to compute total column AOD at each wavelength except for 0.935 μm channel, which is used to retrieve total column water vapor (Giles et al., 2019). In addition to direct Sun measurements, sky radiance measurements are performed at 4 wavelengths (0.44, 0.675, 0.87, and 1.02 μm). The field of view of the radiometer is narrow (1.2^{o}). The triplet measurements of direct solar irradiance are made every 15 minutes under clear sky conditions. A silicon photodiode detector is used for the measurements in these wavelength channels with a filter bandpass of 0.002 μm for 0.34 and 0.38 μm wavelength channels, and of 0.01 μm for other wavelength channels (Giles et al., 2019). The level 2, version 3 algorithm is the most updated ver-

sion of AERONET datasets with improved methods for cloud screening, quality control, final calibration (pre- and post-) applied, and cirrus cloud detection and removal (Giles et al., 2019), which are utilized (https://aeronet.gsfc.nasa.gov/).

2.1.1 AERONET direct measurements

Aerosol optical depth (AOD) represents the exponential decrease of direct solar radiation (extinction), which is prevented from reaching the ground due to aerosols present in the atmospheric column. The spectral AOD ($\tau(\lambda)_{\text{Aerosol}}$) is computed by subtracting the cloud-free direct Sun measured spectral total optical depth ($\tau(\lambda)_{\text{Total}}$) (Eq. 2.1) from the optical depths contributed by Rayleigh scattering, water vapor, and atmospheric trace gases (i.e., ozone (O_3), nitrogen dioxide (NO_2), carbon dioxide (CO_2), methane (CH_4)) (Eq. 2.2).

$$\tau(\lambda)_{\text{Total}} = -\frac{1}{m}\left[\ln\left(\frac{I}{I_0}\right) - 2\ln\left(\frac{d_o}{d}\right)\right] \tag{2.1}$$

where I is the measured solar radiation intensity and I_o is the extraterrestrial solar radiation intensity, m is atmospheric air mass, d is the instantaneous Sun-Earth distance, and d_o is the Sun-Earth distance when I_o values are obtained.

$$\tau(\lambda)_{\text{Aerosol}} = \tau(\lambda)_{\text{Total}} - \tau(\lambda)_{\text{Rayleigh}} - \tau(\lambda)_{\text{H}_2\text{O}} - \tau(\lambda)_{\text{O}_3} - \tau(\lambda)_{\text{NO}_2} - \tau(\lambda)_{\text{CO}_2} - \tau(\lambda)_{\text{CH}_4} \tag{2.2}$$

Rayleigh optical depth ($\tau(\lambda)_{\text{Rayleigh}}$) is calculated based on optical air mass (Kasten & Young, 1989) and surface pressure over the location (Bodhaine et al., 1999). The water vapor optical depth ($\tau(\lambda)_{\text{H}_2\text{O}}$) is calculated by utilizing precipitable water at 0.935 μm. Optical depths due to O_3 and NO_2 are determined by the total column Total Ozone Mapping Spectrometer (TOMS) monthly average climatology (1978–2004) of O_3 concentration and Ozone Monitoring Instrument (OMI) monthly average climatology (2004-2013) of NO_2 concentration, respectively. CO_2 and CH_4 optical depths are estimated by surface pressure (in hPa) and their absorption coefficients derived from the High-Resolution Transmission (HITRAN) molecular absorption database. AE is calculated by the spectral slope of AODs (in the logarithmic scale) in the wavelength range of 0.44−0.87 μm. The uncertainty in AE increases with the decrease in AOD (Wagner & Silva, 2008). Spectral Deconvolution Algorithm (SDA) retrieved fine mode fraction (FMF) at 0.50 μm is calculated as the ratio of fine mode AOD to total AOD (O'Neill et al.,

2003). The uncertainty of all these aerosol parameters from AERONET direct measurement is provided in Table 2.1. The cloud screening criteria applied in AERONET level 2 AOD are based on the fact that the temporal and spatial variation of optical depth for aerosols plus clouds is much greater than aerosols alone (Smirnov et al., 2000; Giles et al., 2019). Variations in AOD in both short-term (e.g., a few minutes) and long-term (e.g., daily) are analyzed for cloud screening. Variability in AODs (for 0.675, 0.87, and 1.02 μm) from triplet measurements (i.e., difference between maximum and minimum values) is required to be less than the maximum of 0.01 and 1.5% of AOD simultaneously for the cloud-screened dataset (Giles et al., 2019). Further, the standard deviation (σ) from daily measured AODs should be <0.015 after triplet cloud screening, and after that, the AOD and AE values should be within 3σ for the cloud-screened dataset. The details of the cloud-screening-related quality control are provided in Giles et al. (2019).

Table 2.1: *Aerosol variables which are used in the study, their definition and uncertainty retrieved from AERONET.*

Aerosol variable	Definition	Uncertainty
Aerosol optical depth (AOD)	Columnar integration of aerosol extinction in the atmosphere – quantifies the attenuation of solar radiation due to aerosol extinction (scattering + absorption) from the top of the atmosphere to the surface.	$<\pm$0.02 for λ <0.44μm; $<\pm$0.01 for λ >0.44μm (Holben et al., 2001)
Ångström exponent (AE)	Spectral slope of AOD in logarithmic scale – typically small AE (<1) indicates dominance of coarse mode aerosols, while higher AE (>2) suggests the dominance of fine mode aerosols.	–
Fine mode fraction (FMF)	Ratio of fine mode AOD to total AOD – quantifies the contribution of fine mode aerosols in total AOD.	~10% (O'Neill et al., 2003)

Single scattering albedo (SSA)	Ratio of aerosol scattering to total extinction – quantifies the scattering and absorbing nature of aerosols, e.g., less absorbing: SSA $\geq$0.95, moderately absorbing: 0.90$\leq$SSA$<$0.95, more absorbing: SSA$<$0.90.	$\leq \pm$0.03 for $AOD_{0.44}$ $\geq$0.4; $\pm$0.05-0.07 for $AOD_{0.44}$ $\leq$0.2 (Dubovik et al., 2000; Sinyuk et al., 2020)
Absorption AOD (AAOD)	AOD multiplied by (1–SSA).	$\pm$0.01 (Mallet et al., 2013)
Absorption Ångström exponent (AAE)	Spectral slope of AAOD in logarithmic scale – quantifies the spectral dependence of AAOD. AAE is $\sim$1 for BC (Bond et al., 2013), $\sim$2.2–2.6 for dust, and $\sim$0.84–1.16 for carbonaceous aerosols (Chung et al., 2012).	–
Asymmetry parameter (g)	Average of cosine of the scattering angles for scattered radiation – provides the angular distribution of aerosol scattered radiation, $g = 0$: isotropic, $g = 1$: entirely forward scattering.	$\pm$0.02 (Dubovik et al., 2000)
Volume size distribution (dV(r)/dlnr) ($\mu m^3/\mu m^2$)	Aerosol volume with radii between r and $r + dr$ per unit area in the atmospheric column – retrieved at 22 logarithmically equidistant discrete radius (r) values from 0.05$\leq r \leq$15 μm (fine: $r <1\mu m$, coarse: $r >1\mu m$).	$\leq$10% in maxima and $\leq$35% in minima for intermediate aerosol size range (0.1$\leq r \leq 7\mu m$); up to 80–100% at edges ($r <0.1\mu m$ and $r >7\mu m$) (Dubovik et al., 2000)
Aerosol direct radiative effect (DRE) (Wm^{-2})	Difference in the shortwave radiative flux with and without presence of aerosols – quantifies the loss/gain of radiative flux at any atmospheric level.	$<$5% in calibrated solar flux and sky radiance (Dubovik et al., 2000; García et al., 2008)

2.1.2 AERONET inversion retrievals

Sky radiance measurements in the almucantar plane, along with the direct solar irradiance measurement, provide the fundamental input to retrieve aerosol volume size distributions (VSD: dV(r)/dlnr) and refractive indices from the inversion algorithm in the AERONET database (Dubovik & King, 2000; Dubovik et al., 2000, 2006). In the almucantar plane, instrument scans at a constant viewing zenith angle (e.g., equal to the solar zenith angle in the almucantar plane), including 56 azimuth angles that vary from -180^{o} to 180^{o} with respect to the solar azimuth angle. Pairs of sky radiance measurements (i.e., positive and negative azimuth angles) at identical scattering angles must agree within 20% (i.e., symmetry check), and at least 14 such angular pairs within the designated scattering angle ranges are required for level 2 retrieval to follow the quality-control criteria (Holben et al., 2006). In sky radiance measurements, the symmetry check is used as the quality control criterion for screening out the cloud cover and very inhomogeneous aerosol conditions (e.g., thick plumes) (Holben et al., 2006; Sinyuk et al., 2020). The minimum solar zenith angle required for the level 2 product is 50^{o} to ensure the range of scattering angle measurements of at least 0^{o} to 100^{o} (Holben et al., 2006). The microphysical model used in the AERONET retrieval is a homogeneous internal mixture of spheres and spheroids (thereby accounting for both spherical and non-spherical particles), which are distributed throughout a uniform aerosol layer (Dubovik et al., 2006). Since aerosols are internally mixed in the model, the AERONET algorithm assumes that the same complex refractive index applies to all aerosols, independent of their size. This assumption is essential for obtaining a unique solution, as it distributes the absorption uniformly across all retrieved particle sizes.

The aerosol VSD and refractive index are adjusted in a forward radiation model to get a statistically optimized best-fit solution with the actual direct and sky radiance measurements, accounting for measurement accuracy as well as *a priori* constraints (Dubovik & King, 2000). Aerosol VSD is retrieved for 22 logarithmically equidistant discrete radius (r) in the range from 0.05 to 15 μm. The real part ($n(\lambda)$) (1.33$\leq n(\lambda) \leq$1.6) and imaginary ($k(\lambda)$) (0.0005$\leq k(\lambda) \leq$0.5) parts of the complex refractive index are retrieved for the wavelengths corresponding to sky radiance measurements. After retrieving the optimized VSD and refractive index, they are used to compute the SSA, AAOD, absorption AE (AAE), and asymmetry parameter (g). Aerosol total volume concentration (TVC) is calculated by the integration of VSD in the entire radius range from 0.05

to 15 μm. In VSD, the minimum within the aerosol radius interval from 0.439 to 0.992 μm is used as a separation point between fine and coarse mode aerosols. This separation point is further used to define fine and coarse volume concentration. AERONET level 2 quality-control criteria requires solar zenith angles to be $>50^{o}$ in clear sky conditions for all inversion retrieved aerosol parameters, and AOD at 0.44 μm ($AOD_{0.44}$) to be >0.4 for retrieving SSA, AAOD, and complex refractive index to avoid more uncertain aerosol absorption estimates (Holben et al., 2006). The uncertainty of all these aerosol parameters retrieved from the AERONET inversion algorithm, which are used, is provided in Table 2.1. It should be noted that the higher errors in the edges of VSD do not significantly affect its main feature (e.g., concentration, median, effective radius) because VSD typically has low values at the edges (Dubovik et al., 2002).

An intercomparison of AERONET SSA with in situ aircraft measurements during the DRAGON-MD and DISCOVER-AQ experiments revealed a good agreement with AERONET SSA, and most of the coincident measurement pairs were within the uncertainty of the SSA values (Schafer et al., 2014). Another study showed that the majority of SSA comparisons when $AOD_{0.44}$ is >0.2 were within the expected error in the intercomparison of AERONET SSA with in situ profile measurements (Andrews et al., 2017). The level 2 criterion of $AOD_{0.44}$ >0.4 is often too strict, considering that $AOD_{0.44}$ is <0.4 at many sites around the globe (Andrews et al., 2017; Ansari & Ramachandran, 2024b). Due to which, level 1.5 inversion retrievals of SSA, AAOD, and AAE datasets are utilized for $0.2\leq$ $AOD_{0.44}$ <0.4 only when other level 2 quality-assured datasets were available (e.g., Arola et al. (2015); Choi et al. (2021); Ansari & Ramachandran (2025b)), thereby reducing the sampling bias as the results are applicable to a range of AODs, and not biased towards high AOD conditions only (Bond et al., 2013; Arola et al., 2015).

2.1.3 Aerosol direct radiative effect (DRE)

The net perturbation in instantaneous shortwave radiative flux due to the presence of aerosols is referred to as *aerosol direct radiative effect (DRE)*. AERONET operational DRE values are estimated for broadband solar spectrum (0.2−4.0 μm) with and without the presence of aerosols, which are quality-controlled, cloud-screened, and well-calibrated. The AERONET retrieval of flux calculations accounts for absorption and multiple scattering effects using the Discrete Ordinate Radiative Transfer (DISORT) approach (Nakajima & Tanaka, 1988; Dubovik et al., 2006; García et al., 2008). The broadband fluxes

are calculated by a corresponding module of the radiative transfer model GAME (Global Atmospheric ModEl) (Dubuisson et al., 1996) by the spectral integration in 0.2−4.0 μm using >200 spectral sub-intervals. The GAME model estimates gaseous absorption, primarily from H_2O, CO_2, and O_3, using the correlated k-distribution method (Lacis & Oinas, 1991). This approach efficiently incorporates the effects of gaseous absorption and its interaction with multiple scattering, while maintaining computational feasibility. The same AERONET aerosol module, which is governed by the retrieved size distribution, complex refractive index, and spherical fraction, is used to recalculate extinction, SSA, and phase function in each of these sub-intervals for input in the radiative transfer model (Dubovik & King, 2000; Dubovik et al., 2000). The surface spectral reflectance was estimated by utilizing the climatological values of the MODIS retrieved surface reflectance. Complex refractive index and surface reflectance are interpolated or extrapolated from AERONET retrieved values in each spectral sub-interval.

Aerosol DRE at top of atmosphere (TOA) ($\mathrm{DRE_{TOA}}$) and surface (SFC) ($\mathrm{DRE_{SFC}}$) is defined as the change in the net radiative flux ($\mathrm{F_{Net}} = \mathrm{F^{\uparrow}}$ (upward flux) $-$ $\mathrm{F^{\downarrow}}$ (downward flux)) in the presence ($\mathrm{F^{A}_{Net}}$) and absence ($\mathrm{F^{C}_{Net}}$) of aerosols:

$$\mathrm{DRE_{TOA}} = (\mathrm{F^{A}_{Net}} - \mathrm{F^{C}_{Net}})_{\mathrm{TOA}} \tag{2.3}$$

$$\mathrm{DRE_{SFC}} = (\mathrm{F^{A}_{Net}} - \mathrm{F^{C}_{Net}})_{\mathrm{SFC}} \tag{2.4}$$

In AERONET, DRE is defined by considering the $\mathrm{F^{\uparrow}}$ at TOA and $\mathrm{F^{\downarrow}}$ at SFC:

$$\mathrm{DRE_{TOA}} = \mathrm{F^{\uparrow C}_{TOA}} - \mathrm{F^{\uparrow A}_{TOA}} \tag{2.5}$$

$$\mathrm{DRE_{SFC}} = \mathrm{F^{\downarrow A}_{SFC}} - \mathrm{F^{\downarrow C}_{SFC}} \tag{2.6}$$

AERONET $\mathrm{DRE_{SFC}}$ is found to be overestimated as upward fluxes in both aerosol-laden and aerosol-free conditions are not taken into account (García et al., 2012). The surface albedo is an important factor for accurately estimating DRE, and it is more crucial when it is >0.30 (García et al., 2012). This is called critical surface albedo above which the net effect of aerosols changes from cooling to warming at TOA. The surface albedo correction is applied in AERONET $\mathrm{DRE_{SFC}}$ by multiplying it by (1–SA) (Eq. 2.7), where SA represents the spectral average of surface albedo at the four AERONET wavelengths

(0.44, 0.675, 0.87 and 1.02 μm), to correct the overestimation in $\mathrm{DRE_{SFC}}$.

$$\mathrm{DRE_{SFC}} = (\mathrm{F^{\downarrow A}_{SFC}} - \mathrm{F^{\downarrow C}_{SFC}}).(1 - \mathrm{SA}) \tag{2.7}$$

It is noted that AERONET DRE is estimated for the whole shortwave region (0.2−4.0 μm), but spectral SA is averaged for only AERONET wavelengths (0.44−1.02 μm) as the latter is not provided as an operational AERONET product. However, the mean difference in the $\mathrm{DRE_{SFC}}$ calculated by considering SA in the whole shortwave region (0.2−4.0 μm) and in AERONET wavelengths (0.44−1.02 μm) was found to be <10% (García et al., 2012). Therefore, considering the SA averaged at AERONET wavelengths (0.44−1.02 μm) is a good approximation for estimating the $\mathrm{DRE_{SFC}}$ (García et al., 2012). DRE is normalized by $\mathrm{AOD_{0.55}}$ to calculate aerosol DRE efficiency (DREE), which indicates the rate of DRE per unit AOD, thereby ruling out the influence of aerosol loading in DRE. A similar surface albedo correction (Eq. 2.7) is also applied in AERONET $\mathrm{DREE_{SFC}}$.

AERONET measured broadband solar fluxes have shown excellent agreement (slope of 0.98 $\pm$ 0.00 and bias of -5.32 ± 1.00 $\mathrm{Wm^{-2}}$) and are well-correlated (correlation of 99%) with ground-based pyranometer measurements in various environmental conditions (e.g., mineral dust, biomass burning, urban industrial, maritime aerosols, background continental, and free troposphere) (García et al., 2008). On the global scale, the relative error in the observed solar radiation was found to be 2.1 $\pm$ 3.0% with a small overestimation of 9 $\pm$ 12 $\mathrm{Wm^{-2}}$ (García et al., 2008). Uncertainty in the calibrated sky radiance measurements is ∼5% or better (Holben et al., 1998; Dubovik et al., 2000). The same magnitude of correlation and agreement is also expected at TOA, since the methodology is the same as that of the surface (e.g., aerosol and gaseous distribution, radiative transfer model) (García et al., 2008, 2012). Furthermore, the inter-comparison of AERONET $\mathrm{DRE_{TOA}}$ and $\mathrm{DRE_{SFC}}$ with model simulated DRE (derived using AERONET measured AOD, SSA, and g) was found to be very good (correlation coefficient ≥0.90) over the sites in the Indo-Gangetic Plain (IGP) and South Africa (Ramachandran & Kedia, 2012; Adesina et al., 2014).

DRE and DREE in the atmosphere (ATM) ($\mathrm{DRE_{ATM}}$, $\mathrm{DREE_{ATM}}$) is calculated as the difference between $\mathrm{DRE_{TOA}}$ and $\mathrm{DRE_{SFC}}$, and $\mathrm{DREE_{TOA}}$ and $\mathrm{DREE_{SFC}}$, re-

spectively:

$$\mathrm{DRE_{ATM}} = \mathrm{DRE_{TOA}} - \mathrm{DRE_{SFC}} \tag{2.8}$$

$$\mathrm{DREE_{ATM}} = \mathrm{DREE_{TOA}} - \mathrm{DREE_{SFC}} \tag{2.9}$$

Atmospheric warming due to the energy absorbed by aerosols is quantified in terms of aerosol-induced atmospheric heating rate (HR, in K day^{-1}), which is calculated as:

$$\mathrm{HR} = \frac{\mathrm{g}}{\mathrm{c_p}} \times \frac{\mathrm{DRE_{ATM}}}{\Delta \mathrm{P}} \times 24 \times 3600 \tag{2.10}$$

where g is the acceleration due to gravity (9.8 ms^{-2}), c_p is the specific heat capacity of air at constant pressure (1006 J kg^{-1} K^{-1}), and ΔP is the pressure difference between the elevation of observation site and 5 km asl. This is the common procedure to compute the aerosol-induced HR since most of the aerosols in the troposphere reside between the surface and 5 km asl (Ramachandran, 2018). Earlier studies have clearly shown that the incorporation of vertical profiles of aerosols did not significantly affect the net DRE at TOA, SFC, ATM, and HR with respect to their values obtained without including the vertical profiles of aerosols (Ramachandran & Kedia, 2010; IPCC, 2021; Ramachandran et al., 2023), as the net energy absorbed in the atmosphere is found to be same regardless of whether vertical profiles are considered. However, accounting for the vertical distribution of aerosols primarily alters the vertical profile of DRE. Therefore, the present study, which focuses on estimating net DRE at TOA, SFC, and in the ATM, is unlikely to be significantly influenced by the exclusion of aerosol vertical distribution.

The AERONET estimates of DRE and DREE are calculated across all AOD values, though the uncertainty in retrieved SSA is relatively high (>0.05) at low AOD levels (<0.2). However, this increased uncertainty in SSA has minimal impact on flux estimations because both diffuse fluxes and aerosol effects on radiation flux decrease as AOD decreases. Notably, while SSA accuracy declines with lower AOD, the error in AAOD remains steady at ∼0.01, keeping the error in flux relatively constant. Comparisons between modeled and observed broadband solar fluxes and surface radiative effect confirm that, at low AOD, these uncertainties do not significantly affect simulation accuracy (García et al., 2012).

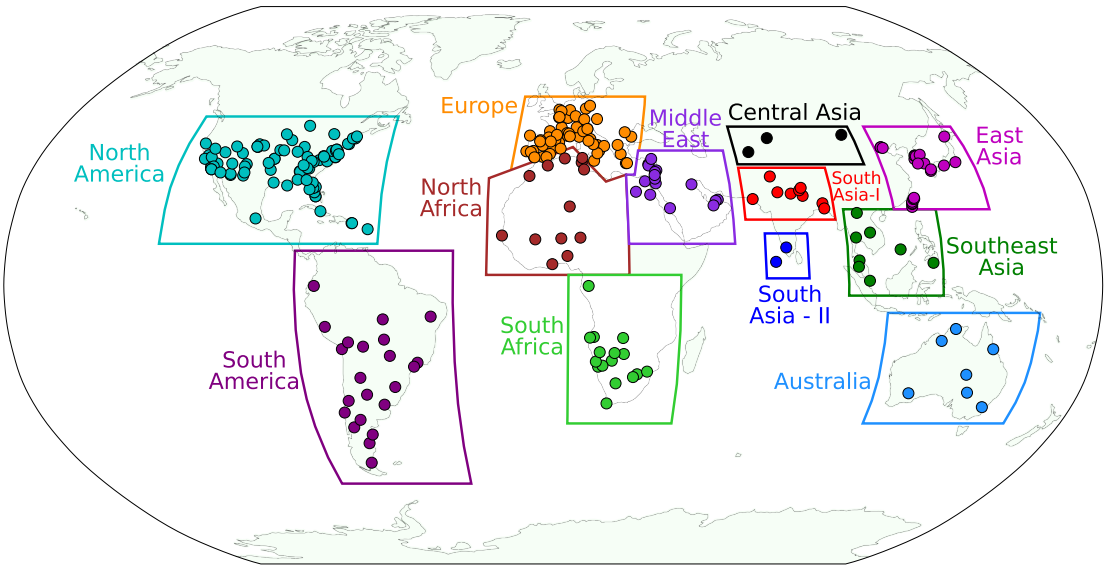

Figure 2.1: *Locations of all the selected observational sites, following the criteria mentioned in Section 2.2, in different regions (shown as polygons) across the globe, indicated by different colors.*

2.2 Selection criteria for observational sites

The chosen study period for the analysis corresponds to 2015–2019. A few major and important criteria are applied for selecting the AERONET sites during 2015−2019 period over Asia and other regions of the globe to strengthen our analysis: (a) each site must include aerosol optical, physical (e.g., AOD, FMF, VSD) and radiative (e.g., DRE) parameters on a continuous basis, (b) measurements must be available for $\geq$9 months in the year, and (c) data coverage must cover all four seasons–winter (December-January-February, DJF), spring (March-April-May, MAM), summer (June-July-August, JJA), and autumn (September-October-November, SON), with $\geq$10 days of data in each season including all the available years. A total of 261 AERONET sites over 12 regions globally are selected based on the criteria outlined above, covering the period from 2015 to 2019. Out of the total 12 regions, 5 are in Asia (Central Asia: 3, South Asia – I: 9, South Asia – II: 2, Southeast Asia: 8, East Asia: 22) and 7 are in other regions of the globe (North America: 86, South America: 22, Europe: 57, North Africa: 13, South Africa: 16, Middle East: 16, Australia: 7) (Fig. 2.1). A detailed list of sites for each region is provided in Table 2.2.

The observational period 2015−2019 is chosen because of the following rea-

sons: (a) the number of AERONET sites, complying with all the above-mentioned important criteria, is maximum over Asia during this period, and (b) the atmospheric/ environmental conditions during this time period are normal compared to the abrupt changes in aerosol emissions that occurred due to COVID-19 induced lockdowns (Ansari & Ramachandran, 2024a; Ramachandran & Ansari, 2025). The seasonal and annual averages of aerosol parameters for all the available year(s) over each site are considered as appropriate representative of aerosol properties for the period of 2015–2019 due to following reasons: (a) the trends in aerosol properties are not significant in the 5-year period which indicates that the effect of changes in natural and/or anthropogenic activities is minimal (Ramachandran & Rupakheti, 2022a), (b) the influence of change in meteorology over a 5-year period in changing the aerosol concentration is relatively small (Zhang et al., 2019), and (c) the seasonal variations of aerosol characteristics are more prominent than their inter-annual variations during the chosen time period (Ansari & Ramachandran, 2023a,b). Episodic wildfire events have substantially increased aerosol emissions over the west coast of the USA and Canada during August 2018, leading to enhanced AOD over North America exclusively during the wildfire period (Tanada et al., 2023; Xue et al., 2025). However, in this study, when more than one year of data is available within the study period (2015–2019) over any study location, which is the case for most sites across North America (Table 2.2), seasonal average aerosol properties are derived by including the data of all available years, thereby accounting for interannual variations, if present. Further, analysis shows that the interannual variability of regional mean AOD over North America during the summer seasons of 2015–2019, when wildfire events are more frequent, is $\sim$0.05.

Table 2.2: *Details of all the selected observational sites (latitude, longitude, elevation (in meters above mean sea level)) over different regions (Central Asia, South Asia – I, South Asia – II, Southeast Asia, and East Asia, North America, South America, Europe, North Africa, South Africa, Middle East, and Australia) across the globe with the availability of AERONET dataset during the period 2015–2019 ('15–'19) following the criteria mentioned in Section 2.2. The number of sites over each region is given in brackets, which total to 261 sites all over the globe. The names of observational sites are the same as those mentioned in the AERONET website (https://aeronet.gsfc.nasa.gov).*

Observational Site (Latitude, Longitude, Elevation)	'15	'16	'17	'18	'19
Central Asia (3)					
1. Dushanbe (38.55 N, 68.86 E, 821 m)	✓	✓			✓
2. Issyk-Kul (42.62 N, 76.98 E, 1650 m)	✓		✓	✓	✓
3. Dalanzadgad (43.58 N, 104.42 E, 1470 m)			✓		✓
South Asia – I (9)					
1. Karachi (24.95 N, 67.14 E, 49 m)		✓	✓	✓	
2. Lahore (31.48 N, 74.26 E, 209 m)		✓		✓	
3. Jaipur (26.91 N, 75.81 E, 450 m)	✓	✓	✓		
4. Kanpur (26.51 N, 80.23 E, 123 m)	✓	✓	✓	✓	✓
5. Gandhi_College (25.87 N, 84.13 E, 60 m)	✓	✓			
6. Lumbini (27.49 N, 83.28 E, 110 m)				✓	
7. Pokhara (28.19 N, 83.98 E, 800 m)	✓		✓	✓	✓
8. Dhaka_University (23.73 N, 90.4 E, 34 m)	✓	✓			
9. Bhola (22.23 N, 90.76 E, 7 m)	✓	✓			
South Asia – II (2)					
1. Karunya_University (10.94 N, 76.74 E, 478 m)			✓	✓	
2. MCO-Hanimaadhoo (6.78 N, 73.18 E, 13 m)		✓			
Southeast Asia (8)					
1. Luang_Namtha (20.93 N, 101.42 E, 557 m)	✓	✓	✓		✓
2. Ubon_Ratchathani (15.25 N, 104.87 E, 120 m)	✓		✓		
3. Silpakorn_Univ (13.82 N, 100.04 E, 72 m)	✓	✓	✓		
4. Tai_Ping (10.38 N, 114.36 E, 4 m)					✓
5. Songkhla_Met_Sta (7.18 N, 100.60 E, 15 m)	✓				
6. USM_Penang (5.36 N, 100.30 E, 51 m)	✓			✓	✓
7. Singapore (1.30 N, 103.78 E, 30 m)	✓			✓	✓
8. ND_Marbel_Univ (6.50 N, 124.84 E, 70 m)	✓	✓			✓
East Asia (22)					
1. Beijing (39.98 N, 116.38 E, 92 m)	✓	✓		✓	
2. Beijing-CAMS (39.93 N, 116.32 E, 106 m)	✓	✓	✓	✓	✓
3. XiangHe (39.75 N, 116.96 E, 36 m)	✓	✓			
4. Anmyon (36.54 N, 126.33 E, 47 m)	✓	✓	✓	✓	✓
5. Yonsei_University (37.56 N, 126.93 E, 97 m)	✓	✓	✓	✓	✓
6. Seoul_SNU (37.46 N, 126.95 E, 116 m)		✓	✓	✓	✓
7. Hankuk_UFS (37.34 N, 127.27 E, 167 m)		✓	✓	✓	
8. Gangneung_WNU (37.77 N, 128.87 E, 60 m)	✓	✓	✓	✓	
9. Pusan_NU (35.24 N, 129.08 E, 78 m)		✓			
10. Gwangju_GIST (35.23 N, 126.84 E, 52 m)		✓			
11. ARIAKE_TOWER (33.10 N, 130.27 E, 15 m)					✓
12. Fukuoka (33.52 N, 130.48 E, 30 m)	✓	✓	✓	✓	
13. Osaka (34.65 N, 135.59 E, 50 m)	✓		✓	✓	✓

14. Chiba_University (35.62 N, 140.10 E, 60 m)		✓	✓	✓	✓
15. Hokkaido_University (43.08 N, 141.34 E, 59 m)		✓	✓		✓
16. Kaohsiung (22.68 N, 120.29 E, 15 m)				✓	✓
17. Chiayi (23.50 N, 120.50 E, 62 m)	✓	✓	✓		
18. Douliu (23.71 N, 120.54 E, 60 m)			✓		
19. Xitun (24.16 N, 120.62 E, 91 m)					✓
20. EPA-NCU (24.97 N, 121.19 E, 144 m)	✓	✓	✓		✓
21. Taipei_CWB (25.01 N, 121.54 E, 26 m)	✓	✓	✓		✓
22. Cape_Fuguei_Station (25.30 N, 121.54 E, 40 m)			✓		✓
North America (86)					
1. ARM_SGP (36.61 N, 97.49 W, 319 m)				✓	✓
2. Ames (42.02 N, 93.77 W, 338 m)	✓		✓		
3. Appalachian_State (36.21 N, 81.69 W, 1080 m)	✓	✓	✓	✓	✓
4. BONDVILLE (40.05 N, 88.37 W, 212 m)	✓	✓	✓		
5. BSRN_BAO_Boulder (40.05 N, 105.01 W, 1604 m)	✓				
6. Bakersfield (35.33 N, 119.00 W, 108 m)			✓	✓	✓
7. Billerica (42.53 N, 71.27 W, 82 m)	✓	✓		✓	✓
8. Brookhaven (40.87 N, 72.88 W, 37 m)					✓
9. CalTech (34.14 N, 118.13 W, 260 m)		✓	✓	✓	✓
10. Camaguey (21.42 N, 77.85 W, 122 m)				✓	✓
11. Cart_Site (36.61 N, 97.49 W, 318 m)	✓	✓	✓		
12. EPA-Res_Triangle_Pk (35.88 N, 78.87 W, 109 m)	✓			✓	
13. Easton-MDE (38.79 N, 76.08 W, 4.5 m)	✓	✓	✓		✓
14. El_Segundo (33.91 N, 118.38 W, 25 m)	✓				
15. Fresno_2 (36.79 N, 119.77 W, 100 m)	✓	✓	✓	✓	✓
16. GSFC (38.99 N, 76.84 W, 87 m)	✓	✓	✓	✓	✓
17. Georgia_Tech (33.78 N, 84.40 W, 294 m)	✓	✓		✓	
18. Goldstone (35.23 N, 116.79 W, 1100 m)	✓	✓		✓	
19. Guadeloup (16.22 N, 61.53 W, 39 m)	✓	✓			
20. Hampton_University (37.02 N, 76.34 W, 12.12 m)				✓	✓
21. IMPROVE-MammothCave (37.13 N, 86.15 W, 235 m)	✓			✓	✓
22. Key_Biscayne2 (25.73 N, 80.16 W, 0 m)	✓	✓		✓	
23. Key_Biscayne (25.73 N, 80.16 W, 10 m)		✓			
24. LISCO (40.95 N, 73.34 W, 12 m)	✓	✓	✓	✓	
25. La_Parguera (17.97 N, 67.05 W, 12.4 m)	✓	✓		✓	✓
26. Lake_Okeechobee (26.90 N, 80.79 W, 9 m)					✓
27. MD_Science_Center (39.28 N, 76.61 W, 15 m)	✓	✓	✓	✓	✓
28. Mexico_City (19.33 N, 99.18 W, 2268 m)	✓	✓			
29. Modesto (37.64 N, 120.99 W, 33 m)			✓	✓	
30. Monterey (36.59 N, 121.85 W, 50 m)	✓			✓	✓
31. NASA_KSC (28.46 N, 80.66 W, 1.2 m)			✓	✓	
32. NASA_LaRC (37.10 N, 76.38 W, 5 m)	✓	✓	✓	✓	✓
33. NEON-CPER (40.81 N, 104.74 W, 1655 m)				✓	✓

34. NEON-Disney (28.13 N, 81.44 W, 19 m)	✓		✓	✓	✓
35. NEON_CLBJ (33.40 N, 97.57 W, 259 m)			✓	✓	✓
36. NEON_CVALLA (40.16 N, 105.17 W, 1539 m)	✓	✓	✓	✓	✓
37. NEON_GRSM (35.69 N, 83.50 W, 579 m)			✓	✓	✓
38. NEON_GUAN (17.97 N, 66.87 W, 128 m)					✓
39. NEON_Harvard (42.54 N, 72.17 W, 348 m)	✓	✓	✓	✓	✓
40. NEON_KONZ (39.10 N, 96.56 W, 415 m)		✓	✓		✓
41. NEON_MLBS (37.38 N, 80.52 W, 1170 m)					✓
42. NEON_MOAB (38.25 N, 109.39 W, 1799 m)		✓	✓	✓	✓
43. NEON_OAES (35.41 N, 99.06 W, 523 m)	✓	✓	✓	✓	✓
44. NEON_ONAQ (40.18 N, 112.45 W, 1656 m)		✓	✓	✓	
45. NEON_ORNL (35.96 N, 84.28 W, 344 m)		✓	✓		✓
46. NEON_OSBS (29.69 N, 81.99 W, 47 m)	✓	✓	✓	✓	
47. NEON_SCBI (38.89 N, 78.14 W, 354 m)	✓	✓	✓	✓	✓
48. NEON_SERC (38.89 N, 76.56 W, 9.7536 m)		✓	✓	✓	✓
49. NEON_SJER (37.11 N, 119.73 W, 368 m)					✓
50. NEON_SRER (31.91 N, 110.84 W, 983 m)					✓
51. NEON_Sterling (40.46 N, 103.03 W, 1372 m)	✓	✓	✓		✓
52. NEON_TALL (32.95 N, 87.39 W, 165 m)		✓	✓	✓	✓
53. NEON_UKFS (39.04 N, 95.19 W, 321 m)		✓	✓	✓	✓
54. NEON_UNDE (46.23 N, 89.54 W, 520 m)	✓	✓	✓	✓	✓
55. Railroad_Valley (38.50 N, 115.69 W, 1437 m)		✓	✓	✓	
56. SEARCH-Centreville (32.90 N, 87.25 W, 126 m)	✓				
57. SEARCH-OLF (30.55 N, 87.38 W, 44 m)	✓	✓			
58. SEARCH-Yorkville (33.93 N, 85.05 W, 394 m)	✓	✓			
59. SERC (38.89 N, 76.56 W, 36.5 m)	✓	✓	✓	✓	
60. SP_Bayboro (27.76 N, 82.63 W, 5 m)	✓	✓	✓	✓	
61. Sandia_NM_PSEL (35.05 N, 106.54 W, 1662.5 m)	✓	✓	✓	✓	✓
62. Santa_Monica_Colg (34.02 N, 118.47 W, 55 m)	✓	✓	✓	✓	
63. Sevilleta (34.35 N, 106.89 W, 1477 m)	✓	✓	✓	✓	
64. Sigma_Space_Corp (38.95 N, 76.84 W, 44.8 m)		✓	✓	✓	
65. Sioux_Falls (43.74 N, 96.63 W, 505 m)		✓	✓		
66. St_Louis_University (38.64 N, 90.23 W, 159 m)	✓		✓	✓	✓
67. TABLE_MOUNTAIN_CA (34.38 N, 117.68 W, 2200 m)		✓	✓	✓	✓
68. Table_Mountain (40.13 N, 105.24 W, 1689 m)			✓	✓	✓
69. Tallahassee (30.45 N, 84.30 W, 49 m)	✓	✓	✓		
70. Thompson_Farm (43.11 N, 70.95 W, 26 m)	✓	✓	✓	✓	✓
71. Toronto (43.79 N, 79.47 W, 186 m)	✓	✓	✓	✓	✓
72. Trinidad_Head (41.05 N, 124.15 W, 105 m)	✓	✓			
73. Tucson (32.23 N, 110.95 W, 779 m)		✓	✓	✓	✓
74. UACJ_UNAM_ORS (31.74 N, 106.43 W, 1127 m)					✓
75. UAHuntsville (34.73 N, 86.64 W, 223 m)		✓		✓	
76. UMBC (39.25 N, 76.71 W, 79 m)	✓	✓			

77. USC_SEAPRISM (33.56 N, 118.12 W, 31 m)	✓		✓		
78. USC_SEAPRISM_2 (33.56 N, 118.12 W, 31 m)		✓			
79. USGS_Flagstaff_ROLO (35.21 N, 111.63 W, 2179.6 m)	✓	✓	✓	✓	✓
80. Univ_of_Houston (29.72 N, 95.34 W, 65 m)	✓	✓	✓	✓	✓
81. Univ_of_Nevada-Reno (39.54 N, 119.81 W, 1410 m)	✓	✓	✓	✓	✓
82. VirginiaTech (37.23 N, 80.42 W, 690 m)					✓
83. Wallops (37.93 N, 75.47 W, 37 m)	✓	✓	✓	✓	✓
84. WaveCIS_Site_CSI_6 (28.87 N, 90.48 W, 33.58 m)	✓	✓	✓		✓
85. White_Sands_HELSTF (32.63 N, 106.34 W, 1207 m)	✓	✓	✓	✓	✓
86. Yuma (32.64 N, 114.58 W, 63 m)				✓	
South America (22)					
1. Alta_Floresta (9.87 S, 56.10 W, 277 m)	✓	✓		✓	
2. Arica (18.47 S, 70.31 W, 25 m)		✓	✓	✓	✓
3. CEILAP-BA (34.56 S, 58.51 W, 26 m)	✓	✓	✓	✓	✓
4. CEILAP-Bariloche (41.15 S, 71.16 W, 840 m)	✓	✓			
5. CEILAP-Comodoro (45.79 S, 67.46 W, 49 m)	✓	✓	✓	✓	✓
6. CEILAP-Neuquen (38.95 S, 68.14 W, 271 m)	✓			✓	✓
7. CEILAP-RG (51.60 S, 69.32 W, 19 m)	✓		✓	✓	✓
8. CUIABA-MIRANDA (15.73 S, 56.07 W, 210 m)	✓	✓	✓		✓
9. Campo_Grande_SONDA (20.44 S, 54.54 W, 677 m)		✓	✓		
10. Huancayo-IGP (12.04 S, 75.32 W, 3313 m)		✓	✓	✓	✓
11. Itajuba (22.41 S, 45.45 W, 856 m)	✓				✓
12. La_Paz (16.54 S, 68.07 W, 3439 m)	✓	✓	✓	✓	✓
13. Petrolina_SONDA (9.07 S, 40.32 W, 381 m)	✓	✓			
14. Pilar_Cordoba (31.67 S, 63.88 W, 333 m)				✓	
15. Quito_USFQ (0.20 S, 78.44 W, 2414 m)				✓	✓
16. SANTA_CRUZ_UTEPSA (17.77 S, 63.20 W, 432 m)				✓	✓
17. Santiago_Beauchef (33.46 S, 70.66 W, 560 m)	✓		✓		
18. Sao_Martinho_SONDA (29.44 S, 53.82 W, 489 m)	✓	✓			
19. Sao_Paulo (23.56 S, 46.73 W, 786 m)		✓		✓	
20. Trelew (43.25 S, 65.31 W, 15 m)	✓	✓	✓		
21. Tucuman (26.79 S, 65.21 W, 481 m)				✓	
22. UdeConcepcion-CEFOP (36.84 S, 73.03 W, 170 m)	✓				
Europe (57)					
1. AAOT (45.31 N, 12.51 E, 10 m)				✓	✓
2. ATHENS-NOA (37.97 N, 23.72 E, 130 m)	✓		✓		
3. Aras_de_los_Olmos (39.95 N, 1.10 W, 1280 m)			✓	✓	✓
4. Arcachon (44.66 N, 1.16 W, 11 m)	✓	✓			
5. Aubiere_LAMP (45.76 N, 3.11 E, 423 m)	✓	✓	✓	✓	✓
6. Badajoz (38.88 N, 7.01 W, 186 m)	✓	✓	✓	✓	✓
7. Barcelona (41.39 N, 2.11 E, 125 m)		✓	✓	✓	✓
8. Bure_OPE (48.56 N, 5.51 E, 393 m)	✓	✓		✓	
9. Burjassot (39.51 N, 0.42 W, 104 m)	✓		✓	✓	✓

10. CENER (42.82 N, 1.60 W, 471 m)	✓	✓	✓	✓	
11. Cabo_da_Roca (38.78 N, 9.50 W, 136 m)	✓	✓	✓	✓	
12. Carpentras (44.08 N, 5.06 E, 107 m)	✓	✓	✓	✓	
13. Coruna (43.36 N, 8.42 W, 67 m)	✓	✓	✓	✓	✓
14. Dunkerque (51.04 N, 2.37 E, 5 m)	✓		✓	✓	✓
15. El_Arenosillo (37.11 N, 6.73 W, 59 m)			✓	✓	✓
16. Ersa (43.00 N, 9.36 E, 80 m)	✓	✓	✓	✓	
17. Evora (38.57 N, 7.91 W, 293 m)	✓	✓	✓	✓	✓
18. FORTH_CRETE (35.33 N, 25.28 E, 20 m)		✓			
19. FZJ-JOYCE (50.91 N, 6.41 E, 111 m)	✓	✓			✓
20. Finokalia-FKL (35.34 N, 25.67 E, 258 m)				✓	
21. Frioul (43.27 N, 5.29 E, 40 m)	✓	✓			
22. Galata_Platform (43.04 N, 28.19 E, 31 m)	✓	✓	✓	✓	✓
23. Gozo (36.03 N, 14.26 E, 111 m)		✓	✓		
24. Granada (37.16 N, 3.61 W, 680 m)		✓	✓	✓	✓
25. HohenpeissenbergDWD (47.80 N, 11.01 E, 989.68 m)		✓	✓	✓	✓
26. Huelva (37.02 N, 6.57 W, 25 m)	✓				
27. IMAA_Potenza (40.60 N, 15.72 E, 770 m)		✓	✓	✓	✓
28. Ispra (45.80 N, 8.63 E, 235 m)	✓	✓	✓	✓	✓
29. Karlsruhe (49.09 N, 8.43 E, 140 m)				✓	✓
30. LAQUILA_Coppito (42.37 N, 13.35 E, 656 m)		✓	✓	✓	
31. Lamezia_Terme (38.88 N, 16.23 E, 8 m)			✓	✓	✓
32. Lecce_University (40.34 N, 18.11 E, 30 m)	✓		✓		✓
33. Leipzig (51.35 N, 12.44 E, 125 m)	✓	✓	✓	✓	✓
34. Lille (50.61 N, 3.14 E, 60 m)	✓	✓	✓	✓	✓
35. Madrid (40.45 N, 3.72 W, 680 m)	✓	✓	✓	✓	✓
36. Magurele_Inoe (44.35 N, 26.03 E, 90 m)		✓	✓		
37. Messina (38.20 N, 15.57 E, 15 m)		✓			
38. MetObs_Lindenberg (52.21 N, 14.12 E, 120 m)	✓			✓	
39. Modena (44.63 N, 10.95 E, 56 m)			✓	✓	
40. Montsec (42.05 N, 0.73 E, 1574 m)		✓	✓	✓	✓
41. Munich_University (48.15 N, 11.57 E, 533 m)	✓	✓	✓	✓	
42. Murcia (38.00 N, 1.17 W, 69 m)	✓	✓	✓	✓	✓
43. Napoli_CeSMA (40.84 N, 14.31 E, 50 m)			✓	✓	✓
44. OHP_OBSERVATOIRE (43.94 N, 5.71 E, 680 m)	✓	✓	✓	✓	✓
45. Palaiseau (48.71 N, 2.22 E, 156 m)	✓		✓	✓	✓
46. Palencia (41.99 N, 4.52 W, 750 m)	✓	✓	✓	✓	✓
47. Palma_de_Mallorca (39.55 N, 2.63 E, 10 m)	✓	✓	✓		
48. Paris (48.85 N, 2.36 E, 50 m)	✓	✓	✓	✓	✓
49. Rome_Tor_Vergata (41.84 N, 12.65 E, 130 m)	✓	✓	✓	✓	
50. Tabernas_PSA-DLR (37.09 N, 2.36 W, 500 m)	✓	✓	✓	✓	✓
51. Thessaloniki (40.63 N, 22.96 E, 60 m)	✓	✓		✓	
52. Toulon (43.14 N, 6.01 E, 50 m)	✓	✓	✓	✓	✓

53. Toulouse_MF (43.57 N, 1.37 E, 160 m)	✓	✓	✓	✓	✓
54. Valladolid (41.66 N, 4.71 W, 705 m)	✓	✓	✓	✓	✓
55. Venise (45.31 N, 12.51 E, 10 m)	✓	✓		✓	✓
56. Vienna_BOKU (48.24 N, 16.33 E, 266 m)				✓	✓
57. Zaragoza (41.63 N, 0.88 W, 250 m)	✓	✓	✓	✓	✓
North Africa (13)					
1. Banizoumbou (13.55 N, 2.67 E, 274 m)	✓	✓	✓	✓	✓
2. Ben_Salem (35.55 N, 9.91 E, 130 m)	✓	✓			✓
3. Dakar (14.39 N, 16.96 W, 21 m)	✓		✓	✓	✓
4. IER_Cinzana (13.28 N, 5.93 W, 285 m)		✓		✓	
5. Ilorin (8.48 N, 4.67 E, 400 m)	✓	✓			✓
6. Koforidua_ANUC (6.11 N, 0.30 W, 205 m)		✓	✓		✓
7. Medenine-IRA (33.50 N, 10.64 E, 33.5 m)	✓	✓	✓	✓	✓
8. Oujda (34.65 N, 1.90 W, 620 m)	✓				
9. Saada (31.63 N, 8.16 W, 420 m)	✓	✓	✓	✓	✓
10. Tamanrasset_INM (22.79 N, 5.53 E, 1377 m)		✓	✓	✓	✓
11. Tizi_Ouzou (36.70 N, 4.06 E, 133 m)	✓	✓			
12. Tunis_Carthage (36.84 N, 10.20 E, 10 m)	✓	✓	✓	✓	✓
13. Zinder_Airport (13.78 N, 8.99 E, 456 m)	✓		✓	✓	
South Africa (16)					
1. Bonanza (21.83 S, 19.59 E, 1382 m)		✓	✓		
2. Gobabeb (23.56 S, 15.04 E, 405 m)	✓	✓	✓	✓	✓
3. HESS (23.27 S, 16.50 E, 1818 m)		✓	✓	✓	✓
4. Henties_Bay (22.10 S, 14.26 E, 20 m)		✓	✓	✓	
5. Lubango (14.96 S, 13.45 E, 2047 m)		✓	✓		✓
6. Maun_Tower (19.90 S, 23.55 E, 951 m)				✓	✓
7. Mongu_Inn (15.27 S, 23.13 E, 1040 m)	✓	✓	✓	✓	✓
8. Namibe (15.16 S, 12.18 E, 11 m)		✓	✓	✓	
9. Pretoria_CSIR-DPSS (25.76 S, 28.28 E, 1449 m)	✓		✓		
10. SEGC_Lope_Gabon (0.20 S, 11.60 E, 280 m)		✓	✓		
11. Simonstown_IMT (34.19 S, 18.45 E, 27 m)				✓	✓
12. Skukuza (24.99 S, 31.59 E, 265 m)			✓	✓	✓
13. Tsumkwe (19.62 S, 20.44 E, 1154 m)		✓	✓		
14. Upington (28.38 S, 21.16 E, 865 m)		✓	✓		
15. Welgegund (26.57 S, 26.94 E, 1480 m)					✓
16. Windpoort (19.37 S, 15.48 E, 1206 m)		✓	✓	✓	✓
Middle East (16)					
1. AgiaMarina_Xyliatou (35.04 N, 33.06 E, 521 m)		✓	✓	✓	✓
2. Cairo_EMA_2 (30.08 N, 31.29 E, 70 m)	✓	✓	✓	✓	
3. CUT-TEPAK (34.67 N, 33.04 E, 22 m)	✓	✓	✓	✓	✓
4. DEWA_ResearchCentre (24.77 N, 55.37 E, 86.8 m)					✓
5. Eilat (29.50 N, 34.92 E, 15 m)	✓	✓		✓	
6. El_Farafra (27.06 N, 27.99 E, 92 m)	✓	✓	✓		

7. IMS-METU-ERDEMLI (36.57 N, 34.26 E, 3 m)		✓	✓		
8. KAUST_Campus (22.30 N, 39.10 E, 11.2 m)	✓	✓	✓		
9. Masdar_Institute (24.44 N, 54.62 E, 4 m)		✓		✓	
10. Mezaira (23.10 N, 53.75 E, 201 m)	✓		✓	✓	
11. Migal (33.24 N, 35.58 E, 200 m)					✓
12. Qena_SVU (26.20 N, 32.75 E, 75.7 m)					✓
13. SEDE_BOKER (30.86 N, 34.78 E, 480 m)	✓	✓	✓	✓	✓
14. Shagaya_Park (29.21 N, 47.06 E, 242 m)			✓	✓	✓
15. Technion_Haifa_IL (32.78 N, 35.02 E, 230 m)			✓		
16. Weizmann_Institute (31.91 N, 34.81 E, 73 m)		✓	✓	✓	✓
Australia (7)					
1. Birdsville (25.90 S, 139.35 E, 46.5 m)	✓	✓	✓		
2. Canberra (35.27 S, 149.11 E, 600 m)	✓	✓	✓		
3. Fowlers_Gap (31.09 S, 141.70 E, 181 m)	✓	✓	✓		
4. Jabiru (12.66 S, 132.89 E, 30 m)		✓			✓
5. Lake_Argyle (16.11 S, 128.75 E, 150 m)	✓	✓	✓	✓	
6. Lake_Lefroy (31.26 S, 121.71 E, 300 m)	✓	✓	✓		✓
7. Lucinda (18.52 S, 146.39 E, 8 m)	✓	✓	✓	✓	✓

AOD is estimated from direct Sun measurements, and these measurements are performed every 15 minutes in cloud-free conditions (Giles et al., 2019). While SSA and DRE are retrieved from almucantar sky radiance measurements, which are made at optical air masses (representing the relative path length of solar radiation travelling through the Earth's atmosphere and strongly dependent on the secant of the solar zenith angle) of 4, 3, 2, and 1.7 in the morning and afternoon during cloud-free conditions when solar zenith angle varies between 50^{o} and 80^{o} (Sinyuk et al., 2020). In this study, SSA corresponding to $AOD_{0.44} \geq 0.2$ retrieved from both level 1.5 and level 2 datasets are utilized (Section 2.1.2). Whereas, DRE retrieved for all AOD conditions (Section 2.1.3) is utilized to be consistent with other aerosol parameters, e.g., AOD, FMF, volume size distribution, and asymmetry parameter.

Thus, after imposing the above-mentioned criteria of the availability of aerosol absorption parameters (SSA and AAOD), the total observational sites for the analysis of aerosol absorption parameters is found to be less (a total of 139 sites; a detailed description of these is provided in Ansari & Ramachandran (2025b)) across the globe compared to the availability of AOD and DRE datasets. Due to different temporal sampling, AOD conditions, and site availability for different aerosol parameters, the number of observational counts for AOD is found to be significantly higher, followed by DRE and SSA, for all the regions (Table 2.3). However, this will not affect the reliability of

Table 2.3: *Total number of observational counts for different aerosol parameters (aerosol optical depth (AOD), single scattering albedo (SSA), aerosol direct radiative effect (DRE)) from the AERONET dataset during the study period of 2015–2019 in all selected regions across the globe, following the criteria mentioned in Section 2.2 and used in the study.*

Regions	Observational counts for different aerosol parameters		
	AOD	SSA	DRE
Central Asia	79336	197	3303
South Asia – I	241618	13699	14136
South Asia – II	20684	870	734
Southeast Asia	174925	1668	4039
East Asia	655862	14355	24594
North America	2378164	2449	115610
South America	451569	1373	20245
Europe	1848400	16045	106602
North Africa	445525	14731	28341
South Africa	875052	3864	31950
Middle East	708257	22451	40023
Australia	280086	116	10728

the inferences drawn because diurnal variation of SSA is less than that of AOD, and all the selected observed sites collectively cover the broader spatial extent in each region (Torres & Ahn, 2024; Ansari & Ramachandran, 2025b).

2.3 Satellite datasets

2.3.1 MODerate resolution Imaging Spectroradiometer (MODIS)

The MODerate resolution Imaging Spectroradiometer (MODIS) collection 6.1 level 3 retrieved AOD (at 0.55 μm wavelength) from both Terra and Aqua satellites obtained by the combined deep blue and dark target (DTDB) algorithm corresponding to the 2015–2019 period at a spatial resolution of $1^o \times 1^o$ is utilized (Levy et al., 2013; Platnick et al., 2015). MODIS onboard both Terra and Aqua satellites operate in sun-synchronous, near-polar, circular orbits at an altitude of 705 km above the Earth. The Terra and Aqua spacecraft cross the equator at about 10:30 (descending southward) and 13:30 LST (ascending northward), respectively, with a swath of 2330 km (cross track). The expected error (EE) in MODIS AOD, which explains the range of one standard deviation

containing at least 67% of the matchups under the normal distribution hypothesis, is $\pm(0.05+0.15\times AOD)$ over land (Levy et al., 2013).

2.3.2 Clouds and the Earth's Radiant Energy System (CERES)

CERES Synoptic (SYN1deg, edition 4.1) 1-hour shortwave radiative fluxes at top of the atmosphere and surface provided at $1^o \times 1^o$ spatial resolution during the study period of 2015–2019 are utilized (Rutan et al., 2015; NASA/LARC/SD/ASDC, 2017) (https://ceres.larc.nasa.gov/). Shortwave radiative flux for two atmospheric conditions of clear-sky (with aerosols and cloud-free conditions) and pristine (clear-sky with no aerosols) are used. Langley Fu–Liou radiative transfer model is used to compute the radiative fluxes at surface and aerosol-free conditions, whereas radiative fluxes at TOA are derived from CERES measured spectral radiances (Fu et al., 1998). Radiative transfer simulations are conducted using aerosol properties from the Model for Atmospheric Transport and Chemistry (MATCH), which are constrained by MODIS (Terra + Aqua) and CERES observations (Fillmore et al., 2022). DRE_{TOA} is computed by subtracting net pristine fluxes from net clear-sky fluxes at the top of atmosphere, and DRE_{SFC} is computed by subtracting net clear-sky fluxes and pristine fluxes at the surface. CERES DRE_{ATM} is calculated by the difference between CERES DRE_{TOA} and DRE_{SFC}, similar to AERONET DRE_{ATM} calculation (Eq. 2.8).

2.4 Model simulations

2.4.1 Modern-Era Retrospective Analysis for Research and Applications-2 (MERRA-2) reanalysis

MERRA-2 is the latest reanalysis dataset provided by NASA's Global Modeling and Assimilation Office (GMAO) at spatial resolution of $0.5^o \times 0.625^o$ (latitude $\times$ longitude) (Gelaro et al., 2017). The assimilation system in MERRA-2 is based on Goddard Earth Observing System (GEOS-5), a weather and climate model. The GEOS-5 model in MERRA-2 includes the assimilation of bias-corrected AOD from Advanced Very High Resolution Radiometer (AVHRR; before 2002), Multi-angle Imaging SpectroRadiometer (MISR; February 2000-June 2014), AERONET (before 2014), and Moderate Resolution Imaging Spectroradiometer (MODIS) measurements from Terra and Aqua satellites (from 2002 onwards) (Randles et al., 2017). Aerosol products simulated by MERRA-2

are radiatively coupled with the Goddard Chemistry, Aerosol, Radiation, and Transport (GOCART) model (Colarco et al., 2010). MERRA-2 simulates aerosol parameters for five species: sulfate, dust, BC, OC, and sea salt aerosols. The anthropogenic SO_2 emissions in MERRA-2 are utilized from the Emissions Database for Global Atmospheric Research (EDGAR v4.2) database of annually varying emissions between 1970 and 2008 (European Commission, 2011). From 2010, the daily emission of biomass burning emitted carbonaceous aerosol and SO_2 emissions are obtained from the Quick Fire Emissions Dataset (QFED) v2.4-r6 (Darmenov & da Silva, 2015). The anthropogenic emissions of primary carbonaceous and sulfate aerosols are utilized from the AeroCom Phase II dataset (HCA0 v1; Diehl et al. (2012)), which is varied annually between 1979 and 2006. The emissions of dust and sea salt aerosols are wind speed dependent (Randles et al., 2017). Detailed information about MERRA-2 is provided by Randles et al. (2017), Gelaro et al. (2017), and Buchard et al. (2017).

MERRA-2 v5.12.4 (M2T1NXAER) (Global Modeling and Assimilation Office (GMAO), 2015a) simulated aerosol optical parameters such as AOD and scattering AOD (SAOD) at 0.55 μm and AE at 0.47-0.87 μm ($AE_{0.47-0.87}$) at a temporal resolution of 1 h during the 2015–2019 period are utilized, to maintain consistency and allow for spatiotemporal collocated validation with AERONET datasets. MERRA-2 simulated AOD and SAOD are used to calculate the SSA (=SAOD/AOD) and AAOD (=AOD – SAOD). MERRA-2 v5.12.4 (M2T1NXRAD) (Global Modeling and Assimilation Office (GMAO), 2015b) simulated net shortwave flux with and without aerosols under clear-sky conditions at the top of the atmosphere (SWTNTCLR and SWTNTCLRCLN, respectively) and surface (SWGNTCLR and SWGNTCLRCLN, respectively) during the period of 2015–2019 at a 1-hour temporal resolution are utilized, ensuring consistent spatiotemporal collocated validation with AERONET DRE. $\mathrm{DRE_{TOA}}$ and $\mathrm{DRE_{SFC}}$ from MERRA-2 are calculated as:

$$\mathrm{DRE_{TOA}} = \mathrm{SWTNTCLR} - \mathrm{SWTNTCLRCLN} \tag{2.11}$$

$$\mathrm{DRE_{SFC}} = \mathrm{SWGNTCLR} - \mathrm{SWGNTCLRCLN} \tag{2.12}$$

The difference between MERRA-2 $\mathrm{DRE_{TOA}}$ and $\mathrm{DRE_{SFC}}$ is used to calculate MERRA-2 $\mathrm{DRE_{ATM}}$, as AERONET $\mathrm{DRE_{ATM}}$ is calculated (Eq. 2.8).

2.4.2 Copernicus Atmosphere Monitoring Service (CAMS) reanalysis

The CAMS reanalysis is provided by the European Centre for Medium-Range Weather Forecast (ECMWF) with the updated Integrated Forecast System (IFS), which uses an extended version of the Carbon Bond 2005 chemical mechanism (Inness et al., 2019; Copernicus Atmosphere Monitoring Service, 2020). MODIS onboard Terra and Aqua satellite collection 6 retrieval AOD is included in CAMS aerosols assimilation (Inness et al., 2019). The spatial resolution of the CAMS reanalysis is $0.75^{o} \times 0.75^{o}$ (latitude $\times$ longitude), and CAMS consists of 60 hybrid sigma–pressure (model) levels in the vertical with the model top at 0.1 hPa (Inness et al., 2019). CAMS simulates the total AOD (at five wavelengths of 0.469, 0.55, 0.67, 0.865, and 1.24 μm), and AODs corresponding to five aerosol species of sulfate, dust, BC, sea salt, and organic matter at 0.55 μm. In CAMS, the anthropogenic emissions of BC, OC, and SO_2 were taken from Monitoring Atmospheric Composition and Climate-CityZen (MACCity) (Granier et al., 2011). The daily global biomass burning emissions of aerosols and reactive gases were provided by Global Fire Assimilation System (GFASv1.2) (Kaiser et al., 2012). Detailed information about the CAMS reanalysis is provided in Inness et al. (2019). CAMS simulated 3-hourly AODs at 0.469, 0.55, 0.67, and 0.865 μm during 2015–2019 are utilized, in order to maintain uniformity and enable a collocated comparison with AERONET observations. Since CAMS does not provide AE, CAMS simulated spectral AODs at 0.469, 0.55, 0.67, and 0.865 μm are used to derive AE at 0.469-0.865 μm ($AE_{0.469-0.865}$) by fitting power-law (e.g., slope of linear fitted line between $ln(\mathrm{AOD})$ and $ln(\lambda)$.

2.4.3 Coupled Model Intercomparison Project Phase 6 (CMIP6) simulations

The CMIP aims to enhance the understanding of climate change (past, present, and future) due to perturbations in the Earth-atmosphere energy balance (Eyring et al., 2016) (https://esgf-node.llnl.gov/search/cmip6/). The CMIP6 "historical" simulations run until 2014 are complemented with a "ScenarioMIP" simulation (Eyring et al., 2016) for the 2015 to 2019 period. CMIP6 simulations comprising the “historical” experiments that run up to 2014, complemented by the “ScenarioMIP” projections covering the 2015-2019 period are considered (Eyring et al., 2016). The Shared Socioeconomic Pathway (SSP245), following the middle-of-the-road SSP2 pathway with a projected global

Table 2.4: *Details of the CMIP6 models the simulations of which are utilized in the thesis.*

No.	Model Name	Institution	Spatial Resolution (Lat × Lon)	Ensemble	References
1	CanESM5	CCCMA, Canada	$2.8^o \times 2.8^o$	2	Swart et al. (2019)
2	GFDL-CM4	Geophysical Fluid Dynamics Laboratory (GFDL), USA	$1^o \times 1.25^o$	1	Held et al. (2019)
3	HadGEM3-GC31-LL	Met Office Hadley Centre, UK	$1.25^o \times 1.875^o$	1	Andrews et al. (2020)
4	IPSL-CM6A-LR	IPSL, France	$1.259^o \times 2.5^o$	1	Boucher et al. (2020)
5	MIROC6	MIROC, Japan	$1.4^o \times 1.4^o$	1	Hajima et al. (2020)
6	NorESM2-LM	Climate Modeling Consortium, Norway	$1.875^o \times 2.5^o$	1	Seland et al. (2020)

mean forcing of 4.5 Wm^{-2} by 2100 relative to pre-industrial levels, is selected for future scenario (Eyring et al., 2016). Simulation results from 6 models from the CMIP6 are utilized, where direct ARF product is available, and the details of these models are given in Table 2.4. All CMIP6 models utilize a consistent emission dataset from the Community Emissions Data System (CEDS) for the historical period (1850-2014) (Hoesly et al., 2018), while future emissions are based on projections extending from 2015 to 2100 (Gidden et al., 2019).

All aerosol parameters (AOD, SSA, and ARF) in the above CMIP6 models are interpolated to a spatial resolution of $1.4^o \times 1.4^o$ (T85) to facilitate the comparison among models' and the averaging of model aerosol products. The respective CMIP6 models and their mean (multi-model mean, MMM) aerosol parameters are compared with AERONET measurements using monthly mean aerosol products. However, it should be noted that this comparison is not as rigorous or robust as the inter-comparisons performed for MERRA-2 and CAMS, primarily due to differences in spatial and temporal

sampling (Table 2.4). A systematic comparison would require extracting model outputs corresponding to the same time and space of AERONET observation, and this information is not available within the CMIP6 database, as the CMIP6 simulated aerosol parameters are available on a monthly basis. In this thesis, the comparison between CMIP6 and AERONET is restricted to monthly means, and further, regional mean values for each region are calculated over the grids where AERONET sites are located (Fig. 2.1, Table 2.2), and as a result, the biases in AOD and SSA in CMIP6 models with respect to AERONET, and the differences between CMIP6 ARF and AERONET DRE over each region are analyzed and discussed.

2.5 Collocated validation of model simulations and satellite retrievals with AERONET

In this thesis, the spatiotemporal collocated validations/evaluations of (a) MERRA-2 simulated $AOD_{0.55}$, $AE_{0.47-0.87}$, $SSA_{0.55}$, $AAOD_{0.55}$, and DREs (e.g. DRE at TOA, SFC, and ATM), (b) CAMS simulated $AOD_{0.55}$ and $AE_{0.469-0.865}$, and (c) CERES retrieved DREs with AERONET datasets are performed over Asia and other regions of the globe on annual and seasonal scales.

AERONET $AOD_{0.55}$ is derived from the measured $AOD_{0.50}$ and $AE_{0.44-0.87}$ using the power-law relation $AOD_{0.55} = AOD_{0.50} \times (0.50/0.55)^{AE}$ for a seamless comparison with model simulated AODs at 0.55 μm. Numerical simulations revealed that the difference between AE derived using AODs obtained at these two wavelength ranges of 0.44-0.87 μm and 0.47-0.87 μm, respectively, is negligible (Su et al., 2023). Thus, MERRA-2 simulated $AE_{0.47-0.87}$ (derived from AODs in the wavelength range of 0.47-0.87 μm) and CAMS derived AE (AODs in the wavelength range of 0.469-0.865 μm) can be compared with AERONET AE (derived from AODs in the wavelength range of 0.44-0.87 μm). The linear interpolation method is utilized to calculate AERONET SSA at 0.55 μm using the SSA retrieved at 0.44 and 0.675 μm for the evaluation of the MERRA-2 SSA. To evaluate MERRA-2 AAOD, AERONET AAOD at 0.55 μm is calculated using the power law relation given as $AAOD = K\lambda^{-AAE}$, where AAE is derived from spectral AAODs in the wavelength range of 0.44 to 0.87 μm.

For the collocated validation of MERRA-2 and CAMS simulations and satellite retrievals with AERONET dataset, the hourly mean aerosol optical and radiative

parameters from the AERONET dataset are utilized to maintain uniformity with the temporal resolution of models (Fig. 2.2). The hourly averaged AERONET measurements are compared with corresponding model and satellite outputs from the spatial grid cell that contains the observation sites. This approach effectively minimizes spatial differences between the AERONET and model and satellite outputs, and maintains temporal resolution, thereby reducing representation errors and improving the reliability of the validation (Schutgens et al., 2017). When sites are close enough to each other and >1 AERONET site is found in a single grid, no significant spatial variation in AOD, AE, and SSA between these sites was observed as the sites were close. Thus, when there is >1 AERONET site in a single grid, then the same model and satellite outputs in that particular grid are taken over those sites for comparison.

For the quantitative validation of the satellite-retrieved and model-simulated products, statistical parameters, including the root mean square error (RMSE), mean bias error (MBE), and Pearson correlation coefficient (R), are calculated. In addition, for some aerosol parameters (i.e., wherever it is available), EE (for AOD, AE, AAOD) and

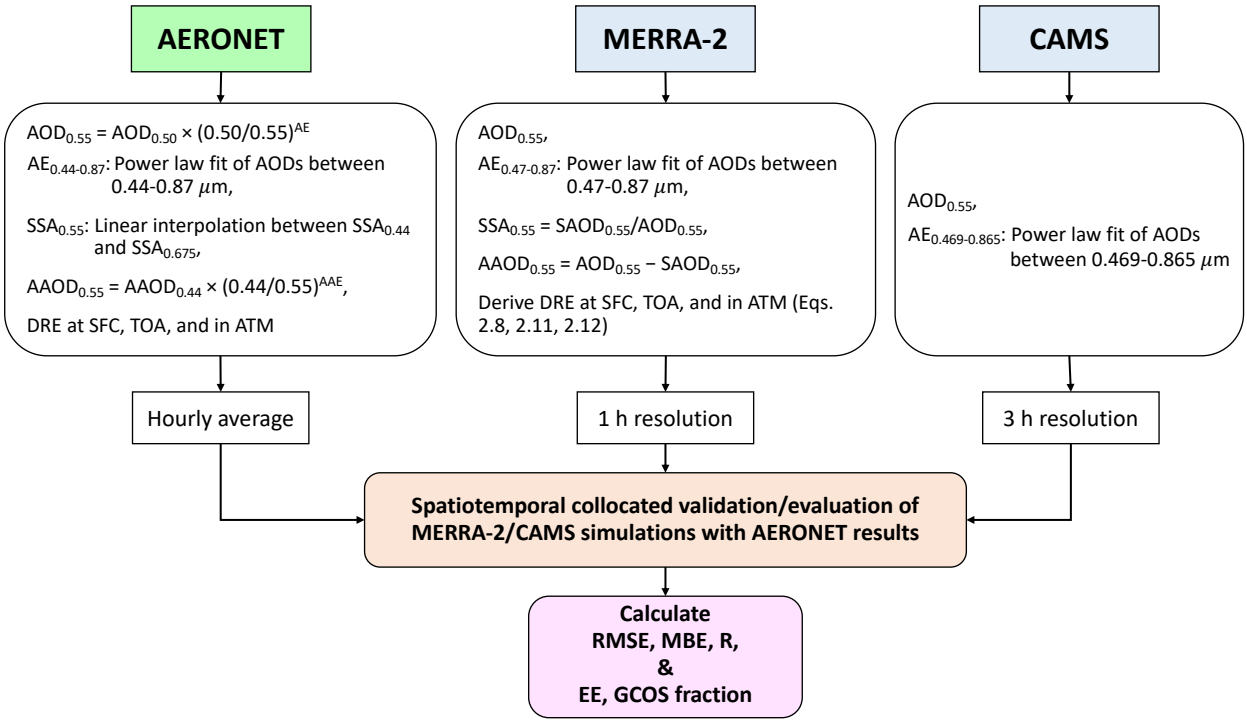

Figure 2.2: *Flowchart illustrating the steps involved in the validation/evaluation of columnar aerosol optical and radiative properties simulated by models (MERRA-2 and CAMS) with results obtained from AERONET analysis.*

Global Climate Observing System (GCOS) fraction (%) (for AOD, SSA) are calculated. GCOS fraction is the fraction of the number of model simulated datasets that satisfy the GCOS requirement. The EE of AOD retrieved from the MODIS DT algorithm over land is $\pm(0.05 + 0.15 \times \mathrm{AOD}_{\mathrm{AERONET}})$ (Levy et al., 2010). The same EE for MODIS-DT AOD is chosen to validate MERRA-2 and CAMS simulated AODs since MODIS-DT AOD has been assimilated into both models (Randles et al., 2017; Inness et al., 2019). The EE for AE is chosen to be ± 0.4 from previous studies (Levy et al., 2010; Su et al., 2023). The EE for AAOD is defined as $\pm(0.01 + 0.1 \times \mathrm{AAOD}_{\mathrm{AERONET}})$, which is used to validate the MERRA-2 simulated AAOD (Ou et al., 2022; Bakatsoula et al., 2023). GCOS sets out a generalized and stricter observational requirement for the required data record of AOD and SSA, which is demanded by the climate modeling community. For AOD, the GCOS requirement is that the accuracy of AOD should be max(0.03 or 10% of AOD) (Popp et al., 2016). By taking the uncertainty of 0.01 for AERONET AOD, the GCOS requirement is defined as max(0.04 or 10% of AOD) (Chen et al., 2020). The accuracy required for SSA under the GCOS requirement is 0.03, which is the same as the uncertainty in AERONET SSA (Popp et al., 2016).

3

Optical and Physical Characteristics of Aerosols

The climate feedback due to the rapid changes in the aerosol emissions over Asia is found to be uncertain because of the limitations in capturing the aerosol trends by the current climate models and the lack of regional and seasonal scale characterization of columnar aerosol properties based on high-quality observational datasets (IPCC, 2021; Li et al., 2022; Kok et al., 2023). The diverse and intense aerosol emissions across Asia substantially influence the physicochemical and optical properties of aerosols. Thus, a detailed regional and seasonal investigation of columnar optical and physical characteristics of aerosols, along with accurate quantification of aerosol absorption parameters over Asia using high-quality observations, is essential to investigate the aerosol emissions, sources, and composition, thereby improving assessments of their radiative and climate impact over Asia.

This chapter presents the spatial and regional distribution of columnar aerosol optical and physical properties (AOD, AE, FMF and VSD) and absorption parameters (SSA and AAOD) over Asia and other regions of the globe, based on the AERONET dataset on seasonal and annual scales. Further, a comprehensive assessment of the spatiotemporal collocated validation of simulated aerosol parameters, including AOD (from MERRA-2, CAMS, and CMIP6), AE (from MERRA-2 and CAMS), SSA (from MERRA-2 and CMIP6), and AAOD (from MERRA-2), with AERONET observations across Asia and other regions of the globe is performed. Model performances are systematically evaluated by quantifying associated biases and investigating potential sources of discrepancies in the simulation of various aerosol parameters. Furthermore, a comparative analysis of the seasonal and annual variations in aerosol characteristics and model per-

formance over Asia relative to other regions of the globe is conducted to provide global insights into the regional variation of aerosol characteristics and model performances.

3.1 Aerosol optical depth, Ångström exponent, and fine mode fraction over Asia

AOD, AE, and FMF exhibit large spatial, regional, and seasonal variation over Asia, which is attributed to the spatial and seasonal changes in aerosol emissions, aerosol types, and transport mechanisms (Fig. 3.1). On an annual scale, AOD is >0.4 for nearly half of the total observation sites in Asia (18 out of total 44 sites), which indicates the highly polluted environmental condition over these sites. These sites are mainly concentrated in South Asia (except Hanimaadhoo, a background island site), followed by East Asia (mainland China and Taiwan) and Southeast Asia (Thailand and Singapore) (Fig. 3.1a) (Ansari & Ramachandran, 2024b).

Central Asia is primarily affected by dust transported from Taklamakan, Aralkum, Kyzylkum, Karakum, and Gobi deserts, and it is relatively less affected by anthropogenic emissions compared to the other regions in Asia (Rupakheti et al., 2020, 2023). The annual mean AOD over Central Asia (∼0.16) is relatively lower than other regions in Asia. On a seasonal scale in Central Asia, Dushanbe experiences a higher AOD (0.35) during the summer season, followed by autumn due to the influence of dust aerosols as it is located in the proximity of Taklamakan, Aralkum, and Karakum deserts, which results in low AE and FMF (Fig. 3.1d) (e.g., Rupakheti et al. (2020)). Whereas the lesser influence of dust and higher contribution from fine anthropogenic aerosols during winter, compared to other seasons, results in higher AE and FMF over Central Asia. Over Issyk-Kul and Dalanzadgad, seasonal mean AOD is always <0.15, and it increases only during the dust storm seasons, which are dominant in spring (e.g., Rupakheti et al. (2023)).

Most sites in South Asia – I (IGP), including both urban and rural, exhibit highest AOD (>0.4) with high values of AE (>1) and FMF (>0.6) during winter and autumn compared to the other regions in Asia, which clearly indicates the dominance of fine mode anthropogenic aerosols (Fig. 3.1b, d) (Ansari & Ramachandran, 2024b). The primary reason for higher aerosol emissions during winter is the increase in local anthropogenic emissions from biomass burning and residential heating, in addition to

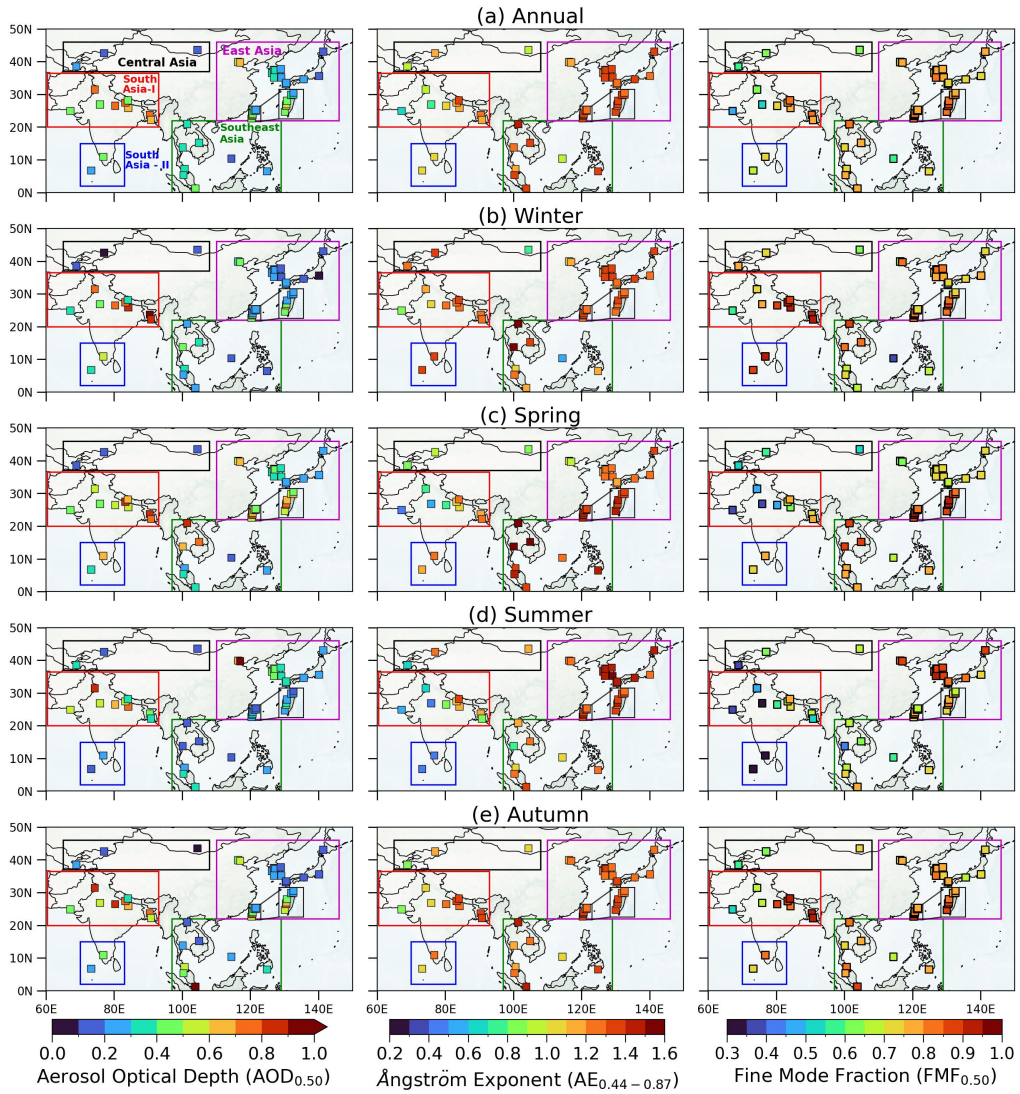

Figure 3.1: *The spatial distribution of aerosol optical depth (AOD at 0.50 μm) (1^{st} column), Ångström exponent (AE in the wavelength of 0.44-0.87 μm) (2^{nd} column), and fine mode fraction (FMF at 0.50 μm) (3^{rd} column) over all selected observational sites in Asia (Table 2.2) on (a) annual and seasonal scales during (b) winter, (c) spring, (d) summer, and (e) autumn. Boxes correspond to different regions in Asia: Central Asia, South Asia – I, South Asia – II, Southeast Asia, and East Asia, mentioned in the top left panel.*

industrial and vehicular emissions, with the shallow boundary layer and low wind speed (Kedia et al., 2014; Ramachandran & Rupakheti, 2022b). Whereas in autumn, the intense crop residue burning activities over northwestern IGP sites and the transport of their emissions to east IGP sites give rise to high AOD (Kedia et al., 2014; Jethva & Torres, 2019). During spring, strong westerly winds carry mineral dust aerosols from the western arid regions of the Thar Desert and Arabian Peninsula over South Asia,

which increase the contribution of coarse mode aerosols which lower the AE and FMF values in IGP, and their values exhibit an increasing gradient from west to east IGP (Fig. 3.1c). Whereas, during summer, the transport of dust in addition to sea salt from strong southwesterly winds increases the natural aerosol contribution (Ramachandran et al., 2020a), which results in lower AE and FMF over the entire South Asia – I including east IGP sites (Fig. 3.1d). Over west and central IGP, AOD is found to be higher even during summer despite high wet deposition due to monsoon. Higher AOD during cloud-free conditions is due to anthropogenic emissions during the inactive rainfall period, along with the transported dust and sea salt aerosols (Mhawish et al., 2021). In addition, high relative humidity during summer enhances the hygroscopic growth of hydrophilic aerosols, which increases the scattering efficiency and overall AOD (Bilal & Nichol, 2015; Mhawish et al., 2019, 2021). AOD over IGP sites is relatively higher in the east compared to the west during winter due to higher anthropogenic emissions in the east with shallow boundary layer and calm winds (Ramachandran et al., 2023). Whereas during summer, AOD over IGP sites is relatively higher in the west compared to the east due to the decreasing gradient of dust transported from west to east and a higher strength of summer monsoon in the east leads to a significant reduction in AOD (e.g., over Dhaka and Bhola) through wet deposition (Ramachandran et al., 2020b).

In South Asia – II, Hanimaadhoo experiences relatively higher AOD (0.3) with higher AE (1.2) and FMF (0.8) due to the transport (northeasterly winds) of fine mode anthropogenic aerosols emitted from the Indian subcontinent, except in summer. AOD is low during summer over Hanimaadhoo due to an increase in wet deposition and changes in the wind direction from northeasterly to southwesterly winds, which transport sea salt and dust, resulting in lower AE (0.4) and FMF (0.3) (e.g., Ramachandran & Rupakheti (2020)) (Fig. 3.1d).

The seasonal variation of AOD over Southeast Asia is mostly affected by forest fires and slash-and-burn agricultural activities that occur during the dry seasons. The Indochinese Peninsula (Thailand, Cambodia, Laos, Myanmar, Vietnam, etc.), located in the inland areas of Southeast Asia, experiences a dry season during winter. Biomass burning starts in mid-winter and intensifies from March to May, and ends during summer with the commencement of wet period (Reid et al., 2013; Gautam et al., 2013). As a result, high AOD (>0.6) is observed with the dominance of fine mode aerosols during spring, which gives rise to higher AE (>1.5) and FMF (>0.8) over the sites

in the Indochinese Peninsula (Fig. 3.1c). Transport of sea salt aerosols from strong southwesterly winds and absence of biomass burning emitted aerosols over these sites during the wet period of summer lead to a statistically significant decrease in AE and FMF from spring to summer with p-value $\leq$0.05 at 95% confidence level (CL) (Student's t-test) (Fig. 3.1d). During summer, the monsoonal trough reaches over the Indochina Peninsula and induces the dry period over the Maritime Continent (Brunei, Indonesia, Malaysia, and Singapore). The emergence of significant biomass burning emissions over Sumatra and Kalimantan during autumn and its northward transport by southwesterly wind over Malaysia and Singapore cause a higher AOD (>0.4) over sites in the southwest part of Southeast Asia with higher AE and FMF (e.g., Nguyen et al. (2019)). A very high AOD ($\sim$0.95) is observed during autumn over Singapore, due to a very strong El Niño event coupled with a positive phase of Indian Ocean Dipole that occurred in 2015 (Pan et al., 2018). As a result of the severe drought caused by this El Niño event, the strength (spatial extent) of biomass burning over the Maritime Continent intensified, and its spread resulted in a high AOD over Singapore (Eck et al., 2019).

In East Asia, the high AOD ($\sim$0.4) over sites in East China during winter, compared to South Korea and Japan, is attributed to emissions from residential heating related to coal combustion and biomass burning (mostly in rural sites) with higher population density and shallow boundary layer (Xie et al., 2020). The transport of dust by westerly winds, mainly from the Gobi Desert, followed by the Taklamakan Desert, over East Asia (Chen et al., 2017) gives rise to a statistically significant increase in AOD during spring from winter. AOD shows a decreasing gradient from west to east in East Asia, whereas, AE and FMF exhibit an increasing gradient in the downwind regions of dust transport over sites from west to east (Fig. 3.1c). The highest AOD (>0.6) over East Asia is observed over sites in East China during summer (Fig. 3.1d). During summer, the precipitation and transport of moisture from the southerly winds increase the relative humidity over East China, which enhances the secondary aerosol formation and hygroscopic growth of fine mode aerosols (e.g., sulfate, nitrate, and ammonium), and contribute to higher aerosol extinction due to fine mode aerosols (FMF >0.8) over East China (Che et al., 2018; Nam et al., 2018). The transport by strong southwesterly and westerly winds during spring gives rise to higher AOD and FMF over all the sites in Taiwan, which carry the anthropogenic aerosols from South China, and biomass burning aerosols from the forest fire region in Southeast Asia over Taiwan (Huang et al., 2019).

The large seasonal variation in AOD over different regions in Asia is attributed to changes in natural and anthropogenic emissions from biomass burning, residential heating, vehicular and industrial emissions in fine mode, and transport of mineral dust and sea salt aerosols in coarse mode. The annual- and seasonal-scale analysis of AOD clearly reveals that South Asia – I exhibits the highest AOD in each season (regional average AOD: 0.63 $\pm$ 0.15), followed by South Asia – II (AOD: 0.37 $\pm$ 0.14), East (AOD: 0.36 $\pm$ 0.13), Southeast (AOD: 0.33 $\pm$ 0.10), and Central Asia (AOD: 0.16 $\pm$ 0.07). The high aerosol loading over South Asia compared to the other regions in Asia is ascribed to the combined influence of both fine mode aerosols emitted from high anthropogenic activities like biofuel and fossil fuel combustion and biomass burning (crop residue burning), and coarse mode aerosols from seasonal (spring and summer) transport of dust and sea-salt aerosols (Ramachandran et al., 2020a,b). The mixture of fine and coarse mode aerosols also results in high seasonal variability in AE and FMF values over South Asia, followed by Southeast, Central, and East Asia. The variation in annual mean AOD from urban to nearby semi-urban and rural sites over Asia, especially in South and East Asia, is found to be quite less, clearly indicating that the extent of anthropogenic aerosol emissions from urban sites can be widespread, leading to higher AOD even over nearby locations (including semi-urban and rural) (e.g., Papachristopoulou et al. (2022); Ansari & Ramachandran (2024b)).

3.2 Aerosol volume size distribution and volume concentration over Asia

Seasonal and annual mean VSD over Asia are bimodal in nature, with the first peak in fine mode (0.05-0.99 μm) (<1 μm) and the second peak in coarse mode (1.30-15 μm) (>1 μm) (Fig. 3.2). The magnitudes of these peaks exhibit significant spatial and seasonal variations depending on the changes/variations in aerosol sources, transport mechanisms, and meteorological conditions. Over Dushanbe in Central Asia, the coarse mode peak is more pronounced ($\sim$3 times higher) than the fine mode peak during summer, followed by autumn, due to the dominance of dust aerosols (Fig. 3.2). This leads to higher total volume concentration (TVC) over Dushanbe with high coarse volume fraction (CVF) (Fig. 3.3) (e.g., Rupakheti et al. (2020)). On an annual scale in South Asia – I, from western and central IGP (arid and semi-arid sites) to eastern IGP (urban-industrial sites with high population density) sites, the CVF decreases and

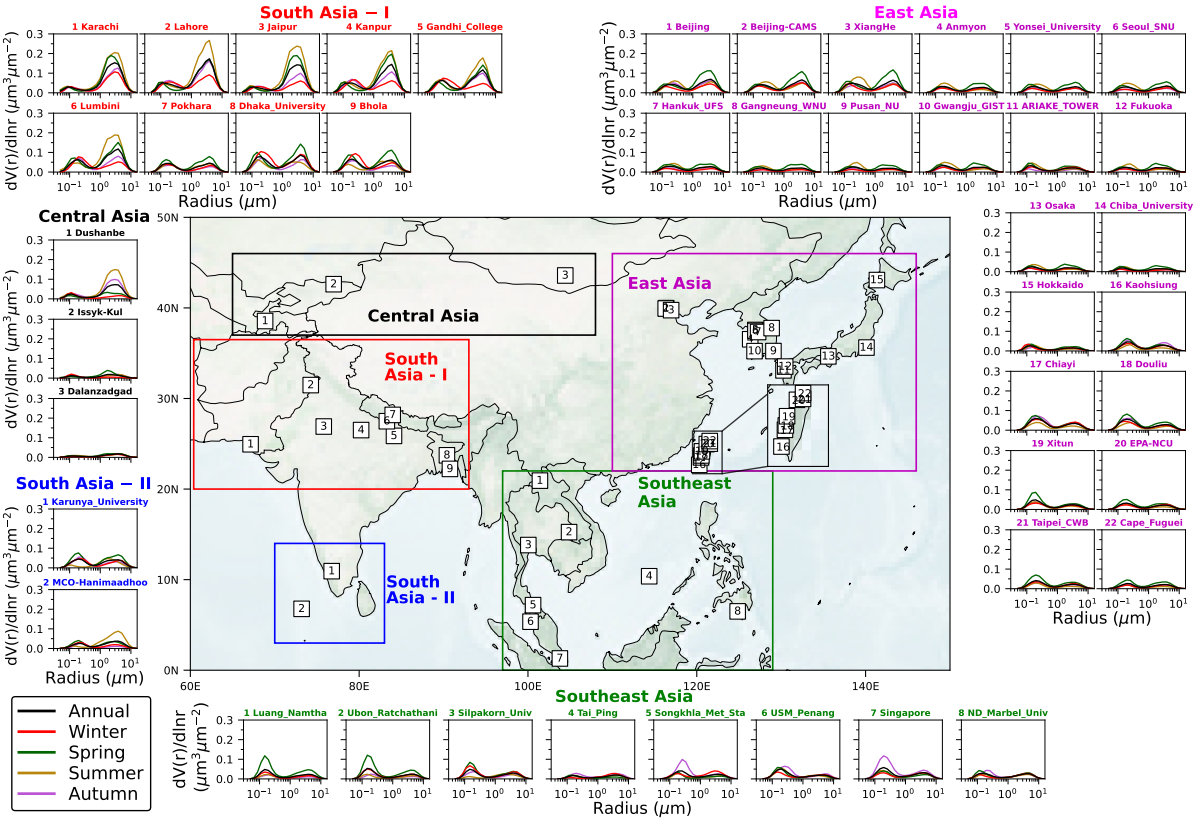

Figure 3.2: *Seasonal and annual mean aerosol volume size distribution (dV(r)/dlnr; in $\mu m^3/\mu m^2$) in the radius range of 0.05-15 μm over all selected observational sites in Central Asia, South Asia – I, South Asia – II, Southeast Asia, and East Asia. Boxes denote different regions in Asia, and the numbers in each box correspond to study locations (Table 2.2).*

the fine volume fraction (FVF) increases with a simultaneous decrease in the magnitude of coarse mode peak (Fig. 3.3). These spatial variations are due to the decreasing eastward gradient of dust transport from its source region to South Asia – I, and the relative increase in the emissions of anthropogenic aerosols in central and east IGP sites in South Asia – I (Ansari & Ramachandran, 2023b). Being a coastal site and located near a source region of dust particles, Karachi experiences comparatively higher dust loading and sea salt aerosols, which result in the highest CVF (∼85%) value with lowest AE and FMF values compared to the other sites in Asia (Figs. 3.1, 3.3) (Ramachandran et al., 2020b).

On an annual scale, the magnitude of VSD in both fine and coarse modes over South Asia – I is mostly higher than the other regions in Asia (Fig. 3.2). The high magnitude of VSD values over South Asia – I is consistent with the high aerosol loading (Figs. 3.1, 3.2). During winter, seasonal mean VSDs in fine mode are equivalent or even

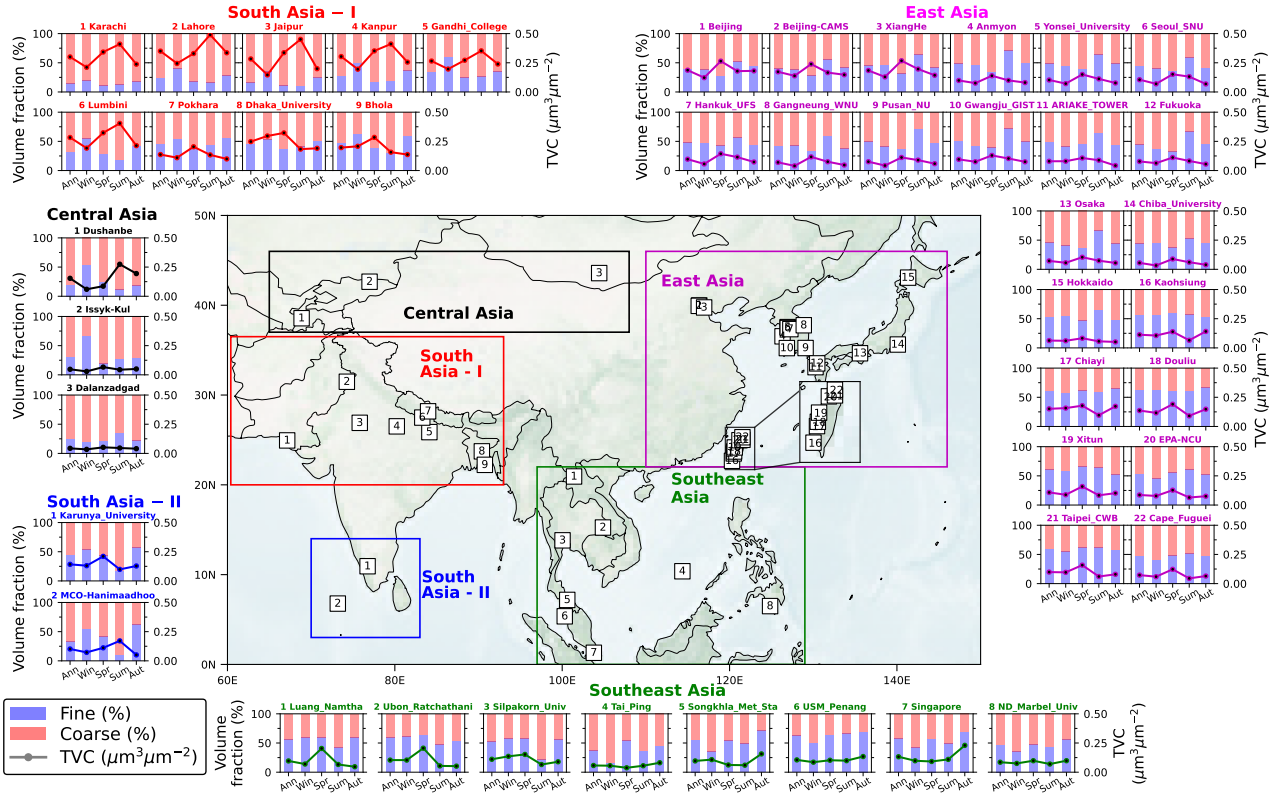

Figure 3.3: *Seasonal and annual mean aerosol volume fraction (%) of fine (FVF) and coarse mode aerosols (CVF) in vertical bar plots (left y-axis) over all selected observational sites in Central Asia, South Asia – I, South Asia – II, Southeast Asia, and East Asia. Annual and seasonal mean total volume concentration (TVC; in $\mu m^3/\mu m^2$) is shown by a line plot (right y-axis) in each panel. FVF and CVF represent the proportions of fine and coarse volume concentrations relative to TVC, respectively.*

higher than coarse mode over the IGP sites, and FVF increases from west to east IGP sites due to higher anthropogenic emissions towards the east, which is correlated with the increasing gradient of AOD and AE towards east IGP sites (Figs. 3.1, 3.2). During spring and summer, the VSD in coarse mode becomes more pronounced (∼2–3 times higher than fine mode) due to the transport of coarse dust and sea salt aerosols over South Asia – I by westerly and southwesterly winds, which also increase the TVC and CVC values by ∼2–3 times than their respective values during winter and autumn.

The regional-average annual mean FVF is the highest (∼55%) over Southeast Asia compared to the other regions in Asia, which clearly shows the dominance of fine mode aerosols over this region and the minimal influence of coarse aerosols. During the forest fire period, the magnitude of fine mode peak is ∼2–3 times higher than the coarse

mode peak. An increase in fine mode aerosols and high FVF (∼60%) over the Indochina Peninsula sites during spring is attributed to the intense biomass burning emissions, which consequently gives rise to higher AOD and FMF over these sites (Figs. 3.2, 3.3). Whereas due to the pronounced biomass burning over the Maritime Continent sites during autumn, the fine mode peaks increase significantly with higher FVF (∼70%).

Over East Asia, the annual mean TVC is higher over East China sites, along with higher AOD, compared to other East Asian sites. Over rural, semi-urban, coastal, and oceanic sites in East Asia, the annual mean TVC is lower, whereas most urban sites (except in Japan) have TVC >0.10 $\mu m^3/\mu m^2$. The annual mean VSD in coarse mode is relatively lower over East Asia (regional average CVF: ∼50%) compared to South and Central Asia (Fig. 3.3), which confirms the lower contribution of coarse mode (i.e., dust and sea salt) aerosols over East Asia compared to Central and South Asia. Coarse mode peak in VSD becomes pronounced only during spring over East China (CVF: ∼70%) due to the transport of dust, and it becomes less pronounced over the eastern part of East Asia (CVF <70%). The enhancement in hygroscopic growth of fine mode aerosols and secondary aerosol formation due to high relative humidity during summer results in higher FVF (>50%) over sites in East China, South Korea, and Japan (Ansari & Ramachandran, 2024b).

The analysis of VSD and volume fraction reveals contrasting features of the dominance of fine and coarse mode aerosols over different regions in Asia. On an annual scale, TVC is the highest over South Asia – I due to the significant contribution of coarse dust aerosols in addition to fine mode aerosols from anthropogenic emissions, which is corroborated by the highest AOD over South Asia – I. Whereas Southeast and East Asia are dominated by fine mode aerosols due to anthropogenic and forest fire emissions, and dominance of dust aerosols is relatively less, which gives rise to higher FVF (>50%) and consequently higher FMF (>0.7). Additionally, the spatial and seasonal variability of TVC is the highest over South Asia – I due to the mixture of fine and coarse mode aerosols, followed by Central Asia, South Asia – II, East, and Southeast Asia, which is consistent with the higher spatial and seasonal variability of AE and FMF over South Asia (Figs. 3.1, 3.2, 3.3) (Ansari & Ramachandran, 2024b).

3.3 Aerosol characteristics over other regions of the globe

The regional-scale analysis of AOD, AE, FMF, and VSD is extended to other regions of the globe, e.g., North America, South America, Europe, North Africa, South Africa, Middle East, and Australia, to examine the regional- and seasonal-scale variability in aerosol characteristics, and to compare the seasonal and annual features of aerosol characteristics over Asia with other regions. In North America, seasonal mean AOD is always <0.2, and AOD is slightly higher during summer (Fig. 3.4). Due to the contrast in the proportions of fine and coarse mode aerosols and aerosol volume concentration, North America is further classified in West, East, and Central North America for analyzing the annual and seasonal variations of VSD in North America. The spatial increase in AE and FMF from west to east North America clearly shows the higher contribution of fine anthropogenic aerosols in Eastern North America sites (Fig. 3.4b, c). AE and FMF are lower over the western coastal site of United States (i.e., West North America), and lowest during spring due to the transport of regional dust from nearby arid regions (e.g., Sonoran and Mojave deserts) and long-range transport of Asian dust plumes (CVF: ∼75%) (e.g., Gkikas et al. (2022)) (Figs. 3.4, 3.5). High population and human activities, along with its meteorology and topography, significantly impact the local air pollution over Mexico City in Central America (Mensink et al., 2020). Urban and industrial emissions, and biomass burning emissions due to forest and agricultural fires occurring during the dry period of spring, give rise to high AOD and AE values and increase TVC over Central America (Ríos & Raga, 2018).

AOD over South America is found to be relatively less during non-biomass burning seasons (e.g., spring and summer) (Fig. 3.4). Over sites located in the tropical forested region of Amazonia (e.g., Alta Floresta), a typical high AOD (>0.4) with high AE and FMF is observed due to intense biomass burning emissions during the Amazonian dry season (late summer and autumn seasons, August-October) (FVF: ∼50%) (Ansari & Ramachandran, 2024b). This intense biomass burning increases the regional mean VSD in fine mode (FVF: ∼45%) and TVC over South America (Fig. 3.5). In the southern part of South America (e.g., CEILAP-BA), the impact of biomass burning events on AOD is less pronounced, and AOD is lower than in other sites, along with low AE (∼1) and FMF (∼0.5). This subregion is affected by dust transport, which originates from the Puna-Altiplano deserts and intensifies during summer when the subtropical jet

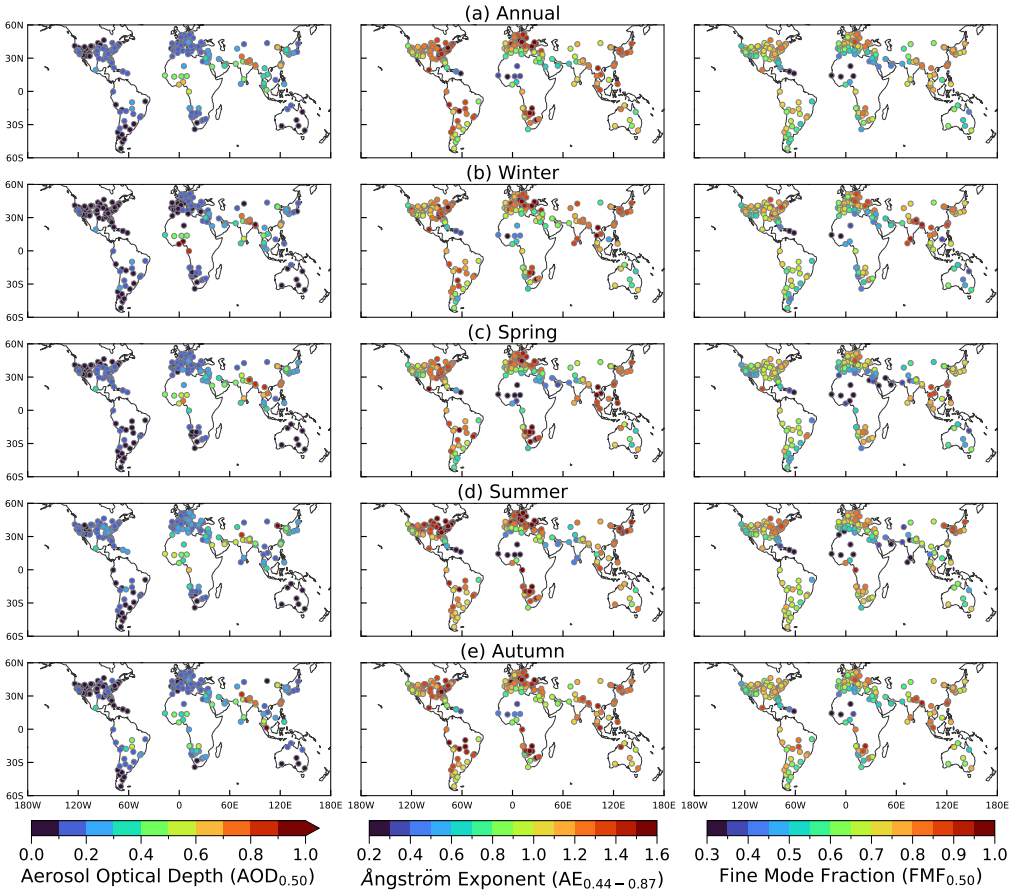

Figure 3.4: *Spatial distribution of aerosol optical depth ($AOD_{0.50}$) (1^{st} column), Ångström exponent ($AE_{0.44-0.87}$) (2^{nd} column), and fine mode fraction ($FMF_{0.50}$) (3^{rd} column) across the globe on (a) annual, and for (b) winter, (c) spring, (d) summer, and (e) autumn.*

stream is at its peak (Gaiero et al., 2013).

AOD over Europe is relatively higher (∼0.15) during summer and spring, and lower during autumn and winter. The major reason behind a higher AOD during summer and spring is the high photochemical activities due to higher solar radiation and temperature, which accelerate the formation of secondary aerosols, including sulfate, nitrates, and secondary OA (Zhao et al., 2018; Filonchyk et al., 2020). In addition, high water vapor content in the atmosphere during summer also favors the hygroscopic growth of aerosols and enhances aerosol extinction (Zhao et al., 2018; Filonchyk et al., 2020). During spring and summer, the southeast part of Europe is affected by dust plumes transported from the Sahara source region through the Mediterranean Sea which increase the aerosol loading and VSD, and decrease AE and FMF values with CVF of ∼70% (Floutsi et al., 2016) (Figs. 3.4, 3.5). An increasing gradient of AOD in

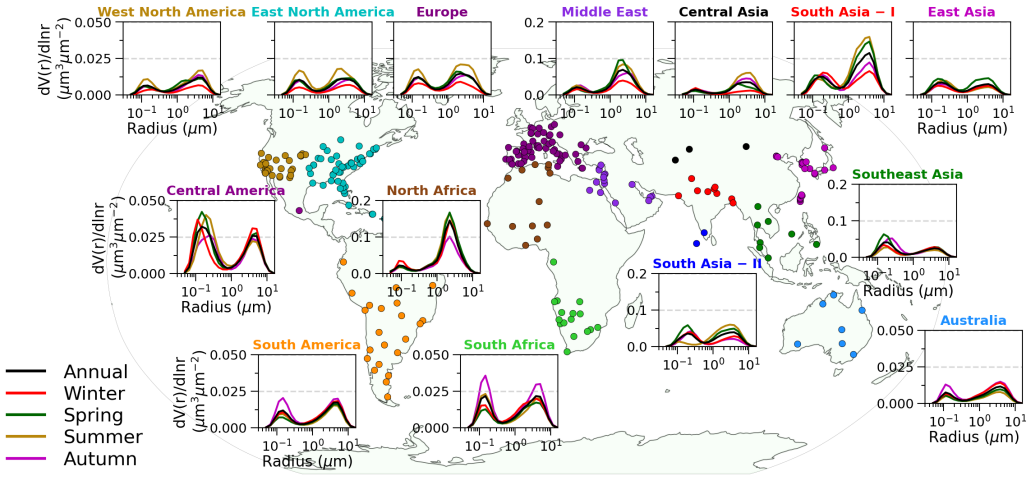

(a) *Aerosol volume size distribution (dV(r)/dlnr)*

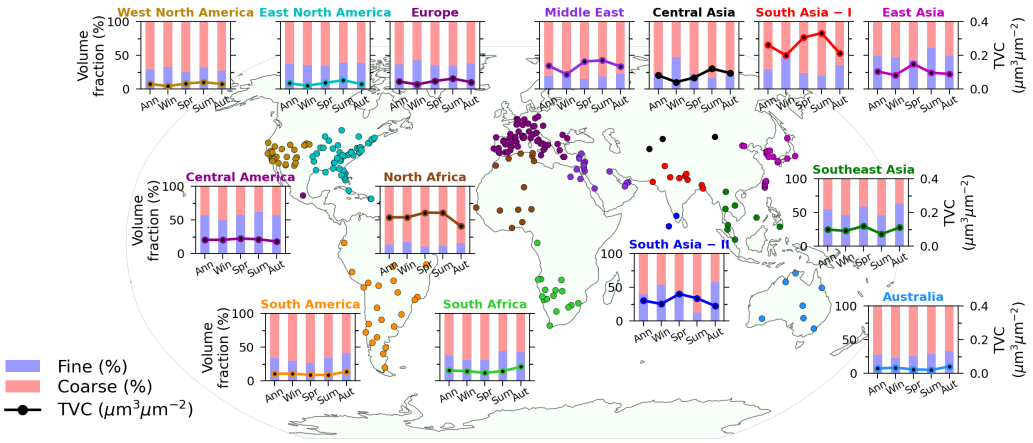

(b) *Volume fractions (%) of fine and coarse mode aerosol to total volume concentration*

Figure 3.5: *(a) Global distribution of regional mean aerosol volume size distribution (dV(r)/dlnr; in $\mu m^3/\mu m^2$) in the radius range of 0.05–15 μm over Central Asia, South Asia – I, South Asia – II, Southeast Asia, East Asia, West North America, East North America, Central America, South America, Europe, North Africa, South Africa, Middle East, and Australia, on annual and seasonal scale. (b) Similar to (a), but for fine and coarse volume fraction (%) (in left y-axis), along with total volume concentration (TVC; in $\mu m^3/\mu m^2$) (in right y-axis). Sites in each region are denoted by circles (Table 2.2).*

total and fine mode aerosols is observed from southwest to northeast parts of Europe, which is attributed to a decrease in the long-range transport of dust plumes, and an increase in anthropogenic emissions and forest and peat wildfires (Ansari & Ramachandran, 2024b).

North Africa and Middle East are mostly influenced by dust aerosols due to the presence of the Sahara, Sahel, and Arabian deserts (e.g., desert of Iraq, Southern

Iran, and North-East of Saudi Arabia), which are more prominent in summer, followed by spring (Mortier et al., 2016). Over Middle East, northwesterly winds are stronger during summer due to low- and high-pressure systems over the Arabian Gulf and eastern Mediterranean, respectively, and they are the main drivers of dust storm events from the Arabian deserts over this region and lead to higher AOD (Yu et al., 2016). This led to high AOD (mostly >0.3) during spring and summer over North Africa and Middle East. The dominance of coarse dust aerosols results in low AE (<0.8) and FMF (<0.5), and high VSD in coarse mode (TVC: ∼0.2 $\mu m^3/\mu m^2$; CVF: ∼80-90%). Along with dust aerosols in North Africa, the intense biomass burning activities in the savanna regions of the Sahel and Sudan occur during winter and early spring (Eck et al., 2010). This led to high AOD (>0.4) and an increase in VSD in fine mode, and their values are relatively higher in the central and southern parts of North Africa. The influence of dust decreases from North to South Africa, and the contribution of biomass burning aerosols increases in South Africa due to the agricultural practices, involving the widespread burning of savannas, woodlands, and forests, during summer and early autumn (Jouan & Myhre, 2024). Thus, AE, FMF, and FVF values are significantly higher over South Africa than North Africa. Peak values of VSD in fine mode and TVC increase by ∼1.5–2 times during peak burning seasons over South Africa.

From the seasonal and annual variations of AOD over Australia, it is clearly evident that AOD is the lowest (<0.2) over Australia compared to the other regions of the globe, and significantly lower compared to Asia (Fig. 3.4). The seasonal mean AOD is slightly higher during autumn and winter when precipitation is less and wind speed is high, whereas it is lower during spring and summer. AOD is high over Eastern Australia (e.g., Canberra) during autumn and winter due to the pronounced forest and bush fire emissions leading to an increase in AE and FMF, and the magnitude of VSD in fine mode (FVF: ∼25%) (Yang et al., 2021) (Figs. 3.4, 3.5). Over Northern and Northeastern Australia, biomass burning and long-range transport of marine aerosols lead to high AOD during autumn and winter (Yang et al., 2021). The long-range transport of marine aerosols over Lucinda (a coastal site) leads to a decrease in AE and FMF (CVF: ∼80%).

Seasonal, annual, and global-scale analyses of aerosol optical and physical properties reveal that AOD values (typically <0.25) are consistently lower at observational sites in North America, South America, Europe, and Australia compared to sites across Asia on both seasonal and annual scales. Similarly, the regional mean VSD

(<0.05 $\mu m^3/\mu m^2$) and TVC (<0.1 $\mu m^3/\mu m^2$) over North America, South America, Europe, and Australia are ∼4 times lower than those observed in South Asia – I, and at least 3 times lower than in other Asian subregions. Furthermore, both seasonal and spatial variability in AOD, AE, and FMF are significantly smaller over North America, Europe, and Australia compared to Asia. These findings clearly indicate that the intensity of aerosol emissions, as well as their spatiotemporal variability across space and time (p-value ≤0.05 by Student's t-test), are substantially higher in Asia (particularly in South Asia), followed by North Africa.

3.4 Aerosol absorption characteristics (SSA and AAOD)

The SSA and AAOD (=AOD×(1–SSA)) values, and their spectra exhibit significant variations due to the seasonal and spatial variabilities in the aerosol sources, types, and scattering/absorbing contributions to total AOD (Figs. 3.4, 3.6, 3.7). Over urban sites, where BC is the major absorber, the spectral variation of AAOD is less and AAE is lower (∼1). Whereas over dust dominated sites, spectral AAOD decreases steeply and AAE is higher (>2) (Russell et al., 2014). Both regional and seasonal variations of AOD (values range from >0.0 to 1.0, in magnitude) are significantly higher compared to variations in SSA (values range between 0.85 and 1.00), which shows the distinct nature of variations between AOD and SSA, and further, these regional and seasonal variations in AOD are more pronounced over Asia (e.g., South Asia – I). A higher variation in AOD compared to SSA occurs because any change in aerosol amounts leads to a change in AOD, whereas it need not necessarily lead to a change of same magnitude in SSA because SSA varies by changes in proportions of scattering and/or absorbing aerosols contributing to the total AOD, which depends on the aerosol size and chemical composition (Dubovik et al., 2002; Ramachandran et al., 2020a; Ansari & Ramachandran, 2024a). SSA values are mostly lower over Central and South Asia – I compared to other regions in Asia. This feature is more pronounced at shorter wavelengths (e.g., regional mean SSA at 0.50 μm over Central Asia: 0.87 ± 0.04, South Asia – I: 0.90 ± 0.01, Southeast Asia: 0.93 ± 0.02, East Asia: 0.94 ± 0.02, and South Asia – II: 0.94 ± 0.02), which is due to the higher amount of dust and its higher absorption at shorter wavelengths over sites in Central and South Asia – I (Song et al., 2021). Consequently, higher aerosol loading with lower SSA over South Asia – I results in a higher loading of absorbing aerosols (AAOD: ∼0.06 ± 0.02), which is ∼50% lower over South Asia – II, Southeast Asia, and

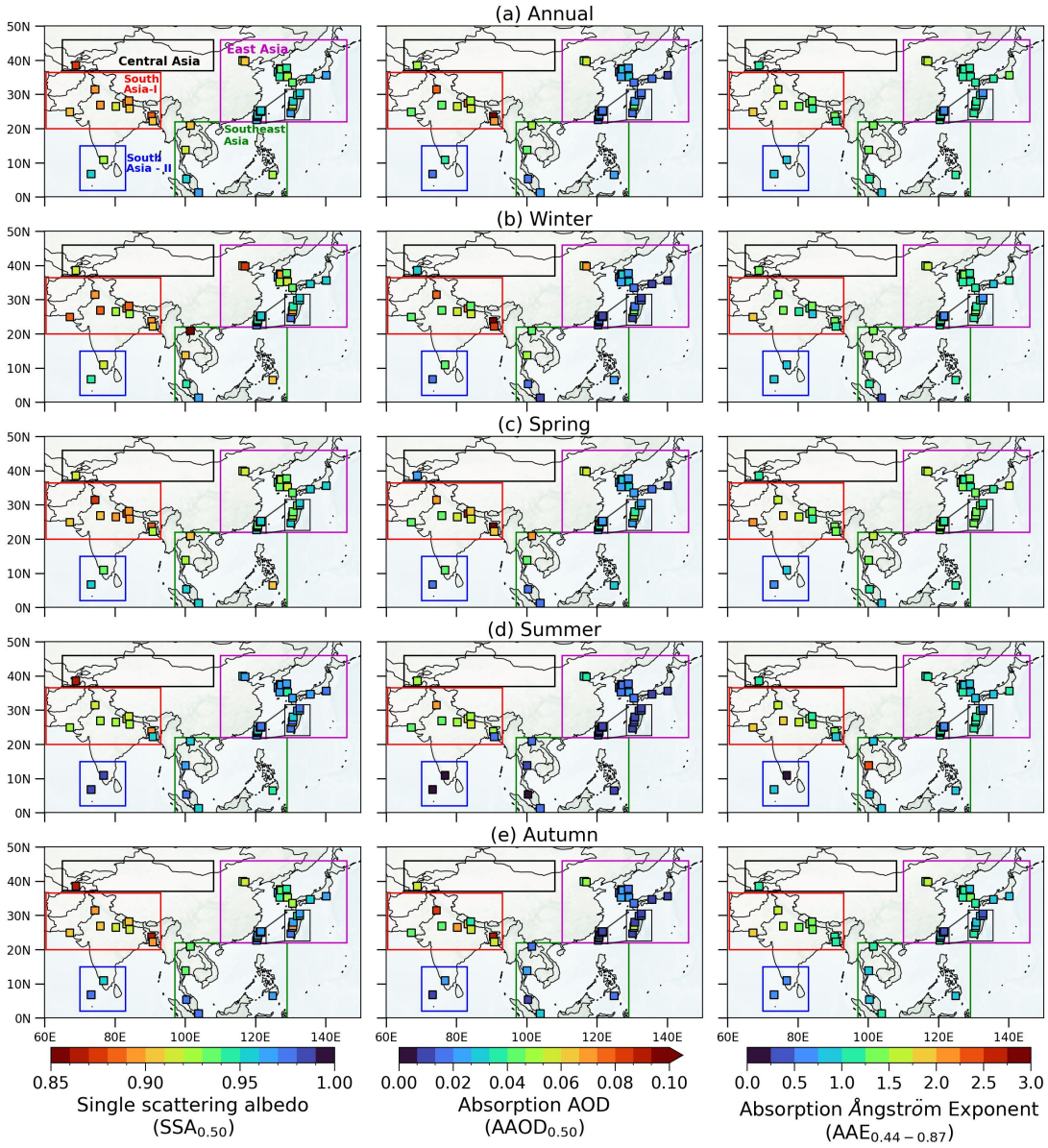

Figure 3.6: *The spatial distribution of single scattering albedo ($SSA_{0.50}$) (1^{st} column), absorption aerosol optical depth (AAOD) (2^{nd} column), and absorption Ångström exponent ($AAE_{0.44-0.87}$) (3^{rd} column) over Asia on (a) annual and seasonal scales during (b) winter, (c) spring, (d) summer, and (e) autumn. Boxes correspond to different regions in Asia, mentioned in the top left panel.*

East Asia (Figs. 3.6, 3.7).

Over Dushanbe (Central Asia), the proximity to the Taklamakan, Karakum, and Aralkum deserts results in high AOD (∼0.35) and lower SSA (∼0.85) during summer and autumn due to dust transport, which also leads to higher seasonal mean AAOD (∼0.06) at shorter wavelengths (Rupakheti et al., 2020). Over South Asia – I, the trans-

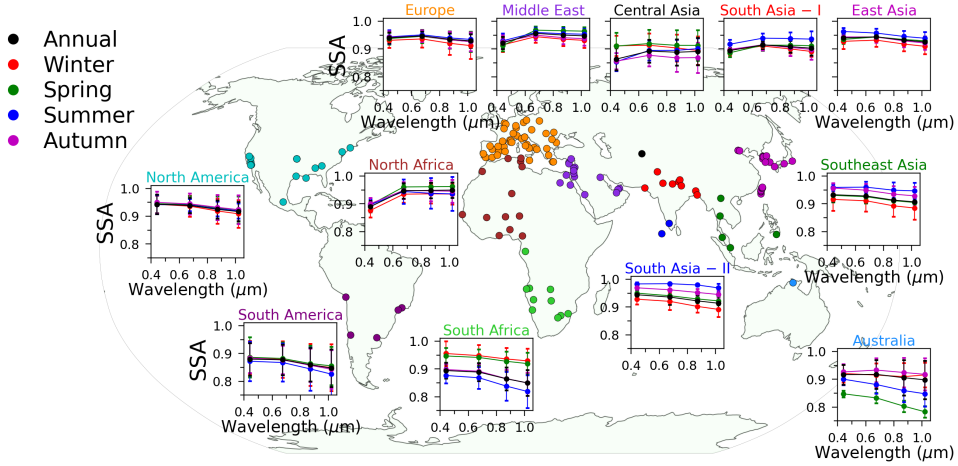

(a) *Regional mean single scattering albedo (SSA)*

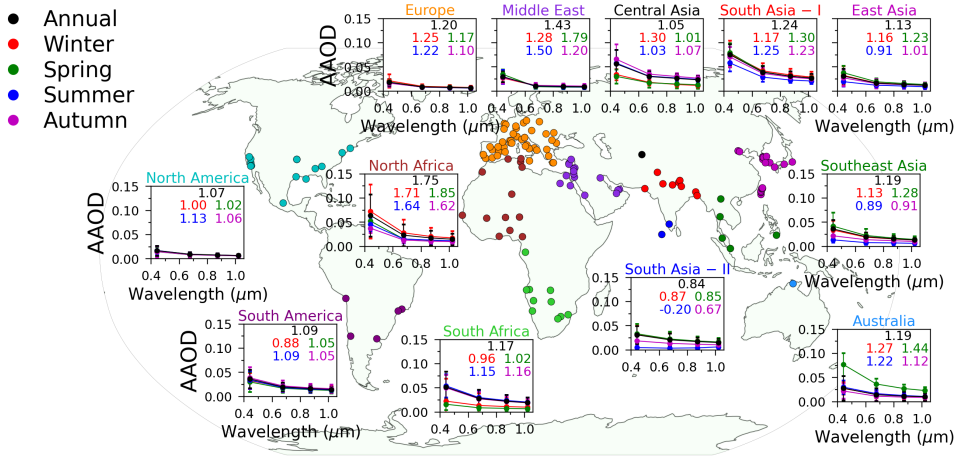

(b) *Regional mean absorption aerosol optical depth (AAOD)*

Figure 3.7: *Spectral variation of regional mean (a) single scattering albedo (SSA) and (b) absorption aerosol optical depth (AAOD) in the wavelength range of 0.44–1.02 μm on annual and seasonal scales over 12 different regions across the globe. Annual and seasonal mean absorption Ångström exponent (AAE) values are written in (b) in the respective color.*

port of dust by strong westerly winds during spring and summer results in lower SSA and higher AAOD. It also leads to an increasing and decreasing spectral gradient (in the wavelength range between 0.44 and 0.675 μm) of SSA and AAOD, respectively, which results in higher AAE (Figs. 3.6, 3.7). During winter, northeasterly winds transport continental anthropogenic aerosols from the Indian subcontinent to South Asia – II (e.g., Hanimaadhoo), which leads to high AOD and lower SSA over this site (Ramachandran & Rupakheti, 2020). During winter and autumn, spectral g decreases as a function of wavelength over South Asia (I–II) due to the dominance of the fine mode aerosols. Whereas, spectral g values are higher and exhibit less variation as a function

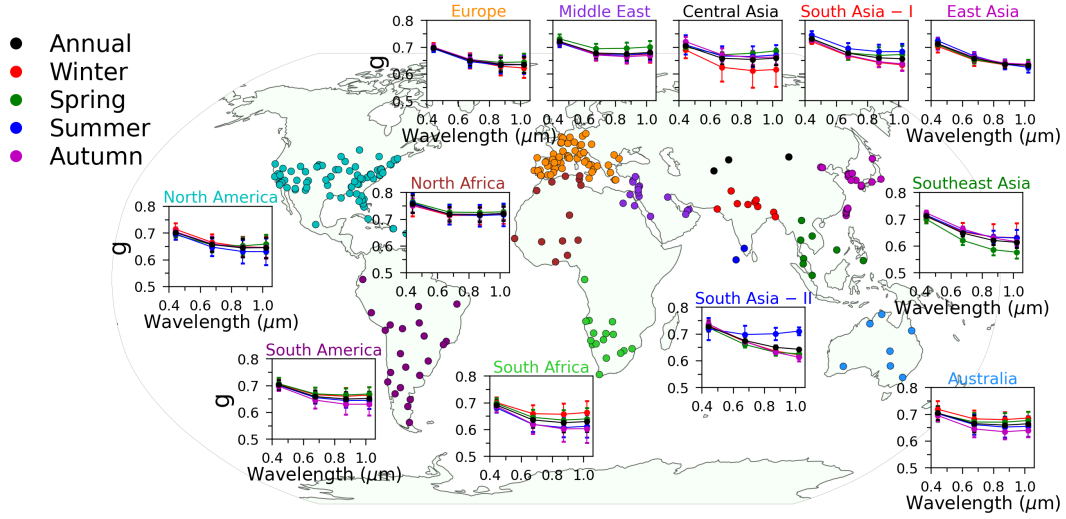

Figure 3.8: *Spectral variation of regional mean asymmetry parameter (g) in the wavelength range of 0.44–1.02 μm on annual and seasonal scales over 12 different regions across the globe.*

of wavelength during spring and summer due to dominance of coarse mode aerosols, which increase the forward scattering by aerosols (Fig. 3.8). Spectral SSA ($\geq$0.92) and AAOD (<0.06) are higher and lower respectively, during the summer season over South, Southeast, and East Asia due to the suppression of regional and local burning activities (wet deposition due to higher precipitation), the transport of sea salt particles by strong south-westerly winds from the Arabian Sea (dominant scatterers), and hygroscopic growth of aerosols due to high relative humidity (Fig. 3.6) (Ramachandran et al., 2020a). Decreasing gradients in AOD and AAOD from west to east in East Asia are observed, which is similar to the increasing gradient in SSA (Ansari & Ramachandran, 2025b). High AOD and AAOD over East China during all the seasons are attributed to higher anthropogenic aerosol emissions from the populated and industrial sites in East China, and transport of dust from the Gobi and Taklamakan deserts (Chen et al., 2017; Xie et al., 2020). During the dry seasons of winter and spring in the Indochina Peninsula region in Southeast Asia, intense biomass burning events related to slash-and-burn agricultural activities and forest fires occur (Gautam et al., 2013). These fires enhance the amount of carbonaceous aerosols (BC and BrC), which leads to a low SSA (<0.90) and high AAOD ($\sim$0.07), and decreasing gradient of spectral SSA (Ansari & Ramachandran, 2025b). During the same seasons, the abundance of fine mode aerosols from biomass burning emissions leads to decrease in g with increasing wavelength (Fig. 3.8).

North Africa and Middle East experience higher AOD (mostly >0.3) throughout the year, and spectral features of SSA (e.g., higher and lower absorption at shorter and longer wavelengths, respectively) are the same and do not exhibit significant seasonal variability. The dominance of dust induces the increasing spectral gradient of SSA (in the wavelength range of 0.44-0.675 μm) and a large spectral dependence of AAOD, which produces the highest AAE (>2) over North Africa and Middle East (Fig. 3.7). The dominance of coarse mode dust aerosols over North Africa leads to high spectral g values with less spectral variation for all wavelengths (0.44-1.02 μm) compared to other regions of the globe (Fig. 3.8). The intense savanna biomass burning in Sudan and Sahel regions of North Africa usually occurs in winter (Eck et al., 2010), and due to the mixing of biomass burning aerosols with dust, the amount of absorbing aerosols increases. This leads to low spectral SSA and high spectral AAOD over North Africa during winter (Fig. 3.7). During the peak fire season of summer, followed by autumn, the influence of absorbing aerosols (BC and BrC) from intense biomass burning is evident in lower SSA and higher AAOD in each wavelength, and SSA becomes even lower ($\sim$0.85) in longer wavelengths over South Africa, which confirms the high absorption of aerosols (Fig. 3.7). Urban-dominated aerosols over North America and Europe possibly lead to high SSA in shorter wavelengths, and it slightly decreases in longer wavelengths (Fig. 3.7). The regional mean SSA is higher (>0.92) for all wavelengths over North America and Europe with lower AOD (<0.2) and AAOD (<0.02), clearly confirming the lower emissions of absorbing aerosols in a cleaner environment. SSA typically reaches its peak in the local summer season (JJA in the Northern Hemisphere and DJF in the Southern Hemisphere), which is primarily due to the suppression of regional and local burning activities on account of higher precipitation, and increase in secondary aerosols associated with more intense photochemical reaction rates (Dong et al., 2023).

The distinct seasonal features in the spectral variations and magnitudes of SSA and AAOD over South Africa, Southeast Asia, Australia, and North Africa (savanna of the Sahel and Sudan regions) are attributed to the seasonal cycle of natural and anthropogenic biomass burning events (e.g., agricultural burning, wildfire, forest fire) (Fig. 3.7) (Hu et al., 2007; Dong et al., 2023). Whereas the high seasonal variability in spectral SSA and AAOD over Central, South, and East Asia is due to seasonal patterns of dust storms, anthropogenic aerosol emissions from residential heating and biomass burning emissions, and increase in wet deposition and changes in wind pattern during the local

monsoon season (summer). The seasonal variabilities in spectral SSAs and AAODs over Australia, South Africa, Southeast Asia, Central Asia, South Asia (I–II), and North Africa are statistically significant (p-value <0.05) (Ansari & Ramachandran, 2025b). The spectral features of increasing SSA at shorter wavelengths in dust dominated regions and decreasing SSA at longer wavelengths over biomass burning regions are consistent with Russell et al. (2014). A weak seasonality in spectral SSA and AAOD over North America, South America, and Europe clearly suggests less seasonal variation in the aerosol size distribution and net contributions of scattering and absorption of aerosols to total extinction compared to other regions. Overall, in comparison to inter-annual variation in SSA and AAOD during the 5-year study period (2015–2019), the intra-annual variation in SSA among all the seasons is found to be higher and statistically significant (p-value <0.05) for all the wavelengths over most of the sites across the globe. This is due to the significant changes in the level and type of aerosol emissions as a function of seasons within a year, depending on the emissions from natural and anthropogenic activities, and meteorological conditions, which vary highly over each region (Ansari & Ramachandran, 2025b).

3.5 Collocated validation of MERRA-2 and CAMS simulations

3.5.1 Global assessment of MERRA-2 and CAMS simulated AOD and AE

On the regional scale in Asia, the collocated validation of MERRA-2 and CAMS simulated AOD with AERONET AOD shows that, except over Central Asia, both models (MERRA-2 and CAMS) do not capture AERONET AOD well within the GCOS requirement of AOD (GCOS fraction (GF): <40%) (Figs. 3.9–3.12). GF values are relatively higher over Central Asia for both models. For MERRA-2, data points less than GCOS requirement are relatively higher. The performance of CAMS AOD is better than MERRA-2 because of low bias and CAMS AOD is better correlated with AERONET AOD over all regions in Asia (except Central Asia). In the regional scale validation of model AEs, data points <EE> are always >60%, however, model AEs have low correlation over Asia except South Asia (I-II) (Figs. 3.13–3.16). The bias for CAMS AE is relatively higher (>0.1) than MERRA-2 over South and East Asia, which can be due to overestimation in fine mode aerosols and/or underestimation in coarse mode aerosols. It is to be noted that most CAMS AE values are >1.2 and they go up to ∼1.6, which clearly shows the high dominance

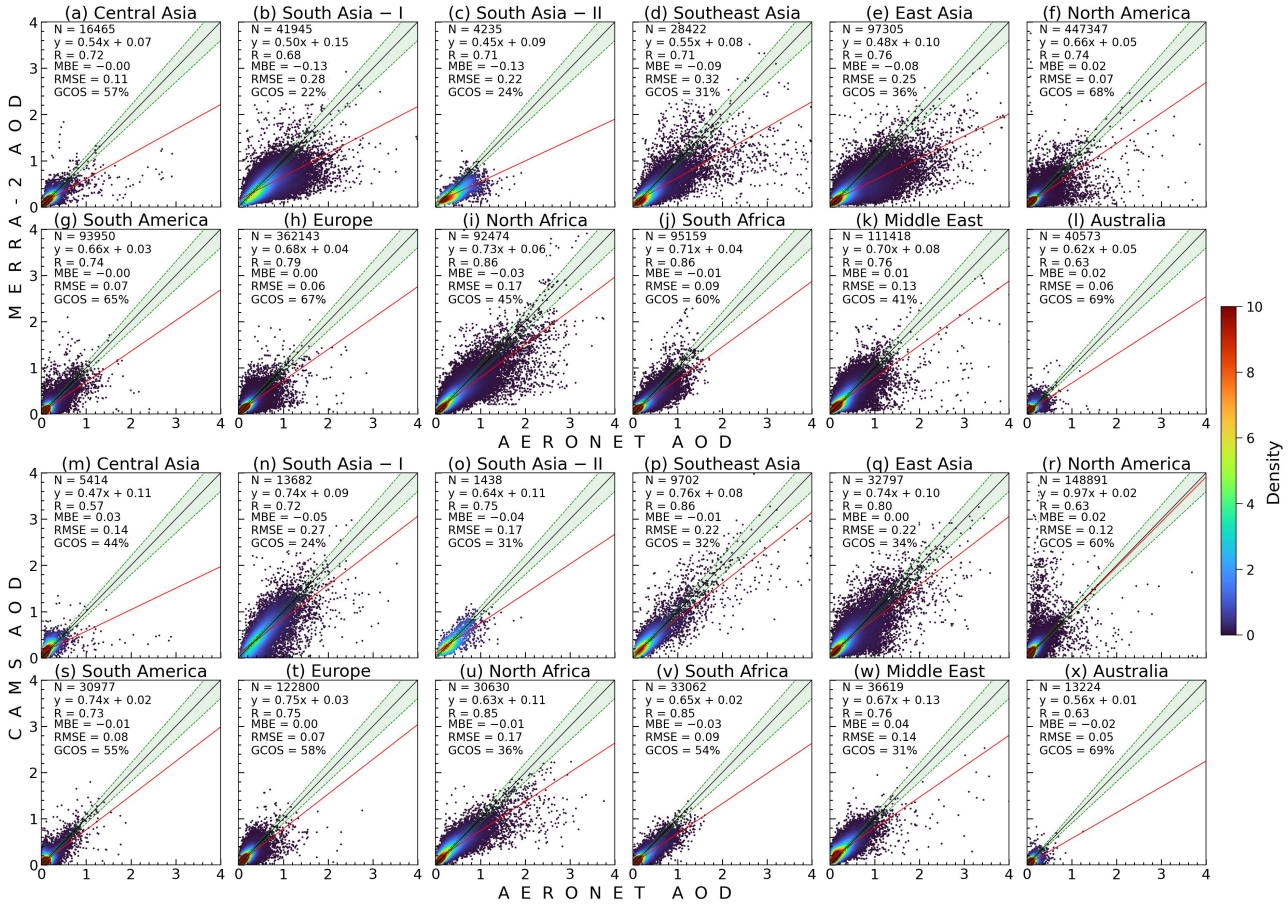

Figure 3.9: *Collocated validation of MERRA-2 (a-l) and CAMS (m-x) simulated aerosol optical depth (AOD) AERONET measured AOD at 0.55 μm over 12 regions across the globe. The solid red and black lines correspond to linear fitted line and 1:1 line, respectively. The green shaded region in each panel represents the range of GCOS requirement for AOD (=max(0.04 or 0.1$\times$AOD)), and the data points that satisfy the GCOS requirement are given as GCOS fraction (%). Total number of collocated data points (N), statistics of fitted line, mean bias error (MBE), and root mean square error (RMSE) are shown in each panel. The color bar indicates the probability density function derived from the kernel density estimation.*

of fine mode aerosols in simulated AOD, which can lead to an overestimation in fine anthropogenic aerosols (e.g., sulfate, nitrate, and OA), and biomass burning aerosols.

The site-wise validation of model AOD clearly shows that on an annual scale, CAMS AOD shows a significantly better spatial agreement with AERONET observations compared to MERRA-2 over South Asia (I–II) with a smaller bias (MBE <0.1) and better correlation (R >0.7) (Figs. 3.11, 3.12, 3.17). The seasonal scale validation, provided in

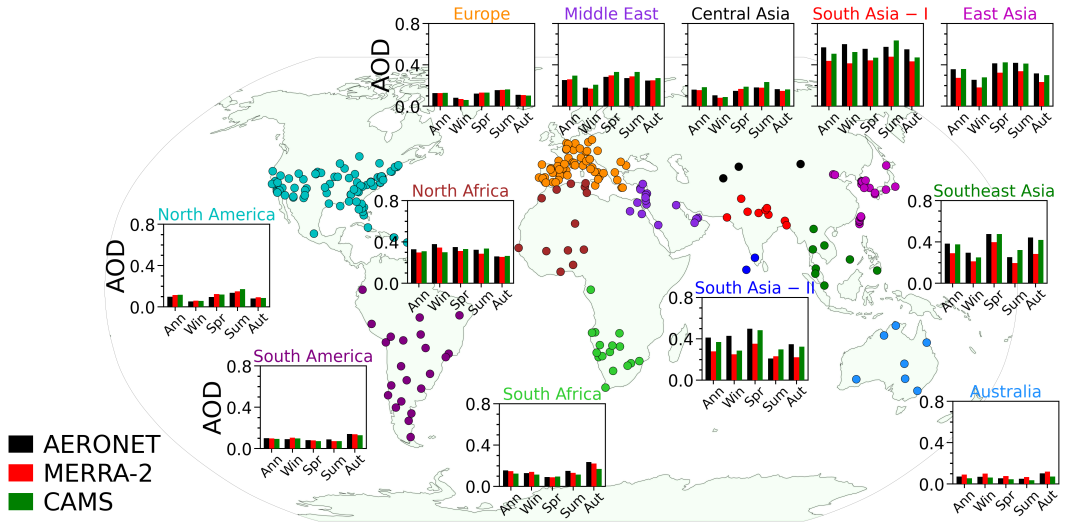

Figure 3.10: *Regional variation of annual and seasonal mean AOD at 0.55 μm by AERONET observation and MERRA-2 and CAMS simulations over 12 different regions across the globe.*

Ansari & Ramachandran (2024b), reveals that the better performance of CAMS model over Asia is consistent throughout the year. MERRA-2 highly underestimates AERONET AOD and exhibits a high negative bias (absolute value of MBE is mostly >0.2) and low R (<0.7) over IGP during winter, followed by autumn, when aerosol loading is higher, with a high contribution of fine anthropogenic aerosols (Figs. 3.9, 3.10). Whereas, for CAMS, the absolute value of MBE is <0.2 during winter and autumn. The utilization of recent and updated anthropogenic emissions inventories in CAMS could be a possible reason for the better performance of CAMS over MERRA-2 (Ansari & Ramachandran, 2023a, 2024b). The high overestimation of CAMS AE over South Asia (I–II), during winter, followed by autumn, indicates the overestimation of fine mode aerosols over South Asia (Ansari & Ramachandran, 2024b)). It must be noted that over the elevated sites in Central Asia and South Asia – I, the correlation is not good for model AODs (R<0.7). High negative bias and low correlation in models could arise due to the challenges involved in resolving the topography of high-altitude sites in addition to regional and local emissions as it is in close proximity to an aerosol hotspot that can cause high uncertainties in emissions, and removal and transport mechanisms, which can contribute to a high negative bias in AOD (Ramachandran et al., 2023)).

Over Southeast Asia, the performance of CAMS AOD has a good spatial agreement with AERONET compared to MERRA-2 AOD on an annual scale (Figs. 3.9, 3.11,

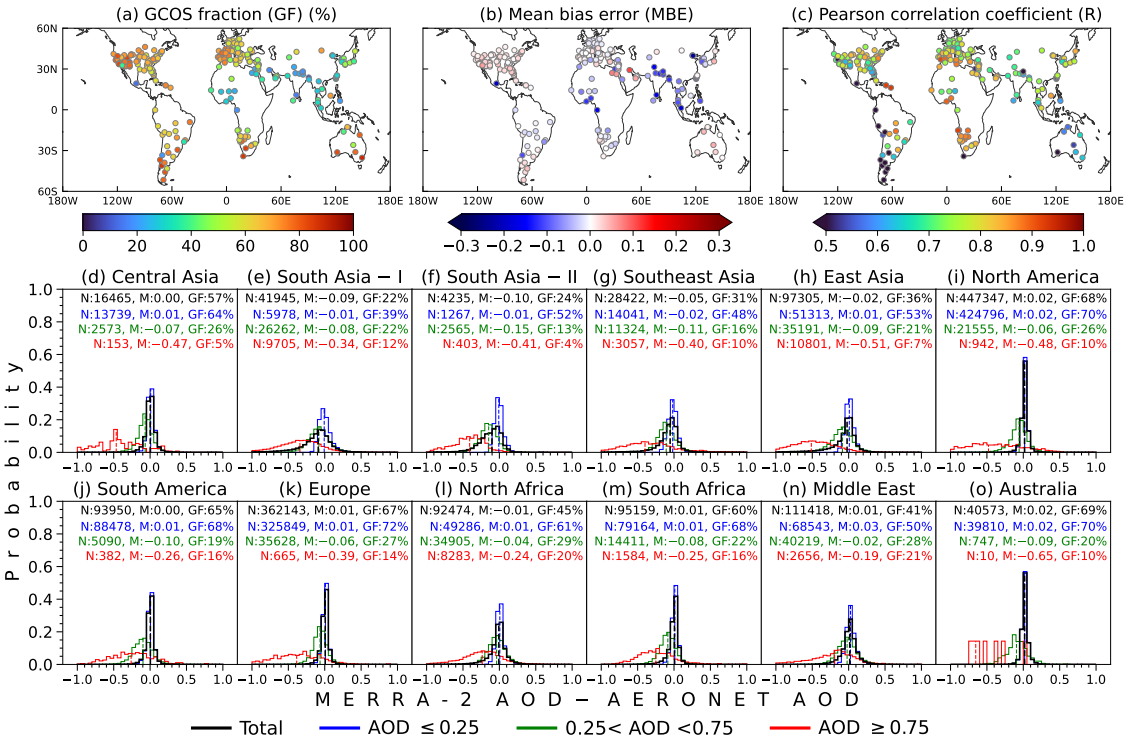

Figure 3.11: *The spatial distribution of (a) Global Climate Observing System (GCOS) fraction (GF; in %), (b) MBE, and (c) R derived from the collocated validation of MERRA-2 simulated AOD with AERONET AOD at 0.55 μm. Probability distribution of the difference between MERRA-2 AOD and AERONET AOD over 12 regions (d-o) across the globe, including the values of N: total collocated data points, M: median (rounded off to 2 decimal places), and GF for total (including all ranges) and different ranges of AERONET AOD values are shown. The vertical dashed lines in different colors correspond to the median of each probability distribution.*

3.12, 3.17). The performance of both models is slightly better over the Indochina Peninsula compared to the Maritime Continent. The seasonal-scale collocated validation, provided in Ansari & Ramachandran (2024b), showed that during the dry season over Southeast Asia, when AOD is higher due to biomass burning emissions, the bias in MERRA-2 is higher with low correlation compared to other seasons. The underestimation of MERRA-2 over Southeast Asia during the dry season is consistent with earlier studies (Che et al., 2019a). Since both models utilize the daily emissions of biomass burning aerosols, the underestimation by MERRA-2 in Southeast Asia is most likely due to the strong biomass burning activities during dry seasons and the underestimation of biomass burning aerosols, especially related to OC emissions (Buchard et al.,

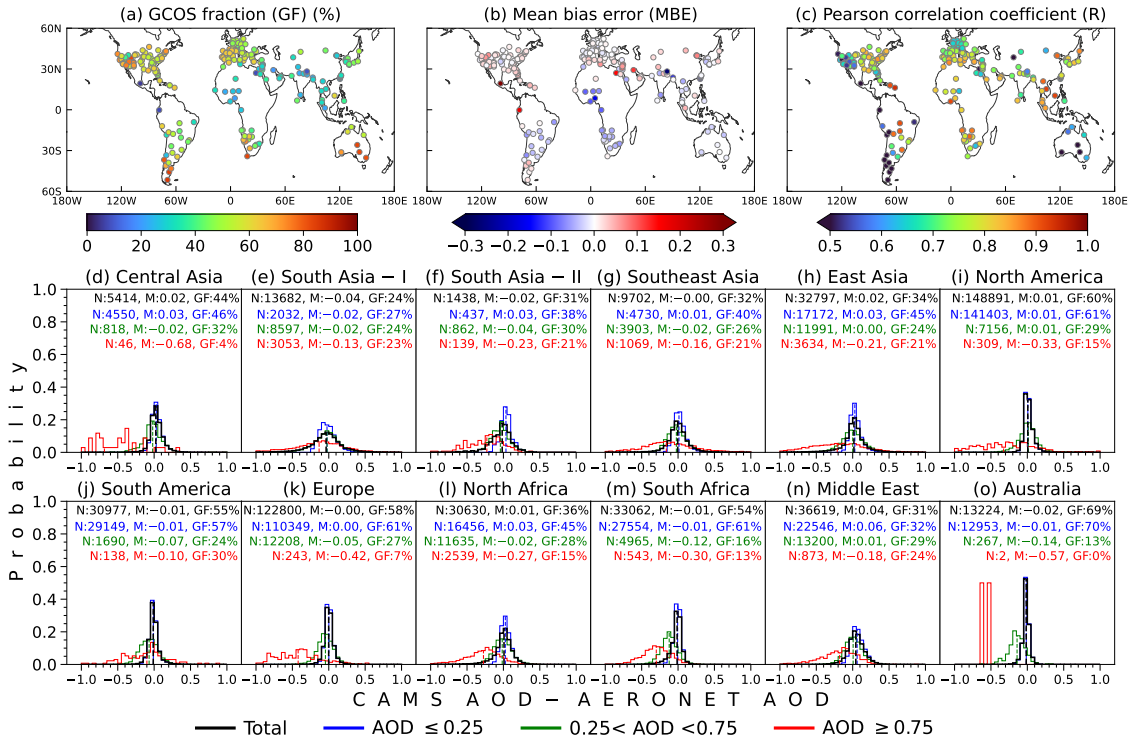

Figure 3.12: *Similar to Fig. 3.11, but for the collocated validation of CAMS AOD with AERONET AOD at 0.55 μm.*

2016, 2017). Both models consistently overestimate AERONET AE in Southeast Asia, indicating an overestimation of fine-mode aerosols in the simulations. It is noteworthy that during an intense biomass burning period (autumn), when mean AOD over Singapore is high because of the El Niño impact on fire activities, the bias in CAMS AOD is low (<0.1). Over East Asia, both model simulated AODs have a good correlation with AERONET AOD in East China, South Korea, and Japanese sites (R >0.7). Biases of model AODs are higher in East China. It is lower over South Korea and Japan (Figs. 3.9, 3.11). MERRA-2 highly underestimates the observed AOD in East China sites (MBE: ∼–0.2). Both model AE data points are >80% within EE over East Asia, but CAMS overestimates AE, similar to South Asia (I-II) (Figs. 3.13, 3.16).

For low AOD (≤0.25), the probability distribution of the difference in both models and AERONET AOD is narrow with relatively less bias and higher GF over each Asian region (Figs. 3.11d-h, 3.12d-h). The probability distribution becomes flatter, and its magnitude decreases with an increase in AOD. It is clearly evident that the underestimation in MERRA-2 AOD increases for high AOD (≥0.75), and its median values increase when the bias is negative. Whereas the median value of bias and GF in CAMS

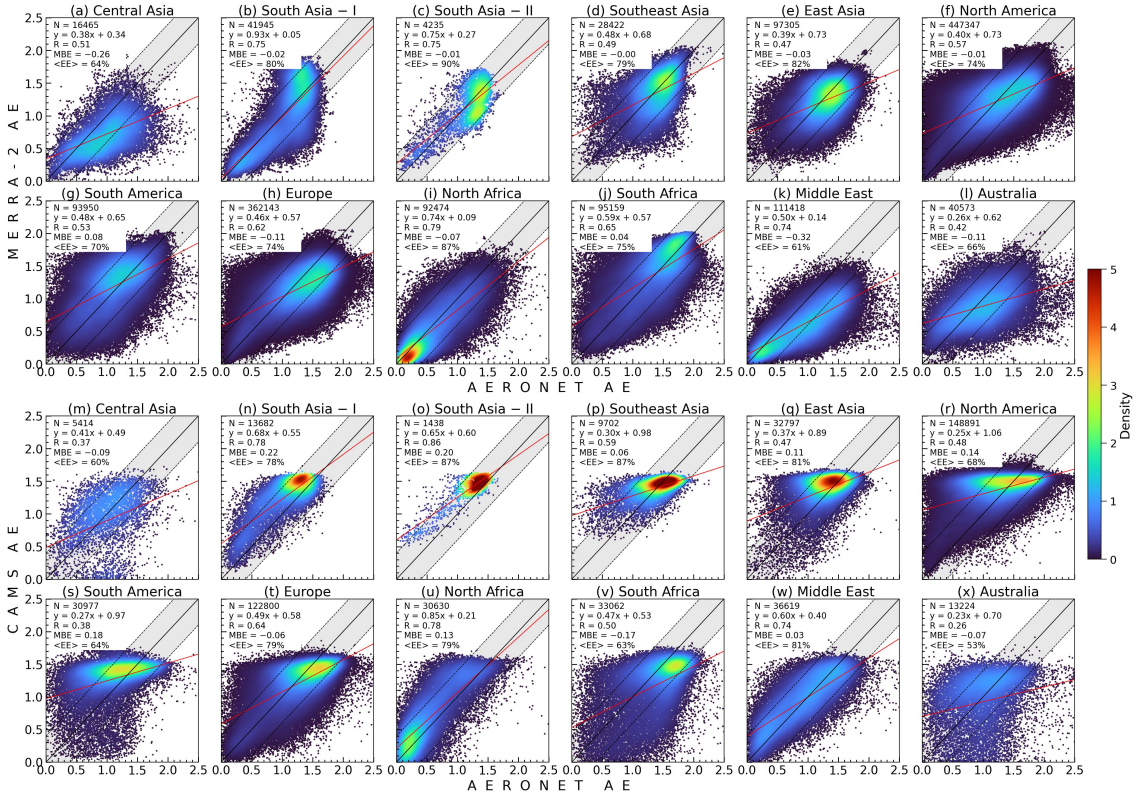

Figure 3.13: *Same as Fig. 3.9, but for the collocated validation of MERRA-2 (a-l) and CAMS (m-x) simulated Ångström exponent (AE) with AERONET measured* $AE_{0.44-0.87}$. *The dashed black lines and grey shaded region indicate the range of expected error (EE) of AE (±0.4), and the data points within EE (<EE>; in %) are provided in each panel. The total number of collocated data points (N), statistics of the fitted line, and mean bias error (MBE) are also shown in each panel.*

AOD are relatively lower and higher, respectively, for high AOD compared to MERRA-2, which confirms the better performance of CAMS AOD even in high AOD conditions. The major reason for the better performance of CAMS is due to the utilization of updated and recent emission inventories for anthropogenic aerosols and their precursor gases in CAMS, which is crucial for the better simulation of AOD, especially over Asia, where anthropogenic emissions have changed significantly in recent decades (Ramachandran et al., 2020a; Quaas et al., 2022; Ansari & Ramachandran, 2024b). Whereas the anthropogenic emissions in MERRA-2 vary on a yearly basis, and major emissions databases are extended/applicable only up to before the year 2010 (e.g., 2008 and 2006 are terminal years for anthropogenic SO_2 and OC/BC emissions, respectively) (Buchard et al., 2017). The better performance of CAMS when compared to MERRA-2 in simulating

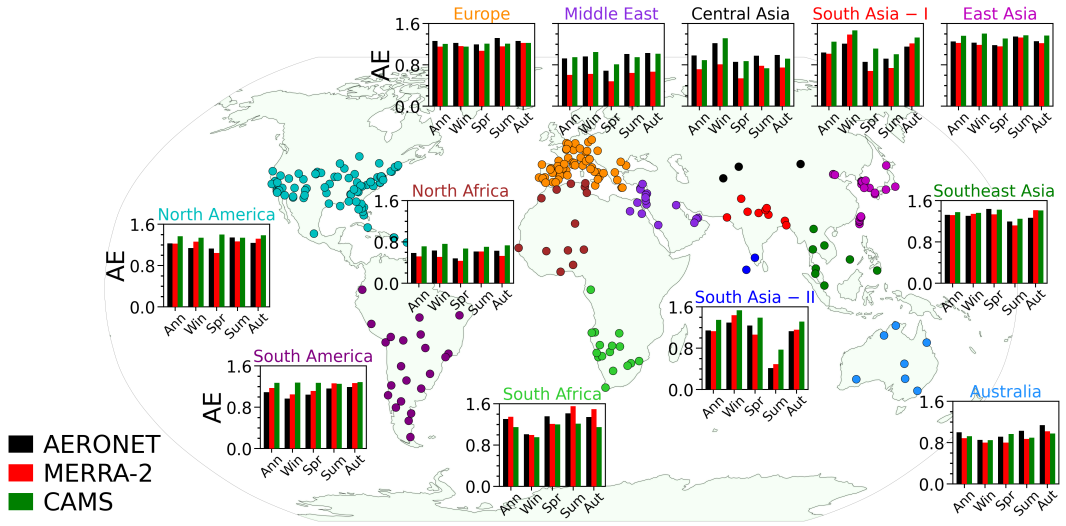

Figure 3.14: *Same as Fig. 3.10, but for Ångström exponent ($AE_{0.44-0.87}$).*

AOD over Asia was also observed in a previous study (Gueymard & Yang, 2020).

A high underestimation (median: –0.5) and low GF (∼7%) in MERRA-2 simulated AOD occur during higher AOD conditions over East Asia (e.g., East China sites) compared to South Asia. The lower performance over East China is due to a lack of treatment of nitrate aerosols, inadequate anthropogenic emissions with only interannual variability, and relatively lower AOD observations have been assimilated in MERRA-2 compared to South Asia (Buchard et al., 2017; Che et al., 2019a). The probability distribution of bias in model AE is comparatively lower in magnitude and flatter than in model AOD, and the bias in model AE is mostly lower in high AE conditions (Fig. 3.16). The bias in CAMS AE is highly positive for low AE (<1) over each region in Asia, which is due to the overestimation of fine anthropogenic and biomass burning aerosols by CAMS (Xian et al., 2024).

This collocated validation of MERRA-2 and CAMS over Asia reveals significant inter-regional and seasonal changes in their performance and exhibits significant intra-regional changes as well, posing a challenge for models. Each region of Asia, especially South (I-II), Southeast, and East Asia, is heavily influenced by regional emissions, which lead to high aerosol loading with its significant spatiotemporal variation due to diverse aerosol emissions from both natural and anthropogenic sources with significant seasonal and spatial changes in their contributions. These conditions of different aerosol characteristics, along with varying terrain and meteorological conditions, create substantial challenges for accurate simulation of aerosols in models, which require continuous im-

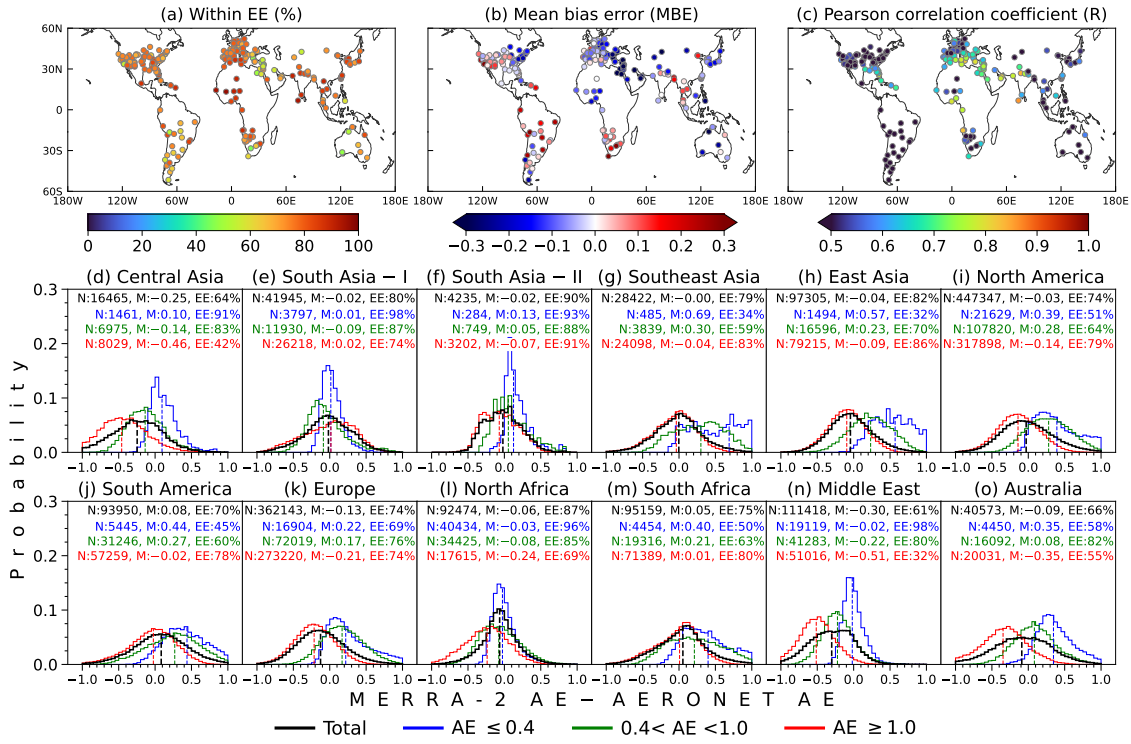

Figure 3.15: *The spatial distribution of (a) MERRA-2 data points within EE (in %), (b) MBE, and (c) R derived from the collocated validation of MERRA-2 simulated AE with AERONET measured AE. Probability distribution of the difference between MERRA-2 AE and AERONET AE over 12 regions (d-o) across the globe, including the values of N (total collocated data points), M (median), and EE (data points within EE) for total (including all ranges) and different ranges of AERONET AE values are shown. The vertical dashed lines in different colors represent the median of each probability distribution.*

provement and updating of emissions inventories, long-range transport mechanisms, and better parameterizations and data assimilation algorithms.

On a regional scale, the validation of MERRA-2 and CAMS AOD clearly shows that their performances are good (GF >50%) in simulating AOD over the other regions of the globe (except over Middle East and North Africa) compared to Asia (Figs. 3.9, 3.17). It also indicates the low uncertainty in both local and regional emission inventory, parameterizations, and transport mechanisms over these regions compared to Asia. Similar to Asia, the biases in MERRA-2 and CAMS AODs and GFs are higher and lower with broader probability distribution for high AOD (>0.4) conditions, respectively, and the biases of model AODs and GFs are lower and higher with narrow probability distribution for low AOD conditions, respectively, over all the regions. However, it is noted

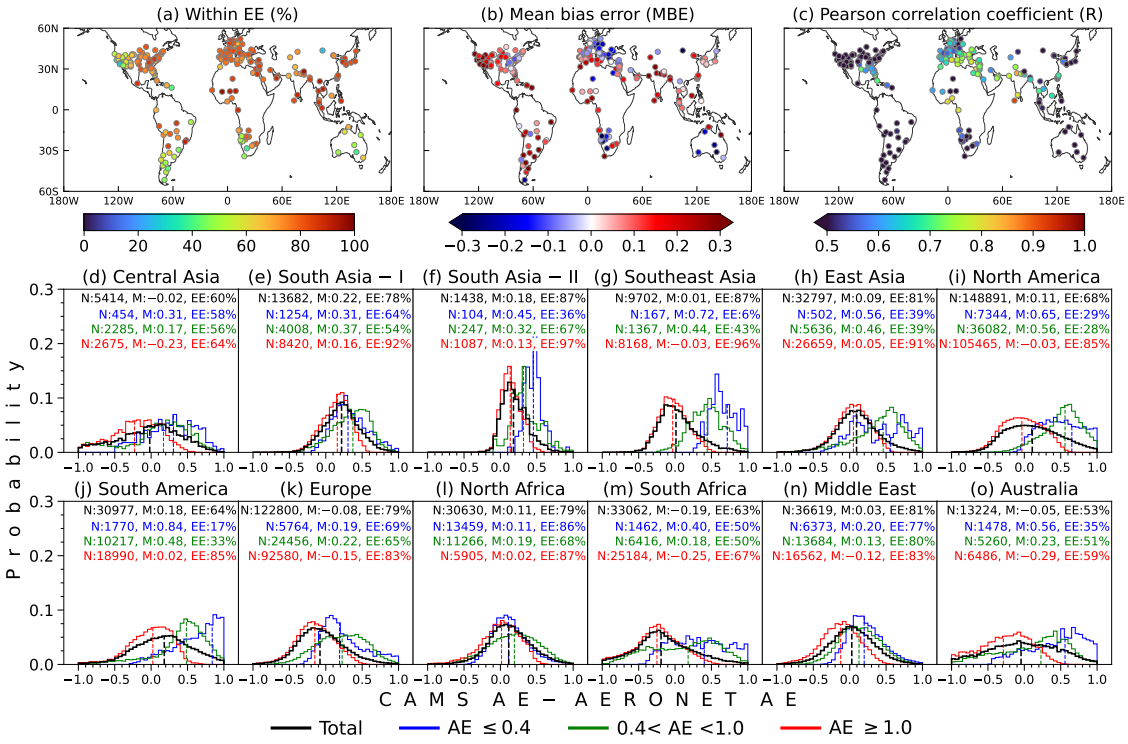

Figure 3.16: *Similar to Fig. 3.15, but for the collocated validation of CAMS AE with AERONET AE.*

that the occurrence of high AOD conditions is more frequent over Asia compared to other regions (Fig. 3.4); thus, the overall biases in both model AODs are found to be higher over Asia. A consistent overestimation of AE by CAMS is seen over all the sites in North America, South America, North Africa, and Middle East, which was also observed in Asia (Figs. 3.16, 3.14). This can be due to the overestimation of fine anthropogenic aerosols and biomass burning smoke (BC and OC), and the underestimation of the contribution of coarse mode aerosols such as dust.

It is interesting to note that during the biomass burning period over South America, models are able to capture AOD better with low bias. However, models highly underestimate AOD by an order of ∼0.2 over sites in central Africa (southern and northern parts of North and South Africa, respectively) during the intense biomass burning period of winter and autumn. This indicates that emissions and parameterizations related to biomass burning aerosols of BC and OC need to be improved over Africa in models to reduce the uncertainty and to better capture the high biomass burning events over Africa. Similar improvements are required in MERRA-2 over biomass burning dominated regions of the Maritime Continent in Southeast Asia, as MERRA-2 exhibits a high

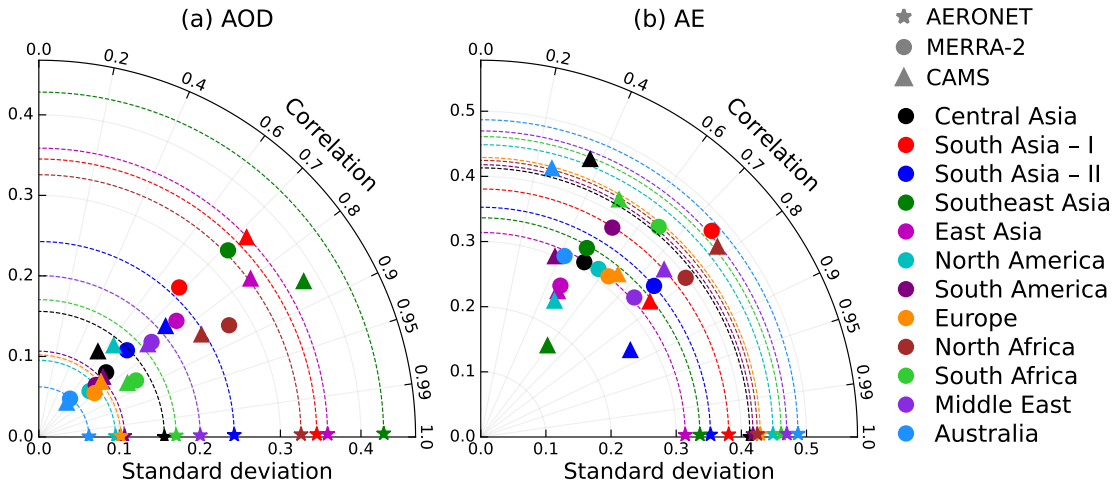

Figure 3.17: *Taylor diagram for collocated comparison of (a) aerosol optical depth (AOD), and (b) Ångström exponent (AE) by MERRA-2 (●) and CAMS (▲) simulations with respect to AERONET measurements. '★' symbols represent the standard deviation of reference AERONET values for different regions. Colors of each symbol indicate the different regions across the globe. The total number of collocated data points in each region of (a) and (b) is the same as in Fig. 3.9 and Fig. 3.13, respectively.*

negative bias (Fig. 3.11). It is found that the bias in both MERRA-2 and CAMS simulated AEs is relatively higher than in simulated AODs across the globe, as the assimilation of AOD is constrained by observations at a specific wavelength (0.55 μm). Whereas AE depends on the spectral distribution of AODs and the relative contributions of fine and coarse mode aerosols, which depend on the contribution of different aerosol species. Consequently, the lack of AOD assimilation in each wavelength and uncertainties in the simulated species-wise AODs lead to higher biases and lower correlations in model-simulated AE compared to AOD. Similar patterns are observed globally, as in Asia, with consistently higher biases and lower correlations in model AEs relative to AODs, highlighting the substantial challenges in accurately simulating spectral AOD distributions and appropriate contributions of fine and coarse mode aerosols as a function of wavelength on a global scale. Furthermore, the inaccurate simulation of spectral AODs can introduce significant biases in the estimation of DRE, as spectral AODs, along with SSA, are critical inputs for evaluating the radiative and climate effects of aerosols (Ansari & Ramachandran, 2024b), which will be discussed in Chapter 5.

3.5.2 Global assessment of MERRA-2 simulated SSA

On the seasonal scale over Central Asia, AERONET SSA varies between 0.80 and 0.95 due to differences in aerosol sources that vary seasonally (Fig. 3.6). However, the seasonal variation in MERRA-2 SSA is quite less and most of its values lie between 0.92 and 0.95 (Figs. 3.18, 3.19a). Bias in MERRA-2 SSA is lower and GF is higher (>60%) over South and Southeast Asia than East Asia. The performance of MERRA-2 SSA over South Asia is consistent in all seasons (MBE <0.03, in magnitude) except in winter when MERRA-2 underestimates SSA (Ansari & Ramachandran, 2025b). Bias in MERRA-2 SSA is found to be higher over East Asia (e.g., China and Japan) with high underestimation (MBE >0.03, in magnitude) and GF of <40%. This underestimation in SSA can be due to the absence of nitrate and ammonium aerosols in the MERRA-2's GOCART module (Buchard et al., 2017), which are scattering in nature. This may result in lower SSA as the concentration of nitrate aerosols is higher in China's intensive industrial areas (Zhang et al., 2012). It also resulted in an underestimation of MERRA-2 AOD over East Asia (e.g., Che et al. (2019a); Sun et al. (2019); Ansari & Ramachandran (2024b)). Additionally, stringent air pollution control measures in China led to a decrease in absorbing aerosols during 2010-2017 (e.g., BC emissions reduced by ∼27%) (Zheng et al., 2018). Underestimation in MERRA-2 SSA over East Asia shows that the recent changes in absorbing aerosol contributions over East Asia are not well captured in MERRA-2 since the emission inventory related to anthropogenic BC/OC emissions was not updated after 2006. This is consistent with a previous study, which showed that MERRA-2 did not capture the declining trend of BC concentration in the last two decades (2006-2022) (Li et al., 2024). A similar underestimation in MERRA-2 SSA is observed over north Europe and west North America (Figs. 3.20, 3.19a). The GF values for MERRA-2 SSA are higher (>60%), and biases are relatively lower over sites in North Africa and Middle East (MBE: ∼–0.02), which are dominated by dust aerosols throughout the year with less seasonal variability in SSA (Fig. 3.20). Over most of the sites which are dominated by biomass burning emissions (e.g., central Africa (southern and northern parts of North and South Africa, respectively), South America, north Southeast Asia), MERRA-2 overestimate AERONET SSA (MBE: ∼0.04) with low GCOS fraction (<50%) and simulate less aerosol absorption (Figs. 3.18, 3.20). The performance of MERRA-2 in simulating AOD is reasonably well (GF: ∼68%) over North America (Fig. 3.9), whereas MERRA-2 underperforms in simulating SSA over the same region (GF: ∼34%)

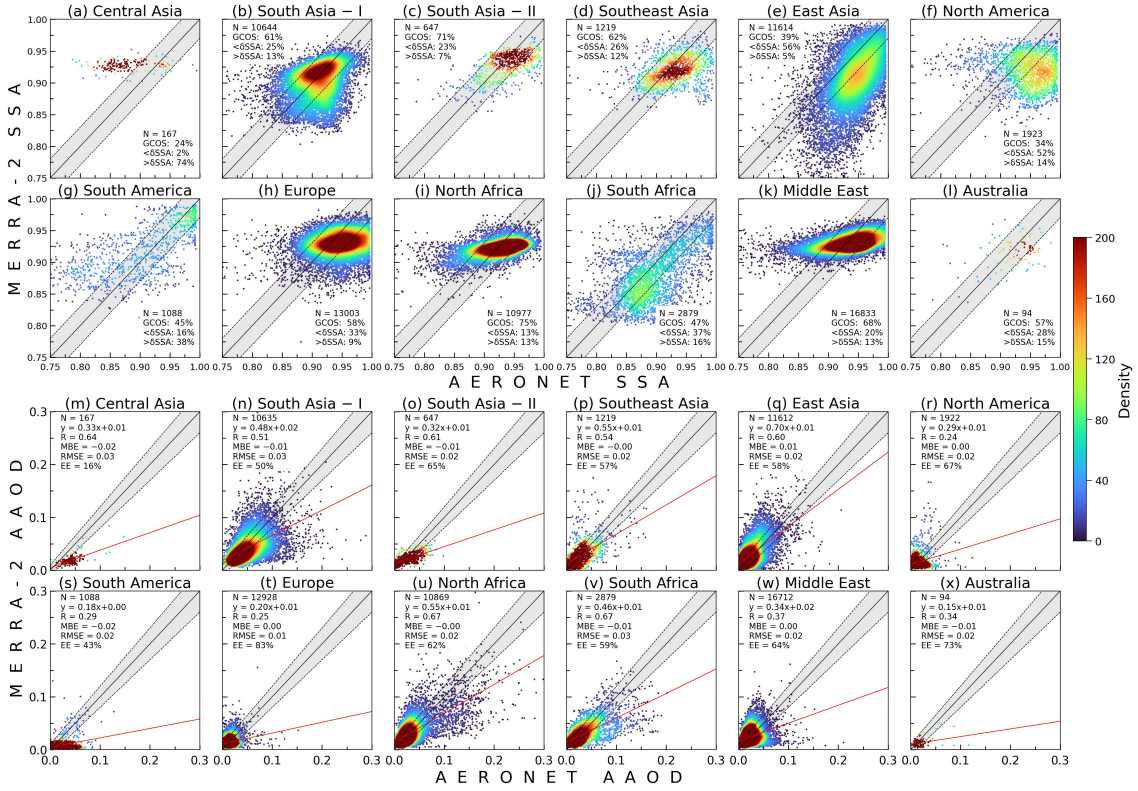

Figure 3.18: *Collocated evaluation of MERRA-2 simulated single scattering albedo (SSA) (a-l) and absorption aerosol optical depth (AAOD) (m-x) with AERONET SSA and AAOD at 0.55 μm, respectively, over different regions across the globe. In (a-l), the gray shaded region represents the range of GCOS requirement for SSA (uncertainty of AERONET SSA (δSSA): $\pm$0.03). The total number of collocated data points (N), % of data points within (GCOS fraction), below, and above δSSA, are given (a-l). In (m-x), the gray shaded region shows the range of expected error (EE) of AAOD ($\pm(0.01 + 0.1\times AAOD_{AERONET})$). Statistics of linear fitted line (red line), mean bias error (MBE), root mean square error (RMSE), and % of data points within EE are also shown (m-x). Solid black line in each panel corresponds to a 1:1 line. Color bar indicates the probability density derived from the kernel density estimation.*

(Fig. 3.18). This discrepancy points to potential biases in aerosol speciation and their mixing state assumptions and optical property parameterizations within MERRA-2.

The probability distribution of bias in MERRA-2 SSA for different ranges of SSA clearly shows that GFs higher and the median values are lower (in absolute terms) when the aerosols are moderately absorbing in nature with 0.90$\leq$ SSA <0.95 compared to aerosols that are less absorbing (SSA $\geq$0.95) and more absorbing (SSA <0.90) in nature

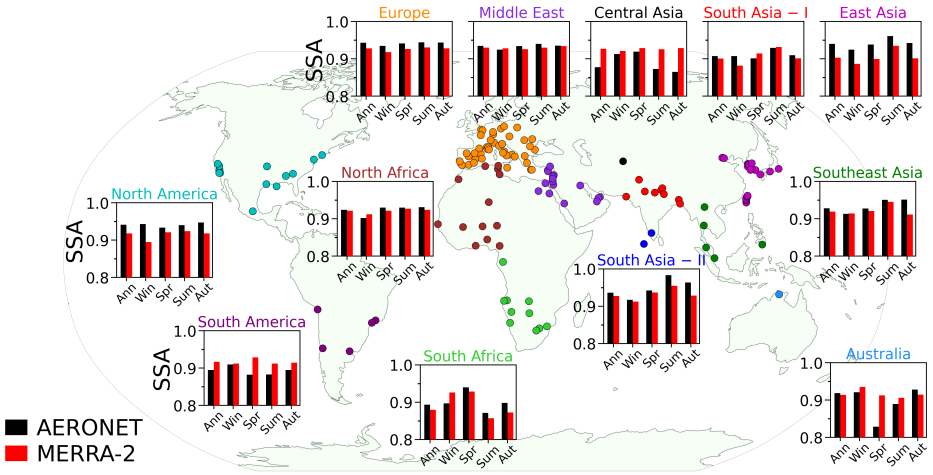

(a) *Regional mean single scattering albedo (SSA)*

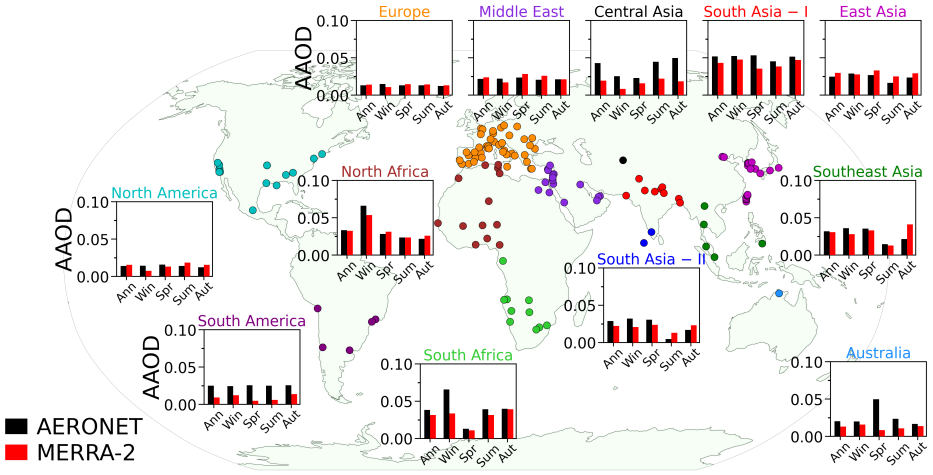

(b) *Regional mean absorption aerosol optical depth (AAOD)*

Figure 3.19: *Same as Fig. 3.10, but for (a) single scattering albedo (SSA) and (b) absorption aerosol optical depth (AAOD) at 0.55 μm by AERONET retrieval and MERRA-2 simulation.*

(Ramachandran et al., 2022) (Fig. 3.20d-o). When SSA $\geq$0.95, median values of the probability distribution are higher in negative magnitude, indicating an underestimation of SSA over all the regions. Whereas when SSA $\leq$0.90, median values of the probability distribution are higher on the positive side, indicating the overestimation of SSA over all the regions except East Asia, where a consistent underestimation in SSA is observed for all ranges of SSA values. This finding also reveals that, in spite of the significant differences in the content and composition of aerosols, MERRA-2 mostly simulates the composition of aerosols as moderately absorbing in nature.

On the regional scale, the variation of bias in MERRA-2 SSA as a function of concurrent AERONET AOD clearly shows that MERRA-2 exhibits low bias in SSA and

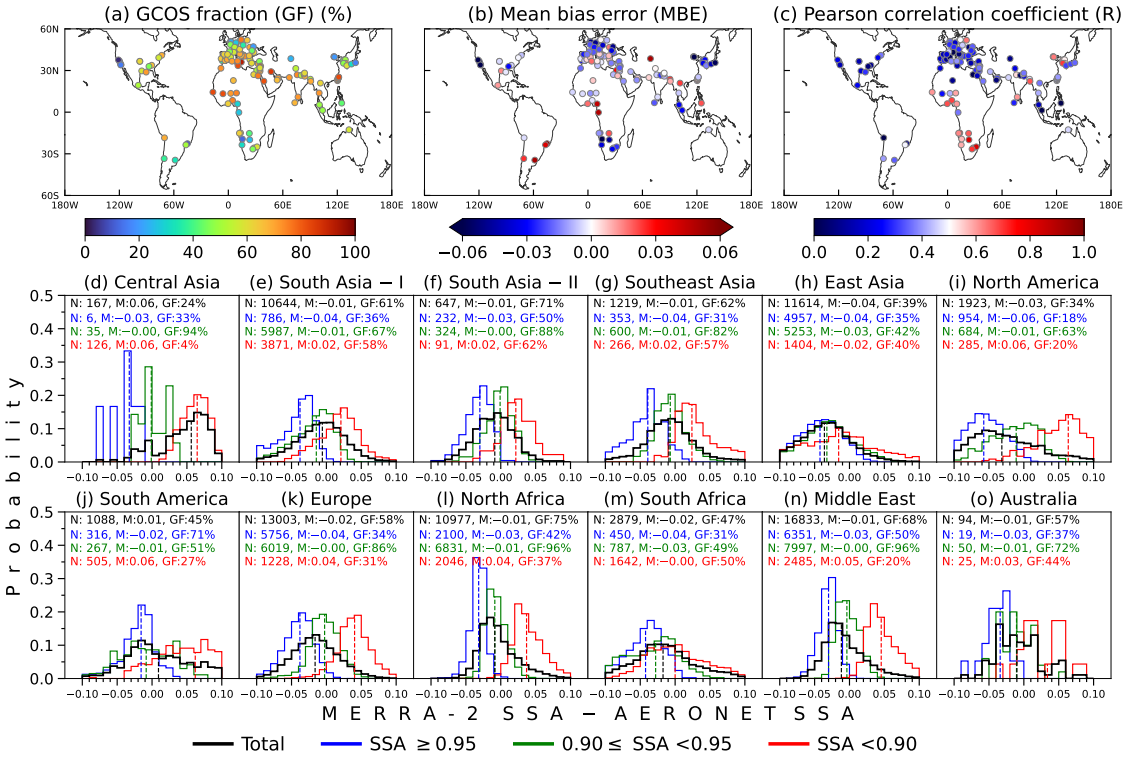

Figure 3.20: *The spatial distribution of (a) Global Climate Observing System (GCOS) fraction (GF: % of MERRA-2 single scattering albedo (SSA) data points within the uncertainty of AERONET SSA (±0.03)), (b) MBE, and (c) R derived from the collocated evaluation of MERRA-2 simulated SSA with AERONET SSA at 0.55 μm. Probability distribution of the difference between MERRA-2 SSA and AERONET SSA over different regions across the globe (d-o), including the values of N: total collocated data points, M: median, and GF for total (including all ranges) and various ranges of AERONET SSA values (less absorbing: SSA ≥0.95, moderately absorbing: 0.90≤ SSA <0.95, and more absorbing: SSA <0.90). The vertical dashed lines in different colors correspond to the median of each probability distribution.*

satisfies the GCOS requirement for the whole range of AOD values over South Asia (I-II), Europe, North Africa, and Middle East (Fig. 3.21). However, a little divergence in SSA bias is found for high AOD value but it is still inside the GCOS requirement. Over Southeast Asia and South America, MERRA-2 exhibits underestimation in SSA for high AOD conditions, which occurs mainly due to the lack/absence of appropriate representation of biomass burning emissions (Ansari & Ramachandran, 2025b). A similar underestimation in MERRA-2 SSA with increasing AOD is also observed over East Asia.

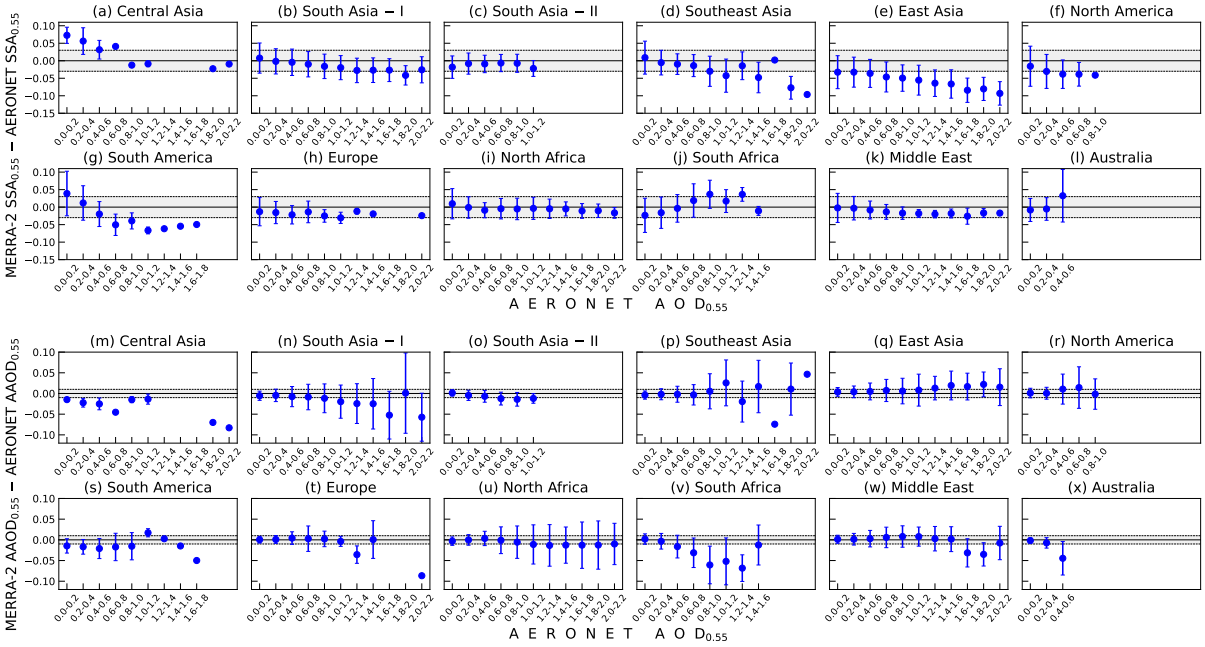

Figure 3.21: *The variation of difference between MERRA-2 single scattering albedo (SSA) and AERONET SSA (a-l), and MERRA-2 absorption aerosol optical depth (AAOD) and AERONET AAOD (m-x) as a function of concurrent AERONET observed AOD values over different regions across the globe. Grey shaded regions represent the uncertainty in AERONET SSA (a-l) and AAOD (m-x), respectively.*

3.5.3 Global assessment of MERRA-2 simulated AAOD

The regional-scale evaluation of MERRA-2 simulated SSA (Figs. 3.18, 3.19a, 3.20, 3.22) and AAOD (Figs. 3.18, 3.19b, 3.22, 3.23) with AERONET datasets on a global scale shows that the linear correlations for MERRA-2 SSA and AAOD evaluations are lower than those for MERRA-2 AOD (Figs. 3.9, 3.11, 3.17). Among SSA and AAOD, the correlation for SSA is even lower, clearly suggesting that the simulations of aerosol absorption parameters are more challenging and complicated compared to AOD. These challenges with model simulation are also observed with satellite retrievals of aerosol absorption parameters (Schutgens et al., 2021). However, the performance of each simulated aerosol parameter significantly varies depending on the region and seasonal cycle of aerosol emissions. One of the possible reasons behind the better performance in MERRA-2 AOD over AAOD and SSA could be that MERRA-2 assimilates AOD from AERONET (before 2014) and MODIS observations (from 2002 onward), which contain information about the total extinction of aerosols. On the contrary, assimilations of

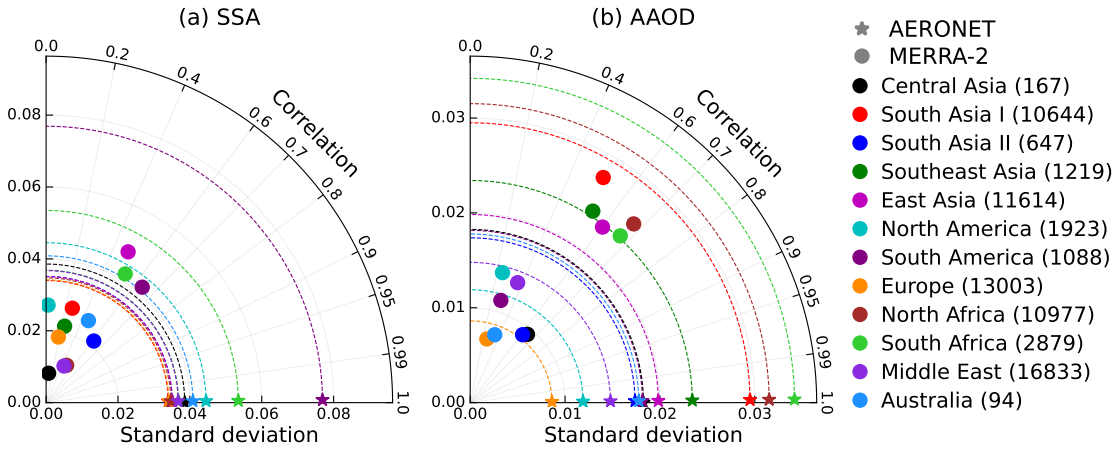

Figure 3.22: *Taylor diagram for collocated comparison of MERRA-2 (●) simulated single scattering albedo (SSA) (a), and absorption aerosol optical depth (AAOD) (b) with respect to AERONET SSA and AAOD values, respectively. '★' symbols represent the standard deviation of reference AERONET values for different regions. Colors of each symbol indicate the different regions of the globe. The total number of collocated data points is shown next to each region in the legend.*

AAOD and SSA are not performed in MERRA-2 due to a lack of partitioning of scattering and absorption in total AOD.

The bias in MERRA-2 AAOD depends on the biases in simulated SSA and AOD. The bias in MERRA-2 AOD was higher over Asia (pronounced in South Asia – I) than the other regions (Section 3.5.1) (Ansari & Ramachandran, 2024b). The overestimation in MERRA-2 SSA resulted in the underestimation of AAOD over Central Asia, with only 16% of simulated AAOD data points being within EE (Fig. 3.18). In the seasonal-scale evaluation, provided in Ansari & Ramachandran (2025b), this underestimation of aerosol absorption is found to be even higher (MBE: –0.03, RMSE: 0.03) during summer and autumn when the transport of dust aerosols is higher over Central Asia. The high underestimation in MERRA-2 AOD over South Asia – I overwhelms the low bias in MERRA-2 SSA, and it leads to an underestimation in MERRA-2 AAOD (MBE: ∼–0.02; RMSE: ∼0.03) and ∼50% of its values are within EE. This underestimation is more pronounced during winter (when anthropogenic contribution is higher) and spring (when SSA is relatively lower) (Ansari & Ramachandran, 2025b). The overestimation in MERRA-2 AAOD over eastern countries of East Asia (e.g., Japan, South Korea) is in line with the underestimation in MERRA-2 SSA. However, the underestimations in both AOD

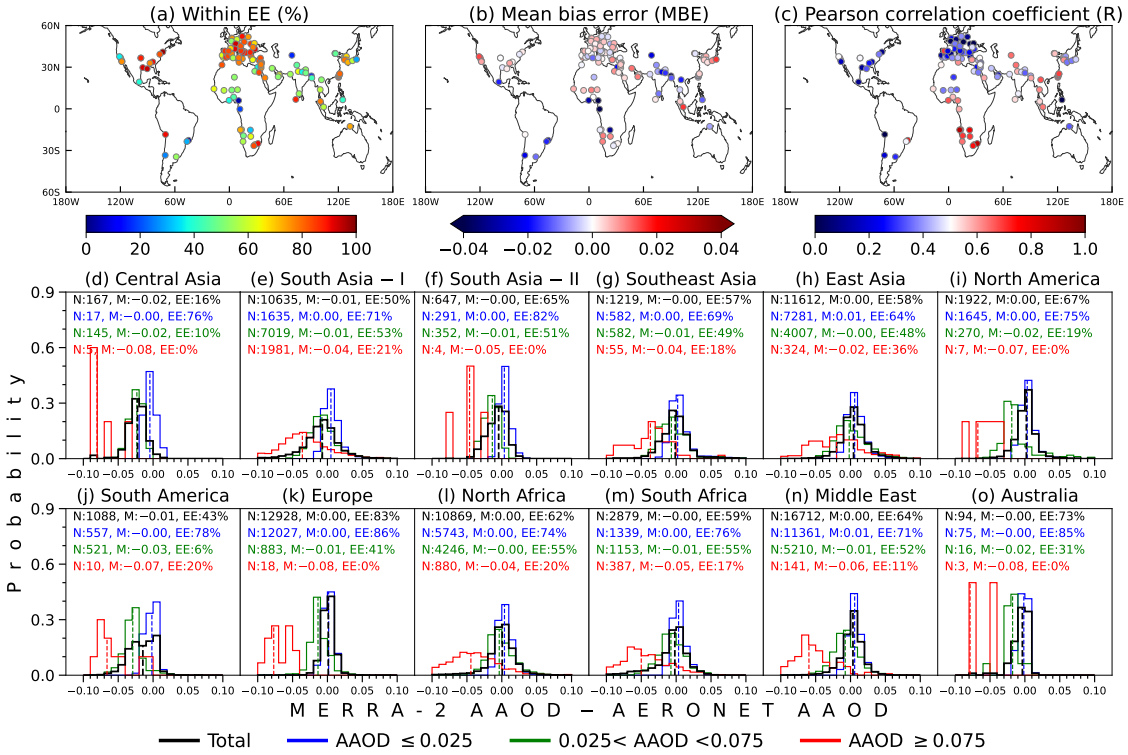

Figure 3.23: *The spatial distribution of (a) % of MERRA-2 absorption aerosol optical depth (AAOD) data points within expected error (EE) of AAOD (=±(0.01 + 0.1×$AAOD_{AERONET}$)), (b) MBE, and (c) R derived from the collocated evaluation of MERRA-2 simulated AAOD with AERONET AAOD at 0.55 μm. Probability distribution of the difference between MERRA-2 AAOD and AERONET AAOD over different regions across the globe (d-o), including the values of N: total collocated data points, M: median, and EE: % of MERRA-2 data points within EE of AAOD for total (including all ranges) and different ranges of AERONET AAOD values. The vertical dashed lines in different colors represent the median of each probability distribution.*

and SSA result in less bias in MERRA-2 AAOD over east China sites. During the peak fire seasons over the biomass burning sites (e.g., central Africa, South America, north Southeast Asia), high underestimation in MERRA-2 AAOD (MBE >0.03, in magnitude) with <50% data points within EE is found, which is corroborated by the overestimation in SSA (Figs. 3.18, 3.23) (Ansari & Ramachandran, 2025b). One of the possible reasons behind the underestimation of aerosol absorption over biomass burning sites could be due to the assumption that OC is mostly scattering in MERRA-2's GOCART module (Randles et al., 2017). MERRA-2 exhibits a slight overestimation in AAOD (MBE <0.02) over North Africa and Middle East, where natural dust is dominant (Fig. 3.23).

Regionally, the spatial distribution and the probability distribution of bias in MERRA-2 AAOD clearly shows that MERRA-2 performs better over North America (central and west), Europe, Middle East, and Australia (where total AOD and AAOD are lower compared to other regions of the globe) with a lower bias and ≥64% of data points are within EE (Fig. 3.23). For low AAOD (≤0.025), the probability distribution is narrow with relatively less bias, and higher data points lie within EE (Fig. 3.23d–o). Whereas for high AAOD (≥0.075), the probability distribution gets flatter with its lesser magnitude, and the underestimation in MERRA-2 AAOD increases over all the regions. Over South Asia – I, central Africa, Central Asia, and South America, where the conditions of high AAOD and AOD values are more frequent, MERRA-2 significantly underestimates (∼–0.05) AERONET AAOD compared to other regions of the globe. The signature of variation of bias in MERRA-2 AAOD as a function of different AAOD values is the same as the bias in MERRA-2 AOD as a function of different AOD values. Bias in MERRA-2 AOD is also lower for low AOD (≤0.25) conditions, and it increases (underestimation) for high AOD (≥0.75) conditions. The variation of bias in MERRA-2 AAOD as a function of concurrent AERONET AOD measurements clearly signifies that MERRA-2 exhibits low bias in AAOD when AOD is lower (<0.4) and it gradually increases (either positive or negative, depending on the region) when AOD increases (Fig. 3.21m-x). For high AOD (>0.6), the underestimation in MERRA-2 AAOD increases over most regions (e.g., Central Asia, South Asia, South America, North Africa, South Africa, Middle East), which is due to high underestimation in MERRA-2 AOD.

MERRA-2 exhibits a large range of bias in AOD (varies between –0.4 and 0.4) compared to bias in SSA (mostly varies between –0.04 and 0.04). However, the effect of bias in SSA is still significant in changing AAOD because SSA has a non-linear impact on AAOD, especially at higher SSA (>0.90). For example, in global mean (average for all regions at 0.55 μm) AAOD = 0.017 (AOD = 0.24, SSA = 0.93), 3% reduction in SSA (=0.90) leads to a ∼40% increase in AAOD (=0.023). Thus, the simulation of SSA is very sensitive to determine AAOD. Further, SSA exerts a nonlinear influence on DRE. For example, for AOD = 0.24 and SSA = 0.93 (mimicking the observed global mean scenario, Figs. 3.4, 3.7), a 3% change in SSA results in a ∼15% change in DRE_{SFC}, changing from –12.62 to –10.73 Wm^{-2}. DRE is estimated employing Santa Barbara DISORT Atmospheric Radiative Transfer (SBDART) model (Ricchiazzi et al., 1998) in the shortwave region (spectral range from 0.2 to 4.0 μm) with spectral values of AOD

and SSA taken from Optical Properties of Aerosols and Clouds (OPAC) model (Hess et al., 1998). Further, the gradient in DRE is steeper when SSA changes from 0.9 to 1.0 than from 0.8 to 0.9 for the same AOD (Ramachandran, 2018). Thus, our findings show that the non-linear effect of SSA on AAOD and DRE depends on the SSA value, and the magnitude of this non-linearity increases for high SSA. Thus, as the annual mean SSA over most regions is in the range of 0.90 to 0.95, a small improvement in SSA can significantly improve AAOD simulation and assessment of the radiative and climate impact of aerosols. Further, although the contribution of BC to total AOD is less than the other aerosol species, BC contributes the largest to AAOD through absorption due to its low SSA (∼0.23). Thus, an accurate simulation of BC AOD compared to other species can significantly reduce the biases in SSA and AAOD.

3.6 Comparison between CMIP6 and AERONET observations

On an annual scale, CMIP6 AOD exhibits underestimation in South Asia – I, Southeast Asia, South Asia – II, and North Africa (Fig. 3.24). However, the bias in CMIP6 AOD

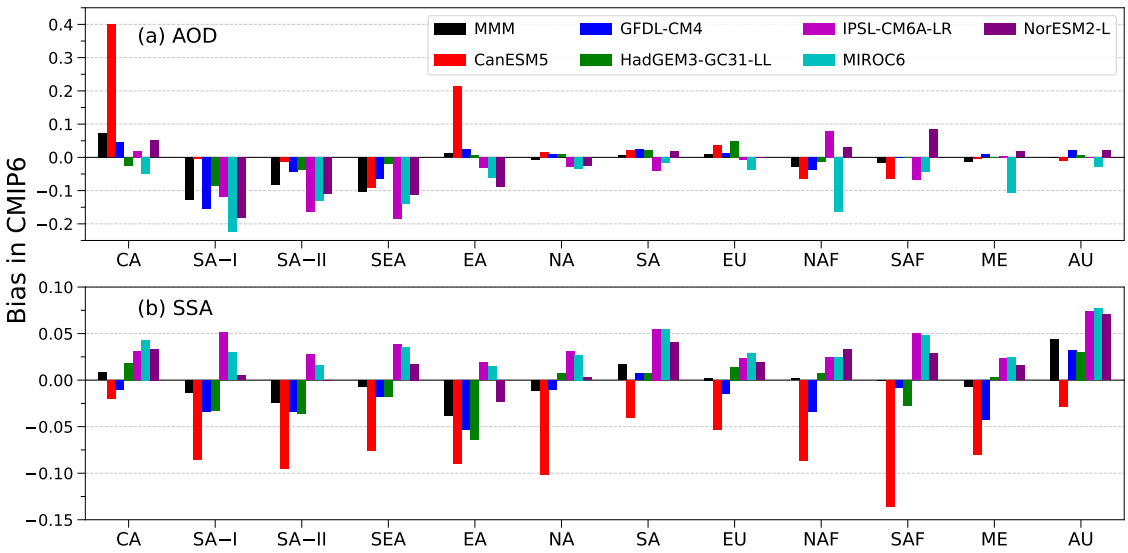

Figure 3.24: *Annual mean bias in (a) aerosol optical depth (AOD) and (b) single scattering albedo (SSA) simulated by multi-model mean (MMM) and individual models from CMIP6 with respect to AERONET calculated from their monthly means over different regions (Central Asia (CA), South Asia – I (SA–I), South Asia – II (SA–II), Southeast Asia (SEA), East Asia (EA), North America (NA), South America (SA), Europe (EU), North Africa (NAF), South Africa (SAF), Middle East (ME), and Australia (AU)) across the globe.*

is relatively smaller in North America, South America, Northern Europe, and Australia, where the AOD values are low and exhibit less spatiotemporal variability. CMIP6 simulations also underestimate AERONET SSA over Asia in all seasons, while tending to overestimate SSA over South America and Australia. Substantial inter-model variability exists in simulated AOD and SSA by CMIP6 models. However, HadGEM3-GC31-LL generally outperforms other models in simulating AOD over regions such as Southeast Asia, East Asia, North America, North Africa, South Africa, and Middle East. Regarding SSA, CanESM5 consistently underestimates AERONET observations, while IPSL-CM6A-LR and MIROC6 tend to overestimate SSA across all the regions (Fig. 3.24).

3.7 Summary and Conclusions

In this chapter, an extensive analysis of the spatial distributions of columnar aerosol optical and physical properties (AOD, AE, FMF, and VSD) and absorption parameters (SSA and AAOD) over Asia and other regions of the globe, based on the AERONET dataset, is performed on seasonal and annual scales. Further, a comprehensive assessment of the spatiotemporal collocated validation of MERRA-2, CAMS, and CMIP6 simulated aerosol

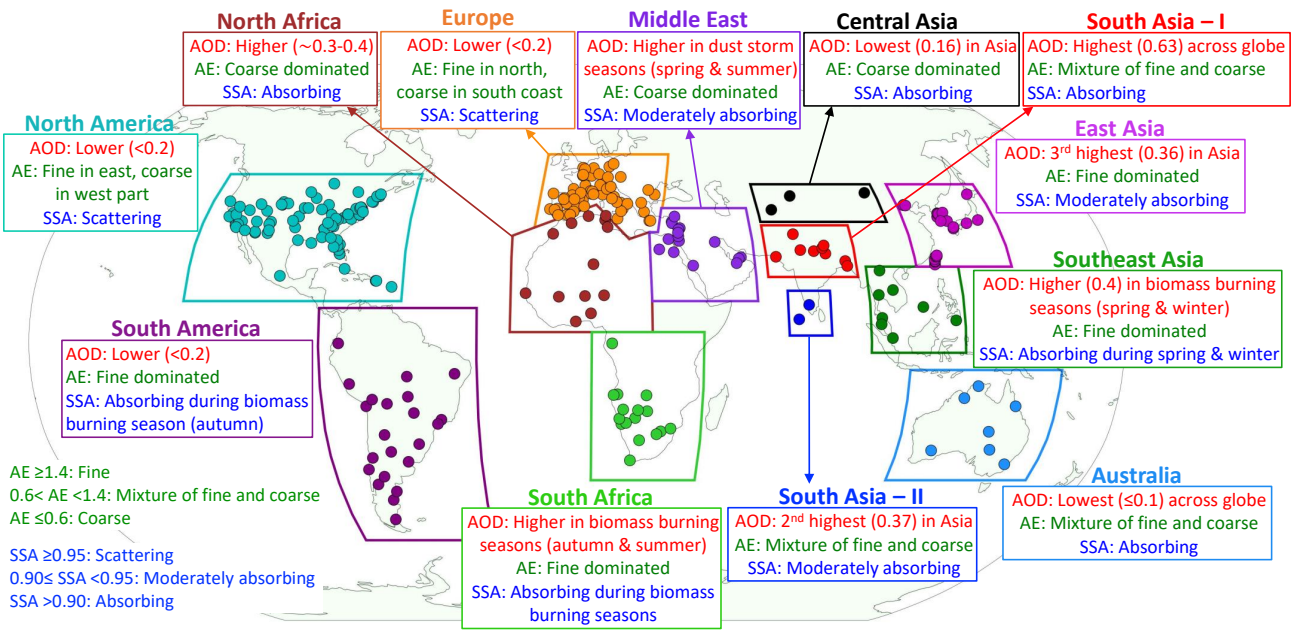

Figure 3.25: *A summary of major findings on aerosol optical depth (AOD), Ångström exponent (AE), and single scattering albedo (SSA) from the present study for different regions across the globe.*

optical properties and absorption parameters is provided over different regions across the globe. The major findings are (Fig. 3.25):

1. In Asia, South Asia – I experiences the highest AOD annually and seasonally (mean AOD: 0.63 $\pm$ 0.15), followed by South Asia – II (0.37 $\pm$ 0.14), East (0.36 $\pm$ 0.13), Southeast (0.33 $\pm$ 0.10), and Central Asia (0.16 $\pm$ 0.07), due to the combined contributions of fine- (from anthropogenic emission) and coarse-mode (from seasonal dust and sea salt transport) aerosols. The spatial and seasonal variations of AOD, AE, FMF, and VSD values are found to be statistically significant across Asia, with predominance in South Asia – I, due to a mixture of both fine and coarse mode aerosols.

2. Seasonal, annual, and global analyses reveal that AOD is significantly lower (<0.25) in North America, South America, Europe, and Australia, compared to Asia. Over the same regions, VSD (<0.05 $\mu m^3/\mu m^2$), and TVC (<0.1 $\mu m^3/\mu m^2$) are at least 3–4 times lower compared to in Asia. Furthermore, both seasonal and spatial variability in AOD, AE, and FMF are significantly smaller over North America, Europe, and Australia compared to Asia.

3. High AOD with lower SSA over South Asia – I result in higher AAOD ($\sim$0.06), which is $\sim$50% lower over other regions in Asia. AAOD is highest (>0.1) over central Africa during winter due to the higher amount of absorbing carbonaceous aerosols from intense biomass burning and their mixing with desert dust. Over North America and Europe, the regional mean spectral SSA is higher (>0.92) with lower AOD (<0.2) and AAOD (<0.02), indicating reduced emissions of absorbing aerosols in relatively cleaner environments.

4. The performance of MERRA-2 and CAMS AOD against AERONET AOD is better over Australia, North America, Europe, South America, and South Africa (low bias and high GF), compared to over Asia. For high AOD conditions, both models tend to underestimate AERONET AOD across all regions, which is more pronounced over Asia. Additionally, the performance of both models is lower in simulating AE than AOD, highlighting significant challenges in accurately representing spectral AOD and the relative contributions of fine and coarse aerosol modes across wavelengths.

5. MERRA-2 mostly simulates aerosol composition to be moderately absorbing in nature (i.e., bias in MERRA-2 is low for 0.90$\leq$ SSA <0.95) despite significant differences in the aerosol content and composition. MERRA-2 exhibits underestimation in SSA for

high AOD values over East Asia, Southeast Asia, and South America.

6. The performance of MERRA-2 AAOD is better over North America, Europe, and Middle East with lower bias and higher data points ($\geq$64%) within EE. Additionally, the underestimation in MERRA-2 AAOD increases for high AAOD, whereas it is lower for low AAOD conditions across the globe. A consistent underestimation in MERRA-2 SSA for high AOD values over East Asia leads to a slight overestimation in MERRA-2 AAOD as the bias in AAOD is reduced by the underestimation in both MERRA-2 AOD and SSA.

7. CMIP6 models exhibit significant inter-model variability. Among these models, the performance of HadGEM3-GC31-LL is better in reproducing AOD across multiple regions, including Asia. CMIP6 MMM AOD underestimates AERONET AOD over most sites in Asia and North Africa, with comparatively smaller biases over North America, South America, Europe, and Australia.

4

Aerosol Types and Absorbing Aerosol Types

Aerosols give rise to the largest uncertainty in accurately quantifying the present and future climate due to lack of observational constraints on optical and physicochemical properties of different aerosol types (Bellouin et al., 2020; Li et al., 2022). Aerosol types over a region are governed by the long-term average of optical, physical, and chemical properties of aerosols, and thus, accurate identification of aerosol types is vital (Dubovik et al., 2002; Giles et al., 2012; Russell et al., 2014; Lu et al., 2023; Wei et al., 2024). One of the major causes behind the high uncertainty in the assessment of the radiative effect of aerosols is associated with aerosol absorption, which is a smaller fraction of aerosol extinction but is the most critical parameter for quantifying the aerosol radiative effect (IPCC, 2021; Li et al., 2022). The lack of accurate global measurements and characterization of aerosol absorption results in this aerosol parameter being poorly constrained and highly underestimated in climate models in various regions across the globe, particularly over Asia (Shindell et al., 2013; Myhre et al., 2017; Kelesidis et al., 2022). The mixing of absorbing aerosols can enhance the absorption efficiency of composite aerosols and can substantially affect the aerosol radiative effects, which imposes a significant challenge in the estimation of aerosol radiative effects (Jacobson, 2001; He et al., 2015). Therefore, accurate global-scale identification and quantification of different aerosol types and absorbing aerosol types are not only essential for satellite retrievals and climate models to enhance the accuracy of radiative and climate impact assessment of aerosols but also for their sustained mitigation, tracking, and control of emissions (Giles et al., 2012; Wei et al., 2024).

A new hybrid algorithm (Wei et al., 2024) is utilized to classify and quantify different aerosol types into Biomass burning (BB), Urban-industrial (UI), Dust, Mixed-fine, and Mixed-coarse types. By utilizing this classification scheme, the global distribution of

different aerosol types is determined on a seasonal scale and discussed. Furthermore, a new scheme is developed in this study to accurately classify and quantify the absorbing aerosol types of Dust, BC, Carbonaceous aerosols (CA), Mixed, Mixed-BC, and Mixed-Dust, by leveraging the spectral characteristics of AOD and SSA of these aerosols. Using the newly developed classification scheme, spatiotemporal variation and distribution of absorbing aerosol types and their influences on AOD and AAOD are analyzed on global and seasonal scales, and discussed.

4.1 Aerosol types

4.1.1 Classification scheme for aerosol types

An innovative hybrid algorithm developed by Wei et al. (2024), which efficiently integrates machine learning and density clustering algorithms, is used to classify the different aerosol types to improve the precision and efficiency of the identification of aerosol types. This hybrid algorithm includes an aerosol optical property dataset for five aerosol types (Biomass burning (BB), Urban-industrial (UI), Dust, Mixed-fine, and Mixed-coarse), which was constructed using the aerosol size distribution parameters (fine- and coarse-mode effective radius and standard deviation), complex refractive index, and Mie scattering model. BB type includes combustion and simmering of biomass and biofuel from agriculture, wood, grassland, and forest. UI type originates dominantly from fossil fuel combustion over densely populated urban areas (Giles et al., 2012). Mixed type represents the mixed aerosols emitted from biomass burning, fossil fuel combustion, and desert dust, and it is divided into Mixed-fine (dominance of fine aerosols in Mixed type) and Mixed-coarse (dominance of coarse aerosols in Mixed type). However, marine aerosols were not included in this classification algorithm due to the low AOD values with fewer valid aerosol parameters (Wei et al., 2024).

Traditional aerosol classification schemes are often constrained by spatial and temporal limitations, and typically rely on the threshold values of only two aerosol optical parameters, which restricts a comprehensive understanding of aerosol characteristics. In contrast, this new classification scheme demonstrated improved accuracy over previous methods in identifying aerosol types by incorporating multiple aerosol parameters as inputs, enabling better differentiation, especially between UI and Mixed-fine aerosol types. Additionally, the classification results from the new hybrid approach

are more closely aligned with the reference complex refractive indices, indicating better performance compared to the density-based clustering method (Wei et al., 2024). This optical dataset is finally employed in a random forest algorithm for aerosol-type classification based on the aerosol optical property dataset. The aerosol optical property dataset includes four major aerosol parameters: spectral (0.675, 0.87, and 1.02 μm) normalized AOD, extinction AE, and spectral (0.44, 0.675, 0.87, and 1.02 μm) SSA and g for each aerosol type. Normalized AOD is calculated by dividing the spectral AODs by $AOD_{0.44}$ to eliminate the influence of the aerosol concentration. For the training of the random forest model above input spectral aerosol parameters were selected from the aerosol dataset to identify the specific aerosol type. More details of this classification scheme are provided in Wei et al. (2024).

4.1.2 Global distribution of aerosol types

The aerosol types show quite distinct spatial, regional, and seasonal variabilities (Figs. 4.1-4.5). The contribution of Mixed-coarse and Dust aerosol types is higher (∼60-80%) over Central Asia and western South Asia – I (e.g., IGP), as the observation sites in these regions are located near dust sources (e.g., Taklamakan, Aralkum, and Thar deserts, and western arid regions of the Arabian Peninsula) (Fig. 4.1). The contribution of Mixed-coarse and Dust increases over Central Asia (∼80%) and South Asia – I (∼60%) during summer, followed by spring, due to dust transport from the above dust sources (Fig. 4.5). Over South Asia – I, a decreasing gradient of Dust and Mixed-coarse aerosol types, and an increasing gradient of Mixed-fine and UI aerosol types from west IGP to east IGP sites are observed (Fig. 4.1). These contributions are attributed to seasonally varying meteorological conditions and transport of dust aerosols, along with the spatial distribution of anthropogenic aerosol sources. A decrease in dust aerosols and an increase in anthropogenic emissions from the populated, urban, and industrial sites enhance the contributions of Mixed-fine (∼55 %) and UI (∼20%) aerosol types, followed by BB type (∼15%), in east IGP sites. The increase in dust aerosol type in west IGP sites leads to lower SSA in shorter wavelength (0.44 μm), whereas the decrease in dust and increase in UI and BB types over east IGP sites give rise to higher SSA in shorter wavelength but lower SSA in longer wavelength (>0.675 μm) compared to west IGP sites (Figs. 3.6, 3.7a) (Smaran & Vinoj, 2024).

The sites in the Indochina Peninsula region (north Southeast Asia) experience

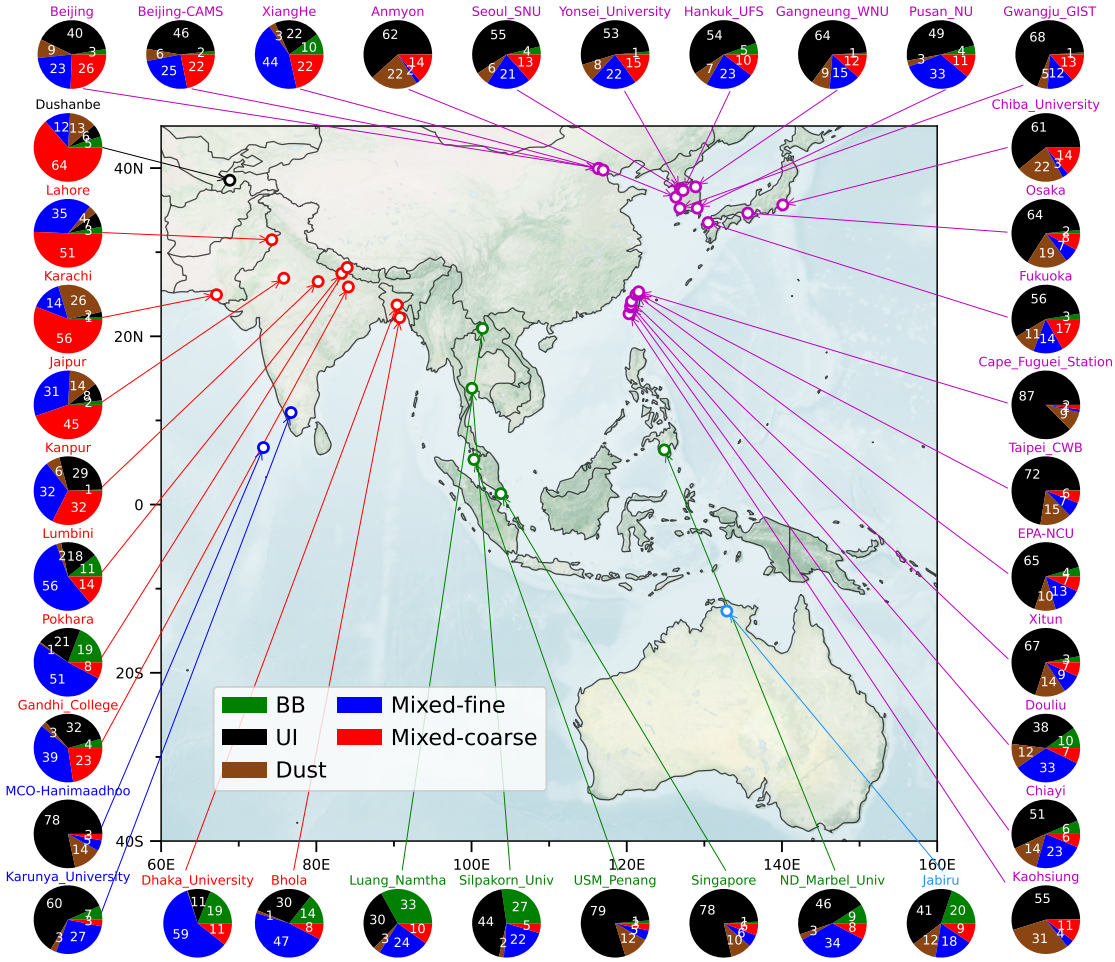

Figure 4.1: *Annual mean contributions (%) of different classified aerosol types (biomass burning (BB), urban-industrial (UI), Dust, Mixed-fine, and Mixed-coarse) shown by pie charts over all selected sites in Central Asia (black), South Asia – I (red), South Asia – II (blue), Southeast Asia (green), East Asia (magenta) and Australia (cyan) (Table 2.2).*

a high contribution of BB aerosol type (∼30%), resulting from intense biomass burning emission (e.g., slash-and-burn agricultural activities and forest fires) during dry seasons (winter and spring) which enhances the emission of carbonaceous aerosols and lead to higher AAOD and lower SSA (Figs. 3.6, 4.1, 4.5). The coastal urban sites in Southeast Asia (e.g., Singapore) and East Asia (e.g., Chiba, Osaka, Fukuoka, Taipei), densely populated and industrial cities, are mainly dominated by UI aerosols. UI type is >50% over East Asia during all the seasons (Fig. 4.5). The higher contribution of Mixed and dust aerosol types over East China sites is due to high anthropogenic aerosol emissions from urban and industrial areas, with the seasonal transport of dust aerosols, and their contribution gradually decreases from west to east in East Asia. Jabiru in Australia ex-

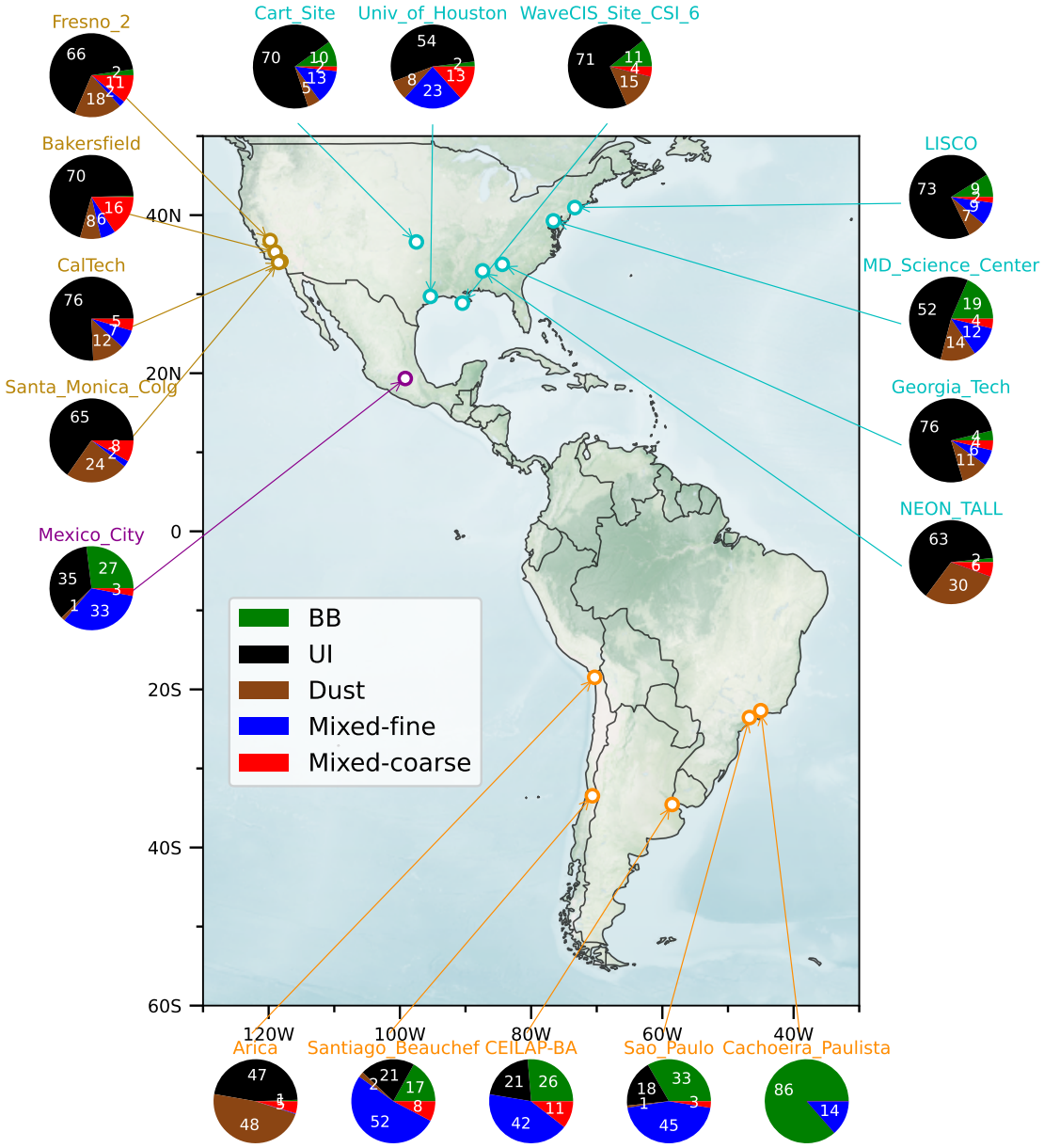

Figure 4.2: *Same as Fig. 4.1, but over East North America (cyan), West North America (brown), Central America (magenta), and South America (orange).*

periences majorly UI, BB, and Mixed-fine types due to anthropogenic activities, biomass burning, and dust transported from the inland deserts in Australia (Fig. 4.1).

The UI aerosol type is the dominating aerosol type over most sites in North America, especially over urban sites in East North America that have >50% contribution of UI type throughout the year (Figs. 4.2, 4.5). Urban-dominated aerosols over North America possibly lead to higher (lower) SSA in shorter (longer) wavelengths, respectively (Fig. 3.7a). In addition to the predominant UI aerosol type, Dust and

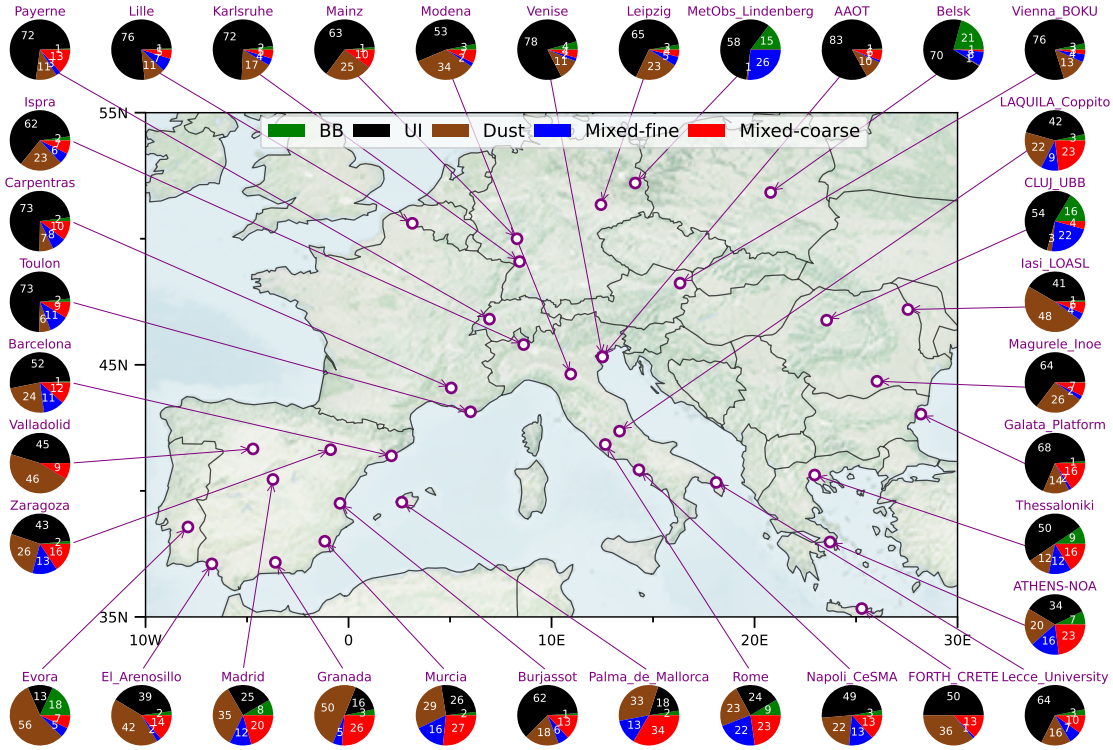

Figure 4.3: *Same as Fig. 4.1, but over Europe.*

Mixed-coarse aerosol types are also present over West North America due to the dust emissions from the inland desert in West North America. Mexico City (in Central America) is one of the largest urban megacities in the world, where high population and human activities, along with its meteorology and topography, significantly impact the local air pollution (Mensink et al., 2020). In addition to UI type over Mexico City, BB and Mixed-fine types are found to be higher due to forest and agricultural fires occurring during the dry period (winter and spring) (Ríos & Raga, 2018).

In South America, the BB aerosol type is dominant due to agricultural crop residue burning and intense forest fires during the Amazonian dry season (e.g., summer and autumn) (Hoelzemann et al., 2009) (Figs. 4.2, 4.5). In large urban populated and/or capital cities of Santiago_Beauchef, CEILAP-BA (Buenos Aires), and Sao Paulo, anthropogenic sources enhance the contribution of UI and mixed-fine aerosol types in addition to BB type. The presence of Dust aerosol type over Arica during summer can be attributed to the dust originating from the Puna-Altiplano deserts, which intensifies during the peak season of the subtropical jet stream (Gaiero et al., 2013). The sites in southern Europe exhibit a higher contribution of Dust aerosol type, followed by Mixed-coarse and UI types, due to transport of dust aerosols from the Sahara and Arabian

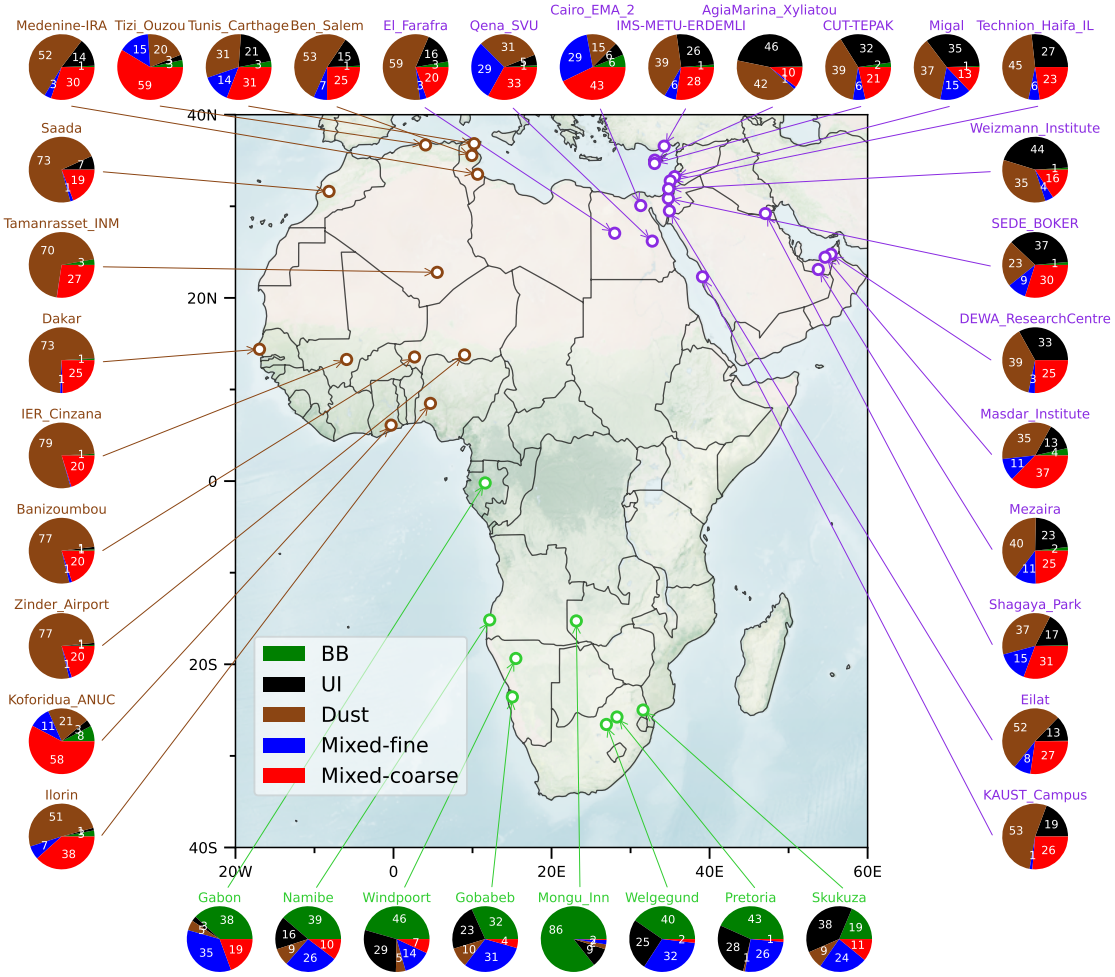

Figure 4.4: *Same as Fig. 4.1, but over North Africa (brown), South Africa (green), and the Middle East (magenta).*

Deserts through the Mediterranean Sea which get mixed with urban pollution resulting in lower AE and SSA compared to the sites in northern Europe (Floutsi et al., 2016; Ansari & Ramachandran, 2025b) (Figs. 3.4, 4.3). However, the contributions of dust and mixed aerosol types decrease from southern to northern European sites, and the UI type becomes the dominant aerosol type (>40%) due to the presence of urban populated and industrial sites in northern Europe. In addition, a small contribution of BB aerosol type is also observed mostly in the northwest European sites, which is the result of anthropogenic agricultural residue burning, and forest and peat fires (Filonchyk et al., 2020).

Due to the presence of the Sahara Desert in North Africa and Arabian Deserts in Middle East, respectively, the contribution of Dust aerosol type is higher over North

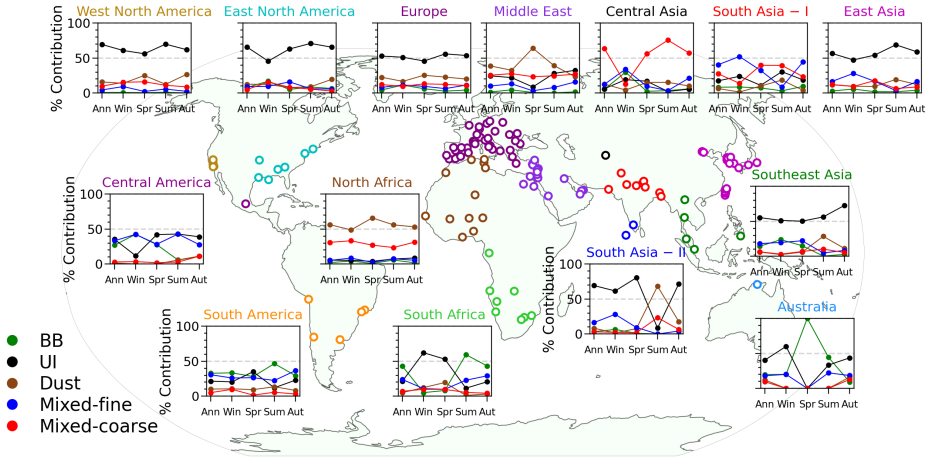

(a)

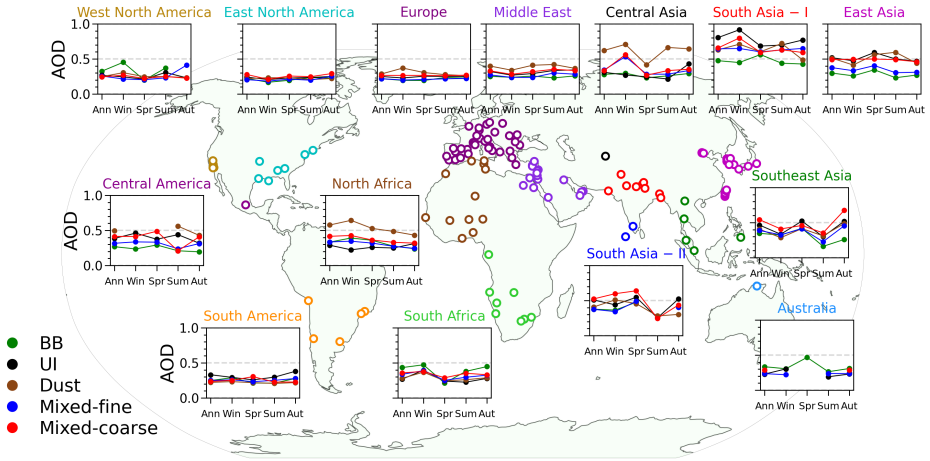

(b)

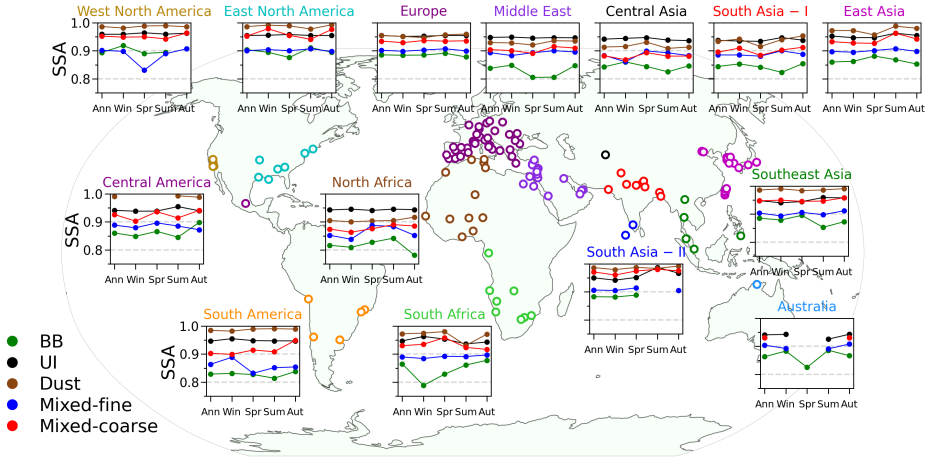

(c)

Figure 4.5: *(a) Annual and seasonal mean % contribution of aerosol types across the globe. Same as (a), but for (b) AOD (at 0.50 μm) and (c) SSA (at 0.44 μm) corresponding to different aerosol types.*

Africa (regional mean: >50%) and Middle East (>30%) throughout the year, followed by Mixed-coarse aerosol type (20-30%) (Figs. 4.4, 4.5). The dominance of Dust aerosol type induces the increasing spectral gradient of SSA in the wavelength range of 0.44-0.675 μm over North Africa and Middle East (Fig. 3.7a). This results in a steeper spectral dependence of AAOD and resulting in higher AAE values over these regions (Ansari & Ramachandran, 2025b) (Fig. 3.7b). The contribution of dust aerosols decreases from northern to southern African sites, and BB aerosol type (20-85%) is primarily dominant in South Africa. It is due to the agricultural practices that involve the widespread burning of savannas, woodlands, and forests, and these peak in summer and early autumn (Jouan & Myhre, 2024), which decreases SSA and increases AAOD (Figs. 3.7, 4.5). UI aerosol type is also present over urban sites in the Middle East and South Africa due to aerosol emissions from industry and fossil fuel combustion (Fig. 4.4).

4.2 Absorbing aerosol types

The distinct characteristics of spectral SSA and size parameters of different absorbing aerosols (e.g., BC, BrC, and dust) can be utilized to potentially identify the dominant absorbing aerosol types using remote sensing and in situ measurements. Previous studies have utilized several combinations of predictors of two aerosol optical parameters from AERONET observations and created a 2-D identification cluster space to classify absorbing aerosol types by choosing threshold values such as $FMF_{0.50}$ vs. Ångström exponent ($AE_{0.44-0.87}$) (Bibi et al., 2017; Rupakheti et al., 2019; Ali et al., 2020; Ramachandran & Rupakheti, 2022b; Ansari & Ramachandran, 2023b), $FMF_{0.50}$ vs. $SSA_{0.44}$ (Lee et al., 2010; Bibi et al., 2017; Rupakheti et al., 2019; Ali et al., 2020), $FMF_{0.50}$ vs. absorption AE ($AAE_{0.44-0.87}$) (Kedia et al., 2014; Bibi et al., 2017; Rupakheti et al., 2019; Ali et al., 2020), $AAE_{0.44-0.87}$ vs. extinction AE ($AE_{0.44-0.87}$) (Giles et al., 2011; Kedia et al., 2014), $AE_{0.44-0.87}$ vs. $SSA_{0.44}$ (Logothetis et al., 2020), and $AE_{0.44-0.87}$ vs. single scattering co-albedo (1-$SSA_{0.44}$) (Logan et al., 2013). Some major drawbacks associated with the 2-D identification space are that in some spaces, either SSA was not included or, if it was included, it was only for a single wavelength, and the threshold limits of classified absorbing aerosol types in some spaces overlapped with each other, thereby reducing the accuracy of those classification schemes and the classified types. Further, none of these classification schemes includes absorbing CA (= BC + BrC). The previous studies applied the respective classification scheme over a few particular sites and/or a

region, however, when applied globally, a large fraction of aerosols remained unidentified over many sites, indicating that the applicability of these classification schemes is restrictive and valid only over a particular region. About 35% of the absorbing aerosol types remained unidentified globally in a previous study (Tian et al., 2018) that used the combination of spectral SSA and AE for aerosol classification (did not contain CA in its classification scheme), and furthermore, the unidentified type fraction was even higher over many sites. A new classification scheme is developed that overcomes the limitations and the uncertainty in the traditional classification methods for absorbing aerosol types, which contributes a large uncertainty in aerosol radiative effect estimates.

4.2.1 Classification scheme of absorbing aerosol types

The SSA indicates the magnitude of aerosol absorption. BC, the strongest absorber per unit mass, has higher absorption in the near-IR range, and its spectral SSA shows a decreasing gradient over regions where BC is the dominant absorbing aerosol (Giles et al., 2012; Tian et al., 2018). BrC has highly wavelength-dependent absorption and has strong absorption in the near-UV range, which decreases in the visible range (>0.4 μm (Kirchstetter et al., 2004; Jethva & Torres, 2011; Kirillova et al., 2016). Whereas, dust absorption increases in shorter wavelengths (UV and short visible) and decreases in longer wavelengths, and thus, SSA for dust increases with wavelength (Giles et al., 2012; Tian et al., 2018). Distinct spectral variations of SSA of these absorbing aerosols can be used to classify the absorbing aerosol types; however, spectral features of SSA of BrC and dust can overlap with each other due to their similar absorption tendency with their higher values of imaginary part of refractive index (IRI) toward near-UV wavelengths (Schuster et al., 2016; Li et al., 2019). Absorbing CA (= BC + BrC) is mostly present in fine mode, and dust dominates in coarse mode size range (Li et al., 2019). Thus, for the classification of absorbing aerosol types, AE values are first used to segregate fine and coarse mode aerosols (Fig. 4.6). It is important to note that both spectral SSA and AE (exponent of spectral AODs) are independent of each other, which are used here to determine the thresholds of AE values for fine and coarse mode aerosols to enable the classification of various absorbing aerosol types.

Long-term (2000-2019) datasets from a total of 32 reference AERONET sites, characterized by different dominant aerosol types (6 sites for dust, 9 sites for UI, 10 sites for BB, and 7 sites for mixed type) are utilized to develop the classification scheme

Table 4.1: *Reference AERONET sites and their dominant aerosol types, the data of which were obtained during 2000–2019, are used for classifying the different absorbing aerosol types (Fig. 4.6). Numbers of data points are given in bracket for each aerosol type.*

Aerosol type	AERONET Sites
Dust (16907)	Banizoumbou, Solar_Village, Dakar, Zinder_Airport, Tamanrasset_INM, Medenine-IRA
Urban industrial (UI) (5048)	MD_Science_Center, GSFC, LISCO, Georgia_Tech, Mexico_City, Lille, Ispra, Belsk, Leipzig
Biomass burning (BB) (7181)	Abracos_Hill, Alta_Floresta, CUIABA-MIRANDA, Mongu, Mongu_Inn, Skukuza, Lubango, Luang_Namtha, Lake_Argyle, Bonanza_Creek
Mixed (25949)	Kanpur, Beijing, Beijing-CAMS, XiangHe, Anmyon, SEDE_BOKER, Ilorin

(Table 4.1). For the fine mode aerosols, AERONET sites dominated by UI and BB are utilized, and for the coarse mode, dust-dominated AERONET sites are utilized as reference sites for quantifying the threshold value of AE between fine and coarse mode aerosols. Simultaneously, sites dominated by mixed aerosols are used to represent the mixture of fine and coarse mode particles. Selection of these reference AERONET sites with known aerosol types is based on a comprehensive literature review (Giles et al., 2012; Hamill et al., 2016), and these sites provide extensive global and temporal coverages (Table 4.1). The flowchart detailing the methodology developed to classify the different absorbing aerosol types based on the spectral features of SSA and AE is given in Fig. 4.7a. These reference sites for aerosol type (Table 4.1) are used to calculate the AE thresholds for fine and coarse mode aerosols and to explain the classification scheme (Fig. 4.6). The results obtained on absorbing aerosol types from the present scheme are found to be consistent with previous studies (Giles et al., 2012; Hamill et al., 2016; Wei et al., 2024; Zhang et al., 2024).

Based on the cluster density plot between SSA and AE for different dominant aerosol types (Fig. 4.6a), AE threshold values are used for segregating aerosols into different size modes of fine, coarse, and mixture of fine and coarse as:

- *Fine*: AE $\geq$1.4 is used as the threshold which indicates pure 'fine' mode aerosols, as $\sim$90% of data points over the UI and BB dominated sites lie in this range, i.e., an AE value of 1.4 represents the 10^{th} percentile of total data points (12229) in UI and

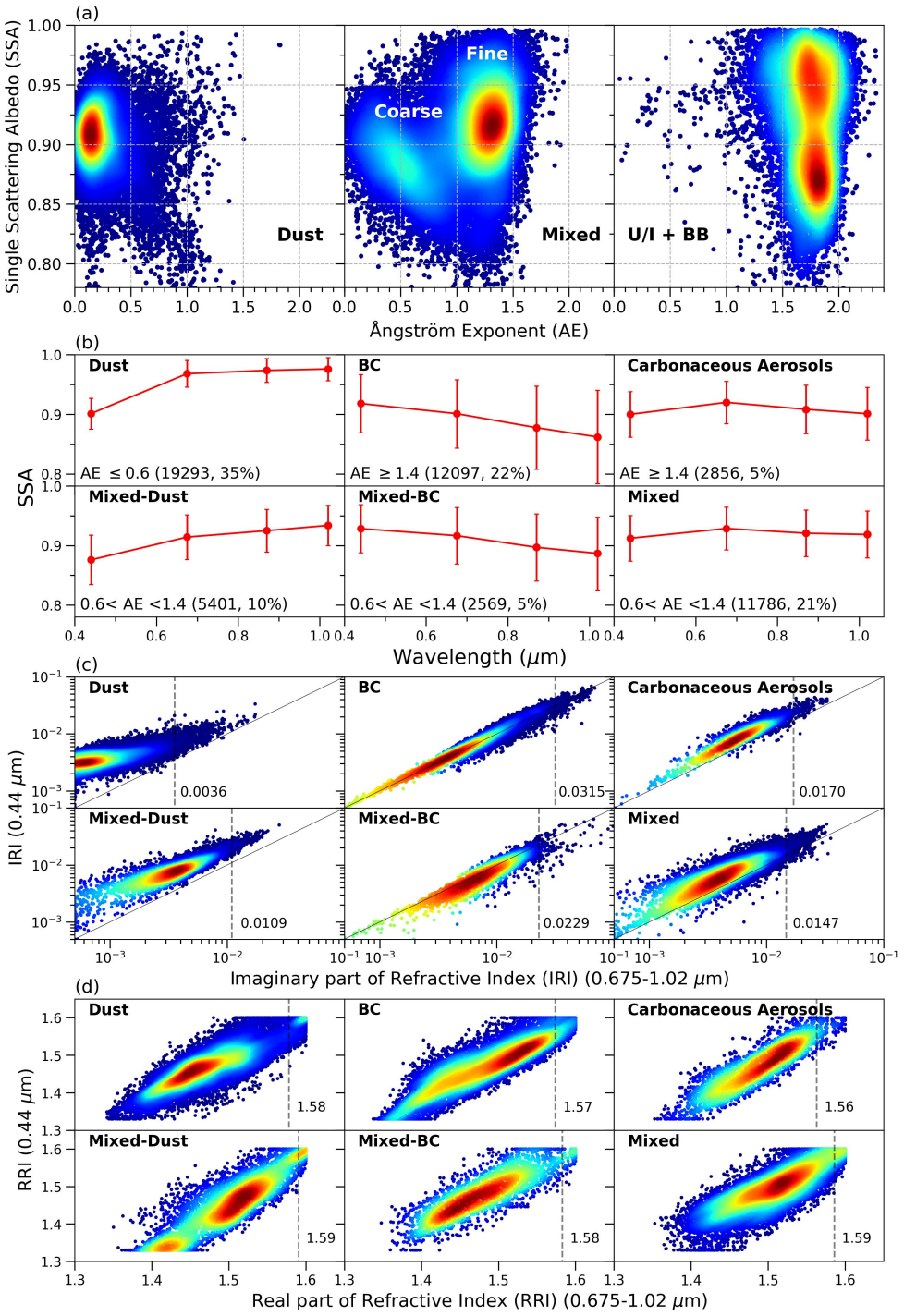

Figure 4.6: *(a) $SSA_{0.44}$ vs. $AE_{0.44-0.87}$ for different aerosol types (Table 4.1). (b) Spectral variation of SSA for the classified absorbing aerosol types from all sites (Table 4.1). Total number of data points and % contribution of each absorbing aerosol type are given in brackets. Variation of (c) imaginary part of refractive index (IRI) at 0.44 μm with average IRI (0.675–1.02 μm), and (d) real part of refractive index (RRI) at 0.44 μm with average RRI (0.675–1.02 μm) for each classified absorbing aerosol type. Vertical dashed lines in (c) and (d) indicate the average IRI and average RRI, respectively, below which 95% of data points lie. Colors in (a), (c), and (d) represent the probability density function computed by kernel density estimation, ranging from lower (blue) to higher (red) density.*

BB-dominated sites.

- *Coarse*: AE $\leq$0.6 is used as the threshold, which corresponds to pure 'coarse' mode

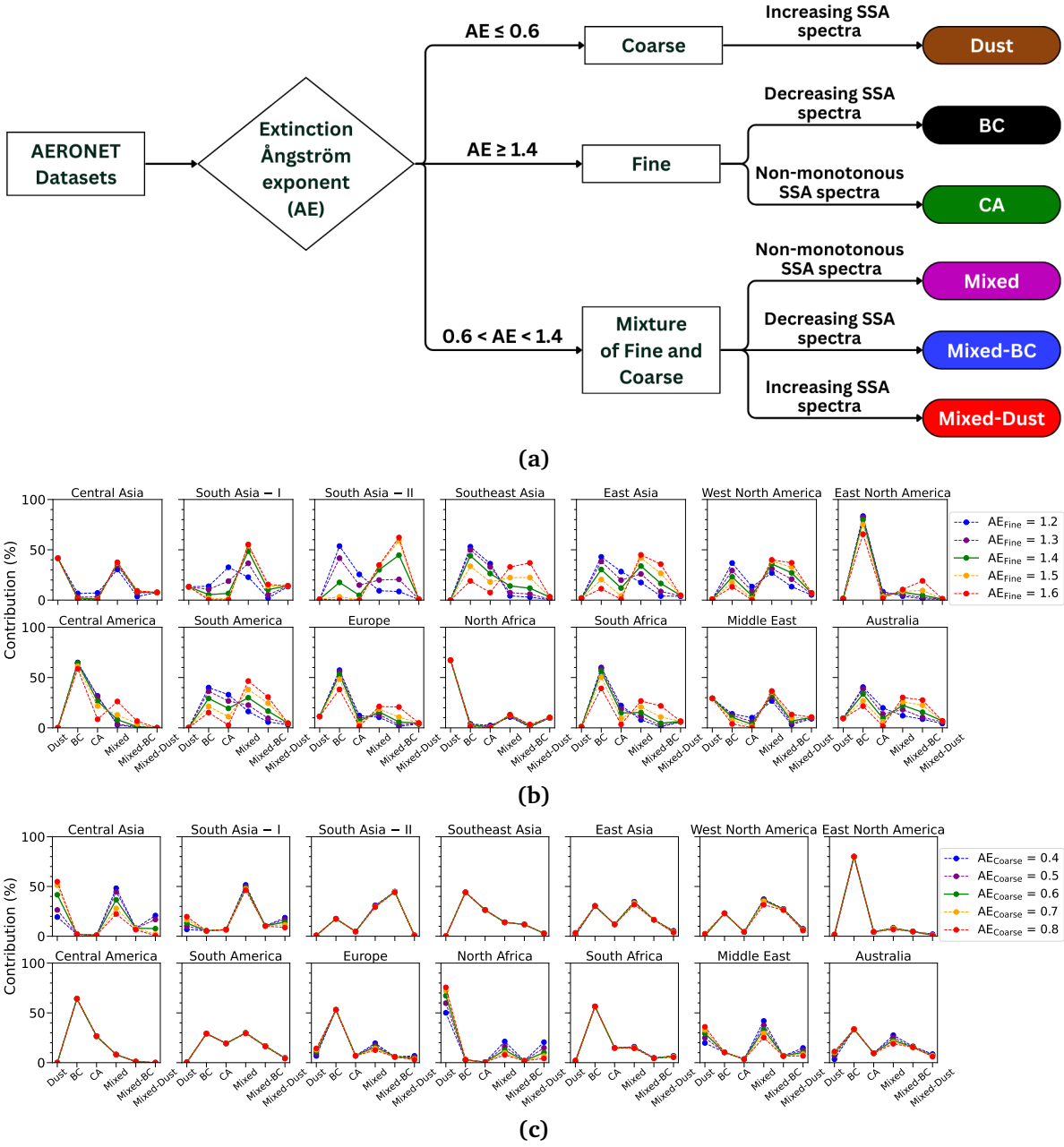

Figure 4.7: *(a) Flowchart for the classification scheme for the identification of absorbing aerosol types of Dust, Black carbon (BC), Carbonaceous aerosols (CA), Mixed, Mixed-BC, and Mixed-Dust by utilizing the extinction Ångström exponent (AE) (for segregating in fine, coarse, and mixture of fine and coarse aerosols) and spectral feature of single scattering albedo (SSA). Regional variation of the contributions of absorbing aerosol types after varying AE for fine (AE_{Fine}) (b) and coarse (AE_{Coarse}) mode aerosols (c) by $\pm$0.1 and $\pm$0.2 from their actual values of 1.4 and 0.6, respectively.*

aerosols because they represent ∼90% of data points in dust-dominated sites, i.e., AE value of 0.6 represents the 90$^{\text{th}}$ percentile of total data points (16907) in dust-dominated sites.

- *Mixture of fine and coarse*: AE values between these two thresholds, i.e., 0.6< AE <1.4, represent the mixture of fine and coarse mode aerosols.

These thresholds, based on a long-term dataset, are able to represent and classify most of the aerosol sizes into fine, coarse, and mixture of fine and coarse modes from reference sites (Table 4.1), which increases the robustness of the classification scheme as these thresholds are applicable under varying aerosol compositions. In the first step of the classification scheme, AE threshold values are used for segregating aerosols into different sizes to avoid any overlap between spectral SSA features of BC, BrC, and dust. After classifying the aerosols into fine, coarse, and mixture of fine and coarse, the spectral feature of SSA is used to identify the specific absorbing aerosol type. Since dust aerosols are dominant in coarse mode and exhibit lower SSA at near-UV and short visible wavelength range, uniformly increasing SSA spectra in coarse mode aerosols are classified as absorbing aerosol type of 'Dust'. Similarly, the uniformly decreasing SSA spectra in fine mode aerosols are classified as absorbing aerosol type of 'BC', which follows the spectral feature of BC-dominated region (Giles et al., 2012). A non-monotonous SSA spectra refers to a non-uniform increase or decrease in SSA with wavelength. For CA, SSA spectra do not uniformly decrease because of lower SSA at shorter wavelengths (e.g., at 0.44 μm) due to the presence of BrC. Therefore, decreasing SSA spectra in longer wavelength (due to BC absorption) with a bending/decrease of SSA at 0.44 μm (due to BrC absorption) exhibit a non-monotonous SSA spectra in fine mode (AE $\geq$1.4) for CA absorbing aerosol type. In the mixture of fine and coarse aerosols (0.6< AE <1.4), all absorbing aerosols can be present simultaneously. However, the spectral features of SSA reflect the dominance of a particular absorbing aerosol in mixed aerosols. In this range of AE, non-monotonous SSA spectra are classified as 'Mixed', representing a mixture of all absorbing aerosols emitted from various sources. Whereas for the same range of AE, uniformly increasing SSA spectra represent 'Mixed-Dust', where dust is dominant in the mixed aerosols, and decreasing SSA spectra represent 'Mixed-BC', where BC is dominant in the mixed aerosols.

A lower IRI in 0.675-1.02 μm (k_{nir}) (0.0036) in Dust absorbing aerosol type reveals lower absorption in higher wavelengths and higher absorption only at 0.44 μm

as most of the data points are above 1:1 line in dust type (Fig. 4.6c). Whereas, for Mixed, Mixed-Dust, and CA types, the dense core area of k_{nir} lies in a higher range, which shows that the absorption of these types is relatively higher than that of the Dust absorbing aerosol type in the 0.675-1.02 μm wavelength range. Dust type encompasses relatively lower absorbing aerosols (higher SSA) and lower spectral real part of refractive index (RRI), likely associated with aerosol hygroscopic growth in high relative humidity levels (Fig. 4.6d) (Chen et al., 2013; Zhou et al., 2023). For BC type, IRI is higher for all wavelengths (k_{nir} = 0.0315), and most of the points are around 1:1 line. Thus, it is clear that this new scheme is able to classify different absorbing aerosol types using the spectral feature of SSA and the size distribution of various absorbing aerosols, and their magnitude of absorption (spectral IRI values) matches well with the intrinsic absorbing characteristics of different absorbing aerosols present in each absorbing aerosol type.

The classification scheme is based on the spectral variation of SSA in particular AE ranges, which depends on the relative differences in SSA across wavelengths rather than its absolute value. Since the error in SSA ($\pm$0.03) is the same in each wavelength, the overall change/difference in spectral SSAs will remain unaffected by its error. Consequently, this uniform error in spectral SSA is not expected to affect the outcomes of the classification scheme. Sensitivity tests were conducted to assess the influence of the selected aerosol parameters in the classification scheme. In these tests, the AE values for fine-mode (1.4) and coarse-mode (0.6) aerosols were individually adjusted by $\pm$0.1 and $\pm$0.2 (Figs. 4.7b, 4.7c). The results indicate that adjusting the AE for fine-mode aerosols by $\pm$0.2 substantially alters the contribution of BC, CA, Mixed, and Mixed-BC types. These changes are particularly pronounced over regions in Asia, where fine-mode aerosols dominate. In contrast, adjustments in the AE for coarse-mode aerosols primarily affect the dust type, with noticeable impacts confined to dust-dominated regions such as Central Asia, North Africa, and the Middle East. Overall, the sensitivity tests reveal that the classification scheme is considerably more sensitive to adjustments in the AE for fine-mode aerosols than for coarse-mode aerosols. Given this sensitivity, the careful selection of AE thresholds for fine-mode aerosols is crucial to ensure the accuracy and consistency of the classification scheme. Furthermore, it is noteworthy that even after varying the AE thresholds within the tested ranges, the global mean contribution of unidentified aerosol types remained <4%. However, expanding the applicability of

this new classification scheme to background aerosol environments would be certainly valuable. This could become feasible in the future, when the uncertainty in SSA retrievals under low-AOD conditions is reduced to the same as that of the uncertainty in AOD ($\pm$0.01-0.02), through advancements in inversion algorithms and observational capabilities.

The global mean of absorbing aerosol types is computed as the mean of 14 regional averages, ensuring equal weight is assigned to each region to minimize the bias in global assessments caused by the comparatively dense network of sites in Europe and North America (Fig. 4.8a). Further, it is found that the seasonal variabilities in aerosol properties (e.g., AOD, SSA) over the high-latitude sites in East North America and Europe are found to be low and not statistically significant (Ansari & Ramachandran, 2024a, 2025b). Thus, the uneven temporal sampling (e.g., limited winter data in high-latitude sites) is not expected to affect the reliability of seasonal comparison. Absorbing aerosol type of BC dominates on a global scale as the single largest type contributing $\sim$30% or more throughout the year, followed by Mixed and Mixed-BC types. BC and the associated types, including the CA, dominate the global aerosol absorption type ($\geq$70%) while Dust and Mixed-Dust types contribute the rest during the year (Fig. 4.8a). The absorption due to Dust type contribution increases in spring and summer to 15% when these particles increase. On a global-mean scale, the annual- and seasonal-mean contributions of different absorbing aerosol types are quite similar (Fig. 4.8a), varying within 10% between seasons.

The spectral variation in SSA of aerosol species, which is significantly different, becomes useful for defining the slope threshold of SSA in the two bands for the respective aerosol absorbing types. Dust absorption is higher only in shorter wavelengths (lower SSA), which steeply decreases in longer wavelengths, whereas BC absorption monotonically increases (lower SSA) as a function of wavelength in the entire shortwave regime. Thus, when the difference in SSA between two consecutive wavelengths in the 0.44–1.02 μm range is positive, and the increase in SSA from 0.44 μm to 0.675 μm is $\geq$0.03 the aerosols are identified as Dust and Mixed-Dust types when AE is $\leq$0.6 and 0.6 $<$ AE $<$ 1.4, respectively; when the difference in SSA between two consecutive wavelengths in the 0.44–1.02 μm range is negative, they are classified as BC and Mixed-BC types when AE is $\geq$1.4 and 0.6 $<$ AE $<$ 1.4, respectively. However, the magnitude of decrease in spectral SSA for BC and Mixed-BC types is found to be lower than the

increase in spectral SSA for Dust and Mixed-Dust types (Fig. 4.6b) (e.g., Dubovik et al. (2002)). This happens due to the differences in the intrinsic absorption characteristics of dust and BC aerosols as the imaginary part of refractive index (signifying absorption) for BC and Mixed-BC types is nearly spectrally invariant, whereas it is higher in shorter wavelengths for Dust and Mixed-Dust types (Fig. 4.6c). As a result, the increase in spectral SSA for Mixed-Dust is higher than the decrease in spectral SSA for Mixed-BC type. As the decrease in spectral SSA for Mixed-BC type is <0.03 defining a threshold is challenging in contrast to Mixed-Dust type for which the increase in spectral SSA is $\geq .03$ (Fig. 4.6). Therefore, a sensitivity analysis was performed by varying the thresholds in the interval of 0.01 from 0.01 to 0.03 in spectral SSA from 0.44 μm to 1.02 μm for BC and Mixed-BC types (Fig. 4.8b) and not for Dust and Mixed-Dust types due to the reasons stated above. Results reveal that the contributions of BC and Mixed-BC types change, and their values decrease (by $\sim$11% and $\sim$5%, respectively) as the threshold value increases, while the contribution of unidentified type increases at the same time. However, the contribution of unidentified type is only $\sim$18% on a global scale even for a high threshold value of 0.03, which is still significantly lower than the unidentified type computed in previous methods (Bibi et al., 2017; Tian et al., 2018; Rupakheti et al., 2019; Ali et al., 2020), proving the robustness of the new classification scheme. Thus, it is clear from this analysis that any risk in classification due to instrument error or SSA uncertainty ($\pm$0.03), (a) only the contributions of BC, Mixed-BC, and unidentified type will be impacted and not the Dust and Mixed-Dust types, and (b) even in that scenario, the percentage of identified absorbing aerosol types ($>$80%) is still significantly higher than the unidentified type ($<$20%). This approach ensures a robust classification of absorbing aerosol types while accounting for both aerosol size distributions and spectral SSA characteristics. The microphysical model used in the AERONET inversion algorithm is a homogeneous internal mixture of different aerosols. It assumes all particles have the same complex refractive index, which is equivalent to assuming all aerosol species are internally mixed. Therefore, all the mixed absorbing aerosol types correspond to internally mixed. It should be noted that for both cases of internally and externally mixed aerosols, no significant errors were observed in the AERONET retrieval of SSA (Dubovik et al., 2000).

One of the limitations of the current classification scheme is that it may not be applicable for low AOD conditions ($<$0.2) due to the higher uncertainty in AERONET

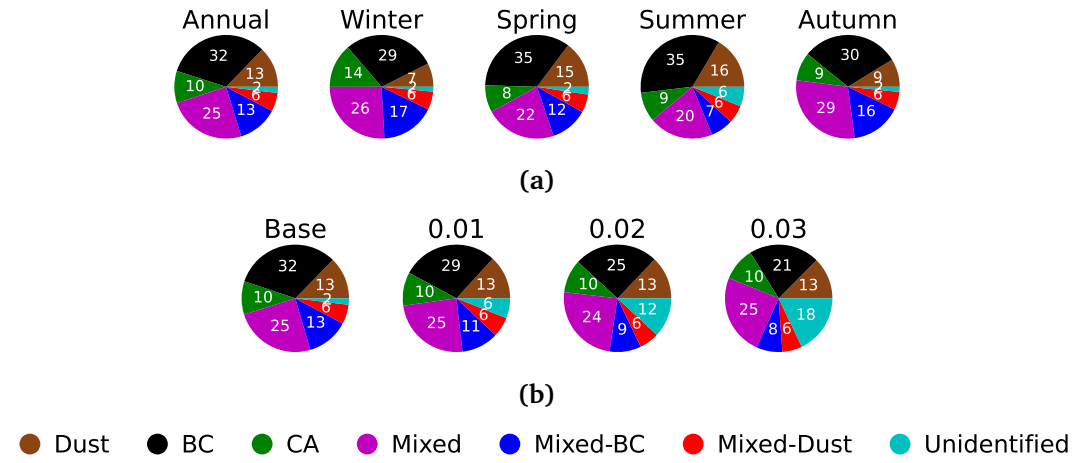

Figure 4.8: *(a) Global annual mean contribution (%) of classified absorbing aerosol types on annual and seasonal scales. (b) Change in global annual mean contribution of absorbing aerosol types (Dust, Black carbon (BC), Carbonaceous aerosols (CA), Mixed, Mixed-BC, and Mixed-Dust) by varying the threshold for a consistent decreasing trend of spectral SSA from base value (>0) to 0.01, 0.02, and 0.03.*

SSA retrievals. It is important to note that in cleaner regions (e.g., remote oceans or polar areas), the abundance of absorbing aerosols is significantly low, with aerosol populations dominated by scattering aerosols (e.g., sea salt). Consequently, the SSA values in these regions tend to be higher, with minimal spectral variation due to the lack of significant absorbing aerosol presence. As a result, classifying marine aerosols over oceanic sites, which exhibit high SSA (∼1), low AOD and AE resulting from their larger particle sizes, poses a challenge (Dubovik et al., 2002; Russell et al., 2014). Since the primary objective of our classification scheme is to classify absorbing aerosol types, applying this method in cleaner regions, where absorbing aerosol contributions are insignificant, would not provide meaningful or representative results. Therefore, the exclusion of low AOD conditions does not compromise the representativeness of results in these regions.

Using this classification scheme, nearly all the known absorbing aerosol types are identified, and the contribution of the unidentified is quite small (mean: ∼2%) (Fig. 4.8). However, contribution of unidentified type can be higher for a specific site, but overall, even in those sites, contribution of the unidentified type is <10% (Figs.4.9-4.12). In contrast, previous methods, using 2-D space with threshold discrimination (Bibi et al., 2017; Rupakheti et al., 2019; Ali et al., 2020), reported a much higher unidentified type contribution, reaching ∼30% at a few sites in Saudi Arabia (Ali et al., 2020) and the global average of unidentified type was estimated to be ∼50%. Similarly,

the unidentified type contribution was estimated to be ∼35% in another method (Tian et al., 2018). In stark contrast, our classification scheme integrates AE with spectral SSA criteria, ensuring that the classification criteria for different absorbing aerosol types do not overlap with each other and reduces the unidentified type to almost nil (∼2%) on a global scale. Thereby, this integrated use of AE and spectral SSA overcomes the drawbacks of previous methods and provides a much better and robust quantification of different absorbing aerosol types (Ansari & Ramachandran, 2025a).

4.2.2 Global distribution of absorbing aerosol types

The absorbing aerosol types show quite distinct spatial and seasonal variabilities (Figs. 4.8-4.13). Dust type is dominant over Central Asia (42%) and western South Asia – I, as the observation sites in these regions are located near dust sources (Fig. 4.9). Dust contribution is higher (∼60%) during summer over Central Asia due to dust transport (Fig. 4.13a). Dust type contribution gradually decreases from west to east IGP. However, the Mixed type increases over the central and east IGP region and becomes the dominant type (∼50%), followed by Mixed-BC type due to high human influenced emissions along with the seasonal (spring and summer) transport of dust (Ramachandran et al., 2020a; Ansari & Ramachandran, 2024b). It may be noted that an independent validation of the present classification scheme using in situ chemical composition measurements is challenging for several reasons. First, most available in situ studies are based on surface-level measurements, while vertical columnar observations, which are more relevant to our classification based on column-integrated aerosol properties, are limited. This makes direct comparison between in situ surface and columnar measurements infeasible. Secondly, absorbing aerosols typically constitute a minor fraction of total aerosol loading, making it difficult to obtain detailed number concentration (more directly linked to columnar extinction over mass concentration) measurements for individual absorbing species from existing studies. However, results from this classification scheme are compared with previous classification methods and Generalized Retrieval of Atmosphere and Surface Properties (GRASP)/Component retrieved columnar mass concentration using the AERONET dataset, and the results are found to be consistent, supporting the reliability of our methodology as detailed below. The present findings are consistent with mixed aerosol type found over the IGP derived using previous classification schemes (Giles et al., 2012; Hamill et al., 2016; Wei et al., 2024). It also

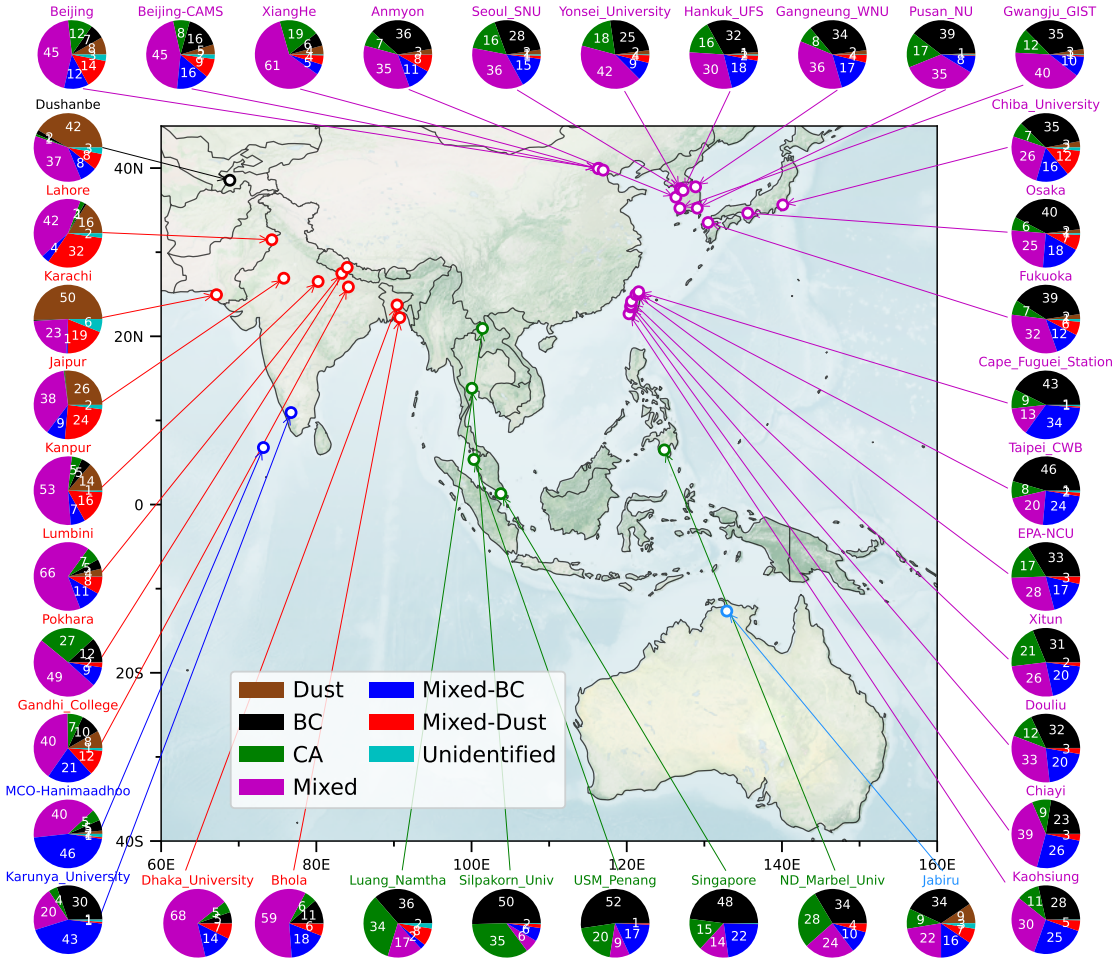

Figure 4.9: *Annual mean contributions (%) of different classified absorbing aerosol types (Dust, Black carbon (BC), Carbonaceous aerosols (CA), Mixed, Mixed-BC, and Mixed-Dust) shown by pie charts over all selected sites in Central Asia (black), South Asia – I (red), South Asia – II (blue), Southeast Asia (green), East Asia (magenta) and Australia (cyan).*

aligns with high columnar mass concentrations of all absorbing aerosols over IGP retrieved from the GRASP/Component algorithm (Zhang et al., 2024). On a regional scale, Mixed type is dominant over South Asia – I annually (∼50%), and the contribution of Dust type (∼30%) increases during spring and summer due to the transport of dust aerosols by strong westerly winds (Fig. 4.13a) (Ramachandran et al., 2020a; Ansari & Ramachandran, 2024b). In South Asia – II, the contribution of Mixed-BC type is higher in all seasons (40-60%) (except summer due to wet scavenging and suppression of burning activities (Smaran & Vinoj, 2024)). Dust type in South Asia – II increases during summer, and it is negligible in other seasons (Fig. 4.13a).

Forest fires of tropical rainforests and slash-and-burn agricultural activities in

Southeast Asia give rise to significant amounts of CA and BC types in all sites (e.g., Luang_Namtha, Silpakorn_Univ) (Fig. 4.9). Regional contributions of BC and CA types are higher (30-50%) during winter and spring over Southeast Asia due to forest fires and agricultural burning (Reid et al., 2013) (Fig. 4.13a). It is consistent with high columnar mass concentrations of BC and BrC found over Southeast Asia (Zhang et al., 2024). In addition, a significant amount of BC type (∼50%) is observed over urban-populated sites such as Penang and Singapore in Southeast Asia. Mixed absorbing aerosol type is dominant (35-60%) over western sites in East Asia (e.g., East China) as these sites are affected by dust aerosols from the Gobi and Taklamakan deserts in addition to anthropogenic emissions (Chen et al., 2017), and columnar mass concentrations of all absorbing aerosols are found to be present and higher as well (Zhang et al., 2024). Whereas, BC, Mixed, and Mixed-BC types are present (∼20-45%) with a small contribution of CA type over Taiwan, and this feature is almost similar for all sites in Taiwan. Jabiru (a rural site in Australia) is affected by biomass burning emissions and dust (during summer), which leads to a higher contribution of BC and Mixed types, followed by CA and Dust types (Yang et al., 2021).

The BC type is dominant (>65%) over East North America as most sites in this region are influenced by UI aerosols dominated by fossil fuel emissions, and less by emissions from biomass burning and dust (Fig. 4.10). Mixed type is slightly higher (15%) over central and southeast parts of North America compared to the eastern part of North America, nevertheless, this region is dominated by BC type. On a regional scale, the contribution of BC type exceeds 50% in all seasons over East North America (Fig. 4.13a), which is consistent with a previous study where columnar mass concentration of BC is found to be higher than other absorbing aerosols over the same region (Zhang et al., 2024). The contribution of fine mode aerosols is relatively lower over West North America compared to East North America due to dust transport from arid regions (such as the Mojave and Sonoran deserts), in addition to anthropogenic emissions from urban populated sites (Gkikas et al., 2022; Ansari & Ramachandran, 2024b) (Fig. 3.4). Thus, the contribution of Mixed type, followed by Mixed-BC type, is higher over West North America, and this feature over West North America is consistent in all seasons (Fig. 4.13), revealing the contrast in the dominant absorbing aerosol type between East and West North America (Fig. 4.10). BC and CA types together are dominant absorbing aerosol type with 91% (BC: 64%, CA: 27%) contribution which is consistent

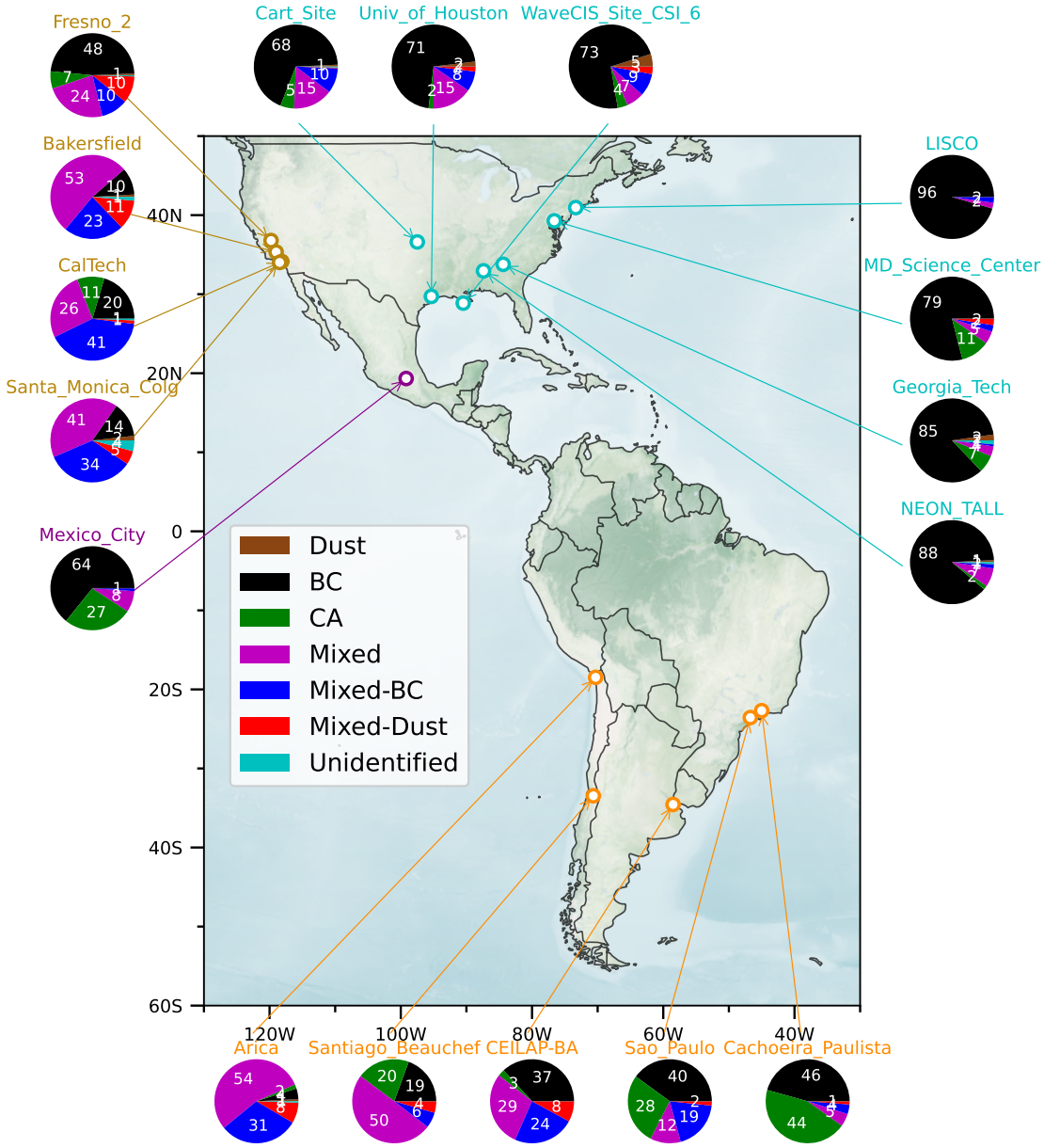

Figure 4.10: *Same as Fig. 4.9, but over East North America (cyan), West North America (brown), Central America (magenta), and South America (orange).*

with aerosol sources over Central America such as from urban and industrial (abundant oil production) emissions, and biomass burning emissions due to forest and agricultural fires occurring during dry period (winter and spring) with its peak emissions in spring (Ríos & Raga, 2018).

In South America, high contributions of BC (∼40%) and CA (∼35%) types are found over Sao Paulo and Cachoeira_Paulista (Fig. 4.10). This occurs due to the impact of local agricultural crop residue burning, and transport of plumes from intense biomass

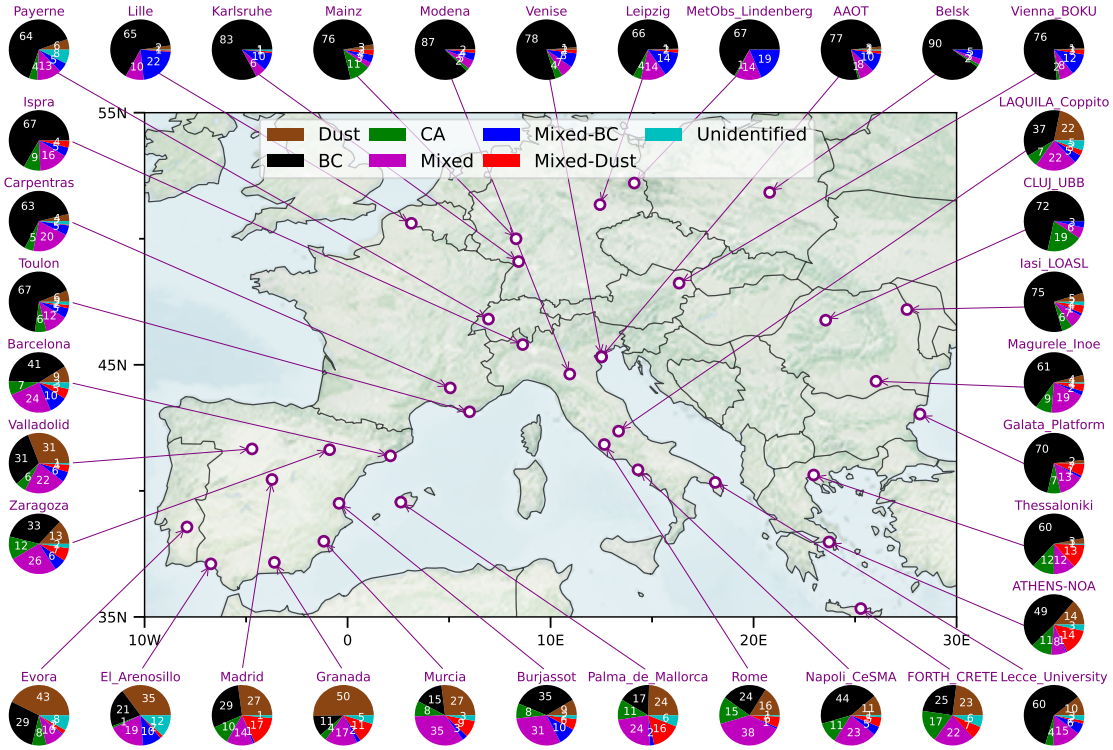

Figure 4.11: *Same as Fig. 4.9, but over Europe.*

burning events such as forest fires from nearby states (especially during the Amazonian dry seasons of summer and autumn), in addition to anthropogenic activities. Capital sites such as Buenos Aires (CEILAP-BA) and Santiago are influenced by anthropogenic emissions and by transport of dust originating from the Puna-Altiplano desert, which becomes more prominent in summer as the subtropical jet stream strengthens (Gaiero et al., 2013). Thus, Mixed, Mixed-BC, and BC types have higher contributions over these capital sites due to aerosols from anthropogenic emissions and dust transport.

The southern part of Europe is majorly affected by Dust type (10-50%), followed by Mixed and BC types, and this feature is more pronounced over southwest European sites (Fig. 4.11). This is due to the transport of dust plumes through the Mediterranean Sea originating from the Sahara and Arabian deserts, and this transport mechanism is more effective during spring and summer (Floutsi et al., 2016). In contrast, in the northern part of Europe, which includes many urban and populated sites, the BC type becomes the dominant type (>60%) due to emissions from urban-industrial activities and forest and grassland fires. Forest and grassland fires over Europe are prominent during summer, which leads to a small annual mean contribution of CA type in most European sites. On a regional scale, the contribution of each absorbing aerosol

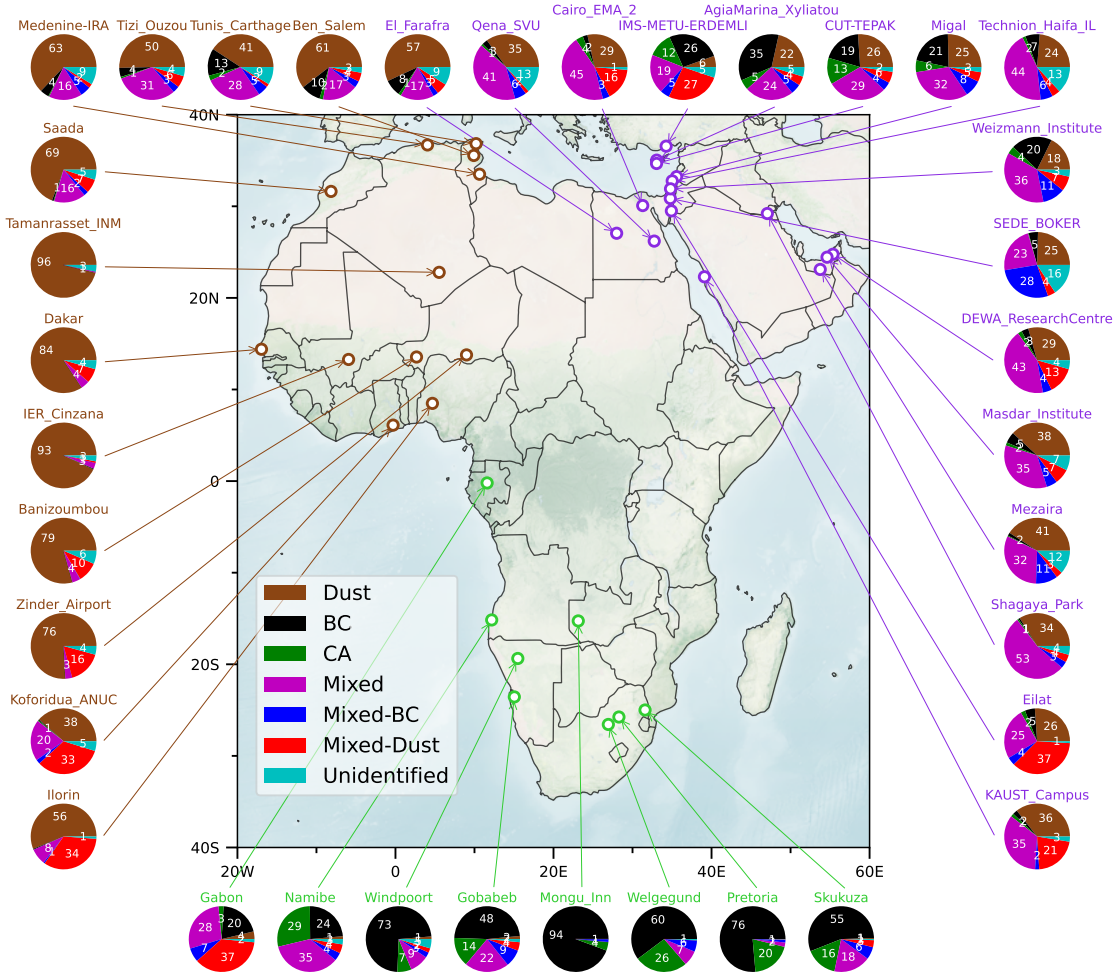

Figure 4.12: *Same as Fig. 4.9, but over North Africa (brown), South Africa (green), and Middle East (magenta).*

type is seasonally less varying, and the BC type dominates in all seasons across Europe (Fig. 4.13a).

The contribution of Dust type is dominant (>50%) over all sites in North Africa in all seasons due to the presence of Saharan desert and its influence (Figs. 4.12, 4.13a). Whereas, the contribution of other types is <20% regionally in each season (Fig. 4.13a). In a few urban sites in northern (e.g., Tunis_Carthage, Tizi_Ouzou) and southern parts (e.g., Ilorin, Zinder_Airport) of North Africa, the contributions of Mixed and Mixed-Dust types, increase respectively. This finding aligns with the generally higher columnar mass concentration of dust over North Africa, along with the presence of BC and BrC in addition to dust at sites located in the southern part of the region (Zhang et al., 2024). BC and CA types are primarily the dominant types in South Africa due to the

widespread agricultural burning involving savannas, forests, and woodlands, and the associated emissions peak in summer and early autumn (Jouan & Myhre, 2024). Aerosol emissions from industry and fossil fuel combustion also increase the amount of BC over urban sites (e.g., Pretoria) in South Africa. Similar to North Africa, Dust type is higher (∼20-40%) over Middle East due to frequent dust storms originating from the Arabian desert (Fig. 4.12). In the Middle East, strong northwesterly winds during summer, driven by high- and low-pressure systems over the eastern Mediterranean and Arabian Gulf, respectively, play a crucial role in dust storms from the Arabian deserts, resulting in a higher contribution of Dust type (Yu et al., 2016) (Fig. 4.13a). However, Mixed type is higher (∼25-50%) over Middle East, and this is due to the mixing of dust with fine anthropogenic aerosols from several industrial emissions (e.g., petroleum, cement), energy generation, and infrastructure (Ali et al., 2020). The dominance of Dust and Mixed type as absorbing aerosol types over Middle East is in agreement with previous studies (Xu et al., 2020; Zhou et al., 2023).

4.2.3 Aerosol characteristics of absorbing aerosol types

In those regions (e.g., East North America, West North America, and Europe) where AOD is lower, the annual mean AODs for most of the absorbing aerosol types are also lower and seasonally less variant (Fig. 4.13b). Over East North America and Europe, BC type is dominant across all seasons (≥45%), and AOD for BC type does not significantly vary seasonally, which shows that aerosol amount due to BC type is almost similar throughout the year. Over North Africa, Middle East, and Central Asia, where dust aerosols are relatively higher due to frequent dust storms, AOD for Dust type is higher compared to other types, and this feature is consistent in all seasons. Similarly, AOD for Dust type over Europe is also higher because the southern part of Europe is impacted by dust aerosols from North Africa and Middle East (Floutsi et al., 2016). AODs of other types over Europe are relatively lower and exhibit less seasonal variability, indicating a more uniform distribution throughout the year. AODs associated with BC and CA types are higher over South Africa, Southeast Asia, and South America during their respective dry seasons (e.g., summer and autumn in South Africa, spring in Southeast Asia, and autumn in South America) when biomass burning activities are at their peak. This seasonal enhancement highlights the strong link between biomass burning and elevated AODs in these regions. It is interesting to note that AODs for each type over South Asia –

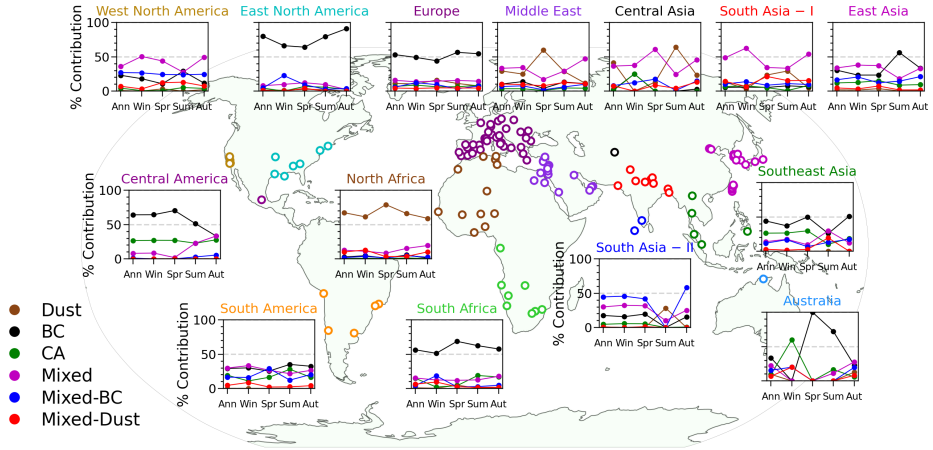

(a)

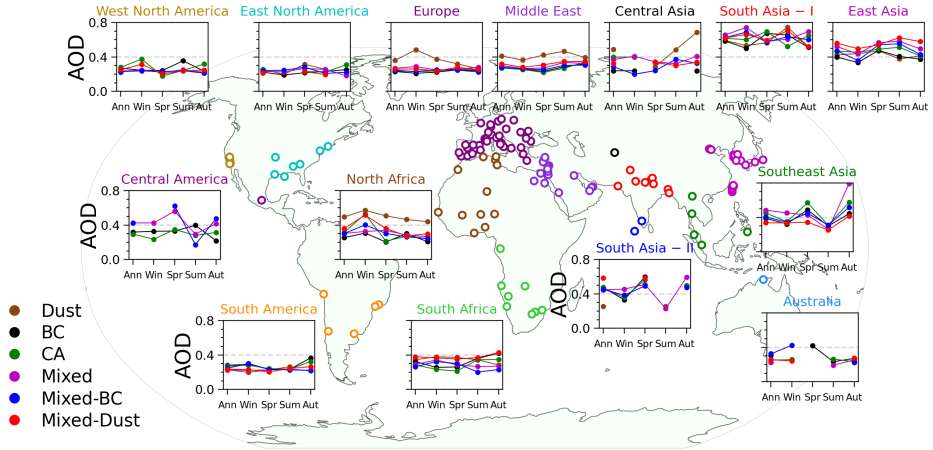

(b)

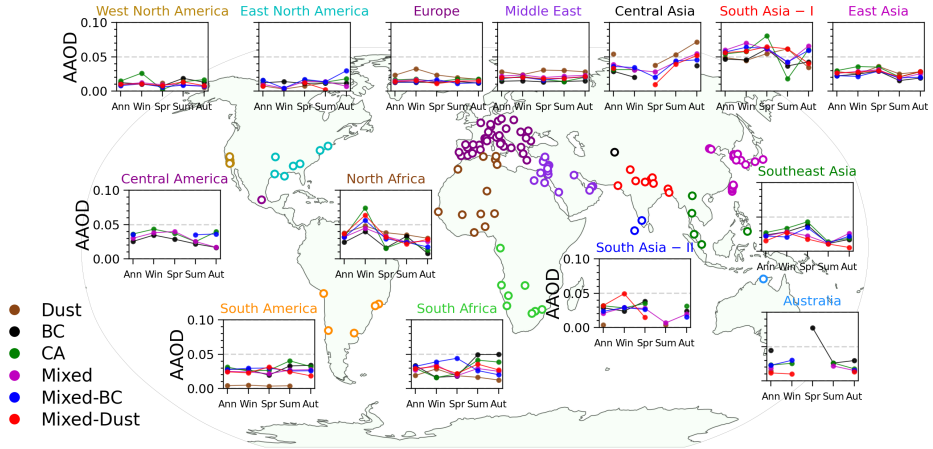

(c)

Figure 4.13: *(a) Annual and seasonal mean % contribution of absorbing aerosol types across the globe. Same as (a), but for (b) AOD and (c) AAOD (at 0.50 μm) corresponding to different absorbing aerosol types.*

I region are >0.4 in every season and reaching up to ∼0.8, due to the consistently high aerosol loading irrespective of any absorbing aerosol type present (Fig. 4.13b). This is

similar over East and Southeast Asia (except summer), where AODs for each type are also higher (>0.3) in each season.

AAOD for each type is lower (mostly <0.02) over West North America, East North America, and Europe (except Dust type) in each season (Fig. 4.13c), suggesting that the columnar amount of absorbing aerosols over these regions is lower not only for the composite aerosols but also for individual types. Both AOD and AAOD for Dust type are higher in Europe, Middle East, and Central Asia, which indicates that dust storm events increase the amount of these aerosols and thereby the absorption (Fig. 4.13). Similarly, AOD and AAOD corresponding to Dust type are also found to be higher over North Africa, where dust storms are more frequent. However, AAODs for CA, Mixed-Dust, and Mixed-BC are higher (>0.05) during winter over North Africa due to an increase in the amount of absorbing CA emitted from intense biomass burning emissions in the savanna of the Sahel and Sudan regions of North Africa and its mixing with dust (Eck et al., 2010). Over Southeast Asia, South Africa, and South America, AODs for BC and CA types and their respective AAODs are higher during dry and biomass burning seasons, respectively. The increase in BC and CA types clearly shows the impact of biomass burning emissions by enhancing aerosol content and their absorption as well. In Asia, AAODs for almost all types decrease during their respective wet periods when precipitation (e.g., wet deposition) is higher (e.g., summer for South, Southeast, and East Asia, and spring for Central Asia). This wet deposition leads to suppression of open biomass burning activities as a result of AAODs, especially of BC and CA types, decreasing significantly (Smaran & Vinoj, 2024).

4.3 Implications

The high uncertainty in the assessment of radiative impact of aerosols by climate models is attributed to the significant variations in optical and physical characteristics of different aerosol types, and aerosol absorption due to their inaccurate characterization – amount and types (IPCC, 2021; Li et al., 2022). In this backdrop, the findings from this global analysis, providing an accurate identification and quantification of different aerosol types and absorbing aerosol types along with their impact on AOD and AAOD based on newly developed classification schemes using high-quality datasets on annual and seasonal scales, are vital. Implementation of these classification schemes in global models (e.g., CAM, GEOS-Chem) can be achieved by integrating the post-processing

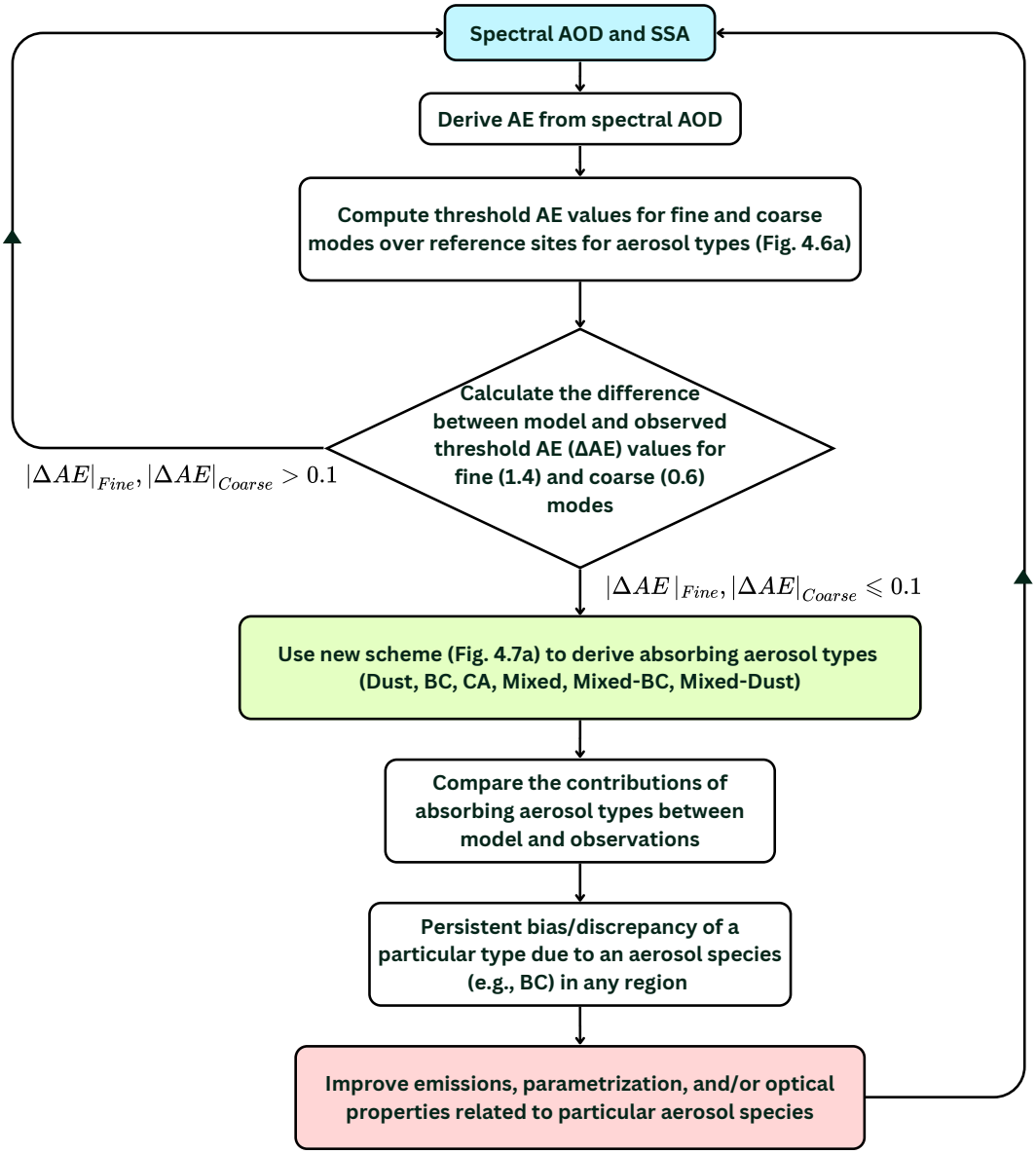

Figure 4.14: *Flowchart illustrating the steps involved in implementing the new classification scheme for identifying absorbing aerosol types in climate models.*

simulation of aerosol types and absorbing aerosol types. To implement both aerosol types and absorbing aerosol types in the models, the simulations of spectral characteristics of aerosol optical properties (e.g., AOD, SSA, g) are required.

A flowchart illustrating the proposed implementation of the new classification scheme for identifying absorbing aerosol types in climate models (Fig. 4.14). It begins with the simulation of spectral AOD and SSA by any climate model, based on their emission inventory for various aerosol species, as well as the associated parameterizations, transport mechanisms, and optical properties defined for each species. Spectral

AOD values are then used to calculate the AE. Next, using a 2-D cluster of SSA and AE values over reference sites or regions for predefined aerosol types, threshold AE_{Fine} and AE_{Coarse} can be computed (Fig. 4.6a). The first criterion is that the absolute difference between the AE_{Fine} and AE_{Coarse} from the model and observation should be <0.01. Threshold AE values and spectral SSA features are now utilized to calculate absorbing aerosol types by utilizing the new classification scheme (Fig. 4.7a). Now, the contribution of different absorbing aerosol types from the model can be directly compared one-to-one with observationally constrained values derived from AERONET. After the comparison, the discrepancies identified between modeled and observed absorbing aerosol types can provide valuable diagnostic insights as to whether they are arising from the differences in the amount of emissions, parametrization (e.g., convection/advection of aerosols), and/or their optical properties. For instance, the persistent bias of BC-dominated types in specific regions can further constrain the range of results and highlights the need to improve sectoral emission factors, parameterizations, and optical properties specifically associated with BC aerosols. In this way, this flowchart provides a structured framework for integrating the proposed classification scheme into global models through post-processing of simulation outputs. It facilitates a one-to-one comparison of model simulated type-wise contribution with observational data and enables the identification of biases for specific aerosol types, ultimately contributing to improved simulation of aerosol characteristics in climate models. By incorporating these observationally constrained absorbing aerosol types, models can dynamically assign more representative spectral SSA and AOD, which will ultimately improve the aerosol radiative effect estimates. These results have yielded quantifiable, useful, and new insights on the spatiotemporal variation and distribution of absorbing aerosol types and their influences on AOD and AAOD (Ansari & Ramachandran, 2025a). This innovative classification approach offers significant potential for advancing research in climate modeling, satellite-based retrieval, and aerosol monitoring applications, for accurately assessing the aerosol-climate interactions, which remain highly uncertain.

4.4 Summary and Conclusions

This chapter provides an extensive analysis of the contribution of different aerosol types and absorbing aerosol types on global and seasonal scales by utilizing new and accurate classification schemes. The major findings are:

1. A new hybrid algorithm is utilized to classify different aerosol types, which integrates machine learning and a density clustering algorithm, incorporating multiple aerosol parameters, which efficiently capture the potential sources of aerosol emissions across the globe. South Asia – I is dominated by Mixed-fine (∼41%), followed by Mixed-coarse (∼27%), UI (∼17%), and BB (∼8%) aerosol type. Whereas UI is a major aerosol type (>50%) over North America, Europe, and East Asia.
2. Contribution of BB aerosol type is relatively higher (>30%) over South Africa, South America, Central America, and Southeast Asia, during their peak fire seasons. Whereas, Dust aerosol type is the predominant aerosol type (∼50%) over North Africa and the Middle East throughout the year.
3. A new classification scheme is developed to classify absorbing aerosol types (Dust, BC, CA, Mixed, Mixed-BC, and Mixed-Dust) by leveraging the spectral characteristics of AOD and SSA of different absorbing aerosols. This method remarkably reduces the contribution of unidentified absorbing aerosol type to almost nil (∼2%) globally compared to >30% in previous methods.
4. South Asia – I is dominated by Mixed absorbing aerosol type (∼50% annually) due to the presence of all absorbing aerosols with elevated Dust type contribution (∼30%) during spring and summer. Similarly, Mixed type dominates the western part of East Asia (35–60%), and it gradually decreases towards the eastern part of East Asia, where BC type has a higher contribution.
5. East North America and Europe (especially the northern part) are mostly influenced by BC type (≥50%) throughout the year, primarily due to fossil fuel combustion from urban and populated sites. Biomass burning emissions amplify the contribution of BC and CA types and significantly enhance the AOD and AAOD over the southern part of North Africa, South Africa, Southeast Asia, and South America during their respective dry seasons.
6. This newly developed classification scheme provides new quantifiable insights on absorbing aerosol types and their influences on AOD and AAOD. Furthermore, a structured framework to integrate this classification scheme into global models through post-processing of simulation outputs is provided, which can contribute to improved simulation of aerosol characteristics in climate models.

5

Aerosol Direct Radiative Effects

The uncertainty linked to the assessment of radiative impact of aerosols is found to be higher over Asia, as the spread in CMIP6 inter-model simulated direct aerosol radiative effect is higher (IPCC, 2021; Li et al., 2022). Thus, simulating aerosol-climate interactions over Asia remains challenging due to evolving emissions, significant spatial heterogeneity, and insufficient observational constraints. Therefore, a global assessment of aerosol radiative effect based on high-quality ground-based AERONET observations is essential for providing accurate observational constraints and for reducing the associated uncertainties in its estimation. Such analysis is particularly critical over Asia, where the magnitude and variability of aerosol amount and aerosol direct radiative effect (DRE) are especially pronounced (IPCC, 2021; Zhang et al., 2022; Ansari & Ramachandran, 2024b, 2025b).

In this chapter, spatial variations of aerosol radiative properties (DRE, DRE efficiency (DREE), and aerosol-induced atmospheric heating rate (HR)) using AERONET datasets on seasonal and annual scales over Asia and other regions of the globe are investigated. The regional performance of MERRA-2 simulated and CERES retrieved DRE (at surface (SFC), top of the atmosphere (TOA), and in the atmosphere (ATM)) with spatiotemporal collocated validations against AERONET retrieved DRE on a global scale is assessed and discussed.

5.1 Global variations of DRE_{TOA}, DRE_{SFC}, and DRE_{ATM}

5.1.1 Asia

The DRE and DREE exhibit significant spatial and seasonal variations, which are directly linked to spatial and seasonal variations in AOD and SSA due to the changes in aerosol

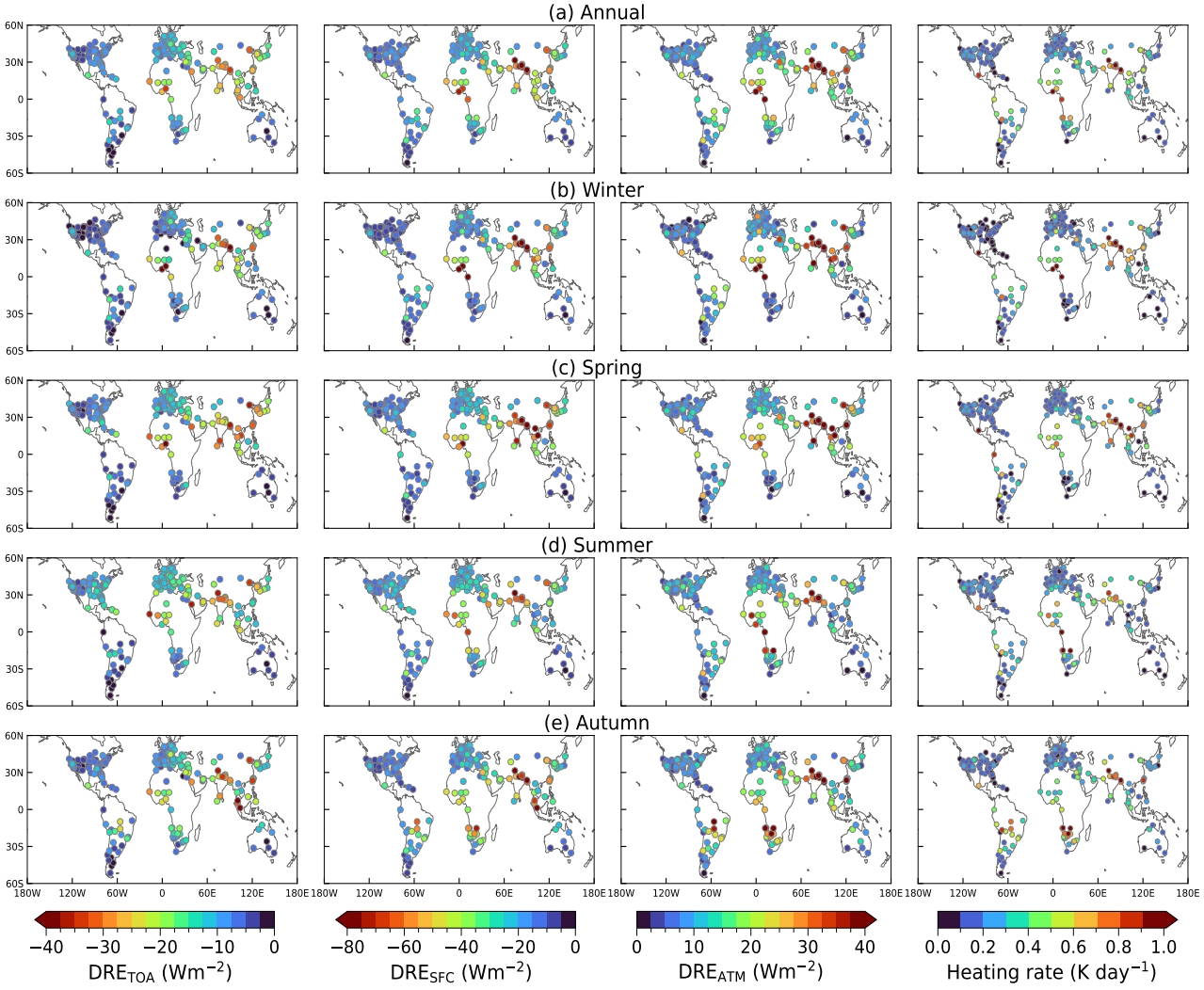

Figure 5.1: *Spatial distribution of aerosol direct radiative effect (DRE; in Wm^{-2}) at the top of the atmosphere (DRE$_{TOA}$) (1st column), surface (DRE$_{SFC}$) (2nd column), and in the atmosphere (DRE$_{ATM}$) (3rd column), and aerosol-induced atmospheric heating rate (K day^{-1}) (4th column) from the AERONET sites across the globe (Table 2.2) on (a) annual, and for (b) winter, (c) spring, (d) summer, and (e) autumn.*

sources, types, and aerosol scattering and absorbing efficiency (Figs. 3.1, 3.4, 3.6, 3.7a, 5.1, 5.3). In Central Asia, the annual mean values of DRE$_{TOA}$ (∼–7 Wm^{-2}), DRE$_{SFC}$ (∼–17 Wm^{-2}), and DRE$_{ATM}$ (∼10 Wm^{-2}) over AIssyk-Kul and Dalanzadgad are relatively lower in magnitude due to low AOD (∼0.12) over these sites. In comparison, DREs (at TOA, SFC, and in ATM) are ∼2 times higher over Dushanbe and their values increase during summer, followed by autumn due to a higher amount of dust aerosols, as it is located in proximity to Taklamakan, Karakum, and Aralkum deserts (Fig. 5.1) (Rupakheti et al., 2020). In South Asia – I, the absolute values of DRE$_{TOA}$ (<–20 Wm^{-2}; goes up to

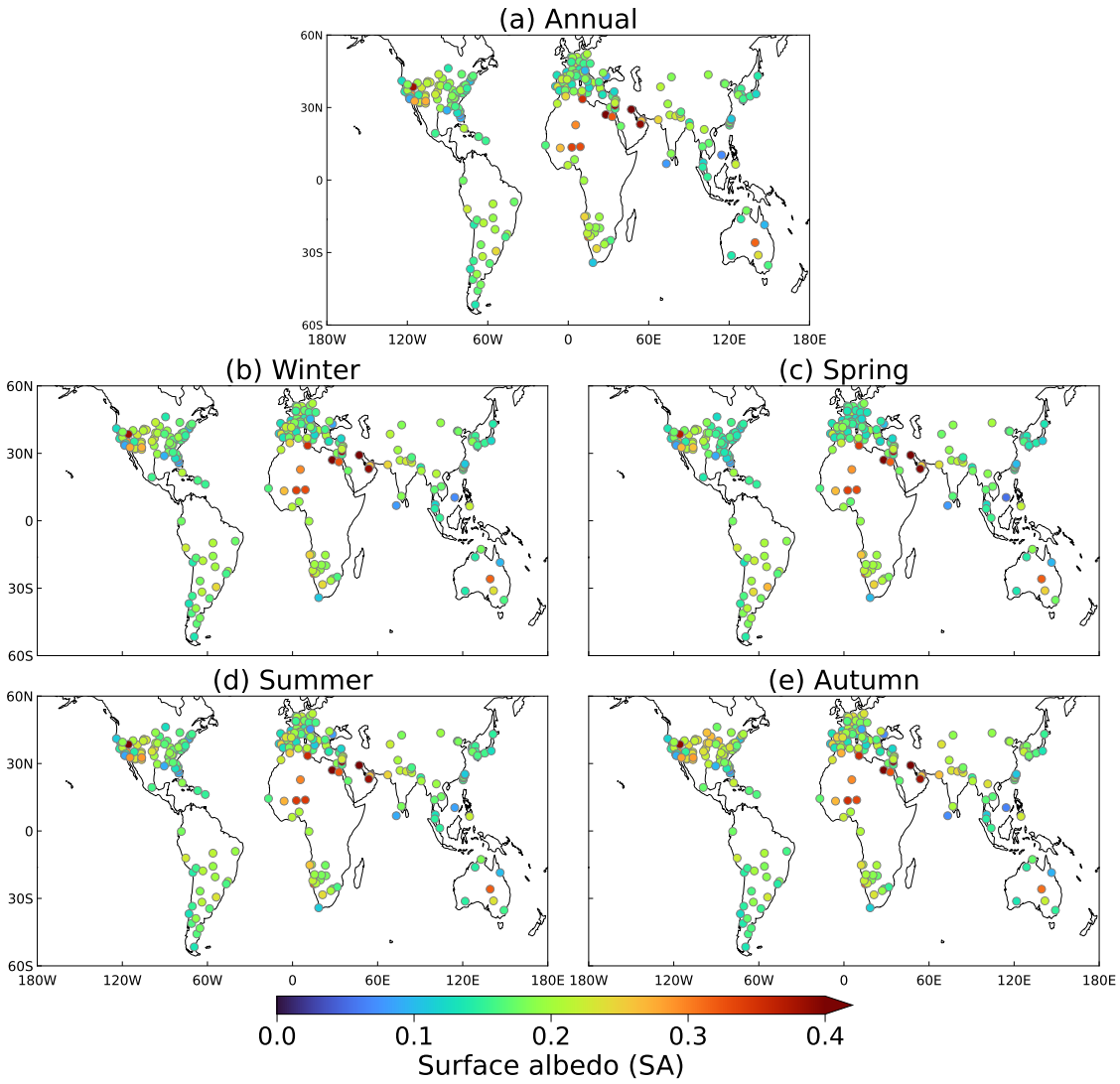

Figure 5.2: *Global distribution of spectral averaged surface albedo (SA) in the wavelength region of 0.44-1.02 μm on (a) annual scale, and for (b) winter, (c) spring, (d) summer, and (e) autumn.*

–45 Wm^{-2}) and DRE_{SFC} (<–50 Wm^{-2}; going up to –120 Wm^{-2}) are significantly high during winter, followed by autumn, compared to most of the sites around the globe (Fig. 5.1). This high aerosol SFC and TOA cooling is due to high AOD (>0.4), dominated by fine anthropogenic aerosols, with SSA of ∼0.90 (Figs. 3.1, 5.1). This high amount of aerosols leads to the suppression of a significant amount of solar radiation reaching the surface and enhances the scattered solar radiation at TOA (more negative), leading to a cooling. Consequently, it also leads to high DRE_{ATM} (>30 Wm^{-2}) and HR (>0.6 $Kday^{-1}$) as aerosols with high AOD and moderately absorbing in nature (SSA: ∼0.90) increase the high solar absorption and aerosol-induced atmospheric heating in the at-

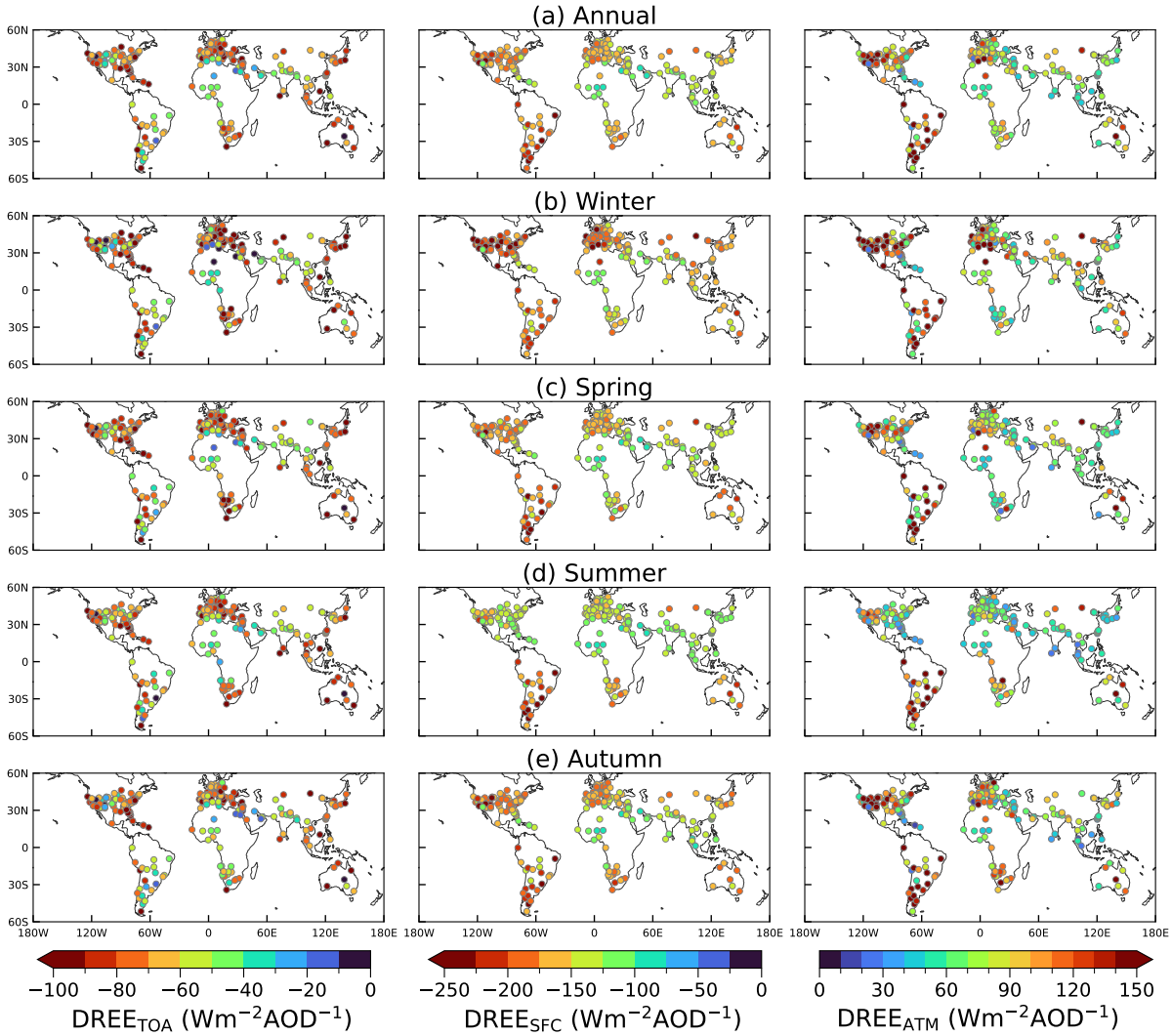

Figure 5.3: *Global distribution of aerosol direct radiative effect efficiency (DREE; in $Wm^{-2}AOD^{-1}$) at top of the atmosphere ($DREE_{TOA}$) (1^{st} column), surface ($DREE_{SFC}$) (2^{nd} column), and in the atmosphere ($DREE_{ATM}$) (3^{rd} column). Results are presented as (a) annual mean and for (b) winter, (c) spring, (d) summer, and (e) autumn.*

mosphere. DRE_{SFC} decreases (in absolute term) during spring, however, it is still <–50 Wm^{-2} (up to –70 Wm^{-2}) due to the increase in mineral dust transported from arid regions (e.g., Thar Desert and Arabian Peninsula) by the prevalence of strong westerly winds, enhancing coarse-mode aerosols (Ansari & Ramachandran, 2024b). However, DRE_{ATM} and HR are relatively lower over South Asia during summer due to higher SSA (Figs. 3.6, 5.1). High SSA during summer is primarily attributed to wet deposition processes that suppress regional and local emissions from biomass burning and forest fires, and the influx of sea salt aerosols from the Arabian Sea (scattering aerosols), further

contributing to higher SSA values (Fig. 3.6). Except summer, DRE_{SFC} (∼–45 Wm^{-2}) and DRE_{TOA} (∼–25 Wm^{-2}) are high over South Asia – II which is attributed to the influx of anthropogenic aerosols (originate from the Indian subcontinent) transported by prevailing northeasterly winds (Ramachandran & Rupakheti, 2020).

In the inland areas of Southeast Asia, Indochinese Peninsula, DREs (DRE_{TOA}: ∼–30 Wm^{-2}; DRE_{SFC}: ∼–75 Wm^{-2}; DRE_{ATM}: ∼45 Wm^{-2}) and HR (∼0.9 $Kday^{-1}$) are significantly higher during spring compared to other seasons (Fig. 5.1). This is attributed to emission of absorbing carbonaceous aerosols (BC and BrC) from intense biomass burning emissions, including slash-and-burn agricultural activities and forest fires, which starts in mid-winter and intensifies in spring (dry season) and leads to high AOD (∼0.73) and low SSA (∼0.89) (Figs. 3.1, 3.6). Similarly, biomass burning emissions are intensified over the Maritime Continent during autumn (dry period) (Nguyen et al., 2019). These emissions and their transport over Malaysia and Singapore by southwesterly winds cause a higher AOD (∼0.5) and increase DRE and HR (Figs. 3.1, 5.1). In East Asia, DRE values are higher over East China compared to South Korea and Japan, which is primarily associated with higher AOD. The transport of dust aerosols over East Asia by westerly winds during spring from the Gobi and Taklamakan deserts also increases the AOD value over East China (Chen et al., 2017). On an annual scale, values of all DREs and HR over East China are ∼2 times higher than over South Korea and Japan (Fig. 5.1).

5.1.2 Other regions of the globe

In North America (except Mexico City), the absolute values of DRE (DRE_{SFC}: ∼–12 Wm^{-2}) and HR (∼0.13 $Kday^{-1}$) are relatively low due to low AOD (<0.1) (Figs. 3.4, 5.1). These values are slightly higher during summer due to relatively higher AOD (∼0.13) than in other seasons, which could be linked to an increase in burned area due to wildfires in boreal regions and the western United States (Ehret et al., 2025). Interestingly, the annual mean DRE_{TOA} over Railroad Valley (located in the Central Nevada Desert) is even positive, where AOD is <0.1, and it is ∼1.5 Wm^{-2} during spring. This occurs due to higher surface albedo (SA: ∼0.40) (Fig. 5.2) which leads to a warming effect at TOA (Chen et al., 2024). In Mexico City (one of the world's largest urban megacities), local air pollution is considerably impacted by intense anthropogenic activities due to dense population, with the combined influence of local meteorological

conditions and surrounding topography (Mensink et al., 2020). On an annual scale, this site experiences high surface cooling (DRE_{SFC}: ∼–38 Wm^{-2}) and high atmospheric warming (DRE_{ATM}: ∼20 Wm^{-2}), and these values slightly increase during the dry period of spring due to forest and agricultural fires (Ríos & Raga, 2018).

In South America, DRE is relatively lower in magnitude during spring and summer. However, intense biomass burning emissions (e.g., forest fire and agricultural burning) in the tropical Amazonia forested region occur during the Amazonian dry season (August–October) with low precipitation and a deeper boundary layer, which significantly increases the amount of absorbing aerosols, leading to high AOD and low SSA (Hoelzemann et al., 2009). It gives rise to high DRE_{SFC} (∼–40 Wm^{-2}) and atmospheric warming (>15 Wm^{-2}; up to 40 Wm^{-2}) and HR >0.4 $Kday^{-1}$ (up to 0.75 $Kday^{-1}$) in the central regions of South America (Fig. 5.1). The southern region of Europe experiences the influence of dust plumes transported from the Sahara Desert through the Mediterranean Sea during spring and summer, which increases the AOD and decreases the SSA values (Ansari & Ramachandran, 2025b). Thus, SFC and TOA cooling are ∼30% higher in these seasons than in other seasons. North Africa and Middle East are mostly influenced by dust aerosols due to the presence of the Sahara, Sahel, and Arabian deserts, which are more prominent in summer, followed by spring (Mortier et al., 2016). Along with dust aerosols in North Africa, the intense biomass burning activities in the savanna regions of the Sahel and Sudan occur during winter and early spring (Eck et al., 2010). This led to high AOD (>0.4) and low SSA (<0.92), which results in high DRE and HR (∼0.5 $Kday^{-1}$) in North Africa, and their values are relatively higher over southern parts of North Africa (Figs. 3.4, 5.1). The proportion of biomass burning aerosols increases over South Africa between July and September primarily due to widespread agricultural burning of savannas, forests, and woodlands (Jouan & Myhre, 2024). During the peak fire season in summer and extending into early autumn, intense biomass burning emissions release substantial amounts of absorbing carbonaceous aerosols, resulting in lower SSA (<0.90) which gives rise to high solar absorption in the atmosphere and result in higher DRE_{ATM} (>15 Wm^{-2}; up to 40 Wm^{-2}) and HR (>0.4 $Kday^{-1}$; up to 1 $Kday^{-1}$) in most sites in South Africa. AOD is the lowest (<0.2) for all seasons in Australia compared to other regions in the globe (Figs. 3.4, 5.4a). The annual mean DRE_{SFC} >–15 Wm^{-2} and DRE_{ATM} <10 Wm^{-2}, and these values slightly increase during autumn due to forest and bush fire over Eastern Australia, and biomass burning over

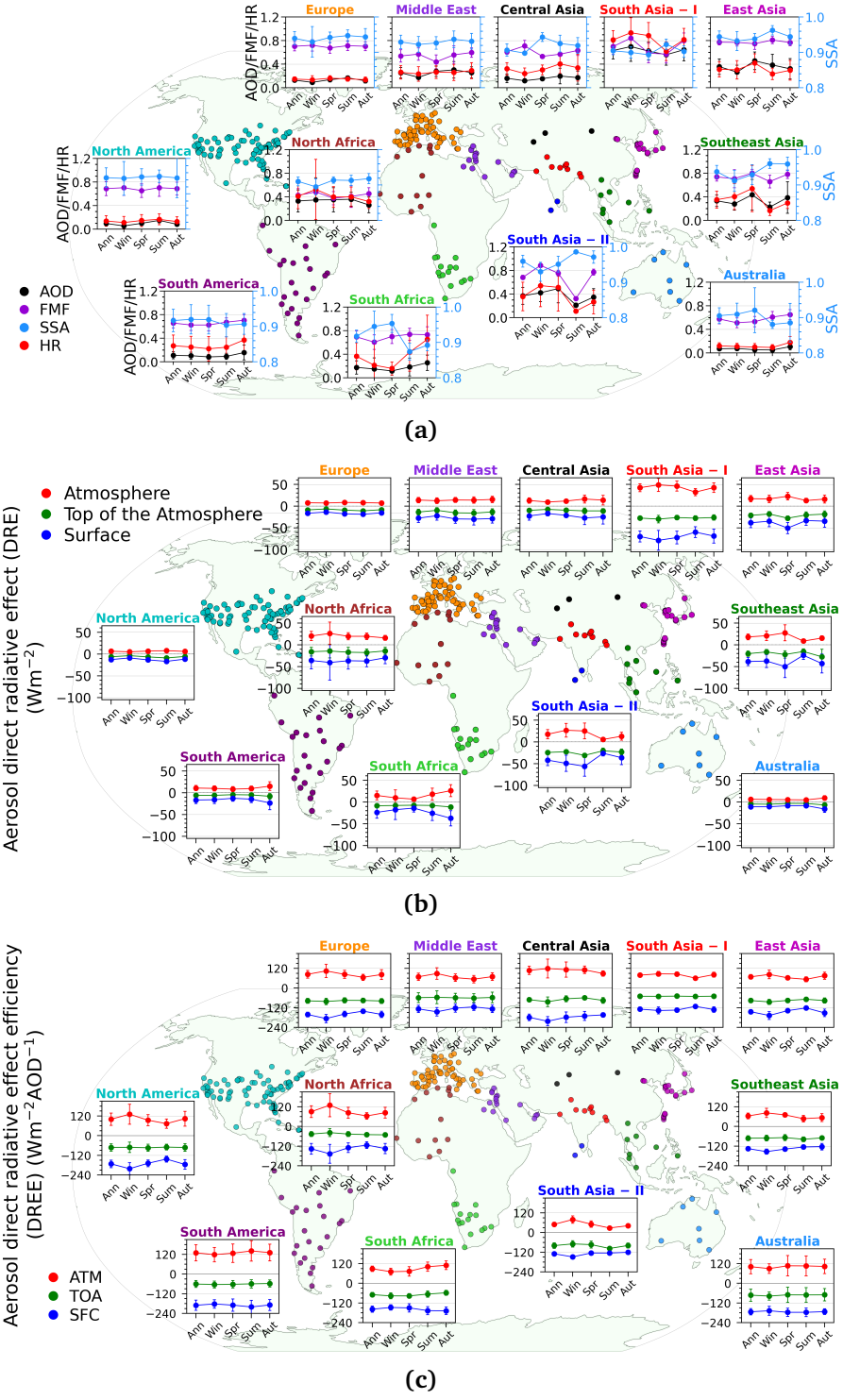

Figure 5.4: *(a) Regional variation of annual and seasonal mean $AOD_{0.50}$, $FMF_{0.50}$, and HR (in Kday^{-1}) (on left y-axis) and $SSA_{0.50}$ (on right y-axis) across the globe. Same as (a), but for aerosol DRE (in Wm^{-2}) and (c) DREE (in Wm^{-2}AOD^{-1}) at SFC, TOA, and in the ATM.*

Northern Australia (Yang et al., 2021).

On the regional scale, AOD, DREs (at SFC, TOA, and in ATM), and HR over North America, Europe, and Australia are ∼2–4 times lower than in Asia with relatively less spatiotemporal variations (Fig. 5.4a, 5.4b) (Ansari et al., 2025). DRE_{TOA} and DRE_{SFC} are the lowest, and DRE_{ATM} and HR are the highest in South Asia – I where DRE_{SFC}, DRE_{ATM}, and HR are ∼2–3 times higher than other regions in Asia (Fig. 5.4). Compared to other regions in the globe, DREs (in absolute terms) and HR are ∼2–6 times higher (varies from region to region) over South Asia – I with statistically significant spatiotemporal variations (p-value <0.05 calculated by Student's t-test), and these values are even more higher during winter. The high values of DREs and HR over South Asia, compared to other regions, are attributed to high AOD (∼0.63) with SSA of ∼0.90 due to a combined contribution from fine mode aerosols produced by intense anthropogenic sources (fossil fuel and biofuel combustion, and biomass and crop residue burning) and the seasonal transport of coarse mode dust aerosols, particularly during spring and summer (Ramachandran et al., 2020a; Ansari & Ramachandran, 2024b). Seasonal cycle of the anthropogenic and natural intense biomass burning activities (e.g., forest fire, wildfire, agricultural burning) contributes to higher seasonal variation in regional mean DRE values over North Africa (in addition to dust aerosols), South Africa, and Southeast Asia. Whereas, the high seasonal variations in regional DRE over South Asia – I, South Asia – II, and East Asia are attributed to the seasonal variations of anthropogenic emissions (e.g., biomass burning, residential heating) and dust storms, along with enhanced wind reversal and wet deposition associated with the regional monsoon (i.e., summer).

Aerosol DREs at each level exhibit substantial variability with changes in AOD and SSA, and the magnitude of this variability depends on the range of AOD and SSA values (Fig. 5.5). For instance, at a constant higher AOD (∼1), a decrease in SSA (e.g., from scattering (≥0.95) to absorbing (<0.90) conditions) significantly reduces the TOA cooling (i.e., less negative DRE_{TOA}), and enhances the SFC cooling (i.e., more negative DRE_{SFC}) and ATM heating (i.e., larger DRE_{ATM}) across all regions. In contrast, for a constant lower AOD (∼0.2), these effects are comparatively weaker, primarily due to lower aerosol loading. The occurrence of TOA warming (i.e., positive DRE_{TOA}) is more frequent for lower SSA (<0.8) over North Africa and Middle East, due to higher surface albedo (>0.25) in these regions (Figs. 5.2, 5.5a). At a constant lower SSA (∼0.9), an increase in AOD substantially intensifies SFC cooling and ATM heating, whereas the

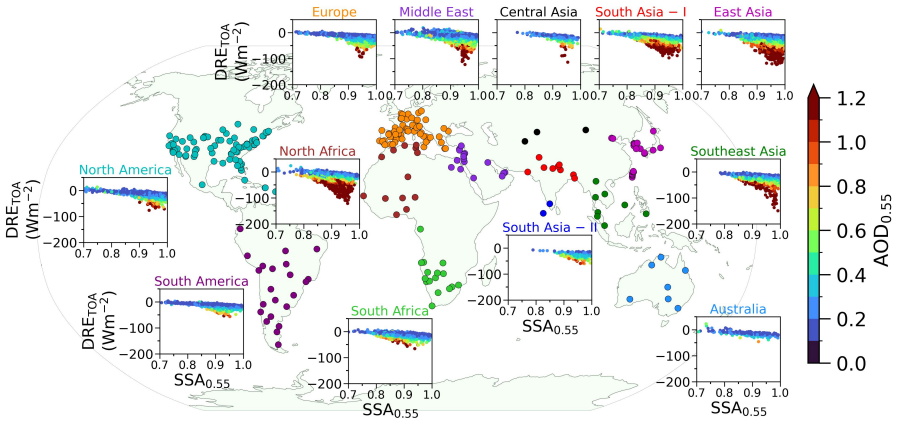

(a)

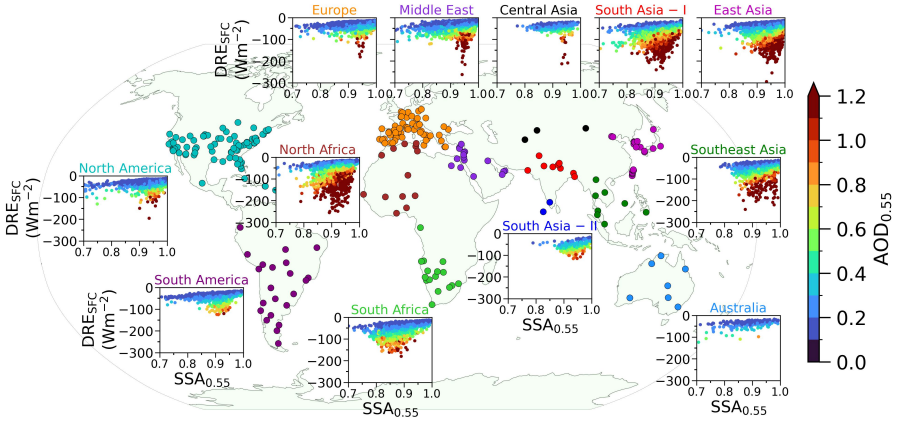

(b)

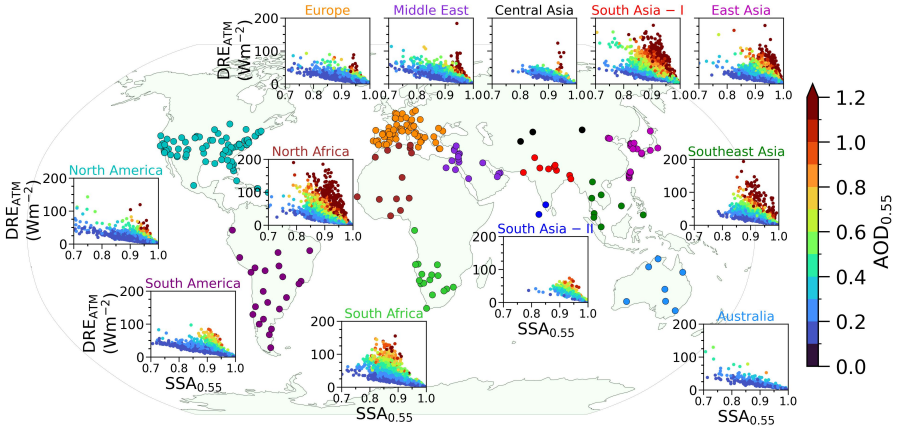

(c)

Figure 5.5: *Regional variation of DRE (in Wm^{-2}) at top of the atmosphere (DRE_{TOA}) (a), surface (DRE_{SFC}) (b), and in the atmosphere (DRE_{ATM}) (c) with $SSA_{0.55}$ as a function of $AOD_{0.55}$ across different regions of the globe.*

corresponding enhancement in TOA cooling is relatively smaller due to the stronger absorption by aerosols. Among all DRE components, the non-linear dependence of DRE_{ATM} on SSA is most pronounced - for a constant AOD, a reduction in SSA leads to a dispro-

portionately larger increase in ATM heating compared to the associated changes in SFC and TOA cooling. This response arises from enhanced absorption of solar radiation within the atmosphere (i.e., increased aerosol-induced atmospheric solar heating) as SSA decreases.

5.2 Global variations of DREE at TOA ($DREE_{TOA}$), SFC ($DREE_{SFC}$), and in the ATM ($DREE_{ATM}$)

5.2.1 Asia and SSA-driven variations

Over South Asia – I, ATM heating efficiency (∼85 $Wm^{-2}AOD^{-1}$) and SFC cooling efficiency (∼–135 $Wm^{-2}AOD^{-1}$) are notably higher during the winter and spring seasons due to lower SSA (Figs. 3.6, 5.3). During the same seasons, a similar enhancement in ATM heating efficiency and SFC cooling efficiency is observed over the Indochina Peninsula (Southeast Asia) and East China (East Asia). The reduction in SSA increases aerosol absorption of solar radiation, thereby intensifying atmospheric heating, while the opposite effect is seen under higher SSA conditions (Derimian et al., 2016). Conversely, during the monsoon season, higher SSA over South Asia (I–II), Southeast Asia, and East Asia results in reduced ATM heating efficiency and enhanced TOA cooling efficiency. Regionally, South Asia – II exhibits the lowest ATM heating efficiency (∼1.3–2 times lower) compared to other Asian regions due to relatively higher SSA values (Fig. 5.4c). In contrast, Central Asia shows the highest ATM heating efficiency within Asia, attributable to its lower SSA (Fig. 5.4c).

5.2.2 Biomass-burning regions

During periods of intense biomass burning, such as summer and autumn in South Africa and South America, winter in the southern part of North Africa, and winter and spring in Southeast Asia, an increase in absorbing CA results in lower SSA values, which in turn enhances ATM heating and SFC cooling efficiencies (Fig. 5.3).

5.2.3 Low-AOD regions and non-linear AOD-DRE behavior

Over North America and Europe, TOA cooling efficiency is relatively higher, attributable to higher SSA (∼0.95) in these regions (Figs. 3.7a, 5.3, 5.4c). Interestingly, despite the

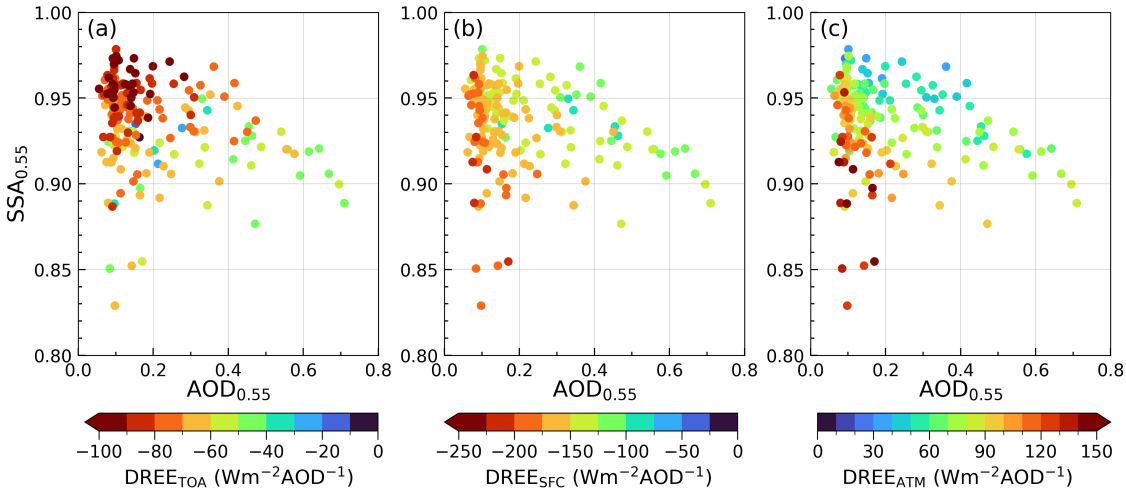

Figure 5.6: *The variations of annual mean (a) $DREE_{TOA}$, (b) $DREE_{SFC}$, and (c) $DREE_{ATM}$ as a function of $AOD_{0.55}$ and $SSA_{0.55}$ over all the observational sites across the globe.*

higher SSA values, both ATM heating efficiency (∼90 $Wm^{-2}AOD^{-1}$) and SFC cooling efficiency (∼–165 $Wm^{-2}AOD^{-1}$) are higher over North America and Europe compared to other regions (e.g., South Asia – I, Southeast Asia, East Asia, Middle East) (Figs. 5.3, 5.4c). This elevated DREE in North America and Europe can be attributed to the non-linear relationship between DRE and AOD (Derimian et al., 2016), where DREE tends to be higher at lower AOD levels for a given aerosol composition with the same SSA (Fig. 5.6) (Derimian et al., 2016). Additionally, the sensitivity of DREE to SSA variations (i.e., increased ATM heating and SFC cooling with lower SSA) is more pronounced in low AOD (<0.2) than in high AOD conditions (Fig. 5.6). Since the regional mean AODs over North America and Europe are relatively low (∼0.10) (Figs. 3.4, 5.3, 5.4c), DREE at SFC and in the ATM are amplified.

This global assessment of DREE indicates that for inter-regional comparison of SSA effects on DRE, DREE (defined as DRE per unit AOD at 0.55 μm) may not be an appropriate parameter when AOD values differ substantially between regions (e.g., AOD of ∼0.10 over North America and Europe against an AOD of ∼0.63 over South Asia – I). However, for intra-regional comparisons, or when inter-regional AOD differences are minimal, DREE remains a useful metric for evaluating SSA impacts on radiative effect (Ansari & Ramachandran, 2023b; Tian et al., 2023). For instance, over South and North America where AODs are similar (∼0.1) (Fig. 5.4a), lower SSA over South America (0.88) contributes to higher ATM heating efficiency (∼130 $Wm^{-2}AOD^{-1}$) and SFC cooling efficiency (∼–190 $Wm^{-2}AOD^{-1}$) as compared to North America (0.94)

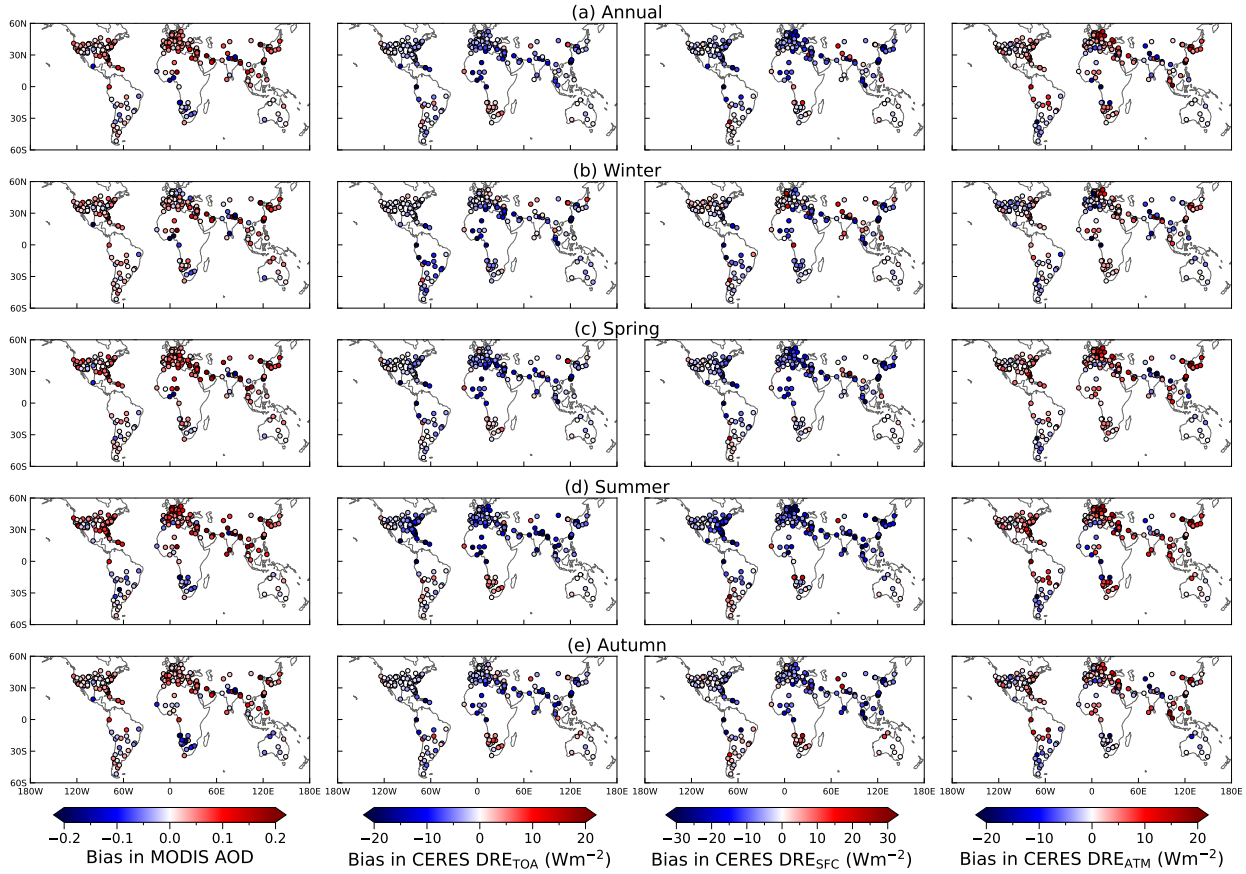

Figure 5.7: *Spatial distribution of mean bias in MODIS aerosol optical depth (AOD) (1^{st} column), CERES retrieved aerosol direct radiative effect (DRE; in Wm^{-2}) at top of atmosphere (DRE_{TOA}) (2^{nd} column), surface (DRE_{SFC}) (3^{rd} column), and in the atmosphere (DRE_{ATM}) (4^{th} columns) with respect to AERONET values on (a) annual and seasonal scales during (b) winter, (c) spring, (d) summer, and (e) autumn.*

(Figs. 3.7a, 5.3), emphasizing the above.

5.3 Global assessment of CERES retrieved DRE

Spatiotemporal collocated comparison of DRE retrieved from CERES SYN1deg hourly dataset with AERONET shows that CERES TOA and SFC cooling are generally higher (i.e., negative MBE in CERES DRE_{TOA} and DRE_{SFC}) than AERONET with relatively high RMSE over most sites in Asia, Middle East, Europe, and North Africa (Figs. 5.7, 5.8). In CERES, aerosol optical properties (e.g., AOD, SSA, g, refractive indices) are prescribed by the MATCH aerosol transport model, which are further utilized in the radiative transfer model (Fillmore et al., 2022). Since MATCH AOD is constrained and assimilated with

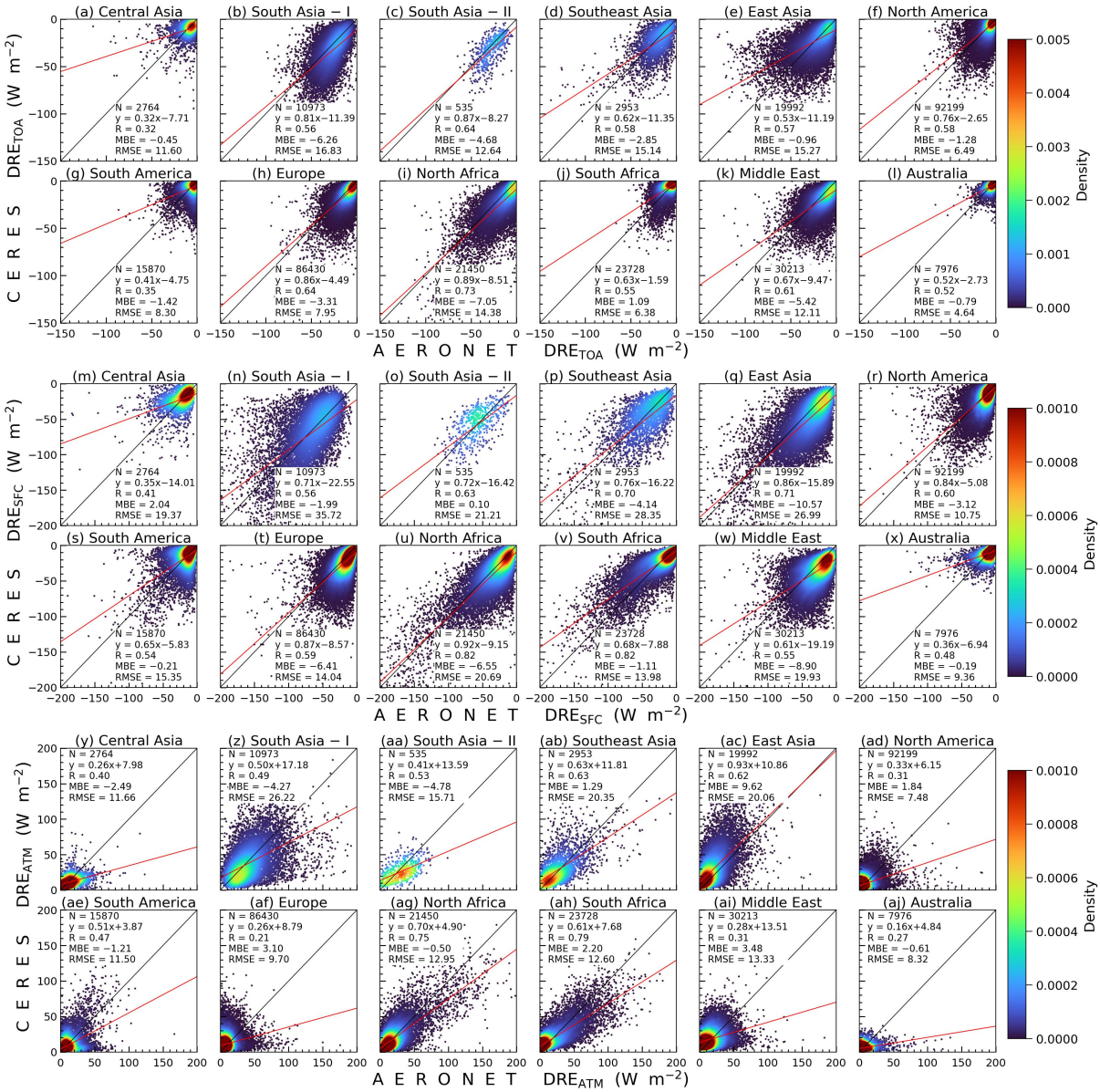

Figure 5.8: *Collocated validation of CERES retrieved aerosol direct radiative effect (DRE; in Wm^{-2}) at the top of the atmosphere (DRE_{TOA}) (a-l), surface (DRE_{SFC}) (m-x), and in the atmosphere (DRE_{ATM}) (y-aj) with respective AERONET DRE values over 12 different regions across the globe. The solid red and black lines correspond to linear fitted line and 1:1 line, respectively. The total collocated data points (N), statistics of linear fitted line, mean bias error (MBE), and root mean square error (RMSE) are shown in each panel. The kernel density estimation (KDE) derived probability density function is represented in color bar.*

the MODIS observations, it closely matches with MODIS AOD (Fillmore et al., 2022). Thus, the overestimation of MODIS AOD over Asia, Middle East, Europe, and North Africa results in stronger SFC and TOA cooling by CERES compared to AERONET (Figs.

5.7, 5.8). This underestimation is more pronounced during summer, coinciding with larger MODIS AOD overestimation (Fig. 5.7d).

The bias in MODIS retrieved AOD against AERONET AOD values varies with regions and seasons (Fig. 5.7). Overall, the performance of MODIS AOD is better in regions with low AOD values and relatively low bias, such as North America, South America, and Australia. In general, MODIS AOD overestimates over most sites in Asia, Middle East, Europe, and North Africa, which is mostly related to deficiencies in the represented aerosol model (Levy et al., 2010). During winter and spring over IGP and North Africa, and during summer and autumn in South Africa, when AOD is substantially high (>0.3; up to 0.8), MODIS substantially underestimates AERONET AOD by a factor of ∼1.4 (Figs. 3.4, 5.7). The main source of significant bias over regions with high AOD (e.g., biomass burning and dust regions) is primarily interrelated to variations in aerosol models, including assumptions about particle size distribution and refractive index, as well as the characterization of surface reflectance anisotropy (Schutgens et al., 2020). This finding is consistent with a previous study (Chen et al., 2022).

Biases in CERES DRE_{TOA} and DRE_{SFC} are smaller over North America, South America, and Australia, due to less bias in MODIS AOD over these regions. It is found that in comparison to AERONET on an annual scale, CERES ATM heating is lower over most sites in South Asia – I even when MODIS AOD is higher. One of the possible reasons could be due to high SSA prescribed by MATCH, which leads to lower aerosol absorption and DRE_{ATM}. On the regional scale, the MBE (absolute) and RMSE in the comparison of CERES DRE_{TOA} and DRE_{SFC} is higher over Asia, North Africa, and Middle East, and it is also higher over South America, South Africa, and Southeast Asia during their peak biomass burning seasons (Figs. 5.7, 5.8). These high errors in CERES DRE_{TOA} and DRE_{SFC} are found over high AOD regions, and these errors are likely driven by the inaccurate representation of aerosol optical properties and types by the MATCH model, which is utilized in the radiative transfer model.

5.4 Global assessment of MERRA-2 simulated DRE

The accuracy of MERRA-2 simulated DRE largely depends on its representation of simulated AOD (Ansari & Ramachandran, 2024b) and SSA (Ansari & Ramachandran, 2025b) (Figs. 5.9–5.12). On the regional scale, the correlations between MERRA-2 simulated DRE_{TOA} and DRE_{SFC} with AERONET retrievals are generally high (R >0.60) across the

globe, and it is relatively higher than the correlation for DRE_{ATM} (Fig. 5.12). However, correlation between MERRA-2 and AERONET DRE declines over some sites in South America, Mexico, and Australia due to MERRA-2 SSA overestimation (Figs. 3.20, 5.9–5.12).

In Asia, MERRA-2 significantly overestimates DRE_{TOA} (MBE: up to ~10 Wm^{-2}) and DRE_{SFC} (up to ~20 Wm^{-2}), while underestimating DRE_{ATM} (up to ~–20 Wm^{-2}) (i.e., underestimation of TOA and SFC cooling and ATM heating) over most sites, particularly in South Asia – I, South Asia – II, Southeast Asia, and East China, where AOD and DREs (at TOA, SFC, and in ATM; in magnitude) values are relatively high (Figs. 3.1, 5.9–5.12). This underestimation in SFC and TOA cooling and ATM heating by MERRA-2 over these regions is due to the substantial underestimation in MERRA-2 AOD compared

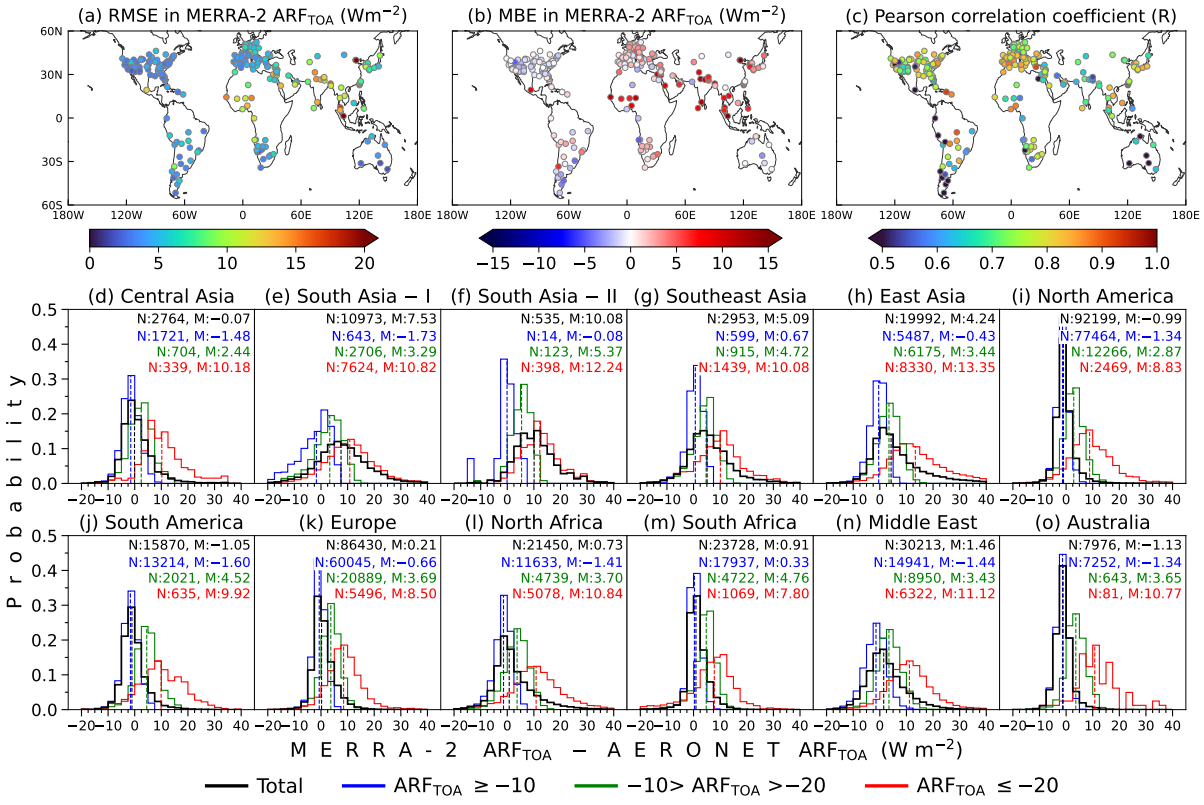

Figure 5.9: *Spatial distribution of (a) root mean square error (RMSE), (b) mean bias error (MBE), and (c) Pearson correlation coefficient (R) derived from collocated validation of MERRA-2 DRE_{TOA} with AERONET DRE_{TOA}. Probability distribution of the difference between DRE_{TOA} from MERRA-2 and AERONET over all regions (d-o) for total and different ranges of AERONET DRE_{TOA} (N: total collocated data points, M: median). Vertical dashed lines represent the median of the distribution.*

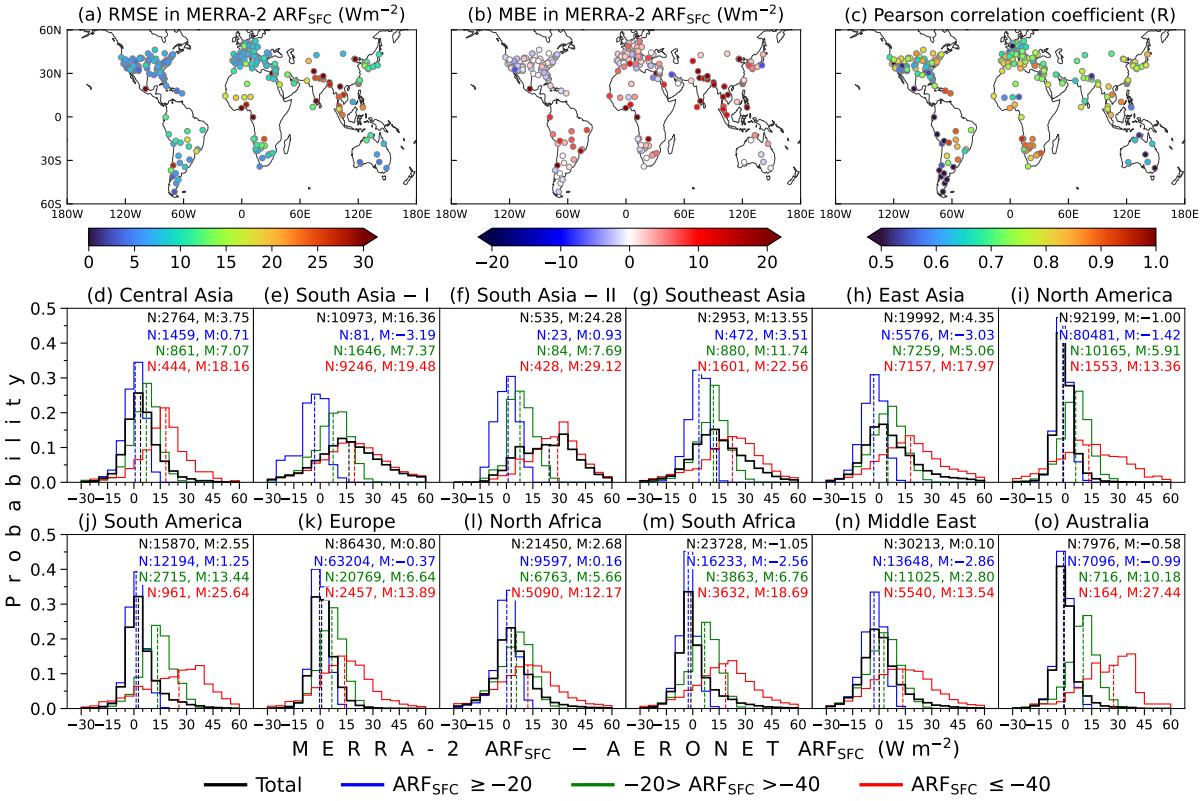

Figure 5.10: *Similar to Fig. 5.9, but for the collocated validation of MERRA-2 DRE$_{SFC}$ with AERONET DRE$_{SFC}$.*

to AERONET observations (Figs. 3.9, 3.11) (Ansari & Ramachandran, 2024b). Similar high overestimation in MERRA-2 DRE$_{TOA}$ and DRE$_{SFC}$ is also observed over other high AOD regions such as North Africa, South Africa, and Mexico, primarily linked to AOD underestimation. Interestingly, over low AOD sites in Japan, South Korea, and Northern Europe, MERRA-2 overestimates DRE$_{TOA}$, despite the low bias in MERRA-2 AOD (Fig. 3.11). This overestimation arises from the underestimation in MERRA-2 SSA at these sites (Fig. 3.20) (Ansari & Ramachandran, 2025b), implying an overestimation in the MERRA-2 simulated aerosol absorption, which results in reduced TOA cooling. Similar effects are found at biomass burning sites in South Africa and Southeast Asia, where underestimation in MERRA-2 SSA also enhances the overestimation of DRE$_{TOA}$ compared to AERONET values. The seasonal analysis further indicates that MERRA-2 underestimates SFC cooling and ATM heating during the biomass burning periods in central South America, South Africa, and Southeast Asia, primarily due to the underestimation of AOD (Fig. 5.13).

The probability distribution of differences between MERRA-2 and AERONET

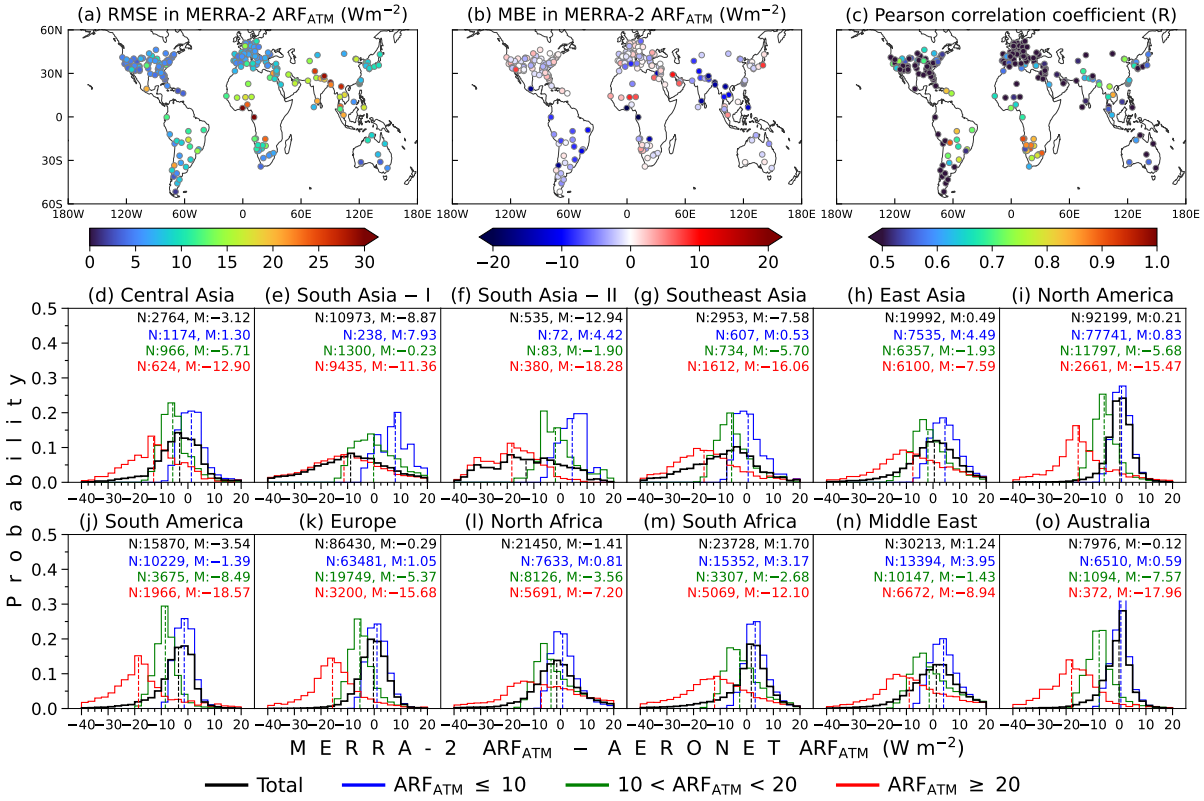

Figure 5.11: *Similar to Fig. 5.9, but for the collocated validation of MERRA-2 DRE$_{ATM}$ with AERONET DRE$_{ATM}$.*

DREs (at TOA, SFC, and in ATM) for different ranges of AERONET DRE values clearly reveals that the biases in MERRA-2 DREs are relatively lower and the distribution is narrower with high magnitude for low DRE values (Figs. 5.9–5.11). Whereas, the distributions become flatter with lower magnitude, and biases become more pronounced for high DRE values. It is found that the overestimation of MERRA-2 DRE$_{TOA}$ and DRE$_{SFC}$ increases (e.g., simulates lower TOA and SFC cooling) for lower (or higher in magnitude) DRE$_{TOA}$ ($\leq$–20 Wm^{-2}) and DRE$_{SFC}$ ($\leq$–40 Wm^{-2}) values, respectively, and the median value of the probability distribution increases over all the regions. Whereas, the underestimation of MERRA-2 DRE$_{ATM}$ increases (e.g., simulates lower ATM heating) for high DRE$_{ATM}$ ($\geq$20 Wm^{-2}) values across the globe. This analysis also reveals that the Asian region (e.g., South Asia – I, South Asia – II, Southeast Asia, and East Asia) where the conditions of high DRE values (at TOA, SFC, and in ATM; in magnitude) are more frequent with significant spatiotemporal variations, experiences relatively large biases in DREs compared to other regions of the globe. These biases are more pronounced over South Asia (I–II) on both regional and annual scales. A high bias in MERRA-2

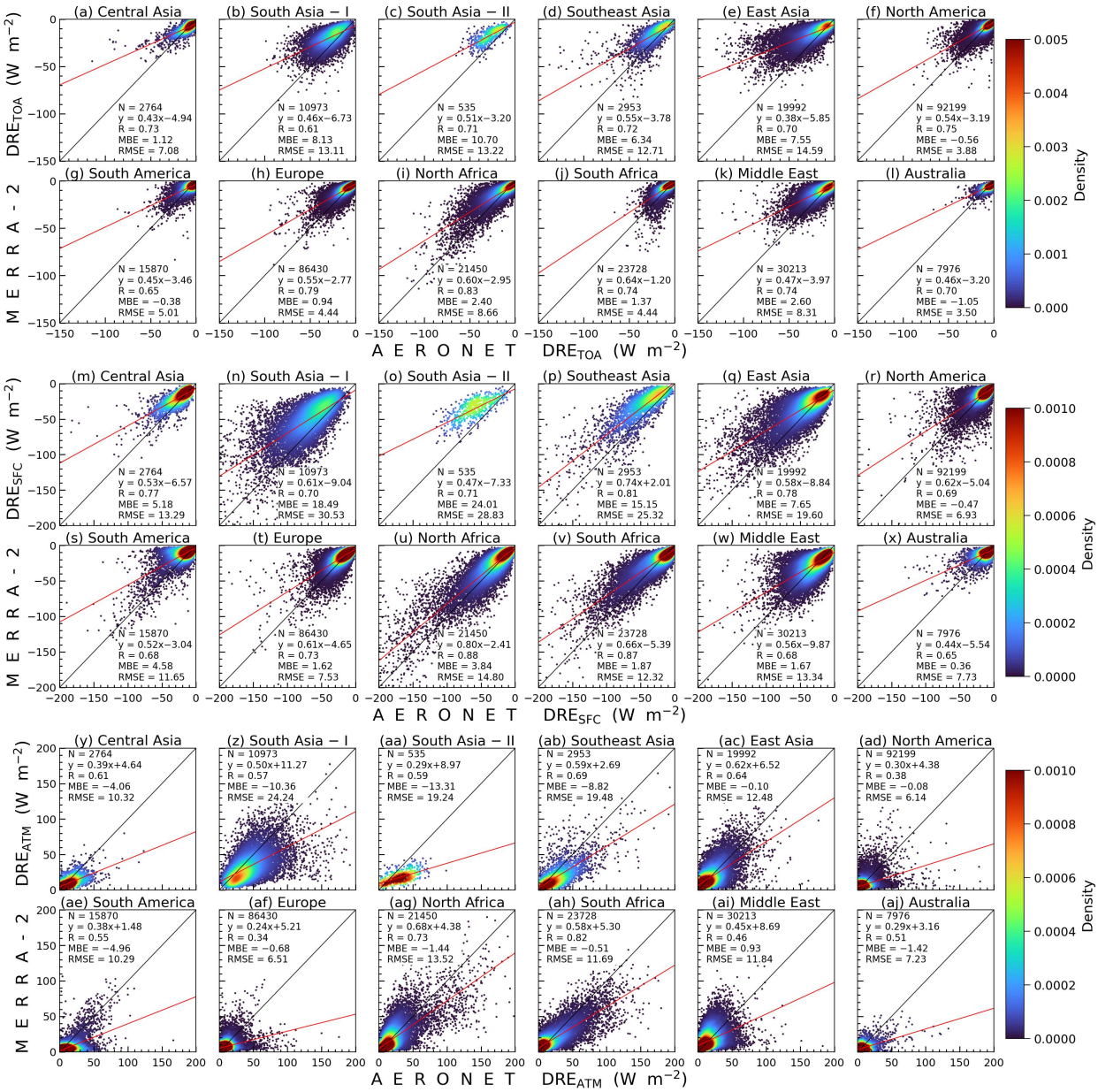

Figure 5.12: *Similar to Fig. 5.8, but for the collocated validation of MERRA-2 simulated aerosol direct radiative effect (DRE; in Wm^{-2}) at the top of the atmosphere (DRE_{TOA}) (a-l), surface (DRE_{SFC}) (m-x), and in the atmosphere (DRE_{ATM}) (y-aj) with respective AERONET DRE values over 12 different regions across the globe.*

DREs (underestimation of MERRA-2 TOA and SFC cooling, and ATM heating) for high DRE conditions (e.g., Asia) over the globe is mostly due to the high underestimation of MERRA-2 AOD when AOD is higher (Fig. 3.11) (Ansari & Ramachandran, 2024b). Similarly, the low biases in MERRA-2 DREs for low DRE conditions resulted from low bias in MERRA-2 AOD for low AOD conditions, perhaps due to the correct representation

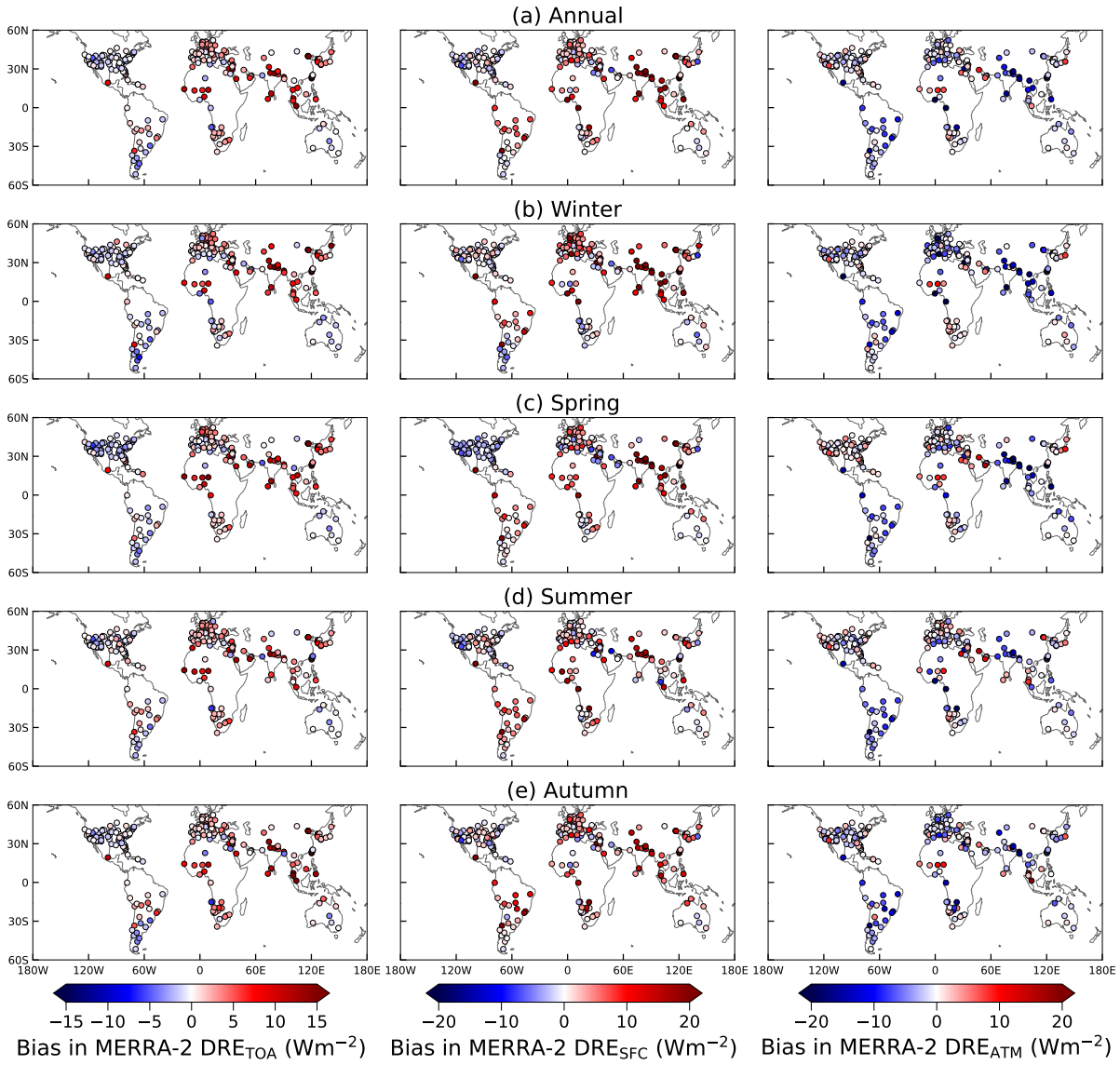

Figure 5.13: *Spatial distribution of mean bias in MERRA-2 simulated aerosol direct radiative effect (in Wm^{-2}) at top of atmosphere (DRE$_{TOA}$) (1st column), surface (DRE$_{SFC}$) (2nd column), and in the atmosphere (DRE$_{ATM}$) (3rd columns) with respect to AERONET values on (a) annual and seasonal scales during (b) winter, (c) spring, (d) summer, and (e) autumn.*

of aerosol emissions. Thus, MERRA-2 performs better in North America, South America, Europe, and Australia, where the magnitudes and spatiotemporal variations of AOD and DRE are substantially lower compared to Asia. Furthermore, the Taylor diagram also validates this finding as the points corresponding to MERRA-2 DRE$_{TOA}$, DRE$_{SFC}$, and DRE$_{ATM}$ are closer to the reference points of AERONET values over North America, South America, Europe, and Australia compared to other regions (Fig. 5.14).

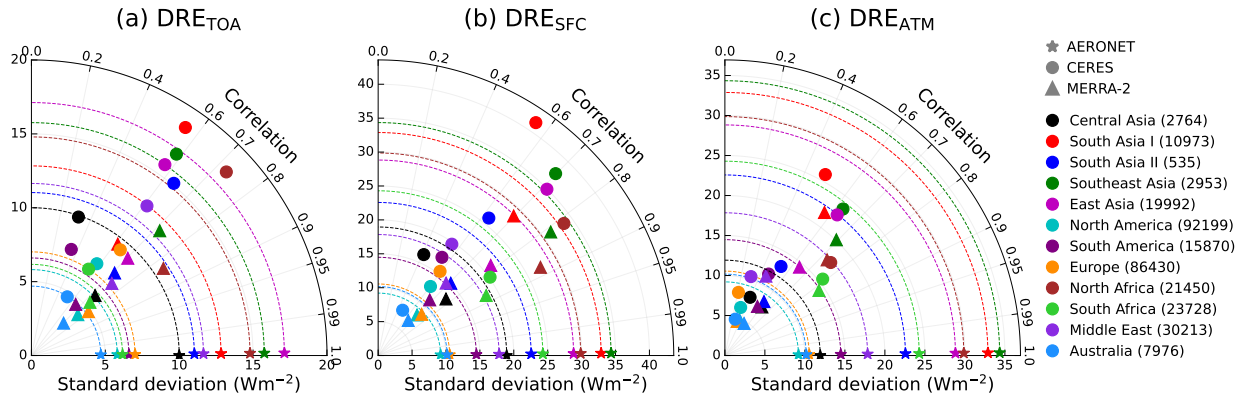

Figure 5.14: *Taylor diagram for collocated comparison of CERES (●) retrieved and MERRA-2 (▲) simulated DRE$_{TOA}$ (a), DRE$_{SFC}$ (b), and DRE$_{ATM}$ (c) with respect to AERONET. '★' symbols represent the standard deviation of reference AERONET values for different regions. Colors indicate the different regions of the globe. The total number of collocated data points is given in brackets next to each region.*

The underestimation of MERRA-2 AOD in high AOD conditions is attributed to the lack of accurate representation of aerosol species, especially related to the absence of nitrate in the GOCART model utilized in MERRA-2, despite their higher concentrations in urban and industrial regions (Zhang et al., 2012; Buchard et al., 2017). Additionally, the underestimation of biomass burning aerosols, particularly OC aerosol emissions, in MERRA-2 also contributes to the underestimation of AOD over biomass burning regions during their respective peak burning seasons (Buchard et al., 2017). Moreover, MERRA-2 assimilates the bias-corrected AOD with MODIS observations, which itself exhibits a large bias in high AOD conditions (Fig. 5.7) (Section 3.5.1). Thus, these limitations could further propagate in MERRA-2, resulting in an overall underestimation of simulated AOD in regions and seasons with high aerosol loading. These combined potential deficiencies lead to systematic biases (underestimations) in MERRA-2 AOD for high AOD conditions, which overall result in simulating less TOA and SFC cooling, as well as ATM heating in high DRE conditions across the globe.

The Taylor diagram (Fig. 5.14) and spatiotemporal collocated comparison of DREs at each level (TOA, SFC, and ATM) by CERES retrievals (Figs. 5.7, 5.8) and MERRA-2 simulations (Figs. 5.9–5.11) with AERONET reveals the significant regional biases in both datasets, and their signs and magnitudes vary across different regions. Notably, MERRA-2 DREs generally demonstrate better performance than CERES across

the globe, reflected by higher correlation and lower RMSE, as well as the points corresponding to MERRA-2 DREs are closer to the reference points of AERONET values than CERES in the Taylor diagram. Both MERRA-2 and CERES exhibit comparatively poorer performance over Asia, where their absolute biases and RMSEs are larger, and data points are relatively far from the reference AERONET point in the Taylor diagram. The lack of updates in the emission inventories of anthropogenic aerosols and their precursor gases in MERRA-2 (e.g., mostly annually varied and updated only up to 2010) (Randles et al., 2017) can lead to a large bias in MERRA-2 DREs. This is particularly important for regions like Asia, where anthropogenic emissions have undergone significant changes in recent decades, directly affecting the accuracy of AOD simulations and associated radiative forcing estimates (Ansari & Ramachandran, 2024b). This highlights the need for substantial improvements in both modeling simulations and satellite-based retrieval frameworks to reduce uncertainties and enhance the accuracy of DRE estimation in these high AOD and complex aerosol source regions.

5.5 Comparison between CMIP6 and AERONET radiative effects

CMIP6 simulated ARF is estimated as the change in DRE from the pre-industrial (1750) to the present-day period, which overall quantifies the change in aerosol distributions from pre-industrial times due to only anthropogenic aerosols (Heald et al., 2014; Elsey et al., 2024). This analysis provides a broad comparison of CMIP6 simulated direct ARF with AERONET DRE at different levels over different regions across the globe (Section 2.4.3). In absolute terms, CMIP6 MMM ARFs at SFC, TOA, and in the ATM are significantly lower than respective AERONET DREs across the globe (Fig. 5.15). Large differences (TOA and ATM: >10 Wm^{-2}; SFC: >20Wm^{-2}) are found over South Asia – I, followed by South Asia – II, Southeast Asia, East Asia, North Africa, and Middle East. Over Asia, where the magnitude and spatiotemporal variabilities in aerosol properties are significantly higher, not only are these differences between CMIP6 MMM and AERONET higher, but also the variabilities among CMIP6 models are found to be higher than in other regions (Fig. 5.15).

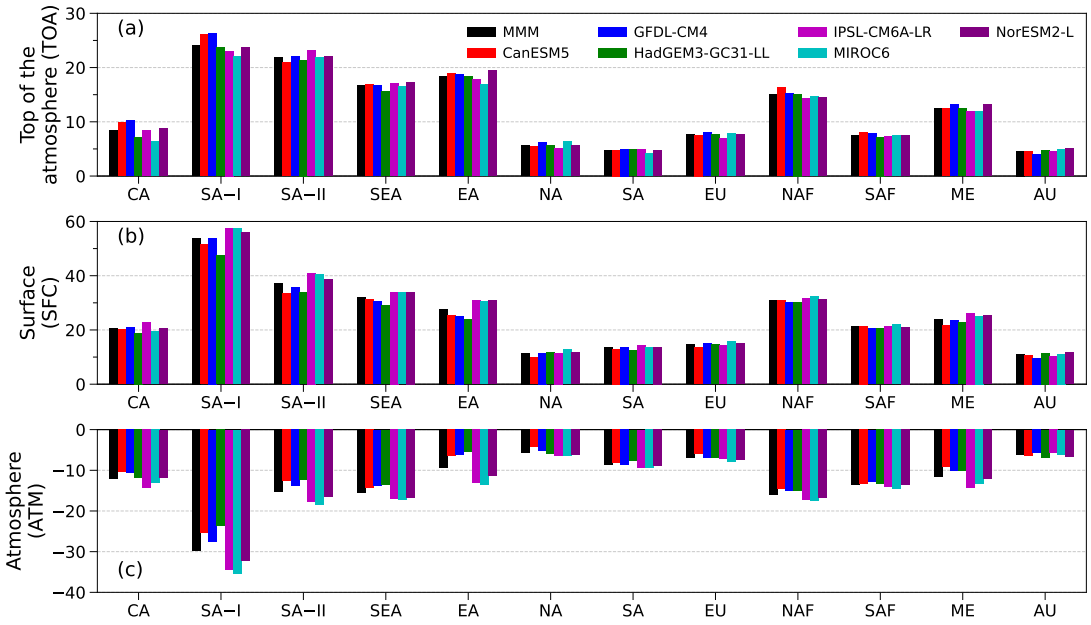

Figure 5.15: *Difference between annual mean direct ARF simulated by the multi-model mean (MMM) and individual models from CMIP6 with respect to AERONET retrieved DRE at top of the atmosphere (TOA) (a), surface (SFC) (b), and in the atmosphere (ATM) (c) calculated from their monthly means over different regions (Central Asia (CA), South Asia – I (SA–I), South Asia – II (SA–II), Southeast Asia (SEA), East Asia (EA), North America (NA), South America (SA), Europe (EU), North Africa (NAF), South Africa (SAF), Middle East (ME), and Australia (AU)) across the globe.*

5.6 Summary and Conclusions

A comprehensive assessment of regional variations in aerosol radiative parameters (aerosol direct radiative effect (DRE), DRE efficiency (DREE), and aerosol-induced atmospheric heating rate (HR)) using high-quality AERONET observations across the globe on seasonal and annual scales, including spatiotemporal collocated validation of DRE from satellite (CERES), and model simulations (MERRA-2 and CMIP6), is performed. The major findings are:

1. Aerosol surface (SFC) (DRE_{SFC}: ∼–70 Wm^{-2}) and top of atmosphere (TOA) cooling (DRE_{TOA}: ∼–30 Wm^{-2}) and atmospheric (ATM) heating (DRE_{ATM}: ∼40 Wm^{-2}; HR: ∼0.80 $Kday^{-1}$) are highest over South Asia – I compared to other regions of the globe with significant spatiotemporal variations, which is attributed to high AOD and lower SSA.

2. AOD, DREs (at SFC, TOA, and in ATM), and HR over North America, Europe, and Australia are ∼2–4 times lower than in Asia, with relatively less spatiotemporal variations. It is found that in the recent period, the episodic events of summertime wildfires and emitted smoke aerosols over the west coast of USA and Canada can significantly increase AOD (>1 during August 2018 and September 2020) and DRE (DRE_{SFC}: up to ∼–300 Wm^{-2} during September 2020) values during the wildfire period (Filonchyk et al., 2022; Tanada et al., 2023; Kassianov et al., 2025; Kelesidis et al., 2025). Nevertheless, it was found that aerosol emissions exhibit a decreasing trend on an annual scale over North America (Quaas et al., 2022).

3. Low SSA enhances both ATM heating efficiency and SFC cooling efficiency over South Asia – I on an annual scale and over biomass burning regions (e.g., South Africa, Southeast Asia, South America) during their respective peak burning seasons.

4. The biases (underestimation in absolute terms) in MERRA-2 DREs against AERONET DREs increase for high DRE values across the globe, due to high underestimation in MERRA-2 AOD in high AOD conditions. These underestimations in MERRA-2 DREs are higher over Asia (more pronounced in South Asia), where elevated values of DRE occur more frequently.

5. Performance of MERRA-2 simulated DREs against AERONET DREs is better in North America, South America, Europe, and Australia, where substantially lower values of AOD and DRE are observed. These findings are further supported by the Taylor diagram analysis.

6. Spatiotemporal collocated validations of MERRA-2 simulated and CERES retrieved DREs against AERONET reveal that MERRA-2 outperforms CERES in reproducing observed DRE values, with higher correlation and lower RMSE. Nevertheless, both (MERRA-2 and CERES) exhibit considerable biases over Asia with large RMSE values.

7. Differences between CMIP6 MMM simulated ARFs and AERONET DREs at each level are found to be higher over Asia with higher variabilities among CMIP6 models compared to other regions of the globe.

This study provides the observationally constrained estimates of DRE (indicating the net aerosol radiative effect on Earth's radiative balance) and DREE (indicating how efficiently aerosols perturb the Earth's radiation budget per unit optical depth) at different levels, revealing regions with high AOD and low SSA (e.g., over South Asia (I–II),

North Africa, South Africa, Southeast Asia) can induce substantial atmospheric heating. Such enhanced atmospheric absorption can strengthen the vertical temperature gradient, leading to increased atmospheric stability that influences monsoon circulation and distribution of precipitation. Further, a high aerosol surface cooling (i.e., lower $\mathrm{DRE}_{\mathrm{SFC}}$) over most Asian regions directly modulates surface temperature, boundary layer dynamics, and consequently, near-surface pollutant dispersion and local/regional air quality. Therefore, the analyses presented in this thesis not only advance our understanding of aerosol radiative impacts but also have valuable significance in the coupled effects of aerosols on atmospheric thermodynamics, cloud and precipitation processes, and regional air quality. Furthermore, the findings from this study underscore the critical need for improving both model simulations and satellite-based retrieval frameworks, particularly over high-AOD, aerosol-complex regions such as Asia.

6

Summary and Scope for Future Work

A brief summary of all the key findings from the analyses performed in this thesis is provided. The scope for future work based on the findings from the thesis is envisaged.

6.1 Summary

This study, a first-of-its-kind, presents a comprehensive assessment of the regional and spatial distributions of columnar optical and physical properties of aerosols and their direct radiative effects by utilizing high-quality ground-based AErosol RObotic NETwork (AERONET) observations over Asia on annual and seasonal scales. The spatiotemporal collocated validations/evaluations of aerosol properties and radiative effects from model simulations (Modern-Era Retrospective Analysis for Research and Applications - 2 (MERRA-2), Copernicus Atmosphere Monitoring Service (CAMS), and Coupled Model Intercomparison Project Phase 6 (CMIP6)) and satellite retrievals (MODerate Resolution Imaging Spectroradiometer (MODIS) and Clouds and the Earth's Radiant Energy System (CERES)) have been performed across Asia. Aerosol characteristics and the performances of model simulations and satellite retrievals over Asia are compared and contrasted with other regions of the globe (e.g., North America, South America, Europe, North Africa, South Africa, Middle East, and Australia), where aerosol content, types, and emissions differ significantly from Asia. A detailed analysis of the regional contributions of different aerosol types (Biomass burning (BB), Urban-industrial (UI), Dust, Mixed-fine, and Mixed-coarse) is conducted globally. Furthermore, a new classification scheme is developed to accurately classify different absorbing aerosol types (Dust, black carbon (BC), carbonaceous aerosols (CA), Mixed, Mixed-BC, and Mixed-Dust). This global study is performed by utilizing the AERONET dataset from a total of

261 observational sites covering 12 different regions across the globe.

The key findings related to these objectives are discussed in detail in *Chapters 3–5*, with a brief summary of each chapter provided below.

6.1.1 Chapter 3: Optical and Physical Characteristics of Aerosols

1. AOD exhibits significant spatiotemporal variations across Asia, where South Asia – I experiences the highest regional mean AOD (0.63 ± 0.15), followed by South Asia –

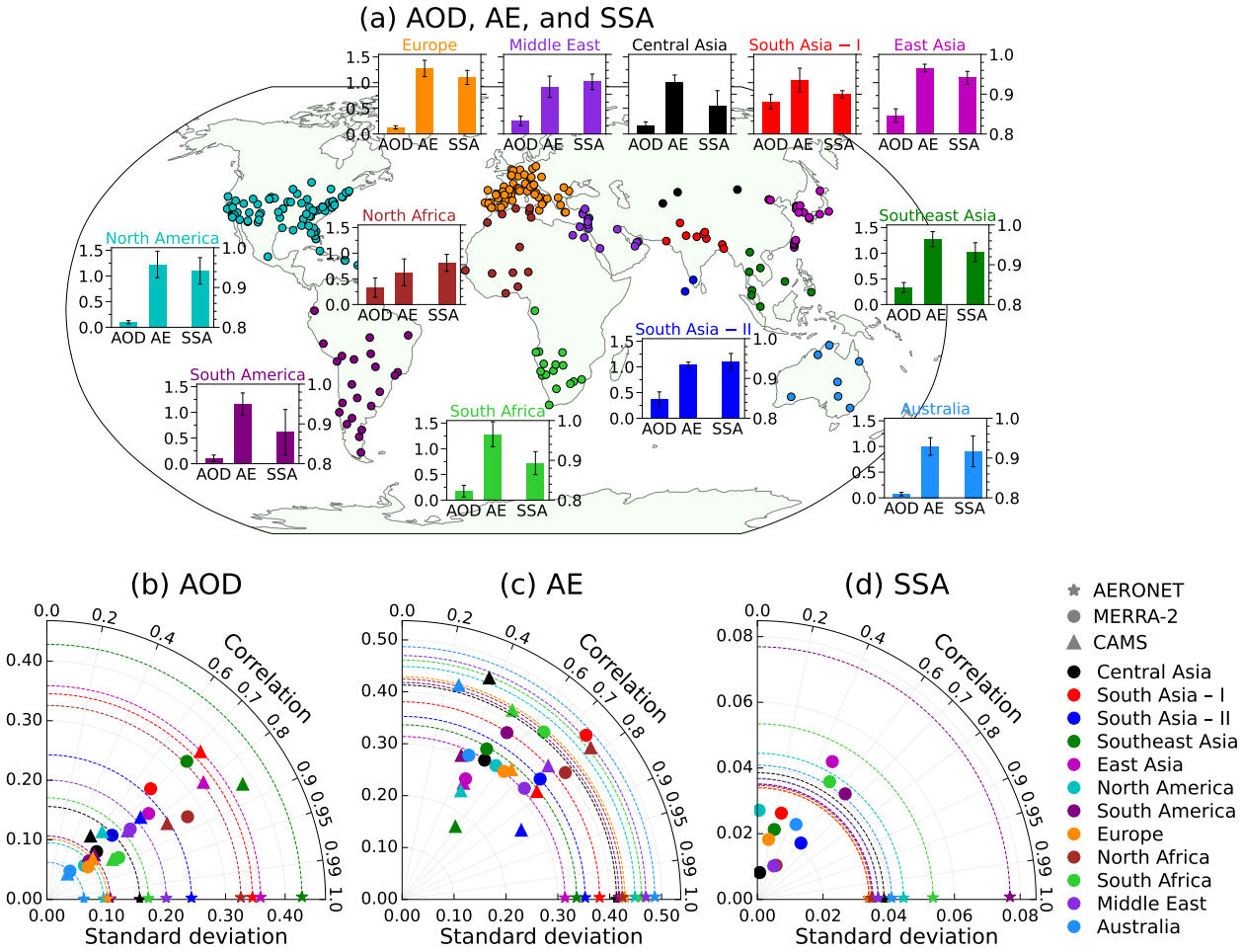

Figure 6.1: *(a) Regional variations of annual mean aerosol optical depth ($AOD_{0.55}$), Ångström exponent ($AE_{0.44-0.87}$) (on left y-axis) and single scattering albedo ($SSA_{0.55}$) (on right y-axis) across the globe. Taylor diagram for collocated comparison of MERRA-2 (•) and CAMS (▲) simulated $AOD_{0.55}$ (b) and $AE_{0.44-0.87}$ (c), and MERRA-2 simulated $SSA_{0.55}$ (d) with respect to AERONET. '★' symbols represent the standard deviation of reference AERONET values for different regions. Colors of each symbol indicate the different regions of the globe.*

II (0.37 $\pm$ 0.14), East (0.36 $\pm$ 0.13), Southeast (0.33 $\pm$ 0.10), and Central Asia (0.16 $\pm$ 0.07) (Fig. 6.1a). These elevated AOD values are attributed to combined contributions from fine- (anthropogenic emissions) and coarse-mode aerosols (seasonal dust and sea-salt transport).

2. AOD is significantly lower (<0.25) over North America, South America, Europe, and Australia, with less spatiotemporal variations (Fig. 6.1a). The volume size distribution (VSD <0.05 $\mu m^3/\mu m^2$) and total volume concentration (TVC <0.1 $\mu m^3/\mu m^2$) are at least 3-4 times lower than in Asia.

3. High AOD and lower SSA over South Asia – I lead to higher absorption AOD (AAOD: $\sim$0.06), which is $\sim$50% higher than in other regions in Asia. Central Africa shows the highest AAOD (>0.1) during winter, driven by enhanced emissions of absorbing CA from intense biomass burning along with dust aerosols. Conversely, North America and Europe experience higher spectral SSA (>0.92) alongside lower AOD (<0.2) and AAOD (<0.02), indicating reduced emissions of absorbing aerosols in relatively cleaner environments.

4. Performance of MERRA-2 and CAMS AOD is notably better (lower bias and higher GCOS fraction) over Australia, North America, Europe, South America, and South Africa. CAMS AOD performs better than MERRA-2 AOD over Asia; however, both models underestimate AOD in higher AOD conditions (Fig. 6.1). Both models exhibit relatively poor performance in simulating Ångström exponent (AE) compared to AOD, reflecting challenges in simulating the spectral distribution of fine- and coarse-mode aerosols. MERRA-2 mostly simulates aerosols to be moderately absorbing in nature (0.90$\leq$ SSA <0.95) despite significant differences in regional aerosol content and composition.

6.1.2 Chapter 4: Aerosol Types and Absorbing Aerosol Types

1. A new hybrid aerosol classification scheme, utilizing multiple aerosol parameters, is used to identify aerosol types globally that efficiently capture the aerosol sources. South Asia – I is predominantly influenced by Mixed-fine aerosol type ($\sim$41%), while UI type dominates (>50%) over North America, Europe, and East Asia. Dust type is the predominant type ($\sim$50%) over North Africa and the Middle East throughout the year (Fig. 6.2a).

2. A new classification scheme is developed to identify absorbing aerosol types by leveraging spectral characteristics of AOD and SSA of different absorbing aerosols. This method significantly reduces the contribution of unidentified type to almost nil (∼2%) compared to >30% in the previous method globally (Fig. 6.2b). This classification scheme reveals that Mixed absorbing aerosol type is dominant over South Asia – I due to the presence of all absorbing aerosols.

3. East North America and Europe are mostly influenced by UI aerosol type and BC

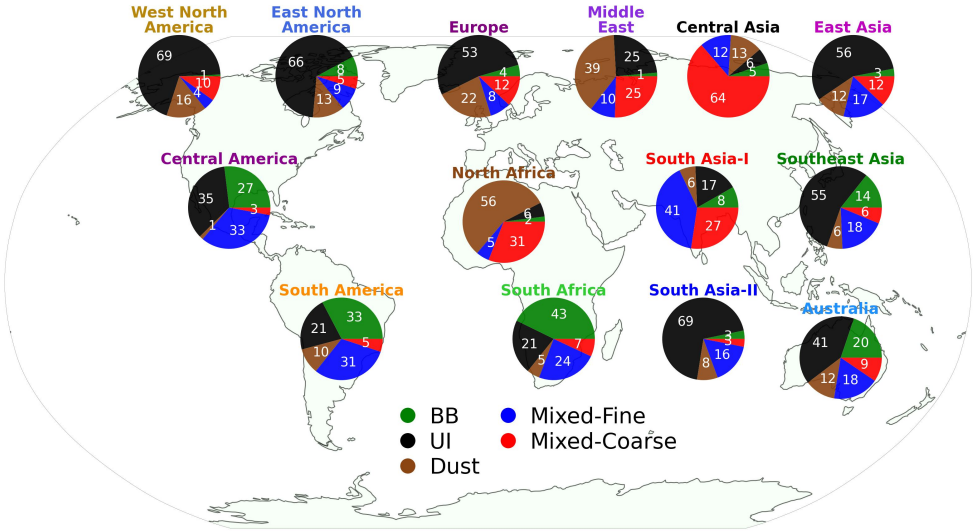

(a) *Aerosol types*

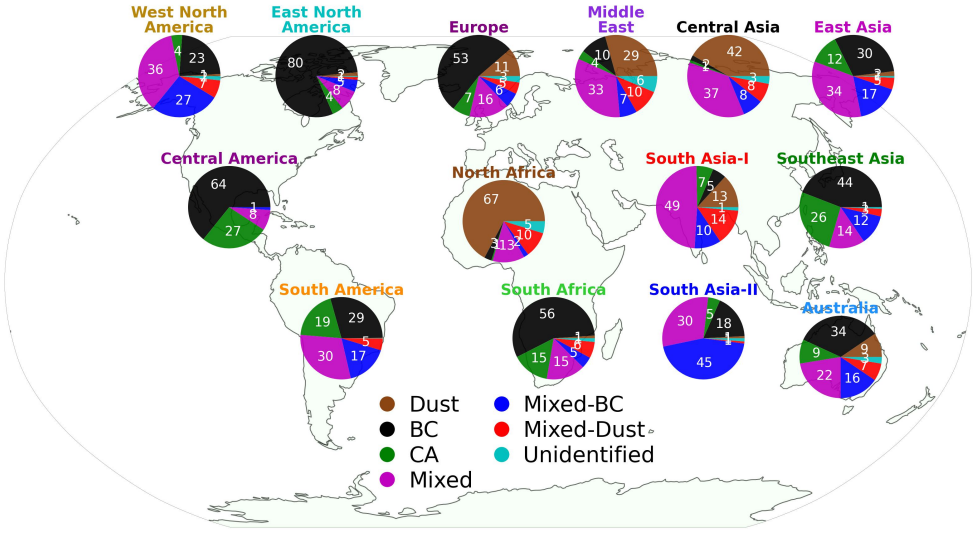

(b) *Absorbing aerosol types*

Figure 6.2: *Regional variation of annual mean % contribution of different (a) aerosol types (Biomass burning (BB), Urban-industrial (UI), Dust, Mixed-fine, and Mixed-coarse) and (b) absorbing aerosol types (Dust, Black Carbon (BC), Carbonaceous Aerosols (CA), Mixed, Mixed-BC, and Mixed-Dust) across the globe.*

absorbing aerosol types primarily due to fossil fuel combustion from urban and populated sites. Whereas, biomass burning emissions over central Africa, South America, Central America, and Southeast Asia during their respective dry seasons amplify the contribution of BB aerosol type and absorbing aerosol types of BC and CA, and significantly enhance the AOD and AAOD due to BC and CA types (Fig. 6.2).

4. A structured framework to integrate aerosol types and absorbing aerosol types information into global climate models is provided through post-processing of simulation outputs, thereby contributing to improving the aerosol simulations in climate models.

6.1.3 Chapter 5: Aerosol Direct Radiative Effects

1. The regional and seasonal analysis of aerosol direct radiative effect (DRE) reveals that South Asia – I experiences the highest surface (DRE_{SFC}: ∼–70 Wm^{-2}) and top-of-atmosphere cooling (DRE_{TOA}: ∼–30 Wm^{-2}), and atmospheric heating (DRE_{ATM}: ∼40 Wm^{-2}; aerosol-induced heating rate (HR): ∼0.80 $Kday^{-1}$) due to aerosols, which is attributed to high AOD and low SSA, with significant spatiotemporal variations. DREs (at SFC, TOA, and in ATM), and HR over North America, Europe, and Australia are ∼2-4 times lower than in Asia (Fig. 6.3a).

2. Low SSA enhances both atmospheric heating efficiency and surface cooling efficiency over South Asia – I and over biomass burning regions (e.g., South Africa, Southeast Asia, South America) during their respective peak burning seasons.

3. Underestimation in MERRA-2 simulated DREs is found to be higher in high DRE conditions, which is linked to high underestimation in MERRA-2 AOD in high AOD conditions. These underestimations are found to be higher over Asia (pronounced in South Asia), where high values of AOD and DRE are more frequent. In contrast, MERRA-2 simulated DREs perform better with respect to AERONET DREs over North America, South America, Europe, and Australia, where significantly lower values of AOD and DRE are observed (Fig. 6.3b-d).

4. MERRA-2 outperforms CERES in reproducing AERONET DREs, with higher correlation and lower bias as revealed by spatiotemporal collocated validations (Fig. 6.3b-d). However, both (MERRA-2 and CERES) show substantial biases over Asia, highlighting the critical need to refine model simulations and satellite retrieval algorithms, especially over aerosol-complex regions with high AOD levels such as over

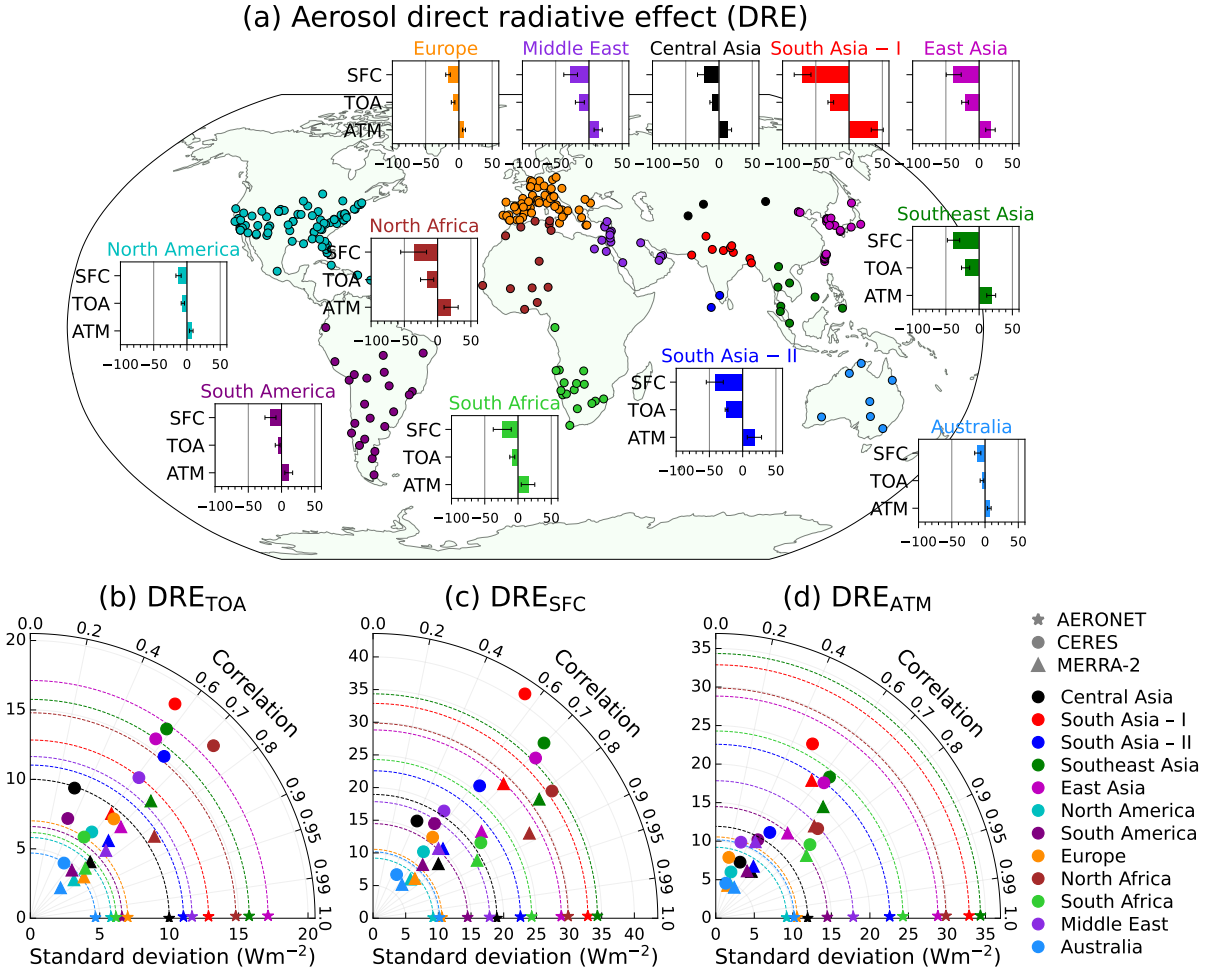

Figure 6.3: *(a) Regional variation of annual mean aerosol direct radiative effect (DRE; in Wm^{-2}) at the surface (SFC), top of the atmosphere (TOA), and in the atmosphere (ATM) across the globe. Taylor diagram for collocated comparison of CERES (●) retrieved and MERRA-2 (▲) simulated DRE$_{TOA}$ (b), DRE$_{SFC}$ (c), and DRE$_{ATM}$ (d) with respect to AERONET. '★' symbols represent the standard deviation of reference AERONET values for different regions. Colors of each symbol indicate the different regions of the globe.*

Asia.

5. Differences between CMIP6 MMM simulated ARFs and AERONET DREs at each level are also found to be higher over Asia with higher variabilities among CMIP6 models compared to other regions of the globe, corroborating the above.

6.2 Insights and Implications

In terms of quantifying the present-day changes in the Earth's radiation budget and accurately projecting future climate scenarios, aerosols remain the most uncertain forcing

agent in the climate system (IPCC, 2021). This uncertainty is particularly pronounced over Asia, where high aerosol loadings and complex mixtures of anthropogenic and natural sources introduce significant challenges in both observations and simulations (Forster et al., 2021). The comprehensive analysis presented in this thesis, leveraging high-quality ground-based AERONET observations, satellite retrievals, reanalysis simulations, and CMIP6 climate model simulations, provides new and valuable quantitative insights into the regional and seasonal variability of aerosol optical and radiative properties on global and seasonal scales, thus far not available. Accurate observational constraints along with a robust assessment of aerosol properties and radiative effects are provided based on model simulations and satellite retrievals, quantifying their regional and seasonal biases and identifying the potential causes of the discrepancies between observations and models, hitherto unavailable. These results offer significant potential for advancing research in climate modeling, satellite-based retrieval, and aerosol monitoring applications, for accurately assessing the aerosol-climate interactions, which remain highly uncertain.

6.3 Scope for future work

The observational constraints on aerosol columnar optical and radiative properties provided in this thesis, with a particular emphasis on Asia, offer a critical resource for validating and refining aerosol simulations in both regional and global climate models. Current climate models often struggle to represent the spatiotemporal variability of aerosols, especially in complex aerosol regions such as Asia, where both natural and anthropogenic aerosols co-occur, due to uncertainties in emission inventories, processes, and parameterization of aerosols and their interaction with radiation. By integrating these observational datasets into model evaluation frameworks, future studies can systematically quantify the magnitude and biases in aerosol optical and radiative properties in the models. These observational constraints can also aid in isolating model deficiencies related to specific aerosol processes, such as aerosol mixing state and absorption properties.

Furthermore, this study provides detailed insights into how model biases amplify under high-AOD conditions with their potential causes. For example, MERRA-2 significantly underestimates AOD over South Asia during winter and autumn when anthropogenic emissions are higher. Further, MERRA-2 significantly underestimates SSA

over East Asia due to the overestimation in simulated absorbing aerosols (e.g., BC). Thus, improving aerosol parameterizations and updating the emissions inventories related to anthropogenic aerosols and their precursors over South Asia, and in particular, absorbing aerosol species (e.g., BC) over East Asia, will produce more accurate aerosol simulations. Reanalysis and model simulations can benefit, in particular, from the observational constraints provided on seasonal scales, by tuning their emissions inventories and aerosol-radiation interaction schemes, thereby enhancing the assessment of aerosol climate impact over Asia.

This study reports the highest regional and annual mean AOD over South Asia across all the regions due to the combined influence of fine (i.e., anthropogenic) and coarse (i.e., natural) mode aerosols. This high AOD over South Asia aligns well with the increasing trend of anthropogenic aerosols (Ramachandran et al., 2025). Further, prevalent meteorological conditions (e.g., wind speed, relative humidity, and atmospheric boundary layer) can significantly influence the aerosol characteristics (Ramachandran et al., 2025). However, a precise quantification of natural and anthropogenic sources of aerosols, the influence of meteorology, and their impact on clouds and precipitation still remains a challenge. This work can be carried out in the future by utilizing the sophisticated high-resolution regional and global models with updated aerosol emissions inventories and processes, which is essential for air quality management, precipitation, and climate assessment over this region (e.g., South Asia) vulnerable to climate change.

This study reveals a high bias in CERES-derived DRE over Asia when compared with AERONET-based estimates, and further shows that CERES exhibits weaker performance than MERRA-2 in capturing AERONET DRE across most global regions. These discrepancies highlight that combining CERES fluxes with MODIS AOD may not be an optimal way due to inherent biases and uncertainties in satellite-retrieved AODs and the assumptions of SSA used in the MATCH model simulations. To overcome these limitations, future work could explore developing an integrated approach that combines CERES TOA fluxes with ground-based AERONET measurements. In this framework, CERES clear-sky TOA fluxes can be empirically related to collocated AERONET AOD through linear or nonlinear regression, while the intercept at AOD = 0 represents the flux under aerosol-free conditions. The difference between the observed and aerosol-free fluxes provides an estimate of DRE at the TOA. Similar relationships can be established for surface fluxes using CERES-derived or ancillary datasets, enabling estimation

of surface and atmospheric DRE. Such an approach would minimize the dependency on satellite-retrieved AOD and assumed SSA, thereby improving the accuracy and consistency of aerosol radiative effect assessments.

One of the key advancements of this thesis is the development of a novel classification scheme for absorbing aerosol types based on the spectral characteristics of AOD and SSA. This method significantly reduces the contribution of unidentified type globally, offering a more accurate classification of absorbing aerosol types. Further, a structured framework is provided to implement this new classification scheme of absorbing aerosol types into models through post-processing of simulation outputs. It enables a direct one-to-one type-specific comparison between model-simulated type-wise contributions and observations, allowing for the identification of biases associated with individual types, thereby supporting the improvement of aerosol representation and simulation in climate models.

References

Adesina, A. J., Kumar, K. R., Sivakumar, V., & Griffith, D. (2014). Direct radiative forcing of urban aerosols over Pretoria (25.75°S, 28.28°E) using AERONET sunphotometer data: First scientific results and environmental impact. *J Environ Sci*, *26*, 2459–2474. doi:10.1016/j.jes.2014.04.006.

Ali, M. A., Nichol, J. E., Bilal, M., Qiu, Z., Mazhar, U., Wahiduzzaman, M., Almazroui, M., & Islam, M. N. (2020). Classification of aerosols over Saudi Arabia from 2004–2016. *Atmos Environ*, *241*, 117785. doi:10.1016/j.atmosenv.2020.117785.

Allen, R. J., & Sherwood, S. C. (2010). Aerosol-cloud semi-direct effect and land-sea temperature contrast in a GCM. *Geophys Res Lett*, *37*. doi:10.1029/2010gl042759.

Andrews, E., Ogren, J. A., Kinne, S., & Samset, B. (2017). Comparison of AOD, AAOD and column single scattering albedo from AERONET retrievals and in situ profiling measurements. *Atmos Chem Phys*, *17*, 6041–6072. doi:10.5194/acp-17-6041-2017.

Andrews et al. (2020). Historical simulations with HadGEM3-GC3.1 for CMIP6. *J Adv Model Earth Syst*, *12*, e2019MS001995. doi:10.1029/2019ms001995.

Ansari, K., & Ramachandran, S. (2023a). Aerosol characteristics over Indo-Gangetic Plain from ground-based AERONET and MERRA-2/CAMS model simulations. *Atmos Environ*, *293*, 119434. doi:10.1016/j.atmosenv.2022.119434.

Ansari, K., & Ramachandran, S. (2023b). Radiative effects of absorbing aerosol types over South Asia. *Sci Total Environ*, *858*, 159969. doi:10.1016/j.scitotenv.2022.159969.

Ansari, K., & Ramachandran, S. (2024a). Global changes in aerosol single scattering albedo during COVID-19. *Atmos Environ*, *333*, 120649. doi:10.1016/j.atmosenv.2024.120649.

Ansari, K., & Ramachandran, S. (2024b). Optical and physical characteristics of aerosols over Asia: AERONET, MERRA-2 and CAMS. *Atmos Environ*, *326*, 120470. doi:10.1016/j.atmosenv.2024.120470.

Ansari, K., & Ramachandran, S. (2025a). Enhancing accuracy in identifying absorbing aerosol types and their radiative impacts. *npj Clim Atmos Sci*, *8*, 351. doi:10.1038/s41612-025-01167-w.

Ansari, K., & Ramachandran, S. (2025b). Global insights on absorption characteristics of aerosols. *Sci Total Environ*, *959*, 178178. doi:10.1016/j.scitotenv.2024.178178.

Ansari, K., Ramachandran, S., & Cherian, R. (2025). Global assessment of aerosol radiative effects: New insights from observations, reanalysis, and climate models. *Sci Total Environ*, *1006*, 180871. doi:10.1016/j.scitotenv.2025.180871.

Arola et al. (2015). Direct radiative effect by brown carbon over the Indo-Gangetic Plain. *Atmos Chem Phys*, *15*, 12731–12740. doi:10.5194/acp-15-12731-2015.

Bakatsoula, V. D., Korras-Carraca, M.-B., Hatzianastassiou, N., & Matsoukas, C. (2023). A comparison of atmospheric aerosol absorption properties from the MERRA-2 reanalysis with AERONET. *Atmos Environ*, *311*, 119997. doi:10.1016/j.atmosenv.2023.119997.

Banerjee, T., Shitole, A. S., Mhawish, A., Anand, A., Ranjan, R., Khan, M. F., Srithawirat, T., Latif, M. T., & Mall, R. K. (2021). Aerosol climatology over South and Southeast Asia: Aerosol types, vertical profile, and source fields. *J Geophys Res Atmos*, *126*, e2020JD033554. doi:10.1029/2020jd033554.

Bellouin et al. (2020). Bounding global aerosol radiative forcing of climate change. *Rev Geophys*, *58*, e2019RG000660. doi:10.1029/2019rg000660.

Bergstrom, R. W., Pilewskie, P., Russell, P. B., Redemann, J., Bond, T. C., Quinn, P. K., & Sierau, B. (2007). Spectral absorption properties of atmospheric aerosols. *Atmos Chem Phys*, *7*, 5937–5943. doi:10.5194/acp-7-5937-2007.

Bibi, S., Alam, K., Chishtie, F., & Bibi, H. (2017). Characterization of absorbing aerosol types using ground and satellites based observations over an urban environment. *Atmos Environ*, *150*, 126–135. doi:10.1016/j.atmosenv.2016.11.052.

Bilal, M., & Nichol, J. E. (2015). Evaluation of MODIS aerosol retrieval algorithms over the Beijing-Tianjin-Hebei region during low to very high pollution events. *J Geophys Res Atmos*, *120*, 7941–7957. doi:10.1002/2015jd023082.

Bodhaine, B. A., Wood, N. B., Dutton, E. G., & Slusser, J. R. (1999). On Rayleigh optical depth calculations. *J Atmos Ocean Technol*, *16*, 1854–1861. doi:10.1175/1520-0426(1999)016<1854:orodc>2.0.co;2.

Bond, T. C., & Bergstrom, R. W. (2006). Light absorption by carbonaceous particles: An investigative review. *Aerosol Science and Technology*, *40*, 27–67. doi:10.1080/02786820500421521.

Bond et al. (2013). Bounding the role of black carbon in the climate system: A scientific assessment. *J Geophys Res Atmos*, *118*, 5380–5552. doi:10.1002/jgrd.50171.

Boucher et al. (2020). Presentation and evaluation of the IPSL-CM6A-LR climate model. *J Adv Model Earth Syst*, *12*, e2019MS002010. doi:10.1029/2019ms002010.

Buchard et al. (2017). The MERRA-2 aerosol reanalysis, 1980 onward. Part II: Evaluation and case studies. *J Clim*, *30*, 6851–6872. doi:10.1175/jcli-d-16-0613.1.

Buchard, V., da Silva, A., Randles, C., Colarco, P., Ferrare, R., Hair, J., Hostetler, C., Tackett, J., & Winker, D. (2016). Evaluation of the surface $PM_{2.5}$ in version 1 of the NASA MERRA aerosol reanalysis over the United States. *Atmos Environ*, *125*, 100–111. doi:10.1016/j.atmosenv.2015.11.004.

Che et al. (2019a). Large contribution of meteorological factors to inter-decadal changes in regional aerosol optical depth. *Atmos Chem Phys*, *19*, 10497–10523. doi:10.5194/acp-19-10497-2019.

Che et al. (2018). Aerosol optical properties and direct radiative forcing based on measurements from the China Aerosol Remote Sensing Network (CARSNET) in eastern China. *Atmos Chem Phys*, *18*, 405–425. doi:10.5194/acp-18-405-2018.

Che et al. (2019b). Spatial distribution of aerosol microphysical and optical properties and direct radiative effect from the China Aerosol Remote Sensing Network. *Atmos Chem Phys*, *19*, 11843–11864. doi:10.5194/acp-19-11843-2019.

Chen, A., Zhao, C., Zhang, H., Yang, Y., & Li, J. (2024). Surface albedo regulates aerosol direct climate effect. *Nat Commun*, *15*, 7816. doi:10.1038/s41467-024-52255-z.

Chen et al. (2020). Validation of GRASP algorithm product from POLDER/PARASOL data and assessment of multi-angular polarimetry potential for aerosol monitoring. *Earth Syst Sci Data*, *12*, 3573–3620. doi:10.5194/essd-12-3573-2020.

Chen, H., Gu, X., Cheng, T., Li, Z., & Yu, T. (2013). The spatial–temporal variations in optical properties of atmosphere aerosols derived from AERONET dataset over China. *Meteorology and Atmospheric Physics*, *122*, 65–73. doi:10.1007/s00703-013-0268-2.

Chen, Q.-X., Han, X.-L., Gu, Y., Yuan, Y., Jiang, J. H., Yang, X.-B., Liou, K.-N., & Tan, H.-P. (2022). Evaluation of MODIS, MISR, and VIIRS daily level-3 aerosol optical depth products over land. *Atmos Res*, *265*, 105810. doi:10.1016/j.atmosres.2021.105810.

Chen, S., Huang, J., Li, J., Jia, R., Jiang, N., Kang, L., Ma, X., & Xie, T. (2017). Comparison of dust emissions, transport, and deposition between the Taklimakan Desert and Gobi Desert from 2007 to 2011. *Sci China Earth Sci*, *60*, 1338–1355. doi:10.1007/s11430-016-9051-0.

Choi et al. (2021). Temporal and spatial variations of aerosol optical properties over the Korean peninsula during KORUS-AQ. *Atmos Environ*, *254*, 118301. doi:10.1016/j.atmosenv.2021.118301.

Chung, C. E., Ramanathan, V., & Decremer, D. (2012). Observationally constrained estimates of carbonaceous aerosol radiative forcing. *Proc Natl Acad Sci*, *109*, 11624–11629. doi:10.1073/pnas.1203707109.

Colarco, P., da Silva, A., Chin, M., & Diehl, T. (2010). Online simulations of global aerosol distributions in the NASA GEOS-4 model and comparisons to satellite and ground-based aerosol optical depth. *J Geophys Res Atmos*, *115*, 14207. doi:10.1029/2009jd012820.

Copernicus Atmosphere Monitoring Service (2020). CAMS global reanalysis (EAC4). Copernicus Atmosphere Monitoring Service (CAMS) atmosphere data store. doi:10.24381/d58bbf47.

Darmenov, A. S., & da Silva, A. (2015). *The Quick Fire Emissions Dataset (QFED) – Documentation of versions 2.1, 2.2 and 2.4*. Technical Report NASA/TM-2015-104606, Vol. 38, p. 183 NASA Global Modeling and Assimilation Office available online at: https://gmao.gsfc.nasa.gov/pubs/docs/Darmenov796.pdf.

Derimian, Y., Dubovik, O., Huang, X., Lapyonok, T., Litvinov, P., Kostinski, A. B., Dubuisson, P., & Ducos, F. (2016). Comprehensive tool for calculation of radiative fluxes: Illustration of shortwave aerosol radiative effect sensitivities to the details in aerosol and underlying surface characteristics. *Atmos Chem Phys*, *16*, 5763–5780. doi:10.5194/acp-16-5763-2016.

Di Biagio et al. (2019). Complex refractive indices and single-scattering albedo of global dust aerosols in the shortwave spectrum and relationship to size and iron content. *Atmos Chem Phys*, *19*, 15503–15531. doi:10.5194/acp-19-15503-2019.

Diehl, T., Heil, A., Chin, M., Pan, X., Streets, D., Schultz, M., & Kinne, S. (2012). Anthropogenic, biomass burning, and volcanic emissions of black carbon, organic carbon, and SO_2 from 1980 to 2010 for hindcast model experiments. *Atmos Chem Phys Discuss*, *12*, 24895–24954. doi:10.5194/acpd-12-24895-2012.

Dong, Y., Li, J., Yan, X., Li, C., Jiang, Z., Xiong, C., Chang, L., Zhang, L., Ying, T., & Zhang, Z. (2023). Retrieval of aerosol single scattering albedo using joint satellite and surface visibility measurements. *Remote Sens Environ*, *294*, 113654. doi:10.1016/j.rse.2023.113654.

Dubovik, O., Holben, B., Eck, T. F., Smirnov, A., Kaufman, Y. J., King, M. D., Tanré, D., & Slutsker, I. (2002). Variability of absorption and optical properties of key aerosol types observed in worldwide locations. *J Atmos Sci*, *59*, 590–608. doi:10.1175/1520-0469(2002)059<0590:voaaop>2.0.co;2.

Dubovik, O., & King, M. D. (2000). A flexible inversion algorithm for retrieval of aerosol optical properties from Sun and sky radiance measurements. *J Geophys Res Atmos*, *105*, 20673–20696. doi:10.1029/2000jd900282.

Dubovik et al. (2006). Application of spheroid models to account for aerosol particle nonsphericity in remote sensing of desert dust. *J Geophys Res Atmos*, *111*. doi:10.1029/2005jd006619.

Dubovik, O., Smirnov, A., Holben, B. N., King, M. D., Kaufman, Y. J., Eck, T. F., & Slutsker, I. (2000). Accuracy assessments of aerosol optical properties retrieved from Aerosol Robotic Network (AERONET) Sun and sky radiance measurements. *J Geophys Res Atmos*, *105*, 9791–9806. doi:10.1029/2000jd900040.

Dubuisson, P., Buriez, J. C., & Fouquart, Y. (1996). High spectral resolution solar radiative transfer in absorbing and scattering media: Application to the satellite simulation. *J Quant Spectrosc Radiat Transf*, *55*, 103–126. doi:10.1016/0022-4073(95)00134-4.

Eck et al. (2019). AERONET remotely sensed measurements and retrievals of biomass burning aerosol optical properties during the 2015 Indonesian burning season. *J Geophys Res Atmos*, *124*, 4722–4740. doi:10.1029/2018jd030182.

Eck et al. (2010). Climatological aspects of the optical properties of fine/coarse mode aerosol mixtures. *J Geophys Res Atmos*, *115*, 19205. doi:10.1029/2010jd014002.

Ehret, A., Turquety, S., George, M., Hadji-Lazaro, J., & Clerbaux, C. (2025). Increase in carbon monoxide (CO) and aerosol optical depth (AOD) observed by satellites in the Northern Hemisphere over the summers of 2008–2023, linked to an increase in wildfires. *Atmos Chem Phys*, *25*, 6365–6394. doi:10.5194/acp-25-6365-2025.

Elsey, J., Bellouin, N., & Ryder, C. (2024). Sensitivity of global direct aerosol shortwave radiative forcing to uncertainties in aerosol optical properties. *Atmos Chem Phys*, *24*, 4065–4081. doi:10.5194/acp-24-4065-2024.

European Commission (2011). Emission Database for Global Atmospheric Research (EDGAR), release version 4.2. http://edgar.jrc.ec.europa.eu.

Eyring, V., Bony, S., Meehl, G. A., Senior, C. A., Stevens, B., Stouffer, R. J., & Taylor, K. E. (2016). Overview of the Coupled Model Intercomparison Project Phase 6 (CMIP6) experimental design and organization. *Geosci Model Dev*, *9*, 1937–1958. doi:10.5194/gmd-9-1937-2016.

Feng, N., & Christopher, S. A. (2015). Measurement-based estimates of direct radiative effects of absorbing aerosols above clouds. *J Geophys Res Atmos*, *120*, 6908–6921. doi:10.1002/2015jd023252.

Fillmore, D. W., Rutan, D. A., Kato, S., Rose, F. G., & Caldwell, T. E. (2022). Evaluation of aerosol optical depths and clear-sky radiative fluxes of the CERES edition 4.1 SYN1deg data product. *Atmos Chem Phys*, *22*, 10115–10137. doi:10.5194/acp-22-10115-2022.

Filonchyk, M., Hurynovich, V., Yan, H., Gusev, A., & Shpilevskaya, N. (2020). Impact

assessment of COVID-19 on variations of SO_2, NO_2, CO and AOD over East China. *Aerosol Air Qual Res*, *20*, 1530–1540. doi:10.4209/aaqr.2020.05.0226.

Filonchyk, M., Peterson, M. P., & Sun, D. (2022). Deterioration of air quality associated with the 2020 US wildfires. *Sci Total Environ*, *826*, 154103. doi:10.1016/j.scitotenv.2022.154103.

Floutsi, A. A., Korras-Carraca, M. B., Matsoukas, C., Hatzianastassiou, N., & Biskos, G. (2016). Climatology and trends of aerosol optical depth over the Mediterranean basin during the last 12 years (2002–2014) based on collection 006 MODIS-Aqua data. *Sci Total Environ*, *551-552*, 292–303. doi:10.1016/j.scitotenv.2016.01.192.

Forster et al. (2021). The Earth's energy budget, climate feedbacks, and climate sensitivity. In *Climate Change 2021: The Physical Science Basis. Contribution of Working Group I to the Sixth Assessment Report of the Intergovernmental Panel on Climate Change* (pp. 923–1054). Cambridge, United Kingdom and New York, NY, USA: Cambridge University Press. doi:10.1017/9781009157896.009.

Fu, Q., Lesins, G., Higgins, J., Charlock, T., Chylek, P., & Michalsky, J. (1998). Broadband water vapor absorption of solar radiation tested using ARM data. *Geophys Res Lett*, *25*, 1169–1172. doi:10.1029/98gl00846.

Gaiero, D., Simonella, L., Gassó, S., Gili, S., Stein, A., Sosa, P., Becchio, R., Arce, J., & Marelli, H. (2013). Ground/satellite observations and atmospheric modeling of dust storms originating in the high Puna-Altiplano deserts (South America): Implications for the interpretation of paleo-climatic archives. *J Geophys Res Atmos*, *118*, 3817–3831. doi:10.1002/jgrd.50036.

García et al. (2008). Validation of AERONET estimates of atmospheric solar fluxes and aerosol radiative forcing by ground-based broadband measurements. *J Geophys Res Atmos*, *113*, D21207. doi:10.1029/2008jd010211.

García, O., Díaz, J., Expósito, F., Díaz, A., Dubovik, O., Derimian, Y., Dubuisson, P., & Roger, J.-C. (2012). Shortwave radiative forcing and efficiency of key aerosol types using AERONET data. *Atmos Chem Phys*, *12*, 5129–5145. doi:10.5194/acp-12-5129-2012.

Gautam, R., Hsu, N. C., Eck, T. F., Holben, B. N., Janjai, S., Jantarach, T., Tsay, S.-C., & Lau, W. K. (2013). Characterization of aerosols over the Indochina peninsula from

satellite-surface observations during biomass burning pre-monsoon season. *Atmos Environ*, *78*, 51–59. doi:10.1016/j.atmosenv.2012.05.038.

Gelaro et al. (2017). The Modern-Era Retrospective Analysis for Research and Applications, Version 2 (MERRA-2). *J Clim*, *30*, 5419–5454. doi:10.1175/jcli-d-16-0758.1.

Gidden et al. (2019). Global emissions pathways under different socioeconomic scenarios for use in CMIP6: A dataset of harmonized emissions trajectories through the end of the century. *Geosci Model Dev*, *12*, 1443–1475. doi:10.5194/gmd-12-1443-2019.

Giles, D. M., Holben, B. N., Eck, T. F., Sinyuk, A., Smirnov, A., Slutsker, I., Dickerson, R. R., Thompson, A. M., & Schafer, J. S. (2012). An analysis of AERONET aerosol absorption properties and classifications representative of aerosol source regions. *J Geophys Res Atmos*, *117*, 17203. doi:10.1029/2012jd018127.

Giles et al. (2011). Aerosol properties over the Indo-Gangetic Plain: A mesoscale perspective from the TIGERZ experiment. *J Geophys Res*, *116*, D18203. doi:10.1029/2011jd015809.

Giles et al. (2019). Advancements in the Aerosol Robotic Network (AERONET) version 3 database - automated near-real-time quality control algorithm with improved cloud screening for Sun photometer aerosol optical depth (AOD) measurements. *Atmos Meas Tech*, *12*, 169–209. doi:10.5194/amt-12-169-2019.

Gkikas, A., Proestakis, E., Amiridis, V., Kazadzis, S., Tomaso, E. D., Marinou, E., Hatzianastassiou, N., Kok, J. F., & García-Pando, C. P. (2022). Quantification of the dust optical depth across spatiotemporal scales with the MIDAS global dataset (2003-2017). *Atmos Chem Phys*, *22*, 3553–3578. doi:10.5194/acp-22-3553-2022.

Gliß et al. (2021). AeroCom phase III multi-model evaluation of the aerosol life cycle and optical properties using ground- and space-based remote sensing as well as surface in situ observations. *Atmos Chem Phys*, *21*, 87–128. doi:10.5194/acp-21-87-2021.

Global Modeling and Assimilation Office (GMAO) (2015a). MERRA-2 tavg1_2d_aer_Nx: 2d, 1-Hourly, Time-averaged, Single-Level, Assimilation, Aerosol Diagnostics V5.12.4, Greenbelt, MD, USA, Goddard Earth Sciences Data and Information Services Center (GES DISC). doi:10.5067/klicltz8em9d.

Global Modeling and Assimilation Office (GMAO) (2015b). MERRA-2 tavg1_2d_rad_Nx: 2d, 1-Hourly, Time-Averaged, Single-Level, Assimilation, Radiation Diagnostics V5.12.4, Greenbelt, MD, USA, Goddard Earth Sciences Data and Information Services Center (GES DISC). doi:10.5067/q9qmy5pbnv1t.

Granier et al. (2011). Evolution of anthropogenic and biomass burning emissions of air pollutants at global and regional scales during the 1980–2010 period. *Clim Change*, *109*, 163–190. doi:10.1007/s10584-011-0154-1.

Gueymard, C. A., & Yang, D. (2020). Worldwide validation of CAMS and MERRA-2 reanalysis aerosol optical depth products using 15 years of AERONET observations. *Atmos Environ*, *225*, 117216. doi:10.1016/j.atmosenv.2019.117216.

Hajima et al. (2020). Development of the MIROC-ES2L earth system model and the evaluation of biogeochemical processes and feedbacks. *Geosci Model Dev*, *13*, 2197–2244. doi:10.5194/gmd-13-2197-2020.

Hamill, P., Giordano, M., Ward, C., Giles, D., & Holben, B. (2016). An AERONET-based aerosol classification using the Mahalanobis distance. *Atmos Environ*, *140*, 213–233. doi:10.1016/j.atmosenv.2016.06.002.

He, C., Liou, K.-N., Takano, Y., Zhang, R., Zamora, M. L., Yang, P., Li, Q., & Leung, L. R. (2015). Variation of the radiative properties during black carbon aging: theoretical and experimental intercomparison. *Atmos Chem Phys*, *15*, 11967–11980. doi:10.5194/acp-15-11967-2015.

Heald, C., Ridley, D., Kroll, J., Barrett, S., Cady-Pereira, K., Alvarado, M., & Holmes, C. (2014). Contrasting the direct radiative effect and direct radiative forcing of aerosols. *Atmos Chem Phys*, *14*, 5513–5527. doi:10.5194/acp-14-5513-2014.

Held et al. (2019). Structure and performance of GFDL's CM4.0 climate model. *J Adv Model Earth Syst*, *11*, 3691–3727. doi:10.1029/2019ms001829.

Hess, M., Koepke, P., & Schult, I. (1998). Optical properties of aerosols and clouds: The software package OPAC. *Bull Am Meteorol Soc*, *79*, 831–844. doi:10.1175/1520-0477(1998)079.

Hoegh-Guldberg et al. (2018). Impacts of 1.5ºC global warming on natural and human systems. In *Global Warming of 1.5°C. An IPCC Special Report on the Impacts of*

Global Warming of 1.5°C above Pre-Industrial Levels and Related Global Greenhouse Gas Emission Pathways, in the Context of Strengthening the Global Response to the Threat of Climate Change, Sustainable Development, and Efforts to Eradicate Poverty (pp. 175–312). Cambridge, UK and New York, NY, USA: Cambridge University Press. doi:10.1017/9781009157940.005.

Hoelzemann, J. J., Longo, K. M., Fonseca, R. M., Rosário, N. M. D., Eibern, H., Freitas, S. R., & Pires, C. (2009). Regional representativity of AERONET observation sites during the biomass burning season in South America determined by correlation studies with MODIS aerosol optical depth. *J Geophys Res Atmos*, *114*, D13301. doi:10.1029/2008jd010369.

Hoesly et al. (2018). Historical (1750-2014) anthropogenic emissions of reactive gases and aerosols from the Community Emissions Data System (CEDS). *Geosci Model Dev*, *11*, 369–408. doi:10.5194/gmd-11-369-2018.

Holben et al. (1998). AERONET—A federated instrument network and data archive for aerosol characterization. *Remote Sens Environ*, *66*, 1–16. doi:10.1016/s0034-4257(98)00031-5.

Holben, B. N., Eck, T. F., Slutsker, I., Smirnov, A., Sinyuk, A., Schafer, J., Giles, D., & Dubovik, O. (2006). AERONET's version 2.0 quality assurance criteria. In S.-C. Tsay, T. Nakajima, R. P. Singh, & R. Sridharan (Eds.), *Remote Sensing of the Atmosphere and Clouds* (p. 64080Q). International Society for Optics and Photonics SPIE volume 6408. doi:10.1117/12.706524.

Holben et al. (2001). An emerging ground-based aerosol climatology: Aerosol optical depth from AERONET. *J Geophys Res Atmos*, *106*, 12067–12097. doi:10.1029/2001jd900014.

Hu, R. M., Martin, R. V., & Fairlie, T. D. (2007). Global retrieval of columnar aerosol single scattering albedo from space-based observations. *J Geophys Res Atmos*, *112*, 2204. doi:10.1029/2005jd006832.

Huang, K., Fu, J. S., Lin, N. H., Wang, S. H., Dong, X., & Wang, G. (2019). Superposition of Gobi dust and Southeast Asian biomass burning: The effect of multisource long-range transport on aerosol optical properties and regional meteorology modification. *J Geophys Res Atmos*, *124*, 9464–9483. doi:10.1029/2018jd030241.

Inness et al. (2019). The CAMS reanalysis of atmospheric composition. *Atmos Chem Phys*, *19*, 3515–3556. doi:10.5194/acp-19-3515-2019.

IPCC (2021). In *Climate Change 2021 – The Physical Science Basis: Working Group I Contribution to the Sixth Assessment Report of the Intergovernmental Panel on Climate Change* (p. 923–1054). Cambridge University Press.

Jacobson, M. Z. (2001). Strong radiative heating due to the mixing state of black carbon in atmospheric aerosols. *Nature*, *409*, 695–697. doi:10.1038/35055518.

Jaenicke, R. (1993). Chapter 1 Tropospheric Aerosols. In P. V. Hobbs (Ed.), *Aerosol–Cloud–Climate Interactions* (pp. 1–31). Academic Press volume 54 of *International Geophysics*. doi:10.1016/S0074-6142(08)60210-7.

Jethva, H., Chand, D., Torres, O., Gupta, P., Lyapustin, A., & Patadia, F. (2018). Agricultural burning and air quality over northern India: A synergistic analysis using NASA's A-train satellite data and ground measurements. *Aerosol Air Qual Res*, *18*, 1756–1773. doi:10.4209/aaqr.2017.12.0583.

Jethva, H., & Torres, O. (2011). Satellite-based evidence of wavelength-dependent aerosol absorption in biomass burning smoke inferred from Ozone Monitoring Instrument. *Atmos Chem Phys*, *11*, 10541–10551. doi:10.5194/acp-11-10541-2011.

Jethva, H., & Torres, O. (2019). A comparative evaluation of Aura-OMI and SKYNET near-UV single-scattering albedo products. *Atmos Meas Tech*, *12*, 6489–6503. doi:10.5194/amt-12-6489-2019.

Jethva, H., Torres, O., Field, R. D., Lyapustin, A., Gautam, R., & Kayetha, V. (2019). Connecting crop productivity, residue fires, and air quality over northern India. *Sci Rep*, *9*, 16594. doi:10.1038/s41598-019-52799-x.

Jin, S., Ma, Y., Huang, Z., Huang, J., Gong, W., Liu, B., Wang, W., Fan, R., & Li, H. (2023). A comprehensive reappraisal of long-term aerosol characteristics, trends, and variability in Asia. *Atmos Chem Phys*, *23*, 8187–8210. doi:10.5194/acp-23-8187-2023.

Jouan, C., & Myhre, G. (2024). Satellite-based analysis of top of atmosphere shortwave radiative forcing trend induced by biomass burning aerosols over South-Eastern Atlantic. *npj Clim Atmos Sci*, *7*, 129. doi:10.1038/s41612-024-00631-3.

Kaiser et al. (2012). Biomass burning emissions estimated with a global fire assimilation system based on observed fire radiative power. *Biogeosciences*, *9*, 527–554. doi:10.5194/bg-9-527-2012.

Kassianov et al. (2025). Radiative impact of record-breaking wildfires from integrated ground-based data. *Sci Rep*, *15*, 8262. doi:10.1038/s41598-025-85103-1.

Kasten, F., & Young, A. T. (1989). Revised optical air mass tables and approximation formula. *Applied optics*, *28*, 4735–4738. doi:10.1364/ao.28.004735.

Kedia, S., Ramachandran, S., Holben, B. N., & Tripathi, S. N. (2014). Quantification of aerosol type, and sources of aerosols over the Indo-Gangetic Plain. *Atmos Environ*, *98*, 607–619. doi:10.1016/j.atmosenv.2014.09.022.

Keil, A., & Haywood, J. M. (2003). Solar radiative forcing by biomass burning aerosol particles during SAFARI 2000: A case study based on measured aerosol and cloud properties. *J Geophys Res Atmos*, *108*. doi:10.1029/2002jd002315.

Kelesidis et al. (2025). Radiative cooling in New York/New Jersey metropolitan areas by wildfire particulate matter emitted from the Canadian wildfires of 2023. *Commun Earth Environ*, *6*, 304. doi:10.1038/s43247-025-02214-3.

Kelesidis, G. A., Neubauer, D., Fan, L.-S., Lohmann, U., & Pratsinis, S. E. (2022). Enhanced light absorption and radiative forcing by black carbon agglomerates. *Environ Sci Technol*, *56*, 8610–8618. doi:10.1021/acs.est.2c00428.

Kirchstetter, T. W., Novakov, T., & Hobbs, P. V. (2004). Evidence that the spectral dependence of light absorption by aerosols is affected by organic carbon. *J Geophys Res Atmos*, *109*, D21208. doi:10.1029/2004jd004999.

Kirillova, E. N., Marinoni, A., Bonasoni, P., Vuillermoz, E., Facchini, M. C., Fuzzi, S., & Decesari, S. (2016). Light absorption properties of brown carbon in the high Himalayas. *J Geophys Res Atmos*, *121*, 9621–9639. doi:10.1002/2016jd025030.

Kok, J. F., Storelvmo, T., Karydis, V. A., Adebiyi, A. A., Mahowald, N. M., Evan, A. T., He, C., & Leung, D. M. (2023). Mineral dust aerosol impacts on global climate and climate change. *Nat Rev Earth Environ*, *4*, 71–86. doi:10.1038/s43017-022-00379-5.

Kumar, M., Parmar, K., Kumar, D., Mhawish, A., Broday, D., Mall, R., & Banerjee, T. (2018). Long-term aerosol climatology over Indo-Gangetic Plain: Trend, prediction

and potential source fields. *Atmos Environ*, *180*, 37–50. doi:10.1016/j.atmosenv.2018.02.027.

Lacis, A. A., & Oinas, V. (1991). A description of the correlated k distribution method for modeling nongray gaseous absorption, thermal emission, and multiple scattering in vertically inhomogeneous atmospheres. *J Geophys Res Atmos*, *96*, 9027–9063. doi:10.1029/90jd01945.

Lee, J., Kim, J., Song, C., Kim, S., Chun, Y., Sohn, B., & Holben, B. (2010). Characteristics of aerosol types from AERONET sunphotometer measurements. *Atmos Environ*, *44*, 3110–3117. doi:10.1016/j.atmosenv.2010.05.035.

Levy, R. C., Mattoo, S., Munchak, L. A., Remer, L. A., Sayer, A. M., Patadia, F., & Hsu, N. C. (2013). The collection 6 MODIS aerosol products over land and ocean. *Atmos Meas Tech*, *6*, 2989–3034. doi:10.5194/amt-6-2989-2013.

Levy, R. C., Remer, L. A., Kleidman, R. G., Mattoo, S., Ichoku, C., Kahn, R., & Eck, T. F. (2010). Global evaluation of the collection 5 MODIS dark-target aerosol products over land. *Atmos Chem Phys*, *10*, 10399–10420. doi:10.5194/acp-10-10399-2010.

Li et al. (2017). India is overtaking China as the World's largest emitter of anthropogenic sulfur dioxide. *Sci Rep*, *7*, 14304. doi:10.1038/s41598-017-14639-8.

Li et al. (2022). Scattering and absorbing aerosols in the climate system. *Nat Rev Earth Environ*, *3*, 363–379. doi:10.1038/s43017-022-00296-7.

Li et al. (2019). Retrieval of aerosol components directly from satellite and ground-based measurements. *Atmos Chem Phys*, *19*, 13409–13443. doi:10.5194/acp-19-13409-2019.

Li, W., Wang, Y., Yi, Z., Guo, B., Chen, W., Che, H., & Zhang, X. (2024). Evaluation of MERRA-2 and CAMS reanalysis for black carbon aerosol in China. *Environ Poll*, *343*, 123182. doi:10.1016/j.envpol.2023.123182.

Li et al. (2016). Aerosol and monsoon climate interactions over Asia. *Rev Geophys*, *54*, 866–929. doi:10.1002/2015rg000500.

Logan, T., Xi, B., Dong, X., Li, Z., & Cribb, M. (2013). Classification and investigation of Asian aerosol absorptive properties. *Atmos Chem Phys*, *13*, 2253–2265. doi:10.5194/acp-13-2253-2013.

Logothetis, S.-A., Salamalikis, V., & Kazantzidis, A. (2020). Aerosol classification in Europe, Middle East, North Africa and Arabian Peninsula based on AERONET version 3. *Atmos Res*, *239*, 104893. doi:10.1016/j.atmosres.2020.104893.

Lu, F., Chen, S., Hu, Z., Han, Z., Alam, K., Luo, H., Bi, H., Chen, J., & Guo, X. (2023). Sensitivity and uncertainties assessment in radiative forcing due to aerosol optical properties in diverse locations in China. *Sci Total Environ*, *860*, 160447. doi:10.1016/j.scitotenv.2022.160447.

Mallet, M., Dubovik, O., Nabat, P., Dulac, F., Kahn, R., Sciare, J., Paronis, D., & Léon, J. F. (2013). Absorption properties of Mediterranean aerosols obtained from multi-year ground-based remote sensing observations. *Atmos Chem Phys*, *13*, 9195–9210. doi:10.5194/acp-13-9195-2013.

Mensink, C., Gong, W., & Hakami, A. (Eds.) (2020). *Air pollution modeling and its application XXVI*. Springer International Publishing. doi:10.1007/978-3-030-22055-6.

Mhawish, A., Banerjee, T., Sorek-Hamer, M., Lyapustin, A., Broday, D. M., & Chatfield, R. (2019). Comparison and evaluation of MODIS Multi-angle Implementation of Atmospheric Correction (MAIAC) aerosol product over South Asia. *Remote Sens Environ*, *224*, 12–28. doi:10.1016/j.rse.2019.01.033.

Mhawish et al. (2021). Aerosol characteristics from earth observation systems: A comprehensive investigation over South Asia (2000–2019). *Remote Sens Environ*, *259*, 112410. doi:10.1016/j.rse.2021.112410.

Mortier, A., Goloub, P., Derimian, Y., Tanré, D., Podvin, T., Blarel, L., Deroo, C., Marticorena, B., Diallo, A., & Ndiaye, T. (2016). Climatology of aerosol properties and clear-sky shortwave radiative effects using Lidar and Sun photometer observations in the Dakar site. *J Geophys Res Atmos*, *121*, 6489–6510. doi:10.1002/2015jd024588.

Myhre et al. (2017). Multi-model simulations of aerosol and ozone radiative forcing due to anthropogenic emission changes during the period 1990–2015. *Atmos Chem Phys*, *17*, 2709–2720. doi:10.5194/acp-17-2709-2017.

Myhre et al. (2013a). Radiative forcing of the direct aerosol effect from AeroCom phase II simulations. *Atmos Chem Phys*, *13*, 1853–1877. doi:10.5194/acp-13-1853-2013.

Myhre et al. (2013b). Anthropogenic and natural radiative forcing. In T. Stocker, D. Qin, G.-K. Plattner, M. Tignor, S. Allen, J. Boschung, A. Nauels, Y. Xia, V. Bex, & P. Midgley (Eds.), *Climate Change 2013: The Physical Science Basis. Contribution of Working Group I to the Fifth Assessment Report of the Intergovernmental Panel on Climate Change*. Cambridge, United Kingdom and New York, NY, USA: Cambridge University Press. doi:10.1017/cbo9781107415324.018.

Nakajima, T., & Tanaka, M. (1988). Algorithms for radiative intensity calculations in moderately thick atmospheres using a truncation approximation. *J Quant Spectrosc Radiat Transf*, *40*, 51–69. doi:10.1016/0022-4073(88)90031-3.

Nam, J., Kim, S.-W., Park, R. J., Park, J.-S., & Park, S. S. (2018). Changes in column aerosol optical depth and ground-level particulate matter concentration over East Asia. *Air Qual Atmos Health*, *11*, 49–60. doi:10.1007/s11869-017-0517-5.

NASA/LARC/SD/ASDC (2017). CERES and GEO-Enhanced TOA, within-atmosphere and surface fluxes, clouds and aerosols 1-hourly Terra-Aqua edition4A. Available at: https://doi.org/10.5067/terra+aqua/ceres/syn1deg-1hour_l3.004a.

Nguyen, T. T., Pham, H. V., Lasko, K., Bui, M. T., Laffly, D., Jourdan, A., & Bui, H. Q. (2019). Spatiotemporal analysis of ground and satellite-based aerosol for air quality assessment in the Southeast Asia region. *Environ Poll*, *255*, 113106. doi:10.1016/j.envpol.2019.113106.

O'Neill, N. T., Eck, T. F., Smirnov, A., Holben, B. N., & Thulasiraman, S. (2003). Spectral discrimination of coarse and fine mode optical depth. *J Geophys Res Atmos*, *108*, 4559. doi:10.1029/2002jd002975.

Ou et al. (2022). Evaluation of MERRA-2 aerosol optical and component properties over China using SONET and PARASOL/GRASP data. *Remote Sens*, *14*, 821. doi:10.3390/rs14040821.

Pan, X., Chin, M., Ichoku, C. M., & Field, R. D. (2018). Connecting Indonesian fires and drought with the type of El Niño and phase of the Indian ocean dipole during 1979–2016. *J Geophys Res Atmos*, *123*, 7974–7988. doi:10.1029/2018jd028402.

Papachristopoulou, K., Raptis, I.-P., Gkikas, A., Fountoulakis, I., Masoom, A., & Kazadzis, S. (2022). Aerosol optical depth regime over megacities of the world. *Atmos Chem Phys*, *22*, 15703–15727. doi:10.5194/acp-22-15703-2022.

Persad et al. (2023). Rapidly evolving aerosol emissions are a dangerous omission from near-term climate risk assessments. *Environ Res: Climate*, *2*, 032001. doi:10.1088/2752-5295/acd6af.

Platnick, S., Hubanks, P., Meyer, K., & King, M. D. (2015). MODIS atmosphere L3 monthly product (08_L3). NASA MODIS Adaptive Processing System, Goddard Space Flight Center. Available at: http://dx.doi.org/10.5067/modis/mod08_m3.006 (Terra), http://dx.doi.org/10.5067/modis/myd08_m3.006 (Aqua).

Popp et al. (2016). Development, production and evaluation of aerosol climate data records from European satellite observations (Aerosol_cci). *Remote Sens*, *8*, 421. doi:10.3390/rs8050421.

Quaas et al. (2022). Robust evidence for reversal of the trend in aerosol effective climate forcing. *Atmos Chem Phys*, *22*, 12221–12239. doi:10.5194/acp-22-12221-2022.

Ramachandran, S. (2018). Atmospheric aerosols: Characteristics and radiative effects. *CRC Press*, (pp. 1–276). doi:10.1201/9781315152400.

Ramachandran, S., & Ansari, K. (2025). Influence of changes in anthropogenic and natural sources on global aerosol optical depth during COVID-19 lockdown: Ground-based observations, satellites, models. *Atmos Environ*, *343*, 120948. doi:10.1016/j.atmosenv.2024.120948.

Ramachandran, S., Ansari, K., & Cherian, R. (2025). Air pollution to atmospheric warming: Effects of increasing anthropogenic aerosols on South Asia's climate. *Earth Syst Environ*, . doi:10.1007/s41748-025-00732-w.

Ramachandran, S., & Kedia, S. (2010). Black carbon aerosols over an urban region: Radiative forcing and climate impact. *J Geophys Res Atmos*, *115*, D10202. doi:10.1029/2009jd013560.

Ramachandran, S., & Kedia, S. (2012). Radiative effects of aerosols over Indo-Gangetic plain: environmental (urban vs. rural) and seasonal variations. *Environ Sci Pollut Res*, *19*, 2159–2171. doi:10.1007/s11356-011-0715-x.

Ramachandran, S., & Rupakheti, M. (2020). Year-round aerosol characteristics and radiative effects in the South Asian pollution outflow over a background site in the Maldives. *Atmos Environ*, *240*, 117813. doi:10.1016/j.atmosenv.2020.117813.

Ramachandran, S., & Rupakheti, M. (2022a). Trends in physical, optical and chemical columnar aerosol characteristics and radiative effects over South and East Asia: Satellite and ground-based observations. *Gondwana Res*, *105*, 366–387. doi:10.1016/j.gr.2021.09.016.

Ramachandran, S., & Rupakheti, M. (2022b). Trends in the types and absorption characteristics of ambient aerosols over the Indo-Gangetic Plain and North China Plain in last two decades. *Sci Total Environ*, *831*, 154867. doi:10.1016/j.scitotenv.2022.154867.

Ramachandran, S., Rupakheti, M., & Cherian, R. (2022). Insights into recent aerosol trends over Asia from observations and CMIP6 simulations. *Sci Total Environ*, *807*, 150756. doi:10.1016/j.scitotenv.2021.150756.

Ramachandran, S., Rupakheti, M., Cherian, R., & Lawrence, M. G. (2023). Aerosols heat up the Himalayan climate. *Sci Total Environ*, *894*, 164733. doi:10.1016/j.scitotenv.2023.164733.

Ramachandran, S., Rupakheti, M., & Lawrence, M. G. (2020a). Aerosol-induced atmospheric heating rate decreases over South and East Asia as a result of changing content and composition. *Sci Rep*, *10*, 1–17. doi:10.1038/s41598-020-76936-z.

Ramachandran, S., Rupakheti, M., & Lawrence, M. G. (2020b). Black carbon dominates the aerosol absorption over the Indo-Gangetic Plain and the Himalayan foothills. *Environ Int*, *142*, 105814. doi:10.1016/j.envint.2020.105814.

Ramaswamy et al. (2019). Radiative forcing of climate: The historical evolution of the radiative forcing concept, the forcing agents and their quantification, and applications. *Meteorological Monographs*, *59*, 14.1–14.101. doi:10.1175/amsmonographs-d-19-0001.1.

Randles et al. (2017). The MERRA-2 aerosol reanalysis, 1980 onward. Part I: System description and data assimilation evaluation. *J Clim*, *30*, 6823–6850. doi:10.1175/jcli-d-16-0609.1.

Reid et al. (2013). Observing and understanding the Southeast Asian aerosol system by remote sensing: An initial review and analysis for the Seven Southeast Asian Studies (7SEAS) program. *Atmos Res*, *122*, 403–468. doi:10.1016/j.atmosres.2012.06.005.

Ren et al. (2025). Black carbon emissions generally underestimated in the global south as revealed by globally distributed measurements. *Nat Commun*, *16*, 7010. doi:10.1038/s41467-025-62468-5.

Ricchiazzi, P., Yang, S., Gautier, C., & Sowle, D. (1998). SBDART: A research and teaching software tool for plane-parallel radiative transfer in the Earth's atmosphere. *Bull Am Meteorol Soc*, *79*, 2101–2114. doi:10.1175/1520-0477(1998)079<2101:sarats>2.0.co;2.

Rupakheti, D., Kang, S., Rupakheti, M., Cong, Z., Panday, A. K., & Holben, B. N. (2019). Identification of absorbing aerosol types at a site in the northern edge of Indo-Gangetic Plain and a polluted valley in the foothills of the central Himalayas. *Atmos Res*, *223*, 15–23. doi:10.1016/j.atmosres.2019.03.003.

Rupakheti, D., Rupakheti, M., Abdullaev, S. F., Yin, X., & Kang, S. (2020). Columnar aerosol properties and radiative effects over Dushanbe, Tajikistan in Central Asia. *Environ Poll*, *265*, 114872. doi:10.1016/j.envpol.2020.114872.

Rupakheti et al. (2023). Characterization of columnar aerosol over a background site in Central Asia. *Environ Poll*, *316*, 120501. doi:10.1016/j.envpol.2022.120501.

Russell et al. (2014). A multiparameter aerosol classification method and its application to retrievals from spaceborne polarimetry. *J Geophys Res Atmos*, *119*, 9838–9863. doi:10.1002/2013jd021411.

Rutan, D. A., Kato, S., Doelling, D. R., Rose, F. G., Nguyen, L. T., Caldwell, T. E., & Loeb, N. G. (2015). CERES synoptic product: Methodology and validation of surface radiant flux. *J Atmos Ocean Technol*, *32*, 1121–1143. doi:10.1175/jtech-d-14-00165.1.

Ríos, B., & Raga, G. B. (2018). Spatio-temporal distribution of burned areas by ecoregions in Mexico and Central America. *Int J Remote Sens*, *39*, 949–970. doi:10.1080/01431161.2017.1392641.

Salamalikis, V., Vamvakas, I., Blanc, P., & Kazantzidis, A. (2021). Ground-based validation of aerosol optical depth from CAMS reanalysis project: An uncertainty input on direct normal irradiance under cloud-free conditions. *Renew Energy*, *170*, 847–857. doi:10.1016/j.renene.2021.02.025.

Samset, B. H., Lund, M. T., Bollasina, M., Myhre, G., & Wilcox, L. (2019). Emerging Asian aerosol patterns. *Nat Geosci*, *12*, 582–584. doi:10.1038/s41561-019-0424-5.

Samset, B. H., Stjern, C. W., Andrews, E., Kahn, R. A., Myhre, G., Schulz, M., & Schuster, G. L. (2018). Aerosol absorption: Progress towards global and regional constraints. *Curr Clim Change Rep*, *4*, 65–83. doi:10.1007/s40641-018-0091-4.

Samset et al. (2025). East Asian aerosol cleanup has likely contributed to the recent acceleration in global warming. *Commun Earth Environ*, *6*, 543. doi:10.1038/s43247-025-02527-3.

Schafer et al. (2014). Intercomparison of aerosol single-scattering albedo derived from AERONET surface radiometers and LARGE in situ aircraft profiles during the 2011 DRAGON-MD and DISCOVER-AQ experiments. *J Geophys Res Atmos*, *119*, 7439–7452. doi:10.1002/2013jd021166.

Schuster, G. L., Dubovik, O., & Arola, A. (2016). Remote sensing of soot carbon – Part 1: Distinguishing different absorbing aerosol species. *Atmos Chem Phys*, *16*, 1565–1585. doi:10.5194/acp-16-1565-2016.

Schutgens et al. (2021). AEROCOM and AEROSAT AAOD and SSA study – Part 1: Evaluation and intercomparison of satellite measurements. *Atmos Chem Phys*, *21*, 6895–6917. doi:10.5194/acp-21-6895-2021.

Schutgens et al. (2020). An AeroCom–AeroSat study: Intercomparison of satellite AOD datasets for aerosol model evaluation. *Atmos Chem Phys*, *20*, 12431–12457. doi:10.5194/acp-20-12431-2020.

Schutgens, N., Tsyro, S., Gryspeerdt, E., Goto, D., Weigum, N., Schulz, M., & Stier, P. (2017). On the spatio-temporal representativeness of observations. *Atmos Chem Phys*, *17*, 9761–9780. doi:10.5194/acp-17-9761-2017.

Seinfeld, J. H., & Pandis, S. N. (2016). *Atmospheric chemistry and physics: From air pollution to climate change*. (3rd ed.). John Wiley & Sons.

Seland et al. (2020). Overview of the Norwegian Earth System Model (NorESM2) and key climate response of CMIP6 DECK, historical, and scenario simulations. *Geosci Model Dev*, *13*, 6165–6200. doi:10.5194/gmd-13-6165-2020.

Shindell et al. (2013). Radiative forcing in the ACCMIP historical and future climate simulations. *Atmos Chem Phys*, *13*, 2939–2974. doi:10.5194/acp-13-2939-2013.

Sinyuk, A., Holben, B. N., Eck, T. F., Giles, D. M., Slutsker, I., Korkin, S., Schafer, J. S., Smirnov, A., Sorokin, M., & Lyapustin, A. (2020). The AERONET version 3 aerosol retrieval algorithm, associated uncertainties and comparisons to version 2. *Atmos Meas Tech*, *13*, 3375–3411. doi:10.5194/amt-13-3375-2020.

Smaran, M., & Vinoj, V. (2024). Evaluation of background black carbon concentration in India. *Aerosol Air Qual Res*, *24*, 230300. doi:10.4209/aaqr.230300.

Smirnov, A., Holben, B. N., Eck, T. F., Dubovik, O., & Slutsker, I. (2000). Cloud-screening and quality control algorithms for the AERONET database. *Remote Sens Environ*, *73*, 337–349. doi:10.1016/s0034-4257(00)00109-7.

Song, Q., Zhang, Z., Yu, H., Ginoux, P., & Shen, J. (2021). Global dust optical depth climatology derived from CALIOP and MODIS aerosol retrievals on decadal timescales: Regional and interannual variability. *Atmos Chem Phys*, *21*, 13369–13395. doi:10.5194/acp-21-13369-2021.

Su, X., Huang, Y., Wang, L., Cao, M., & Feng, L. (2023). Validation and diurnal variation evaluation of MERRA-2 multiple aerosol properties on a global scale. *Atmos Environ*, *311*, 120019. doi:10.1016/j.atmosenv.2023.120019.

Sun, E., Xu, X., Che, H., Tang, Z., Gui, K., An, L., Lu, C., & Shi, G. (2019). Variation in MERRA-2 aerosol optical depth and absorption aerosol optical depth over China from 1980 to 2017. *J Atmos Sol Terr Phys*, *186*, 8–19. doi:10.1016/j.jastp.2019.01.019.

Swart et al. (2019). The Canadian Earth System Model version 5 (CanESM5.0.3). *Geosci Model Dev*, *12*, 4823–4873. doi:10.5194/gmd-12-4823-2019.

Tanada, K., Murakami, H., Hayasaka, T., & Yoshida, M. (2023). Aerosol optical properties of extreme global wildfires and estimated radiative forcing with GCOM-C SGLI. *J Geophys Res Atmos*, *128*, e2022JD037914. doi:10.1029/2022jd037914.

Thorsen, T. J., Ferrare, R. A., Kato, S., & Winker, D. M. (2020). Aerosol direct radiative effect sensitivity analysis. *J Clim*, *33*, 6119–6139. doi:10.1175/jcli-d-19-0669.1.

Tian, P., Yu, Z., Cui, C., Huang, J., Kang, C., Shi, J., Cao, X., & Zhang, L. (2023). Atmospheric aerosol size distribution impacts radiative effects over the Himalayas via

modulating aerosol single-scattering albedo. *npj Clim Atmos Sci*, *6*, 54. doi:10.1038/s41612-023-00368-5.

Tian et al. (2018). Radiative absorption enhancement of dust mixed with anthropogenic pollution over East Asia. *Atmos Chem Phys*, *18*, 7815–7825. doi:10.5194/acp-18-7815-2018.

Torres, O., & Ahn, C. (2024). Local and regional diurnal variability of aerosol properties retrieved by DSCOVR/EPIC UV algorithm. *J Geophys Res Atmos*, *129*, e2023JD039908. doi:10.1029/2023jd039908.

Wagner, F., & Silva, A. M. (2008). Some considerations about Ångström exponent distributions. *Atmos Chem Phys*, *8*, 481–489. doi:10.5194/acp-8-481-2008.

Wang, Z., Lin, L., Xu, Y., Che, H., Zhang, X., Zhang, H., Dong, W., Wang, C., Gui, K., & Xie, B. (2021). Incorrect Asian aerosols affecting the attribution and projection of regional climate change in CMIP6 models. *npj Clim Atmos Sci*, *4*, 1–8. doi:10.1038/s41612-020-00159-2.

Wei, L., Lu, Z., Wang, Y., Liu, X., Wang, W., Wu, C., Zhao, X., Rahimi, S., Xia, W., & Jiang, Y. (2022). Black carbon-climate interactions regulate dust burdens over India revealed during COVID-19. *Nat Commun*, *13*, 1839. doi:10.1038/s41467-022-29468-1.

Wei, X., Cui, Q., Ma, L., Zhang, F., Li, W., & Liu, P. (2024). Global aerosol-type classification using a new hybrid algorithm and Aerosol Robotic Network data. *Atmos Chem Phys*, *24*, 5025–5045. doi:10.5194/acp-24-5025-2024.

Whitby, K. T. (1978). The physical characteristics of sulfur aerosols. *Atmos Environ*, *12*, 135–159. doi:10.1016/0004-6981(78)90196-8.

Wilcox, E. (2010). Stratocumulus cloud thickening beneath layers of absorbing smoke aerosol. *Atmos Chem Phys*, *10*, 11769–11777. doi:10.5194/acp-10-11769-2010.

Wilcox, E. (2012). Direct and semi-direct radiative forcing of smoke aerosols over clouds. *Atmos Chem Phys*, *12*, 139–149. doi:10.5194/acp-12-139-2012.

Xian et al. (2024). Intercomparison of aerosol optical depths from four reanalyses and their multi-reanalysis consensus. *Atmos Chem Phys*, *24*, 6385–6411. doi:10.5194/acp-24-6385-2024.

Xie et al. (2020). Contrasting mixing state of black carbon-containing particles in summer and winter in Beijing. *Environ Poll*, *263*, 114455. doi:10.1016/j.envpol.2020.114455.

Xu, X., Xie, L., Yang, X., Wu, H., Cai, L., & Qi, P. (2020). Aerosol optical properties at seven AERONET sites over Middle East and Eastern Mediterranean Sea. *Atmos Environ*, *243*, 117884. doi:10.1016/j.atmosenv.2020.117884.

Xue, Z., Udaysankar, N., & Christopher, S. A. (2025). An investigation of the impact of Canadian wildfires on US air quality using model, satellite, and ground measurements. *Atmos Chem Phys*, *25*, 5497–5517. doi:10.5194/acp-25-5497-2025.

Yang, X., Zhao, C., Yang, Y., & Fan, H. (2021). Long-term multi-source data analysis about the characteristics of aerosol optical properties and types over Australia. *Atmos Chem Phys*, *21*, 3803–3825. doi:10.5194/acp-21-3803-2021.

Yu, Y., Notaro, M., Kalashnikova, O. V., & Garay, M. J. (2016). Climatology of summer Shamal wind in the Middle East. *J Geophys Res Atmos*, *121*, 289–305. doi:10.1002/2015jd024063.

Zhang, H., Shen, Z., Wei, X., Zhang, M., & Li, Z. (2012). Comparison of optical properties of nitrate and sulfate aerosol and the direct radiative forcing due to nitrate in China. *Atmos Res*, *113*, 113–125. doi:10.1016/j.atmosres.2012.04.020.

Zhang, L., Li, J., Jiang, Z., Dong, Y., Ying, T., & Zhang, Z. (2022). Clear-sky direct aerosol radiative forcing uncertainty associated with aerosol optical properties based on CMIP6 models. *J Clim*, *35*, 3007–3019. doi:10.1175/jcli-d-21-0479.1.

Zhang et al. (2019). Drivers of improved $PM_{2.5}$ air quality in China from 2013 to 2017. *Proc Natl Acad Sci*, *116*, 24463–24469. doi:10.1073/pnas.1907956116.

Zhang et al. (2024). Aerosol components derived from global AERONET measurements by GRASP: A new value-added aerosol component global dataset and its application. *Bull Am Meteorol Soc*, *105*, E1822–E1848. doi:10.1175/bams-D-23-0260.1.

Zhang, Z., Meyer, K., Yu, H., Platnick, S., Colarco, P., Liu, Z., & Oreopoulos, L. (2016). Shortwave direct radiative effects of above-cloud aerosols over global oceans derived from 8 years of CALIOP and MODIS observations. *Atmos Chem Phys*, *16*, 2877–2900. doi:10.5194/acp-16-2877-2016.

Zhao, A. D., Stevenson, D. S., & Bollasina, M. A. (2019). The role of anthropogenic aerosols in future precipitation extremes over the Asian monsoon region. *Clim Dyn*, *52*, 6257–6278. doi:10.1007/s00382-018-4514-7.

Zhao et al. (2018). Intra-annual variations of regional aerosol optical depth, vertical distribution, and particle types from multiple satellite and ground-based observational datasets. *Atmos Chem Phys*, *18*, 11247–11260. doi:10.5194/acp-18-11247-2018.

Zhao et al. (2024). Relative contributions of component-segregated aerosols to trends in aerosol optical depth over land (2007–2019): Insights from CAMS aerosol reanalysis. *Atmos Environ*, *333*, 120676. doi:10.1016/j.atmosenv.2024.120676.

Zheng et al. (2018). Trends in China's anthropogenic emissions since 2010 as the consequence of clean air actions. *Atmos Chem Phys*, *18*, 14095–14111. doi:10.5194/acp-18-14095-2018.

Zhou, P., Wang, Y., Liu, J., Xu, L., Chen, X., & Zhang, L. (2023). Difference between global and regional aerosol model classifications and associated implications for spaceborne aerosol optical depth retrieval. *Atmos Environ*, *300*, 119674. doi:10.1016/j.atmosenv.2023.119674.

List of Publications

Included in thesis

1. **Ansari, K.**, & Ramachandran, S. (2023). Aerosol characteristics over Indo-Gangetic Plain from Ground-based AERONET and MERRA-2/CAMS model simulations. *Atmos Environ, 293*, 119434. doi:10.1016/j.atmosenv.2022.119434
2. **Ansari, K.**, & Ramachandran, S. (2023). Radiative effects of absorbing aerosol types over South Asia. *Sci Total Environ, 858*, 159969. doi:10.1016/j.scitotenv.2022.159969
3. **Ansari, K.**, & Ramachandran, S. (2024). Optical and physical characteristics of aerosols over Asia: AERONET, MERRA-2 and CAMS. *Atmos Environ, 326*, 120470. doi:10.1016/j.atmosenv.2024.120470
4. **Ansari, K.**, & Ramachandran, S. (2024). Global changes in aerosol single scattering albedo during COVID-19. *Atmos Environ, 333*, 120649. doi:10.1016/j.atmosenv.2024.120649
5. **Ansari, K.**, & Ramachandran, S. (2025). Global insights on absorption characteristics of aerosols. *Sci Total Environ, 959*, 178178. doi:10.1016/j.scitotenv.2024.178178
6. **Ansari, K.**, & Ramachandran, S. (2025). Enhancing accuracy in identifying absorbing aerosol types and their radiative impacts. *npj Clim Atmos Sci, 8*, 351. doi:10.1038/s41612-025-01167-w.
7. **Ansari, K.**, Ramachandran, S., & Cherian, R. (2025). Global Assessment of Aerosol Radiative Effects: New Insights from Observations, Reanalysis, and Climate Models. *Sci Total Environ, 1006*, 180871. doi:10.1016/j.scitotenv.2025.180871
8. **Ansari, K.**, & Ramachandran, S. Global classification of aerosol types and their radiative effects. *Sci Total Environ*. *(Under preparation)*

Not included in thesis

9. Ramachandran, S., & **Ansari, K.** (2025). Influence of changes in anthropogenic and natural sources on global aerosol optical depth during COVID-19 lockdown: Ground-

based observations, satellites, models. *Atmos Environ, 343*, 120948. doi:10.1016/j.atmosenv.2024.120948

10. Ramachandran, S., **Ansari, K.**, & Cherian, R. (2025). Air Pollution to Atmospheric Warming: Effects of Increasing Anthropogenic Aerosols on South Asia's Climate. *Earth Syst Environ*. doi:10.1007/s41748-025-00732-w

Conference Proceedings

1. **Ansari, K.**, & Ramachandran, S. (2022). Aerosol-induced Atmospheric Radiative Forcing and Heating Rate over South Asia increase due to Black Carbon (BC) and BC mixed with dust. In American Geophysical Union (AGU) Fall Meeting 2022 Abstracts (Vol. 2022, pp. A34B-01). https://agu.confex.com/agu/fm22/meetingapp.cgi/Paper/1163591

2. **Ansari, K.**, & Ramachandran, S. (2023). Physical and Optical Characteristics of Aerosols over Asia: AERONET, MERRA-2 and CAMS. In Indian Aerosol Science and Technology Association (IASTA) 2023 Conference Proceedings (pp. 140-141). doi:10.5281/zenodo.10321321

3. **Ansari, K.**, & Ramachandran, S. (2023). Single scattering albedo of aerosols during COVID-19 lockdowns: Satellite observations and model simulations. In AGU Fall Meeting 2023 (A21-09). https://agu.confex.com/agu/fm23/meetingapp.cgi/Paper/1386129

4. **Ansari, K.**, & Ramachandran, S. (2024). Aerosol optical and radiative properties over Asia: Ground-based AERONET observations. European Geosciences Union (EGU) General Assembly 2024, Vienna, Austria, 14–19 Apr 2024, EGU24-907. doi:10.5194/egusphere-egu24-907

5. **Ansari, K.**, & Ramachandran, S. (2024). Aerosol absorption characteristics over Asia and the Rest of the World: AERONET observations and model validation. In AGU Fall Meeting 2024 (A07-55). https://agu.confex.com/agu/agu24/meetingapp.cgi/Paper/1669367

6. **Ansari, K.**, & Ramachandran, S. (2024). Global Insights on Optical and Radiative Characteristics of Aerosols. In IASTA 2024 Conference Proceedings (pp. 648-650). doi:10.5281/zenodo.15498453